Factors contributing to the yield strength of polycrystalline nickel-based superalloys

Amy Jane Goodfellow
Corpus Christi College

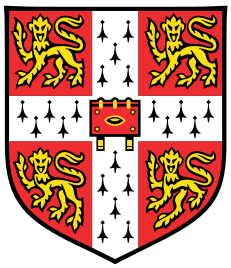

University of Cambridge
Department of Materials Science & Metallurgy

A dissertation submitted for the degree of
Doctor of Philosophy

February 2019

Preface

This dissertation is the result of my own work and includes nothing which is the outcome of work done in collaboration except as declared in the Preface and specified in the text. It is not substantially the same as any that I have submitted, or, is being concurrently submitted for a degree or diploma or other qualification at the University of Cambridge or any other University or similar institution except as declared in the Preface and specified in the text. I further state that no substantial part of my dissertation has already been submitted, or, is being concurrently submitted for any such degree, diploma or other qualification at the University of Cambridge or any other University or similar institution except as declared in the Preface and specified in the text. It does not exceed the prescribed word limit for the relevant Degree Committee.

Parts of this dissertation have been submitted or accepted for publication in:

A.J. Goodfellow, E.I. Galindo-Nava, K.A. Christofidou, N.G. Jones, T. Martin, P.A.J. Bagot, C.D. Boyer, M.C. Hardy and H.J. Stone. Gamma prime precipitate evolution during aging of a model nickel-based superalloy. *Metallurgical and Materials Transactions A*, 49(3):718-728, 2018. (Chapter 3)

A.J. Goodfellow. Strengthening mechanisms in polycrystalline nickel-based superalloys. *Materials Science and Technology*, 34(15):1793-1808, 2018. (Chapter 1)

A.J. Goodfellow, E.I. Galindo-Nava, K.A. Christofidou, N.G. Jones, C.D. Boyer, T.L. Martin, P.A.J. Bagot, M.C. Hardy and H.J. Stone. The effect of phase chemistry on the extent of strengthening mechanisms in model Ni-Cr-Al-Ti-Mo based superalloys. *Acta Materialia*, 153:290-302, 2018. (Chapter 4)

A.J. Goodfellow, E.I. Galindo-Nava, C. Schwalbe and H.J. Stone. The role of composition on the extent of individual strengthening mechanisms in polycrystalline Ni-based superalloys. *Materials & Design*, 173:107760, 2019. (Chapter 2)

A.J. Goodfellow, L.R. Owen, K.A. Christofidou, J. Kelleher, M.C. Hardy and H.J. Stone. The effect of temperature and Mo content on the lattice misfit of model Ni-based superalloys. *Metals*, *Accepted June 2019*. (Chapter 5)

A.J. Goodfellow, J. Kelleher, M.C. Hardy and H.J. Stone. The effect of Mo on load partitioning and microstrain evolution during compression of a series of polycrystalline Ni-based superalloys. *Acta Materialia*, *Submitted April 2019*. (Chapter 5)

Amy Jane Goodfellow

February, 2019

Abstract

Factors contributing to the yield strength of polycrystalline nickel-based superalloys

Today, the aerospace industry is facing progressively more stringent targets to mitigate its environmental impact. To achieve these targets by reducing CO_2 emissions and improving fuel efficiency, jet engines are being operated at higher temperatures and pressures. Although this is possible from an engineering perspective, these conditions are beyond the limit of current materials. Therefore, new materials must be designed that can withstand the more extreme conditions inside the future jet engine.

Polycrystalline Ni-based superalloys are the current materials of choice for use in the turbine discs, where high loads must be withstood at high temperatures and, as such, yield strength is of considerable importance. This thesis has investigated the underlying mechanisms that give rise to the appreciable yield strength of these materials. The aim of this work was to gain an improved understanding of these mechanisms and the microstructural features that affect them, in order to be able to facilitate the design of future, better materials.

In this thesis, Chapters 1 and 2 provide a background to the jet engine and the metallurgy of Ni-based superalloys. A review of the strengthening mechanisms occurring in these materials is given in Chapter 2. In Chapter 3, the individual models of the underlying strengthening mechanisms operating concurrently in Ni-based superalloys were combined to provide predictions of the overall yield strength of a number of commercial alloys. Although these were established models, when all of the individual strengthening mechanisms were taken into account it was found that the models did not compare well in magnitude to experimental yield strength data for the commercial alloys, though the trends were well described. To further explore the capability of these models, the role of composition on each of the individual strengthening mechanisms was investigated for the commercial alloy RR1000. Composition was found to have a complex role on the yield strength due to the multifaceted effect of elemental phase partitioning.

Although these models may enable some prediction of the instantaneous yield strength arising from a particular alloy and microstructure, the microstructural stability of these alloys is critical for maintaining alloy performance during service in gas turbine engines. In Chapter 4, precipitate evolution during ageing in a model polycrystalline Ni-based superalloy was studied via multiple experimental techniques, including SEM, TEM and APT. Variations in phase composition and precipitate morphology, size and volume fraction were observed during ageing, while the constrained lattice misfit remained constant at approximately zero. The experimental composition of the γ matrix phase was consistent with thermodynamic equilibrium predictions, while significant differences were identified between the experimental and predicted composition of the γ' phase. These results have implications for the evolution of mechanical properties in service and their prediction using modelling methods.

To this end, in Chapter 5, a series of model quinary Ni-based superalloys with varying Mo content were studied to investigate the underlying strengthening mechanisms introduced in Chapters 2 and 3. Using microstructural data, the yield strength was modelled by summing the individual effects of each underlying strengthening mechanism. The total predicted yield strength was found to increase with Mo content despite the diminishing contribution of precipitation strengthening. It was shown that solid solution strengthening of the ordered γ' precipitate phase is a key contributor to the overall alloy strength, and that variations in composition between the secondary and tertiary γ' lead to significant changes in mechanical properties that should be accounted for in models of alloy strength.

To further elucidate the role of the individual strengthening mechanisms on the overall yield strength and deformation behaviour, the room temperature deformation mechanisms of the model alloy series were studied by neutron diffraction during compressive testing, as described in Chapter 6. On initial loading, it was found that intergranular load partitioning was operative, followed by interphase partitioning at higher applied loads, with yield of the γ phase and associated strain redistribution to the γ' phase. The initiation of interphase load partitioning was found to be dependant on the magnitude of the lattice misfit, occurring at lower applied stress in alloys with larger lattice misfit. Notably, deformation behaviour was found to be contingent on the complex relationship between lattice misfit and individual phase strength, which were determined in Chapter 5.

As such, this work makes the case that current strengthening models in the literature do not provide a complete and quantitatively accurate picture of the yield strength of such complex materials as Ni-based superalloys. By improving these models, the methods described in this thesis may be collectively used to refine alloy composition and microstructure for optimal yield strength.

Acknowledgements

I am grateful to the Engineering and Physical Sciences Research Council (EPSRC) and Rolls-Royce plc. for their financial support for this project and to Professors Mark Blamire and Paul Midgley for the provision of research facilities within the Department of Materials Science and Metallurgy.

First and foremost, I would like to express my sincere gratitude to my supervisor, Dr. Howard Stone, for his unfailing advice, support and enthusiasm throughout the 4 years of my project. I am particularly indebted to Howard for his constant reassurance, motivation and especially for always being sagacious in his choice of words. My thanks also extend to my industrial supervisor, Dr. Mark Hardy, for useful discussions, advice and for the prolonged attempt to acquire material.

A special thanks must go to Dr. Enrique Galindo-Nava for introducing me to modelling and for all his support on a significant proportion of this work and Dr. Kathy Christofidou, for her help throughout the last 4 years, in particular our time in Canada.

I am grateful to all of the technical staff in the department; particularly to Dr. Hon Tong Pang and Ms. Sue Rhodes for training and helping me in the lab, to Mr. Simon Griggs, Mr. David Nicol and Dr. Jon Barnard for solving microscopy issues, to Mr. Andrew Rayment for mechanical testing, to Mr. Kevin Roberts and Ms. Sue Gymer for aiding me in the process lab and to all members of the workshop for graciously dealing with my last minute requests.

My thanks also extend to those outside of the department with whom I carried out experiments during the course of this work; the atom probe group at the University of Oxford for the prettiest figures in my thesis and Professor Dave Dye and colleagues at Imperial College London for being the ones who enabled me to finally make some material. Chapter 6 of this thesis would not have been possible without the help of Dr. Joe Kelleher at ISIS and Mr. Chad Boyer at Chalk River for their assistance with the neutron experiments. I thank Joe for taking my calls at the most unreasonable hours of the day, and I thank Chad for his unfailing sense of humour, which is how he rolls.

Thank you to all the members of the Rolls-Royce group who have made the last four years so enjoyable, and a huge thank you to the Gordon lab, who took me in as one of their own, even if they never let me forget it. In particular I would like to thank Caspar Schwalbe for always being there through the best and worst of times and for the continuous stream of affectionate swedish messages, and Megan McGregor for looking out for me always. Also, thank you to Duncan Johnstone, for being the consistency throughout my entire materials science career, and to MB for proving that all the best things take 4 years.

Finally, I would not be here without the love and support of my family; my parents, Alan and Alison, and my sister Kate. Thank you, for everything.

Contents

Chapter 1

Introduction

The world is increasingly environmentally conscious, yet at the same time, progressively globalised. In terms of air travel these two trends may seem to be in opposition, as people fly further and more often. These demands for an ever increasing amount of faster, more fuel efficient and cheaper air travel require new engine designs that are pushing the limit of current technology. The advisory council for aviation research and innovation in Europe (ACARE) have set targets for the aviation industry in their Vision 2020 [1] and Flightpath 2050 reports [2], which outline an agenda for the aerospace industry to fulfil the needs of a changing modern society. In terms of engineering and design there exists the knowledge to reach these targets. However, the materials used are now at the limit of current gas turbine engine technology. To reach current targets, new materials are required that can withstand the inimical conditions that will be encountered within future gas turbine engines.

1.1 The Jet Engine

Although seemingly complex, the jet engine functions simply due to Newton's third law of motion; for every action (or force) acting on an object, there is an equal and opposite reaction. Within a jet engine, this applies as air is forced in one direction, creating an equal and opposite force on the engine itself. This thrust moves the engine (and the attached aeroplane) forwards.

A turbojet is a gas turbine in its simplest form and functions in four continuous steps, as shown in Figure 1.1. First, air is drawn into the engine. It is then compressed through the compressor stages and mixed with fuel in the combustor. At this point the air ignites, causing it to expand through the back of the engine. As the hot air is expelled, it provides thrust on the engine and simultaneously powers the compressor by rotating the turbine blades attached to the central shaft. This cycle operates continuously and is governed by the Brayton cycle, which defines the variation of temperature, pressure and volume associated with this sequence [3].

The structure of the gas turbine engine is tailored to optimise this process. The air meeting the front of the engine is initially at atmospheric pressure. It is then directed to the first compressor stage where it encounters a series of rotating blades. These blades are progressively smaller and draw the air further into the engine through an increasingly narrow channel, which causes the air pressure to increase. After passing through a number of these compressive stages, the air pressure and the associated temperature is increased significantly [3].

When this highly compressed air enters the combustor, fuel is injected into the gas stream and ignited. To maximise efficiency there should be no associated drop in air pressure, although some reduction is inevitable. The maximum temperature that the air reaches in the combustor defines the turbine entry temperature (TET), which in turn defines the efficiency of the engine.

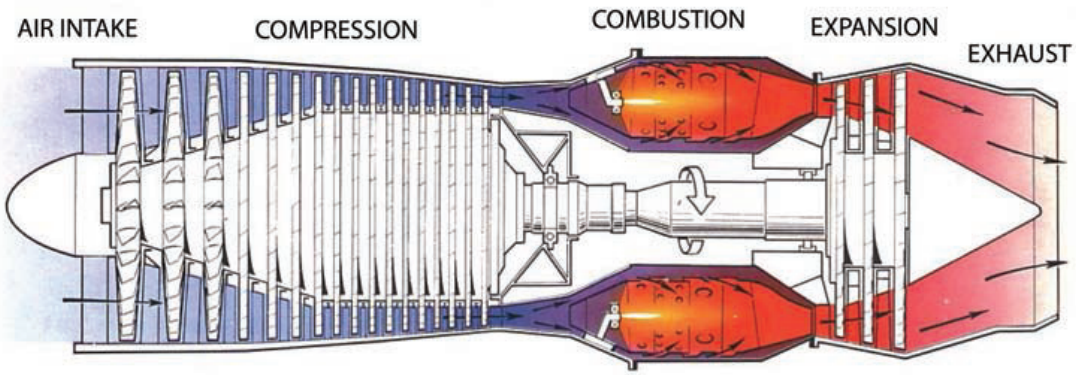

Figure 1.1: Schematic diagram of a turbojet engine, illustrating the four stages of the engine cycle, reproduced from [4].

After combustion the hot, compressed air travels though the high pressure turbines at the end of the engine, which progressively increase in size following a now expanding channel. As the air expands and cools through this section of the engine, it rotates the blades, which are attached to the central shaft, which is in turn attached to the front fan blades. In this way, the hot air passing out of the rear of the engine draws more air into the front of the engine, and the process is continuous. At the same time, the air leaving the engine imparts thrust onto the engine itself, thereby propelling the aircraft forwards.

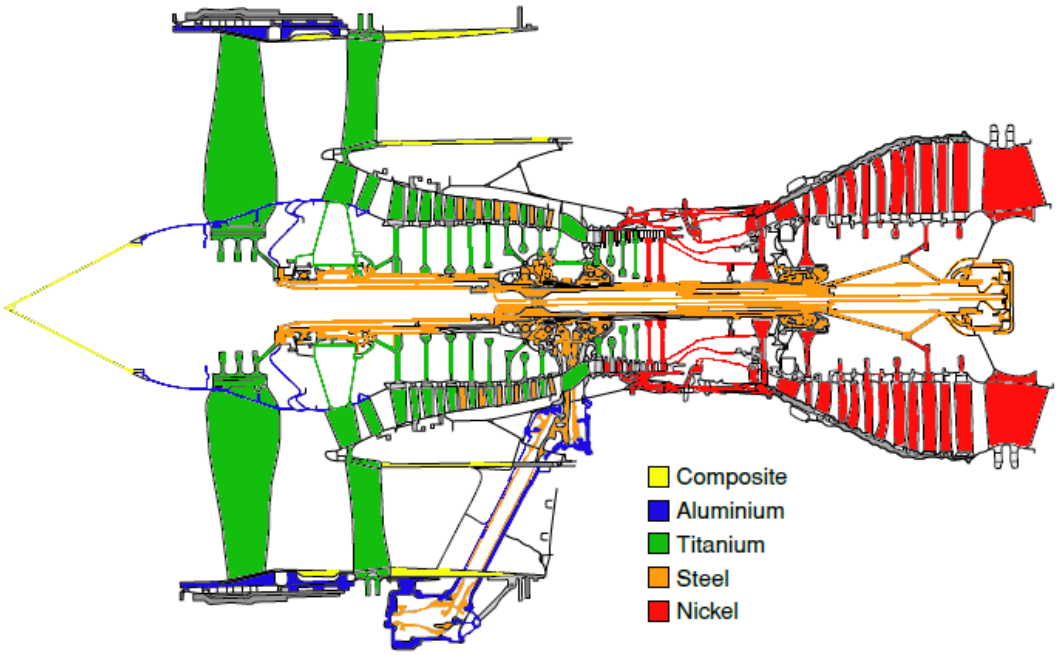

Figure 1.2: Schematic diagram showing material classes used in the Rolls-Royce Trent 800 engine, reproduced (courtesy of Megan McGregor) from [5]

A schematic diagram of a Rolls-Royce Trent 800 engine is shown in Figure 1.2, indicating the different classes of materials used for each component. In the hottest regions of the engine (the combustor and the following blades), Ni-based superalloys are used as only these alloys can withstand the extreme temperatures and stresses encountered in service. In fact, even these materials require a ceramic coating to withstand the most extreme temperatures, which reach over 1700 K [5], far above the melting point

of Ni. Since the fundamental laws of thermodynamics state that more power is extracted from a given expansion ratio at a higher entry temperature, the highest temperature able to be withstood by the materials used in the engine defines the limit of our current capability. Therefore to operate gas turbine engines more efficiently, a higher turbine entry temperature (TET) is required, past the temperature limit of the materials that can withstand the current conditions [6].

1.2 Turbine Discs

A key component of gas turbine engines is the disc. These are crucial engine components that are used to affix the turbine blades to the rotating shaft, enabling mechanical work (and power) from the gas stream to be transferred back to the compressor stage of the engine. Turbine discs experience lower temperatures than the blades ($\sim 650°C$), since they are further from the hot gas stream. However the stresses on the discs are huge, due to the rapid rotational speeds [5]. Further complications arise since the temperatures and stresses achieved differ in the rim and bore of the discs. In a Rolls-Royce Trent 800 engine, a standard rotational speed of the discs is 10,500 rpm, leading to stresses as high as 1000 MPa in the bore, (compared to 180 MPa at the blade root) [5]. While withstanding these acute conditions, discs must be designed to a minimum weight and maximum reliability to ensure cost-effectiveness and safety. The latter is particularly important given that disc failure is often catastrophic.

This combination of high temperature and high stresses is only withstood by the polycrystalline superalloys. These are used in the turbine discs, where the limiting factor is fatigue due to the extreme stresses involved. At temperatures up to $\sim 800°C$, these materials can withstand stresses over 1 GPa without failure [7]. Disc materials must also have high strength (in particular ultimate tensile strength) for overspeed requirements, since they must not fail in situations in which the engine operates at higher rotational speeds than normal.

Fatigue can be split into the regimes of high- and low-cycle fatigue (HCF and LCF respectively). Fatigue in general originates during oscillating loads at stresses in the elastic range, and often occurs at stress concentrations, e.g. defects such as pores [8]. LCF occurs at stress amplitudes near the limit to the elastic regime, with failure often within 10^5 cycles [5]. LCF is caused by events such as take-off and landing [9]. In contrast, HCF occurs at much smaller stress amplitudes - well within the elastic limit - for example those caused by vibrations during service [9]. In this case, failure occurs after 10^5 cycles [5]. The fatigue properties of a particular alloy depend on the loading direction, due to the elastic anisotropy. Elastically soft directions (e.g. $\langle 001 \rangle$) have superior fatigue properties to hard directions (e.g. $\langle 111 \rangle$) [10].

Fabrication

Discs can be produced for gas turbine applications via two routes. Both end in machining of a forged billet, but the billets themselves can be prepared either by ingot or powder metallurgy. The former is used for alloys with fewer alloying additions, whereas the latter is much more expensive, and can therefore only be justified in the case where many alloying elements are involved and inhomogeneity is more problematic [5].

Ingot metallurgy involves three processes - vacuum induction melting (VIM), electro-slag remelting (ESR) and vacuum arc remelting (VAR). The billet is then annealed, worked and forged to reduce inhomogeneity and improve the mechanical properties by reducing grain size.

The powder metallurgy route also involves VIM, but the subsequent billet is then atomised into powder. This powder is then cleaned by sieving to remove ceramic inclusions, then vacuum degassed and hot isostatically pressed to produce a billet. This billet can then be forged, as in the ingot metallurgy

route. Powder metallurgy is more costly than ingot metallurgy and involves a more complex process, but is used to produce much cleaner alloys [5].

Due to the exceptionally high stresses experienced by the turbine discs at relatively low temperatures, alloys used for disc applications must have high resistance to fatigue crack nucleation and growth. This requires sufficient ductility and fracture toughness. Concurrently, maximising yield strength is of the utmost importance. To achieve these properties, polycrystalline alloys of carefully controlled composition and structure are used.

The following guidelines have been suggested for designing disc alloys [5]:

1. The γ' volume fraction should be around 0.40-0.55 to optimise fatigue resistance.
2. An optimum grain size must be produced to simultaneously maximise fatigue and creep resistance.
3. Grain boundary-strengthening elements (B and C) must be present in sufficient quantities, but not high enough to promote the excessive formation of carbides and borides.

There are also other considerations; elemental additions are required to impart solid solution strengthening to the γ phase, whilst avoiding excessive formation of topologically close packed (TCP) phases, and Cr is essential for oxidation resistance. Additionally, the heat treatment used is essential as this defines the volume fraction and size of the γ' precipitates formed. Unfortunately, the optimum size and volume fraction of the precipitates differs in the case of fatigue crack propagation and yield strength. There is also an inverse correlation between fatigue strength and creep strength, since the yield strength and fatigue crack nucleation rate are improved with decreased grain size, whereas the creep life and fatigue crack propagation are improved with increased grain size. As with most things, a compromise is required [11].

Literature exists on the possibility of developing different grain sizes in the bore and rim regions of the disc, using a furnace containing a sharp temperature gradient, but this is not yet commercially used [12]. These dual microstructure heat treatments (DMHT) generate a coarser grain size at the disc rim, where the temperature is higher and creep is therefore more of an issue, but a finer grain structure in the bore, where lower temperatures mean that fatigue resistance is more important. Gayda et al. [13] have shown that DMHT resulted in improved properties compared to conventional heat treated alloys in high temperature tensile, fatigue and creep testing.

It has been shown that small additions of C and B can increase the rupture life of discs, but if the concentration is too high, carbides and borides are formed, and the rupture life is decreased. Reed states the optimum values of C and B are 0.025wt% and 0.03wt% respectively [5]. Further study of this effect is required, however, since the mechanisms of this strengthening are not well understood.

Chapter 2

Literature Review

To provide a background to the experimental work described in this thesis, this chapter provides a review of relevant past literature. The review starts by describing the metallurgy of Ni-based superalloys, including microstructure and composition, before moving on to detail the mechanisms that give rise to the impressive yield strength of these materials. Finally, an outlook is provided which rationalises the reasons for the current work of this thesis, and places this work into the full context of the previous literature.

2.1 Ni-Based Superalloy Metallurgy

Ni-based superalloys consist of a matrix of face-centred cubic (FCC) γ phase, containing a large volume fraction of ordered, coherent γ' phase precipitates (Figure 2.1). These precipitates significantly increase yield strength, through various mechanisms. The metallurgy of these phases is described in detail below.

The γ Phase

Ni is used as the base element for many superalloys due to its excellent high temperature properties. Decker [14] attributes this to two reasons; the unfilled 3d electron shell, and the ability to form coatings of Cr_2O_3 when alloyed with Cr. The former means that Ni provides a good solvent for other elements, forming stable alloys. The latter results in a protective oxide layer which reduces oxygen and sulphur diffusion into the alloy, and that of metallic elements out of the alloy [14].

The γ phase is predominantly Ni with other alloying additions in an A1 (Strukturbericht notation) FCC structure, and forms the disordered matrix phase of Ni-based superalloys. It must be stable over large regions of the phase diagram (Figure 2.2) in order to be suitable for use in high-temperature applications, as the transformation into other phases would be detrimental to the mechanical properties.

Ni is relatively dense compared to other metals such as Al, but the latter cannot be used for high-temperature applications since it is molten at the temperatures experienced in the gas turbine engine. The melting point of Ni, at $\sim 1455°C$, provides the very limit of its use at high temperatures, although this value will depend on the alloying elements included, in addition to the coatings and cooling systems used.

Certain elements (e.g. Cr, Co, Mo and W) are added to Ni-based superalloys for many reasons (Table 2.1).

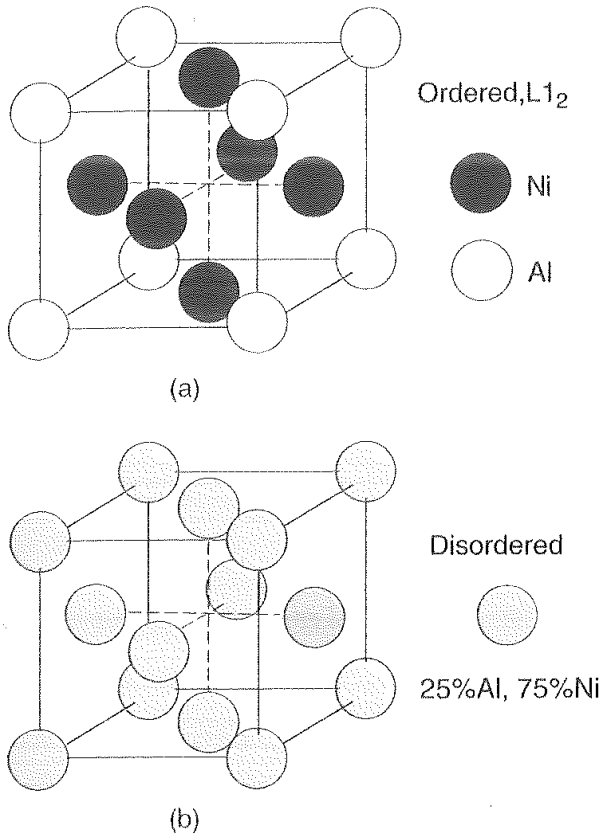

Figure 2.1: Diagrams showing the unit cells of the (a) γ' and (b) γ phases [5]

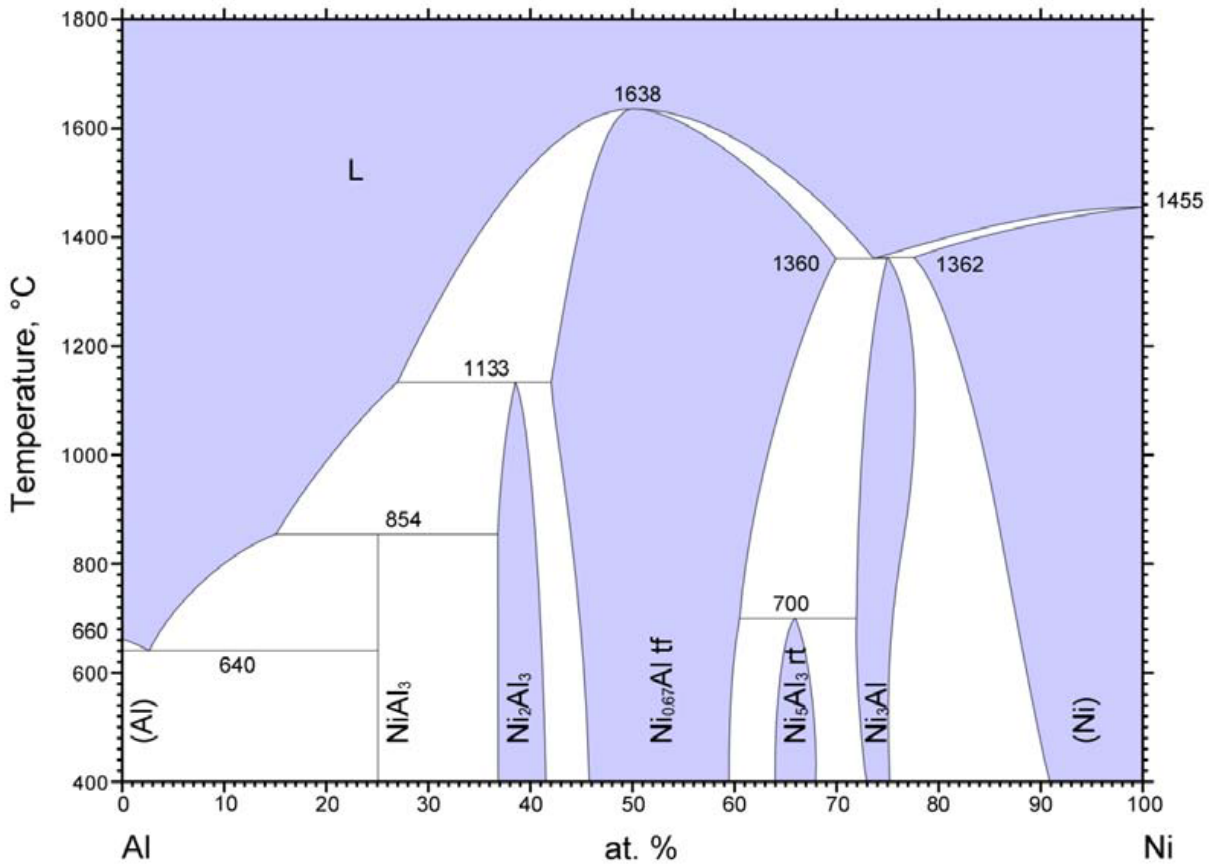

Figure 2.2: The Al-Ni phase diagram [4, 15].

Element	Role
Al	Primary γ' former Increases resistance to oxidation
Co	Increases solid solution strengthening of γ Reduces stacking fault energy Increases susceptibility to topologically close packed (TCP) phase formation
Cr	Increases resistance to oxidation Increases solid solution strengthening of γ Increases susceptibility to TCP phase formation Increases susceptibility to $M_{23}C_6$ carbide formation†
Mo	Increases solid solution strengthening of γ Increases susceptibility to TCP phase formation Increases susceptibility to carbide formation
Nb	Increases solid solution strengthening of γ Increases volume fraction of γ' Reduces γ' size Increases susceptibility to MC carbide formation†
Ta	Increases solid solution strengthening of γ' Increases volume fraction of γ' Increases susceptibility to MC carbide formation†
Ti	γ' former Increases Anti-Phase Boundary Energy (APBE) Increases susceptibility to MC carbide formation† Reduces resistance to oxidation
W	Increases solid solution strengthening of γ Increases susceptibility to TCP phase formation Increases susceptibility to M_6C carbide formation†

Table 2.1: The role of common alloying additions to Ni-based superalloys [5, 16–19]. †M refers to a metal atom.

The γ' Phase

Ni-base superalloys can attribute their exceptional high temperature properties to the presence of coherent γ' precipitates within the γ matrix. γ' precipitates convey strength to these alloys at high temperatures for multiple reasons, which are fully discussed in Section 2.6.

The γ' phase has the stoichiometry $Ni_3(Al, Ti)$ and occurs in the $L1_2$ structure (Strukturbericht notation), with Ni atoms on the face centres, and Al on the cube corners. The lattice parameters of both phases are very similar, so γ' mostly remains coherent with the matrix with a low interfacial energy and has a cube-cube orientation relationship with the γ matrix phase. To reduce any resulting strain in the matrix, the precipitates are often positioned along $\langle 100 \rangle$ directions, which are elastically softer in the γ matrix [5], and as such, the precipitates are positioned in a cube-cube orientation with regard to the matrix [20].

The distribution of precipitate sizes, and their shape, can be controlled by careful selection of heat treatment and cooling rate from high temperature. Often a multi-modal distribution of precipitate sizes is present. The exact size and shape of the precipitates required to provide the desired mechanical properties is dependent on the particular application of the alloy.

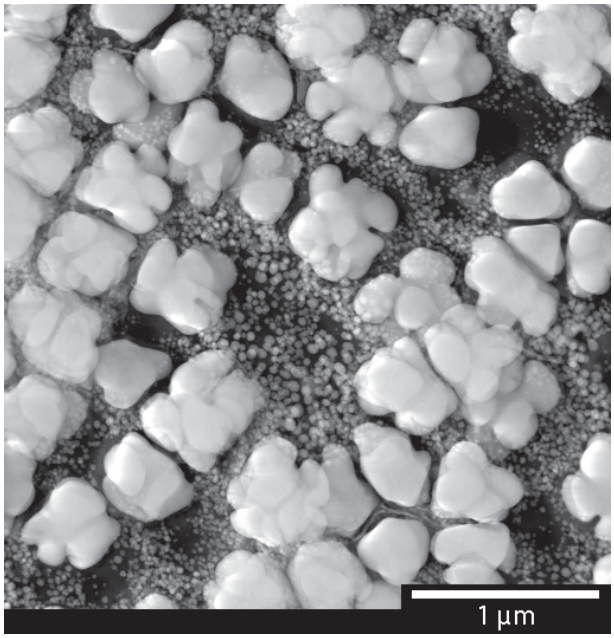

Figure 2.3: A bimodal distribution of secondary and tertiary γ' precipitates in a Ni-based superalloy.

Disc alloys commonly contain trimodal precipitate size distributions with large (primary) γ' precipitates with size of the order of 1 µm. These are only found in alloys heat treated below the γ' solvus temperature, since these precipitates are present in the initial material and dissolve if heat treated above the solvus temperature. Primary γ' precipitates are located on the γ phase grain boundaries and prevent coarsening of the γ grains during heat treatment. Secondary γ' (~ 200 nm) and tertiary γ' (~ 10 nm) (as shown in Figure 2.3) are located within the γ grains and give rise to the impressive mechanical properties of these alloys [21].

In general, precipitates may form by nucleation and growth or by spinodal decomposition from composition fluctuations within the γ matrix [22]. Radis et al. [21] investigated the formation of multimodal γ' distributions in Ni-based superalloys and identified that this occurs through three simultaneous processes. As temperature decreases, initially the Gibbs free energy change on nucleating γ' and the nucleation rate increase. After a certain point however, the levels of solute in the γ matrix are depleted, so both the Gibbs free energy change, and the nucleation rate decrease with decreasing temperature. On further

cooling, channels of higher solute content exist between the precipitates, due to the lower mobility of the solute atoms at lower temperature. These regions then give rise to a second burst of nucleation. As the composition in these regions is different, the resulting γ' compositions formed from these regions will also differ. This explanation is in agreement with the data of Chen et al. [23].

According to Decker [14], the γ' phase forms preferentially over other phases because the Ni atom cannot be significantly compressed, due to its 3d electron state. This negates the formation of phases that require a more significant change in the lattice parameter. Additionally, both γ and γ' phases have very similar crystallographic structures which, along with the similar lattice parameters, eases nucleation and growth of the precipitates.

The γ'' Phase

In alloys containing significant quantities of niobium, the metastable γ'' phase is formed. Depending on the amount of γ'', this phase may offer the major strengthening effect within the alloy, rather than the γ' phase.

The γ'' phase is also ordered, but with a body-centred tetragonal (BCT) structure, $D0_{22}$ (Figure 2.4). The stoichiometry is approximately Ni_3Nb. The structure is very similar to the γ' phase, with Ni atoms occupying the face centres, but in the γ'' phase, the face corners are occupied by Nb atoms. The unit cell is also similar to that of the γ' phase, except that the c-length is approximately double in the γ'' structure. The resulting structure appears as two γ' unit cells separated by an anti-phase boundary (APB).

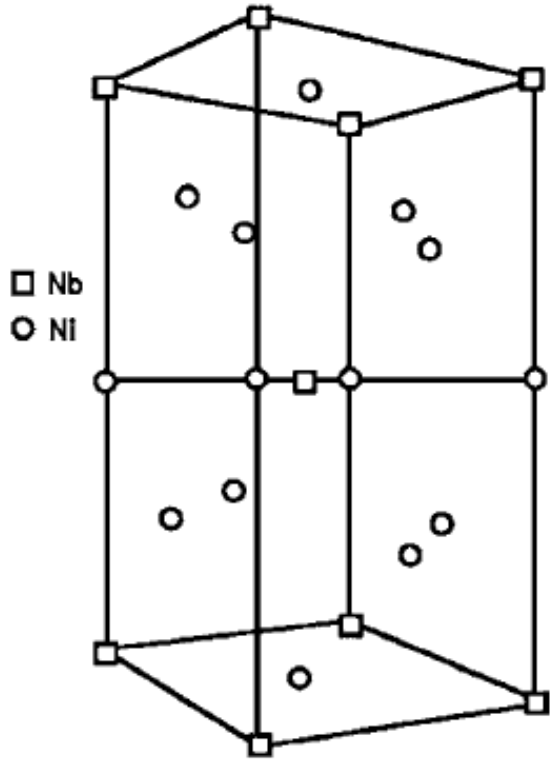

Figure 2.4: Diagram showing the body-centred tetragonal unit cell of the γ'' phase [5]

The γ'' phase has an orientation relationship with the matrix phase, just as the γ' phase. The $\langle 100 \rangle$ directions are aligned and coherent with the matrix, so γ'' is most often seen as discs with faces along $\langle 100 \rangle$. These precipitates have only a small number of operative slip systems, giving good strength

properties to alloys containing this phase (e.g. IN718). Unlike the γ' phase, however, the γ'' phase forms very slowly due to the large lattice misfit [5].

Oblak et al. [24] showed that the shape of the γ'' phase allows the resulting tetragonal distortion to be used to control the orientation or variant of the precipitate present in the microstructure, by applying a directional stress during heat treatment. By optimising the microstructure in this way, the resulting critical resolved shear stress of the alloy can be increased by over 100 MPa.

The δ Phase

The γ'' phase is metastable and, as such, the thermodynamically stable phase, δ, can also exist. δ phase has an orthorhombic structure and is easily formed in alloys strengthened by γ'' during ageing within the temperature range $\sim 650 - 980°C$. δ is detrimental to the mechanical properties because it is incoherent with the matrix, although it has a well defined orientation relationship with some coherent planes. However, it is possible to use δ to control grain size [5].

Carbides and Borides

In superalloys with additions of carbon or boron, carbide and boride phases can form. Various types exist, depending on alloy processing conditions.

It has been shown that carbides such as $M_{23}C_6$ (M referring to a metal atom) form along the grain boundaries in alloys with coarse grains, leading to γ' precipitate-free regions along the γ grain boundaries [25]. Since the γ' precipitates are important strengtheners, this reduces the yield strength.

Some elements aid the formation of carbides and borides, and preferentially exist on the grain boundaries due to their much larger atomic radii than Ni. These include Cr, Mo, Ta, Ti and W. Since these elements partition to the grain boundaries, these carbides and borides are also commonly found at these grain boundaries [5]. Carbides often form as MC initially, but decomposition at lower temperatures during service can occur, resulting in $M_{23}C_6$ or M_6C carbides.

The MC species is often found in interdendritic regions of the matrix phase, since it precipitates from the liquid phase at high temperatures. It has little orientation relationship with the γ phase, so is often globular or blocky in shape [26].

C and B are added to many polycrystalline superalloys to improve creep life, since they preferentially exist on the grain boundaries and can therefore limit grain boundary sliding. Chen and Knowles [27] have shown that the fine, coherent $M_{23}C_6$ carbides present in an experimental superalloy actually improved the creep rupture life by a factor of 10.

Topologically Close Packed (TCP) Phases

Other phases, termed topologically close packed phases, may exist in the microstructure of superalloys. These include Laves, μ and σ phases (Table 2.2). These are readily formed in alloys with large concentrations of elements such as Mo, Cr, W and Re.

TCP phases are so called due to their very high atomic packing density and large, complicated crystallographic structures that are bonded covalently. These structures are composed of many layers of smaller atoms (Ni, Cr), with the larger atoms (Re, W, Ta) occupying the spaces between the layers [28]. Within these layers, atoms are bonded in many shapes depending on the specific TCP phase, including triangles, pentagons and hexagons. The layers themselves tessellate to form one of four coordination environments (the "Kasper co-ordination polyhedra") with coordination numbers of either 12, 14, 15 or 16 [28, 29].

Although TCP phases are based on transition metals in the chemical formula A_xB_y, their compositions range around this exact stoichiometry.

TCP Phase	Stoichiometry	Unit Cell	Examples
μ	A_6B_7	Rhombohedral	W_6Co_7, Mo_6Co_7
σ	A_2B	Tetragonal	Cr_2Ru, $Cr_{61}Co_{39}$, $Re_{67}Mo_{33}$
P		Orthorhombic	$Cr_{18}Mo_{42}Ni_{40}$
R		Rhombohedral	$Fe_{52}Mn_{16}Mo_{32}$

Table 2.2: Common topologically close packed (TCP) phases found in Ni-based superalloys.

2.2 Composition of Commercial Ni-Based Superalloys

Ni-based superalloys are complex materials, often containing upwards of 10 different alloying additions. The most common are Al, Ti and Cr. Other common additions are Co, Mo, W, Ta, Nb, Fe, Re, Zr, B and C. Most of these come from the d-block transition metals of the periodic table.

Different elements partition to either the γ or γ' phase preferentially (although some, such as W, reside in both phases). Elements including Co, Cr, Mo, Ru and Re partition to the FCC γ phase due to their similar atomic size to Ni. In contrast, elements such as Al, Ti, Ta and Nb have larger atomic radii and prefer to reside in the γ' phase. Some elements (B, C and Zr) are very different in atomic size to Ni and so often segregate to grain boundaries or form carbides and borides [5].

The compositions of Ni-based superalloys are varied, particularly between the polycrystalline (PX) alloys used for turbine disc applications and the single crystal (SX) alloys used for turbine blades, where creep is the life-limiting factor (Table 2.3). An obvious difference between the compositions of the PX and SX alloys is that the latter require no grain boundary strengthening elements, such as C and B. Alloy composition has altered over time [5]; the first-generation SX alloys contained high contents of the γ' partitioning elements (Al, Ti, Ta), second- and third-generation alloys contained additions of Re ($\sim$3 at.% and $\sim$6 at.% respectively) for creep resistance, whilst modern alloys have reduced Cr and Mo contents to reduce the lattice misfit, higher Al and Re contents and additions of Ru to reduce creep.

In general, PX superalloys generally contain reduced contents of the γ' partitioning elements, with Ta often omitted. This is due to the fact that the PX alloys typically require lower γ' volume fraction. Also, Fe and Nb are often added to the PX alloys, and the Cr content is typically much higher than in SX alloys [5].

Alloy chemistry can be altered to change the mechanical properties. For example, it has been predicted in a neural network model by Jones and Mackay that the addition of 5 wt. % Mo to Astroloy increases the yield and tensile stresses by roughly 200 MPa [30].

Depending on its size, and whether an element segregates preferentially to the γ or γ' phase, the lattice misfit of the alloy may change. For example, Mo partitions to the γ phase where its large atomic radius results in an increase of the lattice parameter of the γ phase. Since very little Mo partitions to the γ' phase, the lattice parameter of that phase does not change. Overall therefore, Mo additions cause a decreasing lattice misfit in a positively-misfitting alloy (or an increasing negative lattice misfit in a negatively-misfitting alloy). Positively misfitting precipitates are those where the precipitate lattice parameter is larger than that of the matrix. Negatively misfitting precipitates have a larger atomic spacing in the matrix phase.

Alloy	SX/PX	Cr	Co	Mo	W	Al	Ti	Ta	Hf	Re	C	B	Zr	Ni
RR1000	PX	15.0	18.5	5.0		3.0	3.6	2.0	0.5		0.027	0.015	0.06	Bal.
Udimet720	PX	17.9	14.7	3.0	1.25	2.5	5.0				0.035	0.033	0.03	Bal.
Waspaloy	PX	19.5	13.5	4.3		1.3	3.0				0.08	0.006		Bal.
CMSX-4	SX	6.5	9.6	0.6	6.4	5.6	1.0	6.5	0.1	3.0				Bal.
CMSX-10	SX	2.0	3.0	0.4	5.0	5.7	0.2	8.0	00.3	6.0				Bal.
Mar-M002	SX	8.0	10.0		10.0	5.5	1.5	2.6	1.5		0.15	0.015	0.03	Bal.

Table 2.3: Compositions of some commercial SX and PX Ni-based superalloys, in wt.% [5].

2.3 Correlations between γ' Size and Composition

Chen et al. [31] have shown that the composition of primary γ' is not dependent on size. This is expected since these precipitates do not dissolve during the heat treatment and are therefore dependent on the fabrication procedure rather than the subsequent heat treatment. In contrast, Chen et al. found that there is a continuous variation in composition of secondary and tertiary precipitates with size. The contents of some elements (e.g. Co) decrease with precipitate size, whereas others increase (e.g. Al) and some are constant (e.g. Ti, Ta and Cr). A continuation of this study by Chen et al. [23] found that the composition of the secondary γ' are near to that predicted at equilibrium, whereas the tertiary γ' have compositions further from the equilibrium values. These data are required as inputs to many other models in the literature, for example those which use diffusion data to model the strength of these superalloys.

This size dependent compositional variation occurs as the different γ' size distributions (secondary and tertiary γ') form on cooling from the supersaturated γ matrix at different temperatures. As the temperature decreases, the matrix becomes less concentrated in certain elements, which have partitioned into the secondary γ' precipitates as they nucleate. On further cooling, the matrix can again nucleate more γ' precipitates, but as the γ composition is now changed, that of the corresponding γ' is also changed. These (tertiary) γ' end up smaller than the secondary, as they form at lower temperature where atomic diffusional mobility is decreased, and they have less time at temperature to coarsen. Reduced diffusion also affects the final composition of the tertiary γ', since the mobility of the elements are reduced. Therefore, the secondary and tertiary γ' distributions will have different compositions to each other [21], with the tertiary γ' being further from equilibrium.

Additionally, Chen et al. [23, 31] have found that the composition of secondary and tertiary γ' varies continuously with size in RR1000, even within each general size distribution. The composition of Al was found to decrease with increasing size, from 17.0 at.% in tertiary γ' of $\sim$20 nm size to 12.3 at.% in secondary γ' of $\sim$250 nm. In contrast, the content of Co increases with precipitate size, though to a lesser extent than Al (from 7.5 at.% to 8.6 at.%). In the same study [31], Ti, Ta and Cr contents were shown to remain roughly constant with changing precipitate size.

The Ti content in the tertiary γ' was found to be linked to the cooling rate in the same alloy, increasing from $\sim$7.7 at.% to 9.6 at.% as the tertiary γ' size increased from 20 nm to 250 nm for slow cooling rates (1 and 10 K min^{-1}). In contrast, at fast cooling rates (100 K min^{-1}) there was little compositional variation with precipitate size [23].

A possible explanation for these results is the depletion of the matrix supersaturation of certain elements on cooling, resulting in the smaller tertiary γ' precipitates (formed at lower temperatures, later in the cooling process) having a lower content of those elements. The first precipitates to form do so closest to the equilibrium matrix composition, thereby depleting the matrix of certain elements. These precipitates (the largest secondary γ') will therefore have the most near-field equilibrium compositions. It was seen that the Al content is high in the smallest precipitates [31], which could be explained by an increasing supersaturation of Al during cooling, leading to higher Al content in the precipitates formed at lower temperatures. However this would only occur if other elements were concurrently decreasing in supersaturation, which is not the case.

The explanation given by Chen et al. [23, 31] for these results is the unusual diffusion behaviour of Al, namely antisite bridging. Since Al requires a lower activation energy to sit on antisite positions in the ordered γ' lattice than other elements, it more readily diffuses on both sublattices, thereby increasing its diffusivity in the precipitate phase. This explains the increased Al content in smaller precipitates, which form at lower temperatures where diffusion is slower. In contrast, the opposite observed dependence of composition on precipitate size was seen for other elements such as Co, since these elements have lower

mobility at these lower temperatures than that of Al.

2.4 Morphology of the γ' Phase

Controlling the precipitation during cooling from homogenisation or ageing temperatures enables a fine control over the mechanical properties of the resulting alloy [32]. The cooling rate has a significant effect on the shape of the precipitates, which can vary from spheres [33] to cubes to complex dendritic structures [21, 34, 35].

The shape of precipitates is due to the elastic anisotropy of the γ' phase, and the coherency strains involved. For example, the $\langle 111 \rangle$ direction has roughly double the stiffness of the $\langle 001 \rangle$ direction, and the resulting strain energy is minimised by a cubic precipitate shape [6, 36].

In a system without internal stress, coarsening of precipitates is driven simply by the reduction of interfacial energy as proposed in the Lifshitz, Slyozov, Wagner (LSW) theory [37, 38] for very low precipitate volume fractions. This has been shown to occur for some Ni-base superalloys (RR1000, Udimet 720 and the experimental alloy UC01) cooled at slow billet cooling rates. However, more complex cooling results in different morphological changes [39].

The shape of the precipitates in an alloy is also determined by the lattice misfit. In particular, the precipitate shapes will depend on whether the alloy is positively or negatively misfitting, or has zero misfit.

For positively misfitting alloys, the initially spherical precipitates start to become faceted on the $\{001\}$ planes as they grow larger, due to the elastic anisotropy. At this stage, the precipitates and matrix are still completely coherent. Ricks et al. [20] used EDX to determine the compositional variation in the matrix surrounding these precipitates, and found that titanium is depleted near the precipitate interface, whereas chromium is enriched. In the same study it was shown that as the precipitates continue to coarsen, the precipitate corners grow and also develop facets on the $\{001\}$ planes. This coarsening occurs due to growth along the $\langle 111 \rangle$ directions. Subsequent precipitate growth (continued in the $\langle 111 \rangle$ directions) produces a morphology similar to dendrites (Figure 2.5). Similar results are found elsewhere in the literature [35, 40] and explained as the competition between the elastic energy of the precipitates (significant at large particle size) and the interfacial energy (significant at small particle size). However, in positively misfitting Ni-Al alloys, Lund and Vorhees [36] found that the γ' do form elongated rods or plates at long ageing times, but not dendritic morphologies.

Negatively misfitting alloys have been shown to coarsen similarly to positively misfitting alloys [20, 40]. However, the cube corners protrude with an "arrowhead" shape, in contrast to the planar growth described above. Additionally, networks of interfacial dislocations develop early on in the coarsening process, thereby causing a loss of coherency [20]. When the precipitates are sufficiently large, it is suggested that growth actually does occur due to compositional effects (as in real solid-state dendrites) and the solute gradient at the precipitate-matrix interface, as opposed to strain effects [20].

Alloys with zero misfit retain the spherical precipitate shape much longer due to the very low elastic (coherency) strain in the γ matrix [20]. Alloys with very high misfits have much larger resulting coherency strain, and so changes in precipitate morphology (as just described) happen at smaller precipitate size [20, 40]. It has been shown that for a certain ageing time, the larger (more positive) the misfit (and associated coherency strain), the larger the average precipitate size [40].

Alloys with low misfit have been shown to coarsen at a steady rate, with the particle size distribution staying constant during ageing. In contrast, high misfit alloys show a reducing coarsening rate, while the particle size distribution gets sharper throughout ageing [41].

However, there is further evidence to suggest that γ' precipitates do not simply coarsen as described

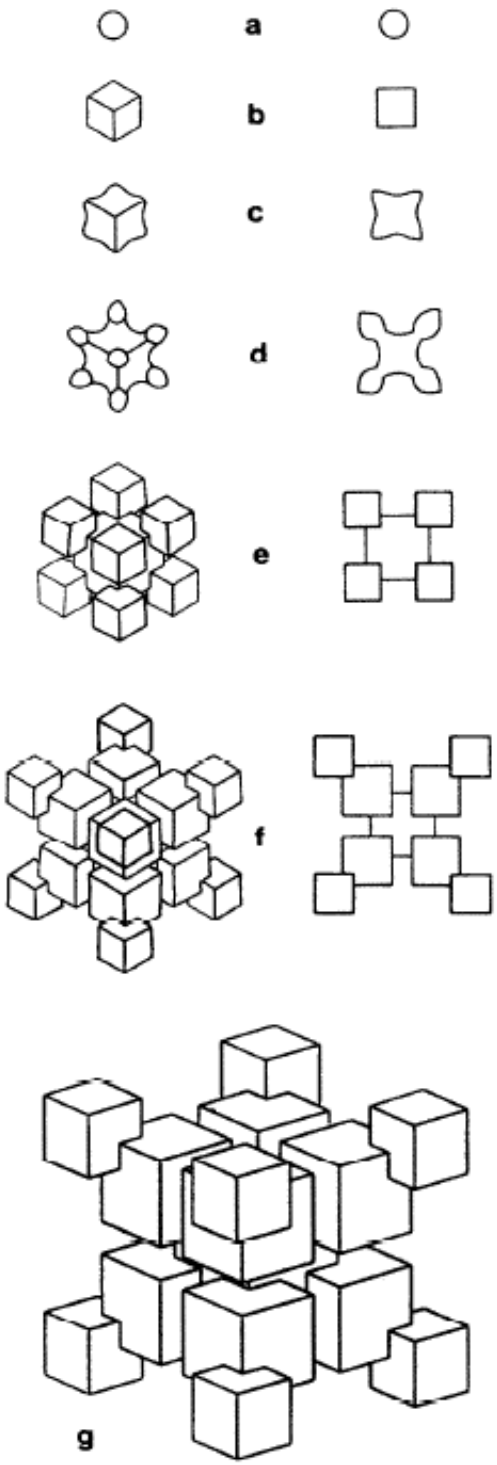

Figure 2.5: Schematics of the differing morphologies seen in precipitates of increasing size [20].

in Figure 2.5 or by Ostwald ripening, but instead, morphological instabilities result in a cyclical variation in precipitate shape during ageing.

Yoo [42] has shown that morphological instabilities arise in spherical γ' particles on rapid cooling. It is suggested that instability occurs when a second phase grows via a diffusion-controlled mechanism, into a supersaturated initial phase. Morphological instability is encouraged in systems with an isotropic interfacial energy, widely spaced precipitates and low lattice misfit and diffusivity within the precipitate phase, thereby promoting a dendritic morphology.

As expected, the coherency strain governs the final precipitate shape, with high lattice misfits producing elongated dendrites, and negligible lattice misfits resulting in more equiaxed dendrites.

It is important to distinguish between morphological instability and the phenomenon of octet splitting. Morphological instability occurs due to faster growth in certain directions, as for standard dendrites. Octet splitting, however, is caused by minimising strain energy, resulting in a similarly dendritic morphology. Yoo [42] stated that morphological instability is not dependent on lattice misfit, simply requiring supersaturation of the matrix phase, whereas octet splitting requires large lattice misfits.

Splitting of γ' precipitates occurs cyclically with ageing time [39, 43, 44]. The driving force is the reduction of interfacial energy, and the rate is controlled by the interface migration speed or diffusion. Secondary γ' precipitates coarsen cyclically, firstly growing in size, then becoming unstable and splitting into smaller precipitates. This process repeats, with splitting occurring when the decrease in elastic strain energy is greater than the resulting increased interfacial energy (Figure 2.6). In agreement with Yoo [42], Chen et al. [43] state that splitting occurs in high misfit alloys. However it is also seen in the near-zero misfitting alloy studied by the latter, and this is unexplained.

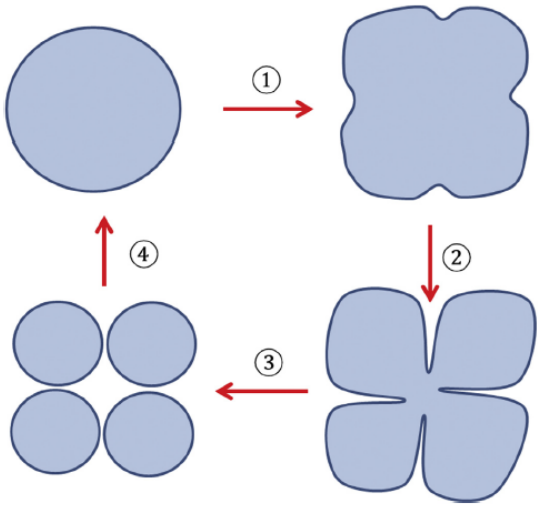

Figure 2.6: Illustration of the cyclical coarsening and splitting of secondary γ' precipitates [43].

The composition of the secondary γ' is also seen to vary cyclically with the splitting phenomenon. Immediately after splitting, Chen et al. [43] found that the Al concentration is a maximum, and the Co concentration is a minimum. These elements otherwise, on average, increase and decrease in the γ' phase with ageing time respectively. Ti content is seen to remain constant with ageing time, although local minima are seen after each splitting event. It is therefore concluded that this compositional variation causes the splitting, by affecting the lattice misfit and therefore the local strain field around each precipitate. This is in agreement with Mitchell and Preuss [35, 39] who concluded that the slow diffusion of Ta results in morphological instability.

As well as morphology and composition, mechanical properties such as hardness are also seen to vary cyclically with ageing time. Additionally, ageing is seen to cause cyclical variation in the presence of

tertiary γ' within the microstructure. For example, in alloy UC01, no tertiary precipitates were seen after 8 hours even though they were clearly visible after only 4 hours [39]. In this same study, it was found that maximum alloy hardness occurred when there were no tertiary γ' precipitates present, and the secondary γ' precipitates were at their smallest size.

Mitchell and Preuss [39] noted the importance of measuring the unconstrained lattice misfit, since the overall misfit strain changes only negligibly in the alloys studied, whereas the unconstrained misfit and elastic strains vary cyclically. Since the elastic strain decreases as the unconstrained misfit becomes more positive, overall there is little visible change in the misfit strain. This highlights the importance of closer investigation of the misfit, as opposed to simply measuring the overall value.

Irregularly-shaped γ' is commonly seen in Ni-based superalloys, and the above-mentioned splitting phenomenon is widely recognised as the mechanism. However, it is suggested that an alternative method, of precipitates coarsening and then merging together to form larger precipitates, results in the same morphology [44]. Both mechanisms are expected to occur at different times, with the latter taking place at high precipitate densities, where impingement occurs more readily. Clearly, splitting would result in a decrease in precipitate size, whereas merging would give an increase. Qui and Andrews [44] conclude that merging occurred during their study of morphological changes during cooling, since no decrease in size was seen.

2.5 Dislocations in Ni-Based Superalloys

In the γ Phase

Since the γ phase of Ni-based superalloys has an FCC structure, dislocations with Burgers vector of $a/2\langle 1\bar{1}0\rangle$ glide in this phase on the $\{111\}$ planes [5]. In fact, each dislocation of such character splits into two partial dislocations, termed Shockley partials (Equation 2.1), which bound a region of intrinsic stacking fault between them (Figure 2.7). The separation of partial dislocations is defined by the balance between the energy of the associated stacking fault and the elastic repulsion of the two partials. The former is minimised by reducing the partial spacing, whilst the latter is minimised by increasing the spacing, and as such, a balance is found at an intermediate separation.

$$\frac{a}{2}\langle 110\rangle\{\bar{1}11\} \rightarrow \frac{a}{6}\langle 211\rangle\{\bar{1}11\} + \frac{a}{6}\langle 12\bar{1}\rangle\{\bar{1}11\} \tag{2.1}$$

In the γ' Phase

When a dislocation of type $a/2\langle 1\bar{1}0\rangle$ gliding on $\{111\}$ in the γ phase enters a precipitate of γ' phase, its Burgers vector no longer corresponds to a lattice vector. Passage of a dislocation of this type therefore creates high energy neighbouring Ni-Ni or Al-Al atoms. Such an interface is termed an Anti-Phase Boundary (APB) and this planar defect has an associated energy which is anisotropic since the number of high energy Ni-Ni or Al-Al bonds is dependant on the exact crystallographic plane on which the APB lies. The APB energy is very small on the $\{100\}$ planes, higher on the $\{111\}$ planes and highest on the $\{110\}$ planes [45].

Therefore, single dislocations of type $a/2\langle 1\bar{1}0\rangle\{111\}$ create an APB when gliding through the ordered γ' phase. A second dislocation following the first will remove this APB, and as such, pairs of dislocations are often found together in the γ' phase. Such dislocation pairs are termed superdislocations, in which a region of APB is bounded between the two superpartial dislocations. Each superpartial may itself dissociate into two partials, as in the γ phase, separated by a stacking fault. As such, there are many possible dislocation dissociation reactions in the ordered γ' structure [46].

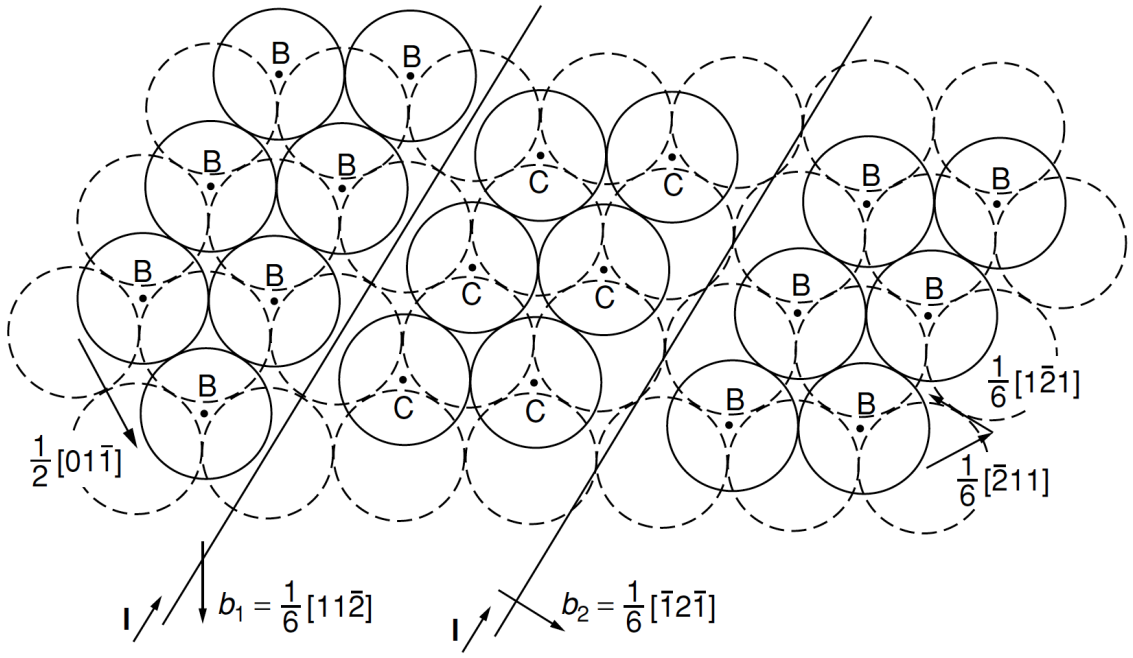

Figure 2.7: Illustration of two partial dislocations bounding an intrinsic stacking fault on a {111} plane of the FCC γ phase [5].

Due to this dissociation of dislocations, the ordered nature of the γ' precipitates gives rise to a remarkable property of this phase - increasing strength with temperature up to $\sim 800°C$. This property is also seen in other ordered $L1_2$-structured compounds (Figure 2.8), which have different bonding characteristics and values of APBE, and therefore different dissociation reactions.

The trend of increasing strength with temperature in the γ' phase arises due to cross-slip of segments of the superpartials onto the {100} planes from the {111} planes. The regions of cross-slipped superpartial dislocation, termed Kear-Wilsdorf locks [48], are sessile as they cannot glide without increasing the APB region, thereby resisting deformation. The energy required for such cross-slip is reduced at higher temperatures, and as such, it becomes more prevalent, causing the strength of superalloys to increase with temperature. At temperatures above $\sim 800°C$ the yield strength is reduced again, due to cube slip ($a/2\langle 1\bar{1}0\rangle\{001\}$) becoming prevalent [49].

The synergistic benefits of an alloy containing both γ and γ' phases to resist dislocation motion are shown in Figure 2.9. Although the strength of the γ phase decreases with temperature and the γ' phase has a lower strength at low temperatures, an alloy containing both γ and γ' phases shows superior strength from 0 to $\sim 800°C$ [50]. This yield strength property in some commercial Ni-based superalloys containing both phases is shown in Figure 2.10.

2.6 Introduction to Strengthening of Ni-Based Superalloys

The exceptional high temperature mechanical properties of Ni-based superalloys can be principally attributed to the γ' phase, which, via multiple concurrent mechanisms, can improve the yield strength by up to a factor of 5 compared to the precipitate-free γ matrix [51].

The γ' precipitate size, composition and morphology all affect the resulting alloy strength. Ardell [51, 52] described precipitation strengthening of superalloys as arising from 5 separate mechanisms; chemical, stacking fault, modulus, coherency and order strengthening. Chemical strengthening arises from the increased surface energy due to the new interface created when a precipitate is sheared by a dislocation.

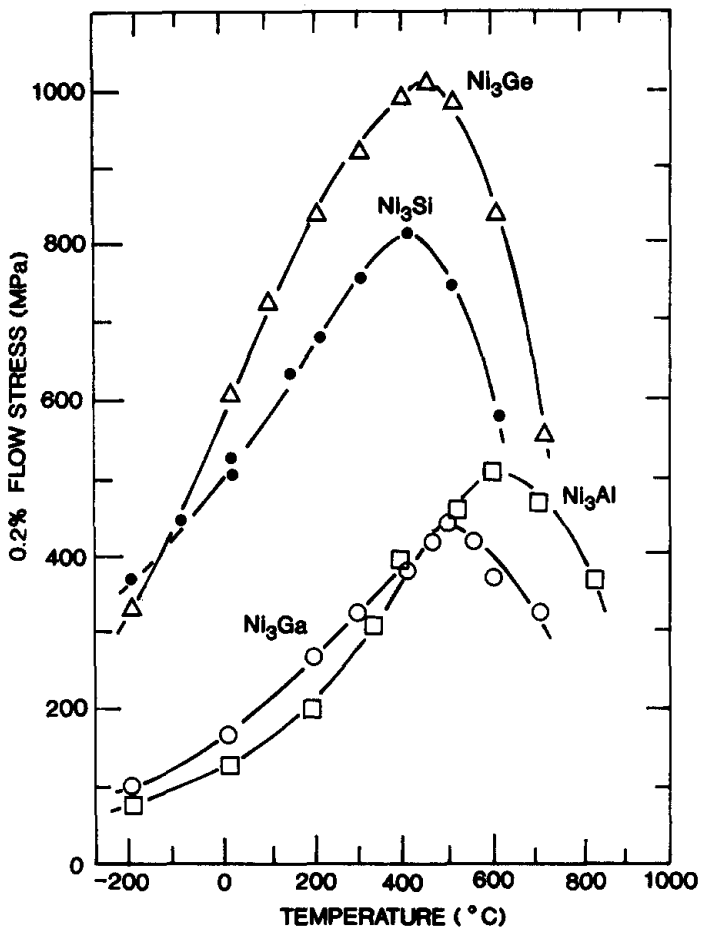

Figure 2.8: The flow stress of some Ni-based $L1_2$ compounds as a function of temperature [47].

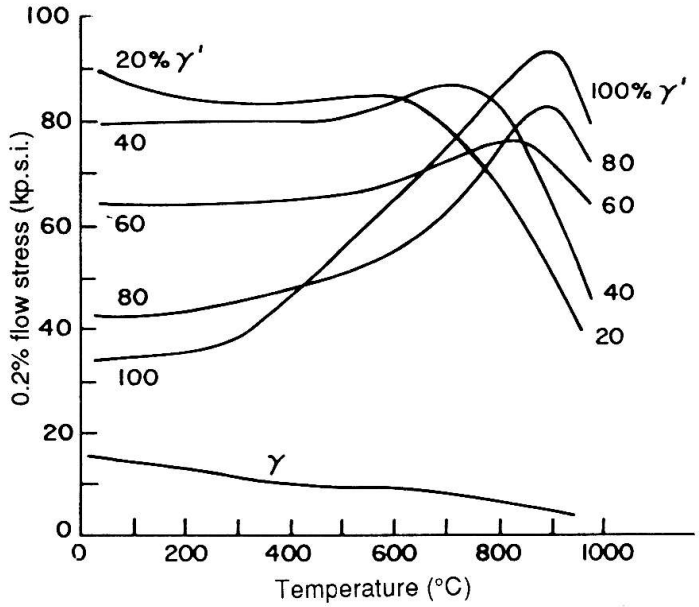

Figure 2.9: The flow stress of the γ and γ' phases and of alloys of varying proportions of these phases in a Ni-based superalloy [50].

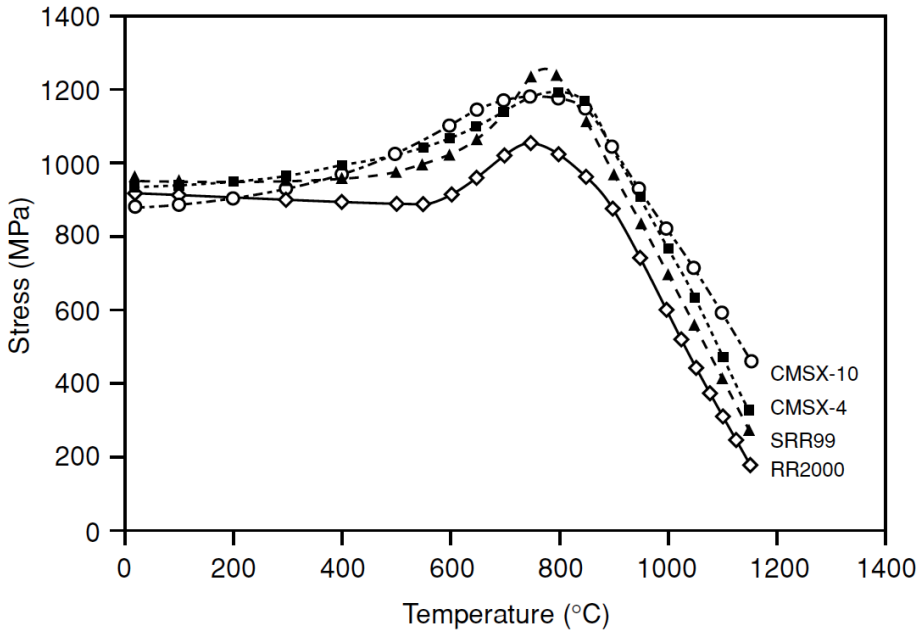

Figure 2.10: Experimental data for some current Ni-based superalloys showing increasing yield strength with temperature up to $\sim 800°C$ [5].

Stacking fault strengthening and modulus strengthening occur due to the different stacking fault energies and elastic moduli of the matrix and precipitate phase respectively. In the former case, when the matrix and precipitate phases have different stacking fault energies, the separation of the two partial dislocations also differs within each phase, impeding the subsequent motion of the dislocations. In the case where the two phases have different elastic moduli, the dislocation energy will differ within each phase, thereby affecting its motion. Coherency strengthening occurs when the lattice parameters of the matrix and coherent precipitate phase differ, therefore causing a strain field to be set up surrounding the precipitate. Finally, order strengthening occurs when the precipitates have an ordered crystal structure, which is disrupted by a dislocation travelling through the precipitate, thereby creating an anti-phase boundary with associated energy (APBE). This description is, however, still not a complete description of the strengthening of Ni-based superalloys, as other factors, for example the presence of grain boundaries, are not included. Any of these mechanisms can be operative at one time, however, one may have a much more significant effect than the others in a particular alloy system, or depending on factors such as precipitate volume fraction or size. This is where the lack of consensus in the literature arises.

For example, Gerold and Haberkorn [53] and Decker [14] also name these same mechanisms as those affecting the yield strength of Ni-based superalloys, however chemical strengthening is ignored since it predicts an overly large effect on the critical resolved shear stress (CRSS) at small particle sizes, which is not seen in experiment. This omission is not inconsistent with Ardell [52], who dismissed the effect of chemical strengthening by stating that this is likely to only be significant at very small precipitate sizes, if at all.

In this initial analysis of Ardell, order strengthening was described as the most significant of these processes [51]. In contrast, Ahmadi [54] has argued that the APBE itself and coherency strain are the most significant mechanisms for increasing the yield strength in alloy Allvac 718Plus, and Kozar et al. [7] concluded that APBE and the volume fraction of the tertiary γ' are the most important factors for increasing the strength of alloy IN100.

Coherency strengthening is also particularly controversial. Raynor and Silcock [33] describe it as

negligible (with order strengthening dominant), whereas other studies [53, 55, 56] conclude that it is the major strengthening mechanism. There are also many examples in the literature between these two extremes [57–60].

Hereon, order and coherency strengthening are considered separately. Stacking fault and modulus strengthening are not considered, since due to the very similar properties of the γ and γ' phases, these mechanisms contribute negligible strengthening in Ni-based superalloys [33, 61, 62]. Chemical strengthening is not discussed either, as this has been shown to have negligible strengthening effect in Ni-based superalloys [61].

Of course, there are further strengthening mechanisms present in Ni-based superalloys, unrelated to the presence of γ'. These include solid solution and grain boundary strengthening. What follows is a more detailed overview of these individual strengthening mechanisms in polycrystalline Ni-based superalloys. Additionally, how to combine these mechanisms to give an overall measurable yield strength is another area of dispute covered in the discussion below.

Solid Solution Strengthening

Ni-based superalloys contain many different elemental additions which may sit on the lattice sites of both the γ and γ' phases. Since the atomic radius of each added element differs to that of the major element (Ni), the crystal lattice is distorted around the substitutional solute atom. The resulting strain field interacts elastically with that of a dislocation, thereby impeding the motion of dislocations and increasing the strength relative to a pure Ni matrix. These interactions arise from both an atomic size misfit, as well as an elastic modulus misfit [63]. The latter arises from the presence of hard or soft regions of the matrix, caused by the presence of solute atoms of differing stiffness to that of the matrix atoms. Although this is an assumption, it has been shown to result in better fit to experimental data than when atomic size mismatch alone is taken as the source of strengthening [64].

The phenomenon of solid solution strengthening is commonly taken into account in the γ matrix phase [65, 66], but is rarely considered in the γ' phase due to its ordered structure [7, 67].

Precipitation Strengthening

It generally is accepted that the amount of strengthening due to the addition of precipitates increases with the volume fraction of γ' particles [54]. Plastic deformation in the disordered γ matrix phase of Ni-based superalloys most commonly occurs by the passage of single dislocations of type $\frac{a}{2}\langle 110\rangle_\gamma$ or their associated partials (where a is the lattice parameter). However, the ordered structure of the γ' precipitates means that the passage of a single dislocation of this type moves atoms into unfavourable, high energy positions, with an associated APBE. Therefore, once ordered γ' precipitates are present in the microstructure, the dislocations must travel in pairs to restore the γ' structure (Figure 2.11) [33].

The mechanism of plastic deformation in Ni-based superalloys depends on the size of the γ' precipitates within the microstructure. When the particles are small (in under-aged and peak-aged alloys), deformation occurs by pairs of $\frac{a}{2}\langle 110\rangle_\gamma$ type dislocations cutting through the precipitates (Figure 2.12), with an anti-phase boundary between them. The leading dislocation creates the anti-phase boundary, while the trailing dislocation removes it.

For small precipitates, which are more easily cut by dislocations, each dislocation of the pair is located within a different precipitate. This arrangement is termed weak-pair coupling (Figure 2.13a). In contrast, in larger precipitates both dislocations in the pair are held closer together by the large APBE, and are found within the same precipitate (strong-pair coupling) (Figure 2.13b). Which of these arrangements is most prevalent differs in different alloys. For example, weak-pair coupling has been determined to be more significant in supersolvus IN100, resulting in an increment of approximately 350 MPa to the yield

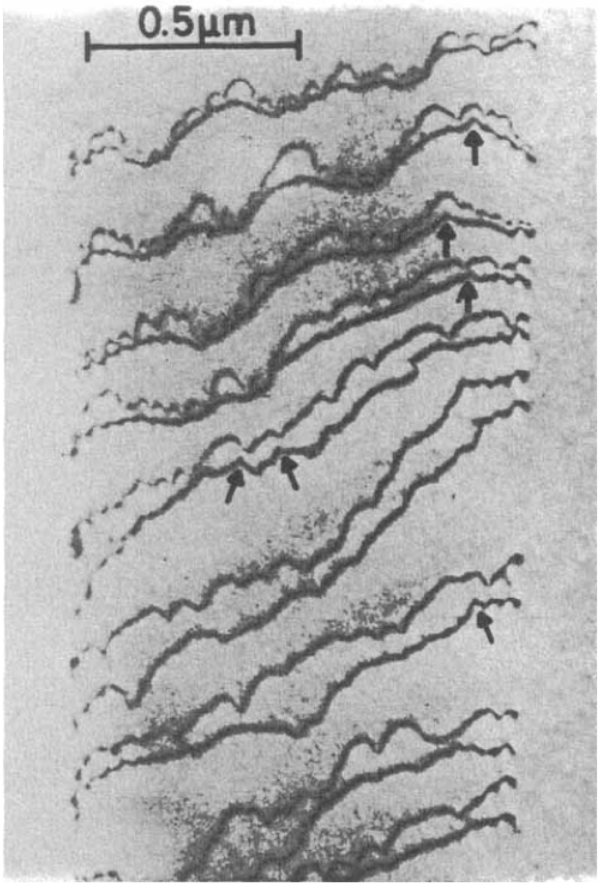

Figure 2.11: Dislocation pairs during *in situ* deformation of a Ni-base superalloy, showing characteristic looping around γ' precipitates [68].

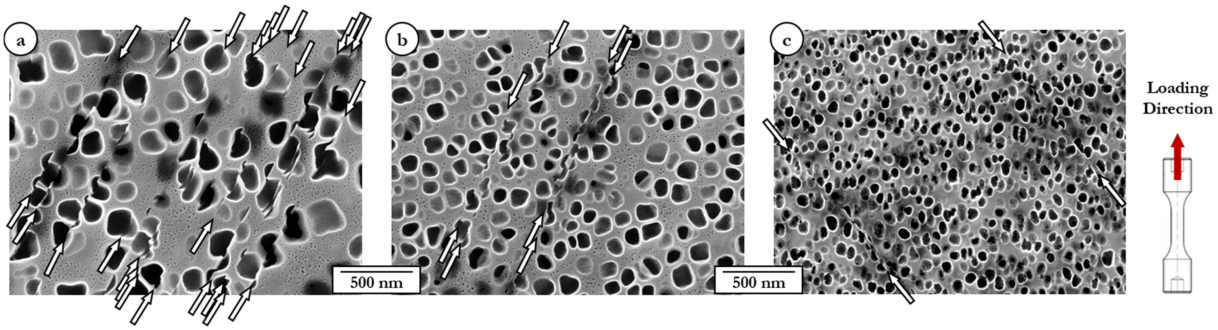

Figure 2.12: Cutting of γ' precipitates by dislocations in a Ni-based superalloy after different cooling rates from solution ((a) 40 °C min^{-1}, (b) 100 °C min^{-1} and (c) 300 °C min^{-1}) [69].

strength, compared to 325 MPa for strong-pair coupling [7]. However, in subsolvus IN100 this trend is reversed, with strong-pair coupling giving rise to $\sim$ 225 MPa of strength compared to just $\sim$ 190 MPa from weak-pair coupling [7]. It is commonly assumed that the maximum strength of superalloys occurs when the precipitate sizes correspond to the transition between strong- and weak-pair coupling, at a constant temperature [65].

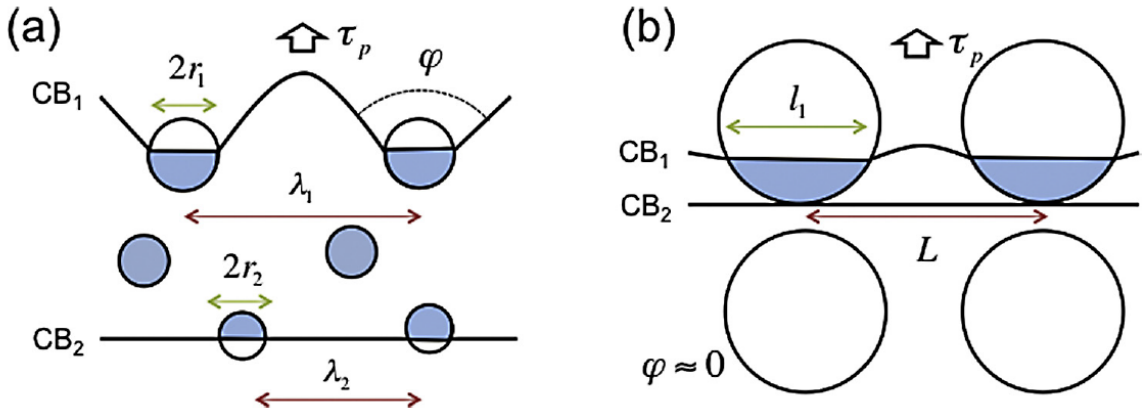

Figure 2.13: (a) Weak- and (b) strong-pair coupling arrangements. CB_1 and CB_2 describe the leading and trailing dislocation of the pair respectively. The anti-phase region is depicted in blue [65].

In overaged alloys the precipitates are yet larger, and deformation occurs not by cutting, but by dislocations looping around the precipitates via Orowan looping [53, 70]. However, Preuss [71] observed that Orowan looping in polycrystalline Ni-base superalloys is not commonly seen. This has also been confirmed by other authors [34, 72], but contradicted by Raynor and Silcock [33] and Chen et al. [27]. It is suggested by Preuss [71] that the lack of Orowan looping could be due to the small values of misfit or the complexity of the bi- or tri-modal particle size distributions that are generally seen in superalloys. This is not inconsistent with [33] or [27]. Similarly, the yield strength model of Kozar et al. [7] does not take into account Orowan looping due to the high volume fraction and small size of the precipitates.

Coherency Strengthening

The strain field resulting from the difference in lattice parameter of the γ matrix and γ' precipitate phases (Figure 2.14) also increases the yield strength by impeding dislocation motion.

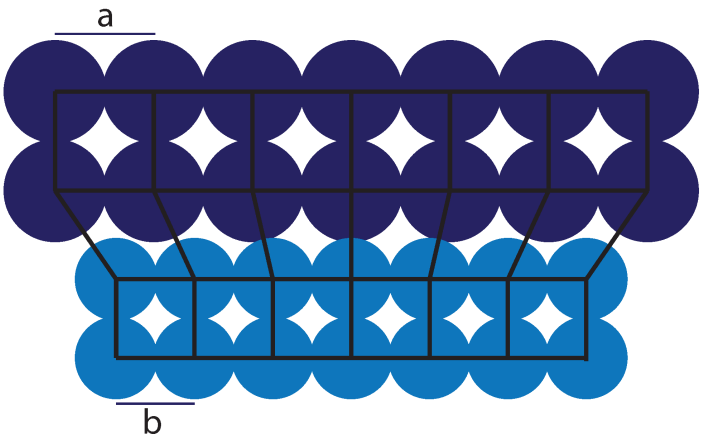

Figure 2.14: Schematic diagram showing the coherency strain set up when a lattice misfit exists between phases of different lattice parameters (a and b).

The overall coherency strain due to γ' precipitation can be thought of as the combination of the unconstrained misfit strain and the elastic misfit strain (Equation 2.2). The former is the strain between the γ and γ' phases if they have their standard, unconstrained, single-phase lattice parameters. When the two phases are in contact, the lattice parameters are forced to change to maintain coherency, and this associated strain is termed the elastic misfit strain [39].

$$\varepsilon_{\text{coherency}} = \varepsilon_{\text{elastic}} + \varepsilon_{\text{unconstrained}} \tag{2.2}$$

Evidently, a key parameter in determining the coherency strengthening effect is the lattice misfit (δ) between the γ and γ' phases. The general equation of the lattice misfit of an alloy is given as

$$\delta = \frac{(a_{\text{m}} - a_{\text{p}})}{a_{\text{m}}} \tag{2.3}$$

where a_{m} and a_{p} are the lattice parameters of the matrix and precipitate phase respectively.

For superalloys, commonly the lattice misfit is defined as

$$\delta = \frac{2(a_{\gamma'} - a_{\gamma})}{(a_{\gamma'} + a_{\gamma})} \tag{2.4}$$

where $a_{\gamma'}$ and a_{γ} are the lattice parameters of the γ' and γ phase respectively [5, 73–76]. Equation 2.4 is equivalent to Equation 2.3 but with respect to an average lattice parameter of γ' and γ.

In calculating the misfit, a distinction must be made between the constrained and unconstrained lattice parameters. The constrained value is that measured in the two-phase material, where the lattice parameters of each phase are forced to be more similar in the vicinity of the interface, to maintain coherency. In positively-misfitting alloys, the lattice parameter of the precipitate phase is larger than that of the matrix, and is therefore forced to decrease. Lattice parameters of each phase measured in their single phase material, being unaffected by a neighbouring phase, are termed unconstrained. In contrast to the constrained lattice parameter, this is a fundamental parameter which does not depend on the size or morphology of the precipitate, nor the interface orientation with respect to the matrix. The use of constrained or unconstrained parameters should therefore be made clear in coherency strengthening models in the literature.

Preuss [71] studied uni-modal particle size distributions, and concluded that lattice misfit is independent of particle size. However, this could be due to the similar composition of the γ' within the narrow size distribution studied. As compositions differ between primary, secondary and tertiary particles [77, 78], this conclusion is unlikely to hold across these cases. However, experimental measurements of the constrained lattice parameters of primary, secondary and tertiary γ' are notably absent from the literature.

Many modern commercial Ni-base superalloys are designed to have a negative misfit between the γ and γ' phases [5]. By definition, negatively misfitting precipitates must be under a tensile stress to maintain coherency with the matrix when constrained. Equivalently, the matrix phase must be under a compressive load (Figure 2.15). This reduces the drive for dislocation motion in the softer γ channels, thereby increasing strength.

During service, tensile stresses are applied to the microstructure. This increases the lattice parameter in the direction of applied load. In a negatively misfitting alloy, this acts to make the matrix and precipitate lattice parameters more similar in the vertical direction, but more different in the horizontal direction. Therefore, when a tensile stress is applied to a negatively misfitting alloy (Figure 2.16 (a)), a larger strain occurs in the horizontal channels between precipitates, and is therefore limited by the stiff precipitates. In positively misfitting alloys (Figure 2.16 (b)), the opposite occurs, and strain is bigger in the vertical channels. In this case, since in the direction of the applied load there are no hard precipitates

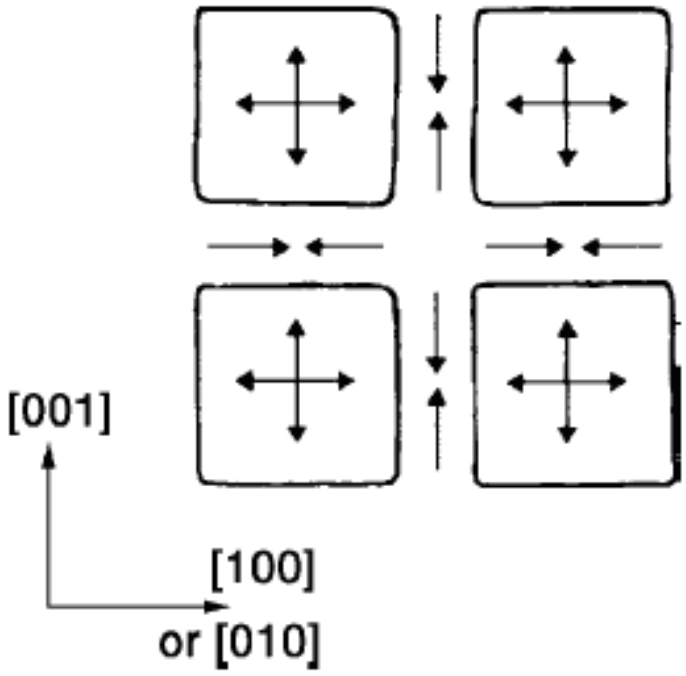

Figure 2.15: The directions of resultant stresses (indicated by arrows) caused by a tensile stress applied to a negatively misfitting alloy [5].

to withstand this load, deformation occurs more easily [74].

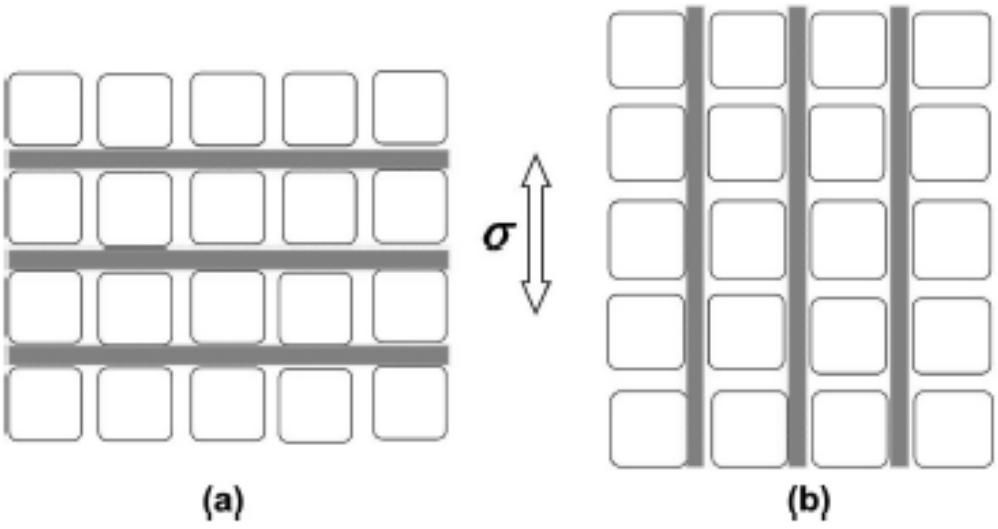

Figure 2.16: Deformation from an applied tensile stress is restricted to the horizontal channels (shaded) between precipitates in negatively misfitting alloys (a), but the vertical channels (shaded) in positively misfitting alloys (b) [74].

During service, the superalloy is held at high temperatures (above 700°C in the polycrystalline discs) which can cause the γ' size to increase by coarsening or coalescence. When this occurs in one direction preferentially, it is termed 'rafting'. This is driven by the coherency strains between the matrix and precipitate phases. One reason for negatively misfitting γ' precipitates is apparent during rafting. For negatively misfitting precipitates under a tensile stress, rafting occurs perpendicular to the load, resulting in improved creep resistance at high temperatures, although this is actually reduced at low temperatures

(below about 950°C) where cutting can more easily occur [6]. For alloys with near-zero misfit (such as polycrystalline (PX) alloys), rafting is less of an issue.

However, Mughrabi [74] argued that a positive misfit (as defined by Equation 2.4) would result in increased strength at high temperatures, and would be beneficial in terms of creep and fatigue resistance. This was deduced for multiple reasons including the facts that the lattice misfit would be lower at higher temperatures (improving creep resistance), and rafting would occur parallel to the applied stress (reducing creep rate and fatigue crack propagation). It was acknowledged that further experiments and modelling are required to confirm this, however. Using 3D discrete dislocation dynamics simulations, Gao [73] also found that very small, positive misfits are preferable for increased resistance to deformation when under tensile loading conditions along [001], although the role of temperature was not included in this study. Gao [73] investigated the movement of dislocations through γ' strengthened alloys using 3D discrete dislocation dynamics (DDD) simulations. Lattice misfit was taken into account by using fast Fourier transformations (FFT) to calculate the stress field caused by the misfit.

The lattice misfit is generally designed to be small ($\sim 10^{-3}$) [74], to minimise coarsening at high temperatures [5]. However, Zhang et al. [79] concluded that bigger misfits give superior mechanical properties (lower creep rate) because this requires more interfacial dislocations, blocking the movement of further dislocations that would shear the precipitates. This is in direct contrast to the work of [80], which found that a reduced misfit increases creep resistance. It was also found that the mechanism of dislocation motion at high temperature (1100°C) differed in two superalloys (TMS-75(+Ru) and TMS-138, with small (-0.16%) and large (-0.33%) lattice misfits respectively) [74]. In the low misfit alloy, dislocations climb around the γ' precipitates, whereas in the large misfit case, cross-slip occurs.

Evidently there is a significant lack of consensus as to the role of coherency strain in these alloys, and the associated optimum sign and magnitude of the lattice misfit. Difficulties arise from the lack of distinction in coherency models between constrained and unconstrained lattice misfits, and the effect of a multimodal particle size distribution with associated compositional differences. It should be noted that the effect of temperature is an added complication.

Grain Boundary Strengthening

Perhaps the most comprehensively studied strengthening effect in superalloys, the presence of grain boundaries also serves to increase the strength of polycrystalline materials. The motion of dislocations is impeded by the presence of these boundaries, therefore when present, larger stresses are required to cause plastic deformation of the material [7]. The effect of grain boundaries on strength is well described, and the established model is detailed in Section 2.7.

2.7 Strengthening Models

Solid Solution Strengthening

The γ Phase

Solid solution strengthening of the γ matrix phase is commonly included in strengthening models in the literature [7, 63, 65, 66, 81, 82], and has been determined to give an increment of around 100 MPa to the yield strength of IN100 [7]. In general, the solid solution strengthening effect can either be modelled by defining the solute atoms as obstacles that pin dislocations, or in contrast, by describing low energy positions in which each dislocation ideally lies [82–84]. In the latter, the presence of solute atoms augments the naturally occurring variable-energy landscape within a crystal lattice.

The presence of discrete solute atoms acting as obstacles to dislocation motion within the disordered γ matrix phase gives rise to strengthening by two factors; the difference in atomic size and the difference in shear modulus of the solute and matrix atoms. By modelling the interaction between a solute atom and a screw dislocation, Fleischer found that the modulus effect is the most significant [63].

However, using a statistical theory, Labusch [81] subsequently reached an alternative result which was corroborated by experimental data. The main difference between the two theories is the description of the dislocation flexibility. Additionally, Fleischer used an average value of the force of interaction of individual solute atoms on a dislocation, whereas Labusch considered a mean field distribution of multiple obstacles. The stress increment ($\Delta\tau$) caused by a solute atom is calculated by Fleischer [63] to be

$$\Delta\tau = \frac{x^{1/2}F^{3/2}}{b(2T)^{1/2}} \tag{2.5}$$

and by Labusch [81] to be

$$\Delta\tau = \frac{x^{2/3}F^{4/3}w^{1/3}}{b(4T)^{1/3}}C \tag{2.6}$$

where b is the magnitude of the Burgers vector, x is the atomic concentration of the solute atoms (the obstacle density), F is the force per unit length experienced by a dislocation from this obstacle, T is the dislocation line tension, and w and C are constants.

The exponent of $\frac{1}{2}$ determined by Fleischer [63] arises from the assumption of low obstacle density, meaning that a dislocation does not immediately encounter another obstacle after overcoming one initially. In contrast, an exponent of $\frac{2}{3}$ emerges from the statistical theory of Labusch [81], when solving the derived equations in the asymptotic limit of low solute content or strong dislocation-solute interactions.

These models were subsequently extended to account for the presence of multiple, different solute atoms by Gypen and Deruyttere [85]. To determine the overall extent of solid solution strengthening using this model, the contribution of each individual element (i) to the yield strength (τ) is calculated and then summed by

$$\Delta\tau = \left[\sum_i \Delta\tau_i^{\frac{1}{q}}\right]^q \tag{2.7}$$

where q is a constant. This model was derived by determining the equivalent concentration of each solute atom; in other words, the number of solute atoms j required to cause the same strengthening as the given number of solute atoms i, where each solute atom produces a different strengthening effect. In this way, the total strengthening of individual elements may be summed without complication arising from the different strengthening effect of each.

Equations 2.5 and 2.6 may be simplified by combining the individual materials constants into one overall constant, (β^γ). Mishima [66] used compression testing of Ni containing small ternary additions of other elements to determine experimentally the increase in the strength of FCC Ni by solid solution strengthening. Using the data of Mishima [66] and other authors [82, 86, 87], the value of β^γ for each individual element studied can be determined. This constant is dependent on both the atomic radius and the elastic modulus of the alloying element. Values for β_i^γ are given in Table 2.4.

Subsequent authors have used different values for the exponent q, depending on what was deemed a better fit to experimental data. Some authors [65, 88] used the value of $\frac{2}{3}$ proposed by Labusch [81]. In contrast, other studies use an exponent of $\frac{1}{2}$ [82]. Using this exponent, it therefore follows that each element in the γ matrix phase (i) provides a contribution of S_i^γ to alloy strength, given by

$$S_i^\gamma = \beta_i^\gamma x_i^{\gamma^{1/2}} \tag{2.8}$$

Element	β_i^{γ} (MPa/at.%$^{1/2}$)	$\beta_i^{\gamma'}$ (MPa/at.%)
Cr	33.7	11
Co	3.94	
Mo	101.5	41.88
W	97.7	40
Nb	118.3	56
Al	22.5	-
Ti	77.5	18.3
Ta	119.1	78.33
Fe	15.3	20.78
Hf	140.1	159
V	40.8	
Zr	235.9	163.7

Table 2.4: Solid solution strengthening coefficients of elements in the γ and γ' phases [66, 67, 82, 86, 87].

where x_i^{γ} is the concentration of element i in the γ phase (in units of atomic percent), and β_i^{γ} is the solid solution strengthening coefficient specific to element i.

Using this value of $\frac{1}{2}$ in Equation 2.7 then enables the calculation of the strength contribution of the γ phase due to solid solution ($\sigma_{\mathrm{SSS}}^{\gamma}$), by summing the effects of each individual element using

$$\sigma_{\mathrm{SSS}}^{\gamma} = (1 - f_{\gamma'}) \left(\sum_i \left(S_i^{\gamma} \right)^2 \right)^{1/2} \tag{2.9}$$

where $f_{\gamma'}$ is the volume fraction of the γ' phase. Many models exist in the literature for summing the solid solution strengthening effect of individual elements. An excellent summary of the various models for solid solution strengthening by ternary additions in the γ phase is given in [85].

The γ' Phase

The presence of alloying elements in the ordered γ' phase has also been shown experimentally to give rise to solid solution strengthening [7, 67, 89–91], however it is rarely included in strengthening models in the literature [65, 88].

In the case of the γ' phase, a variation of Equation 2.8 can be used to determine the strengthening increment associated with each alloying addition ($S_i^{\gamma'}$). However for this phase, the strength has been shown through fitting to experimental data to vary linearly with concentration ($q = 1$) [67,91], in contrast to the $\frac{1}{2}$ exponent (q) for the matrix γ phase. This gives

$$S_i^{\gamma'} = \beta_i^{\gamma'} x_i^{\gamma'} \tag{2.10}$$

where $x_i^{\gamma'}$ is the concentration of element i in the γ' phase (in units of atomic percent), and $\beta_i^{\gamma'}$ is the solid solution strengthening coefficient specific to element i in the γ' phase. Values for $\beta_i^{\gamma'}$ are given in Table 2.4.

The different strengthening increments of the γ and γ' phases (Equations 2.8 and 2.10) arise due to the ordered nature of the γ' phase. In addition to the local lattice distortion and local modulus variations caused by the presence of a misfitting element in the lattice, the ordered nature of the γ' lattice means that variations in atomic bonding also exist, depending on which sub-lattice site the added element resides.

As for the γ phase, the total solid solution strengthening effect of the γ' phase is found by summing the individual contributions of each element, following Equation 2.7, giving

$$\sigma_{\mathrm{SSS}}^{\gamma'} = f_{\gamma'} \sum_i S_i^{\gamma'} \tag{2.11}$$

It should be noted that the composition of the secondary and tertiary γ' precipitates is likely to differ [31] and therefore the extent of solid solution strengthening in each will also differ.

Precipitation Strengthening

Precipitate Shear

The initial models to be proposed for precipitation strengthening involved individual precipitates simplified to point objects distributed at random on a particular glide plane, and the dislocation modelled by its line tension, T_{L} [92]. In these models, the yield stress of the material was taken to be the minimum applied shear stress that enabled the dislocation to traverse the whole glide plane [93].

For a dislocation to move through an array of point obstacles, randomly distributed on the glide plane, Brown and Ham defined the critical shear stress, τ_c, required as

$$\tau_c = \frac{F^{3/2}}{bL\sqrt{2T_{\mathrm{L}}}} \tag{2.12}$$

in which F is the obstacle strength, b the magnitude of the Burgers vector and L the spacing between particles [93]. However, this equation applies only to a single dislocation encountering an obstacle. In superalloys, dislocations travel in pairs with the leading dislocation creating an anti-phase boundary within the precipitate, and the trailing dislocation restoring the original order. This equation therefore needed some adjustment to be applicable to superalloys. One solution to this was by substituting the obstacle strength, F, in Equation 2.12 for the APBE per unit volume of the precipitate that is obstructing the dislocation (i.e. the diameter of the precipitate, d_s), $\gamma_{\mathrm{APB}}\, d_s$ [7].

A force balance is all that fundamentally is required to model the strengthening arising from the presence of ordered precipitates in superalloys. The contributing factors are the external force on the dislocation, the force of repulsion between the two partial dislocations of the pair, and the force from the anti-phase boundary, which acts in opposite senses for the leading and trailing dislocations. This results in two equations - for the leading and trailing dislocation respectively [65];

$$\tau_p b\Lambda_1 + F_{\mathrm{pair}}\Lambda_1 - \gamma_{\mathrm{APB}} l_1 = 0 \tag{2.13}$$

$$\tau_p b\Lambda_2 - F_{\mathrm{pair}}\Lambda_2 + \gamma_{\mathrm{APB}} l_2 = 0 \tag{2.14}$$

where τ_p is the applied shear stress, Λ_1 and Λ_2 are the lengths of the leading and trailing dislocations, respectively, that drive cutting, F_{pair} is the force of the dislocation pair per unit length and l_1 and l_2 are the segment lengths of the leading and trailing dislocations respectively, that are cutting the precipitates.

However, in reality the obstacles are not infinitely small, so a value for the precipitate spacing, L is required. Kozar [7] related the spacing between finite, spherical particles to the volume fraction, $f_{\gamma'}$, and the average planar diameter, d_s by

$$L = \sqrt{\frac{8}{3\pi f_{\gamma'}}} d_s - d_s \tag{2.15}$$

By modelling particles as having finite size, Ardell [52] reached a larger value for the flow stress than that achieved using point obstacles. This directly contradicts that modelled by Melander [94] who found

that the critical resolved shear stress (CRSS) using finite obstacles is smaller than that of point obstacles, since the mean obstacle strength is reduced in the case of finite obstacles.

An improvement to these original models resulted from both modelling the precipitates as having finite shape and size, and defining the mechanism of interaction between the precipitate and dislocation [70]. This enabled the different regimes of dislocation motion - weak-pair coupling, strong-pair coupling and Orowan looping - to be defined and modelled separately.

Brown and Ham [93] concluded that the shear stress required for strong particles is defined by the equation

$$\tau_{\mathrm{c}} = 0.8\frac{Gb}{L}\cos\left(\frac{\phi}{2}\right) \tag{2.16}$$

and that for weak particles is

$$\tau_{\mathrm{c}} = \frac{Gb}{L}\cos\left(\frac{\phi}{2}\right)^{1.5} \tag{2.17}$$

where G is the shear modulus, b is the magnitude of the Burgers vector and ϕ is the breakaway angle of the dislocation. However, these equations are not suited to Ni-based superalloys, as no effect of ordering and the associated APBE in the γ' is considered, and only low volume fractions of γ' are applicable.

In contrast, Reppich [72, 95] defined the shear stress of material containing strong precipitates as

$$\tau_{\mathrm{c}} = \frac{0.86\,\gamma_{\mathrm{APB}}\,f_{\gamma'}^{0.5}w}{bd}\left(1.28\frac{d\gamma_{\mathrm{APB}}}{w\mathrm{T_L}} - 1\right)^{0.5} \tag{2.18}$$

and in the case of weak precipitates,

$$\tau_{\mathrm{c}} = 0.5\left(\frac{\gamma_{\mathrm{APB}}}{b}\right)^{1.5}\left(\frac{bdf_{\gamma'}}{\mathrm{T_L}}\right)^{0.5}A - 0.5\frac{\gamma_{\mathrm{APB}}}{b}f_{\gamma'} \tag{2.19}$$

where γ_{APB} represents the APBE, $f_{\gamma'}$ is the precipitate volume fraction, w is a parameter describing the repulsion between dislocations, d is the mean particle diameter, and A is a numerical coefficient dependent on precipitate shape. Although Equations 2.18 and 2.19 are more suited to superalloys, since ordering and the APBE are taken into account, only low γ' volume fractions are applicable, and the empirical parameter w is required to account for uncertainties and other strengthening mechanisms.

These equations differ to those of a separate investigation by Kozar et al. [7], where strong- and weak-pair coupling were described by Equations 2.20 and 2.21 respectively, even though this model was also based upon the original equation of Brown and Ham (Equation 2.12), but edited for superalloys by taking into account finite precipitate size and the presence of two dislocations linked by an APBE.

$$\Delta\tau_{\mathrm{c}} = \frac{2T_L}{\pi bL_x}\left(\frac{\pi d_s\gamma_{\mathrm{APB}}}{2T_L} - 1\right)^{1/2} \tag{2.20}$$

$$\tau_{\mathrm{c}} = \frac{\gamma_{\mathrm{APB}}}{2b}\left(\sqrt{\frac{\gamma_{\mathrm{APB}}d_s}{2T_L}}\frac{d_s}{L_s} - \frac{\pi}{4}\left(\frac{d_s}{L}\right)^2\right) \tag{2.21}$$

Note that Equation 2.20 is given in terms of an increase in shear stress, whereas Equation 2.21 is simply a shear stress, (as given in [7]). L is the centre-to-centre precipitate spacing, L_s is the spacing between particles (after taking into account finite size), and L_x is the precipitate spacing in the case of strong-pair coupling. L_x is different to L_s since two dislocations are present in the same precipitate, and at the critical configuration for precipitate cutting, the length of the dislocation present within the precipitate is not equal to the precipitate diameter d_s of Equation 2.15. This model is an improvement,

since high volume fractions of γ' may be considered, however, a constant interparticle spacing is assumed, which is not applicable to the case of multimodal particle size distributions, common in superalloys.

Evidently a value for the precipitate spacing is required for these models, but this is also inconsistently defined in the literature. Hüther and Reppich [72] describe the particle spacing (L_x) as $(\pi/f)^{1/2}d_s/2$, based on the average planar spacing in a square lattice. Alternatively, Gerold and Haberkorn [53] obtained expressions for L which vary depending on the flexibility of the dislocation line;

$$L_1 = \frac{2}{3f_{\gamma'}}d_s \tag{2.22}$$

$$L_2 = \left(\frac{\pi}{4\theta f_{\gamma'}}\right)^{\frac{1}{2}}d_s \tag{2.23}$$

$$L_3 = \left(\frac{\pi}{6f_{\gamma'}}\right)^{\frac{1}{2}}d_s \tag{2.24}$$

for rigid, partially flexible and totally flexible dislocations respectively, where θ is the dislocation bending angle.

However, it is unproductive to emphasise the precipitate spacing whilst ignoring the distribution of the precipitates themselves - the precipitate spacing is evidently affected by their distribution on the dislocation glide plane.

Some authors use a square lattice through which the dislocation pairs propagate, for which the obstacle spacing approximates to $N^{-\frac{1}{2}}$ with N as the number of obstacles per unit area [33, 52, 65]. This is not equivalent to other characteristic obstacle spacings, such as the average planar spacing ($N^{-\frac{1}{2}}/2$) or the average obstacle spacing along the dislocation line itself [52]. Another option is to use a statistical, random distribution of particles of random size, which is said to increase the accuracy of results [96, 97].

Foreman and Makin [92] showed that the calculated value for τ_c differs depending on the shape of the array modelled. For strong obstacles (those present in the strong-pair coupling regime), experimental data was predicted well by approximating a regular array of obstacles. Although modelling the dislocation as lying along the length of the square array was shown to give values for τ_c that were too large, when defining L as the average of the square and diagonal lengths (Equation 2.25), the experimental data were fitted well for strong obstacles.

$$L = 0.5(1+\sqrt{2})N^{-\frac{1}{2}} \tag{2.25}$$

In contrast, for weak obstacles (those present in the weak-pair coupling regime), using a regular square array resulted in a significantly larger CRSS than a random distribution. In the case of weak obstacles, the Friedel relation (Equation 2.26) for obstacle spacing on the dislocation line (L_{Friedel}) is shown to fit the experimental data well [92]. Friedel statistics describe the movement of dislocations through an array of obstacles by the sequential "unzipping" and then bowing out from each encountered precipitate [52].

$$L_{\text{Friedel}} = (\frac{Gb}{N\sigma})^{1/3} \tag{2.26}$$

where σ is the force on the dislocation and G is the shear modulus.

Using Equation 2.26 for L, and the same force balance given in Equation 2.13, Raynor and Silcock [33] reached an expression for the increase in shear stress caused by precipitation hardening;

$$\Delta\tau = A\gamma_{\text{APB}}^{\frac{3}{2}}f_{\gamma'}^{\frac{1}{2}}r_s^{\frac{1}{2}}b^{-1}T^{-\frac{1}{2}} - \frac{f_{\gamma'}\gamma_{\text{APB}}}{2b} \tag{2.27}$$

with r_s being the mean planar radius of the precipitates and A a numerical factor. This is in contrast

to [65] although both models originate from the same initial force balance (Equations 2.13 and 2.14). An earlier study [34] reached a different conclusion (Equation 2.28), although there are similarities in the first term.

$$\Delta\tau = 0.28\gamma_{\mathrm{APB}}^{\frac{3}{2}} f_{\gamma'}^{\frac{1}{2}} G^{-\frac{1}{2}} b^{-\frac{3}{2}} r \tag{2.28}$$

These equations, however, apply to precipitate distributions of uniform size and low volume fraction. Therefore, they are still not necessarily applicable to most modern Ni-base superalloys, where the volume fraction of the γ' phase can reach 0.7, and where the precipitate size distribution may be trimodal. Even within a distribution of secondary or tertiary γ' precipitates, there is a range of particle sizes, which is not taken into account in these equations, but will affect the yield strength.

In fact, in contrast to these classical models, it has been shown that weak- and strong-pair coupling models are not reproduced closely by experiment, in particular for high volume fraction alloys [65]. An added complication is the transitional region between weak- and strong-pair coupling. Classical models consider these two regions separately, and assume a smooth convergence between the two regimes. In reality, the two cannot be smoothly joined because they have very disparate arrangements. For example in weak-pair coupling, the leading dislocation curves out around the precipitates. In contrast, in strong-pair coupling the leading dislocation is straight. Clearly a transitional region must occur between the two separate regimes. This inconsistency is paramount in Ni-based superalloys, since the size of the precipitates is often within this transitional region.

Galindo-Nava et al. [65] have attempted to solve these inconsistencies by unifying the weak- and strong-coupling regimes. They defined a transitional region where the leading dislocation has just exited the precipitate while the trailing dislocation is just about to enter the precipitate (Figure 2.17).

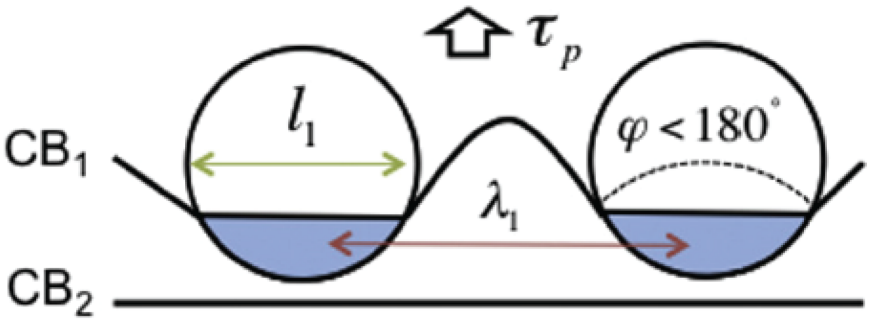

Figure 2.17: Schematic diagram showing the configuration of the dislocation pair in the transitional region between strong- and weak-pair coupling [65].

A further lack of consensus exists regarding what feature of the γ' phase gives rise to the strengthening increase - volume fraction or number density. Most commonly in the literature, the volume fraction is used [7, 33, 95, 98]. However, Galindo-Nava et al. [65] use the number density. This follows from the fact that it is the γ / γ' interface that provides the *initial* barrier to dislocation motion (giving rise to a *yield* strength). Of course after initial yielding, the motion of dislocations through the γ' precipitates also imparts strengthening, therefore at this point, γ' volume fraction may be the more appropriate variable.

Further inconsistencies in the literature arise from the shape of the precipitates and their size distributions. This is significant in the case of superalloys, since precipitate morphologies commonly vary from spherical to cuboidal to octo-dendritic [20] (Figure 2.18). Some models apply purely to spherical particles [99] whilst others consider different morphologies [96, 100, 101]. This is significant, since precipitate

morphology has been shown by discrete dislocation simulations to affect the strength of Ni-based superalloys [70]. It was found that spherical precipitates are stronger than cubic precipitates of size 100 nm and APBE 320 mJ m^{-2}, but as precipitate size and APBE decrease, this has less of an effect. Kozar et al. [7] found that their yield strength model fitted well to the experimental data for a subsolvus IN100 alloy. However, the yield strength for the supersolvus IN100 alloy was overpredicted. This is evidence for the requirement of a full description of the particle size distributions and precipitate morphologies for accurate yield strength modelling.

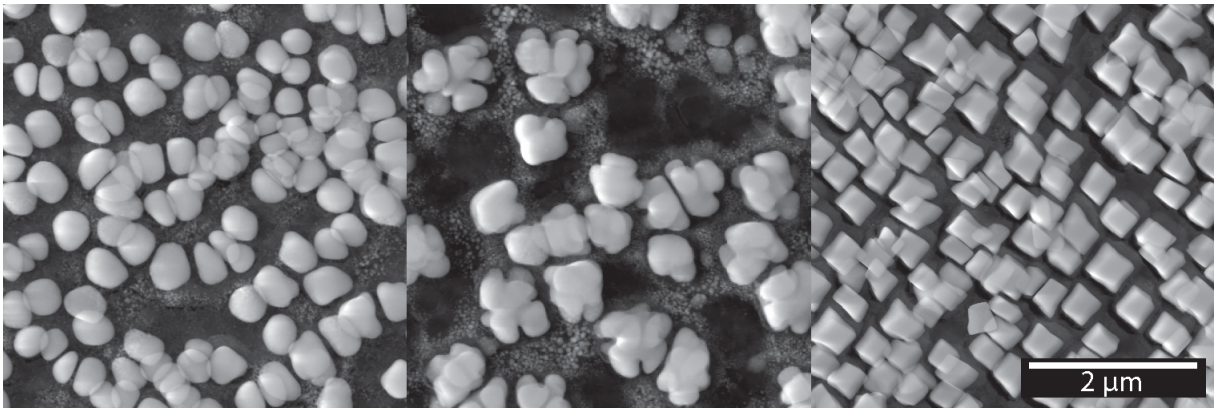

Figure 2.18: Micrographs showing characteristic morphologies of γ' precipitates in model Ni-Al-Ti-Cr-Mo alloys, which can vary from spherical to cuboidal to octo-dendritic.

A further complicating factor arises due to the fact that different deformation mechanisms will occur for different size precipitates, and since superalloys often contain multimodal precipitate size distributions, both strong- and weak-pair coupling may occur simultaneously in a single alloy, in addition to precipitate bowing. Further to this fact, the apparent size of the precipitate seen by a dislocation will differ depending on the slip plane of the dislocation, and will therefore affect the modelled yield strength. This is rarely taken into account in the literature, except by Parthasarathy et al. [101].

A summary of the strengthening models discussed above is given in Table 2.5. To summarise, most current strengthening models contain many assumptions to simplify the complex nature of Ni-based superalloys. These include a constant dislocation line tension, a regular square array of precipitates of equal size and spherical morphology, and dislocation interactions dependent on the precipitate volume fraction rather than the precipitate spacing. An ideal model would remove these assumptions.

Anti-Phase Boundary Energy (APBE)

The Equations 2.13 and 2.14 and the subsequent equations presented in this section were defined using the APBE as the only factor to impede dislocation motion, so precipitation (order) hardening is the only strengthening mechanism considered. The APBE therefore features heavily in these equations, and its value must be determined.

The shearing of precipitates by dislocation pairs gives rise to an anti-phase region between the two dislocations. Within this region the ordering is disrupted, with Al atoms sitting on the Ni sites (for example), and vice versa. The ensuing energy increase caused by these unfavourable nearest-neighbour atoms means that shearing of dislocations through ordered precipitates is less favourable than through a disordered phase. Accordingly, since more energy must be inputted to cause this precipitate shear, the strength of the alloy is increased.

It is clear then, that the magnitude of the anti-phase boundary energy produced must be linked to the overall strengthening effect imparted by the ordered nature of the γ' phase. The APBE may be

Author	Assumptions	Low/ High f	Unimodal/ Multimodal	Limitations
Brown and Ham [93, 102]	Point obstacles, Random particle distribution, Dislocation modelled by its line tension T.	Low	Point Obstacles	No ABPE effect.
Gleiter and Hornbogen [98]	Spherical particles statistically distributed in space, Isotropic crystal, Linear elasticity theory, Constant line tension T.	Low	Unimodal	Predicts that Orowan bowing should never occur.
Foreman and Makin [92]	Point obstacles, Random particle distribution, Dislocation modelled by its line tension T, Different particle arrays.	Low	Point Obstacles	No APBE effect.
Gerold and Haberkorn [53]	L depends on flexibility of dislocation line, Spherical particles, Edge dislocations dominate effect, Straight dislocation lines.	Low	Unimodal	No APBE effect, Doesn't work well for small particles.
Raynor and Silcock [33]	Friedel spacing, Line tension T varied as dislocation bows around particles, Effect of T on other segments of the dislocation considered.	Low	Unimodal	Only strengthening by APBE considered.
Huther and Reppich [72]	Average planar spacing in square lattice, Octahedral or spherical precipitates, Screw dislocations only, Constant line tension T, Particle size small compared to spacing (point obstacles).	Low	Unimodal	Strong-pair coupling regime only, Empirical factor w added to account for uncertainties and other strengthening mechanisms.
Melander [94], Melander and Persson [58]	Spherical particles of finite size, Average line tension T, Both straight edge dislocations in the pair.	Low	Unimodal	APBE and misfit used as fitting parameters.
Rao et al. [70]	Weak/strong/Orowan regimes, Cubic or spherical particles, Leading dislocation is spherical.	Low/High	Multimodal	Small precipitates only, Low APBE only.
Parthasarathy et al. [101]	Cuboidal secondary and tertiary γ', Mean particle size, Dislocations either screw or mixed.	Low/High	Multimodal	APBE used as fitting parameter, Equations based on polynomial fit to model data, Limited parameters investigated, Predicts only one crystal orientation.
Kozar et al. [7]	Spherical particles of finite size, L differs for weak-/strong-pair coupling, All dislocations assumed 60°mixed character	High	Multimodal	Constant interparticle spacing assumed.
Ahmadi et al. [54, 96]	Components of strengthening via APBE, Coherency, modulus and chemistry misfits considered and summed.	Low	Unimodal	Constant phase chemistry (constant APBE) assumed.
Galindo-Nava et al. [65]	Weak-/strong- and intermediate-pair coupling (links transition), Strengthening dependant on particle number density, not f.	Low/High	Multimodal	Constant phase chemistry (constant APBE) assumed.

Table 2.5: Summary of precipitation strengthening models discussed in this thesis.

determined experimentally using the separation distance between the dislocations in a pair [103,104], but this is not trivial, and is subject to much uncertainty. Modelling is therefore a useful alternative.

The original models for APBE in FCC structures involved a study of the bonds broken and reformed across the boundary, taking into account nearest neighbour bonds only [105–108]. However, it was later shown that a minimum of second order nearest neighbour interactions must be accounted for in calculation of the APBE of ordered FCC structures [109]; although further interactions improve the accuracy of the model [110, 111].

A thorough model for the APBE was proposed by Inden et al. for the $L1_2$ and $L1_0$ structures of ordered FCC alloys, in particular Ni_3Fe [112]. The model describes the APBE as a function of composition. Correlation functions were proposed to simplify the modelling of APBEs, and interactions up to the fourth nearest neighbour were included. This model was commonly used by subsequent authors [113–115]. In this study, the APBE on the {111} planes ($\Delta E_{\mathrm{APB}}(111)$), assuming perfect ordering, is determined using the equation

$$\Delta E_{\mathrm{APB}}(111) = \frac{1}{4a^2\sqrt{3}}\left[\left(\xi^I - \xi^{II}\right)^2 + \left(\xi^{III} - \xi^{IV}\right)^2\right]\left[V^{(1)} - 3V^{(2)} + 4V^{(3)} - 6V^{(4)}\right] \tag{2.29}$$

where a is the lattice parameter, ξ are functions describing the site occupancy of the lattice sites ($I-IV$), and $V^{(1)}$ to $V^{(4)}$ are the nearest neighbour interaction energies for the first to fourth nearest neighbour atoms. This equation can be simplified by assuming perfect ordering of the γ' phase. In this case, $\xi^I = -1$ whilst $\xi^{II} = \xi^{III} = \xi^{IV} = 1$, giving

$$\Delta E_{\mathrm{APB}}(111) = \frac{1}{a^2\sqrt{3}}\left[V^{(1)} - 3V^{(2)} + 4V^{(3)} - 6V^{(4)}\right] \tag{2.30}$$

where a is the lattice parameter and $V^{(1)}$ to $V^{(4)}$ are the nearest neighbour interaction energies for the first to fourth nearest neighbour atoms.

The terms $V^{(1)}$ to $V^{(4)}$ are obtained from the internal enthalpy of the γ phase ($\Delta H^{\gamma}_{\mathrm{int}}$) and the ordering enthalpy ($\Delta H^{\gamma'}_{\mathrm{ord}}$) using the following equations

$$V^{(1)} = 0.8V^{(1,3)}_{\mathrm{eff}} \tag{2.31}$$

$$V^{(1,3)}_{\mathrm{eff}} = -\frac{3\Delta H^{\gamma}_{\mathrm{int}} + \Delta H^{\gamma'}_{\mathrm{ord}}\left[\frac{1-x_s}{x_s}\right]}{24N_A x_s(1-x_s)} \tag{2.32}$$

$$V^{(2)} = \frac{\Delta H^{\gamma'}_{\mathrm{ord}}(1-x_s) - \Delta H^{\gamma}_{\mathrm{int}}x_s}{12N_A x_s^2(1-x_s)} \tag{2.33}$$

$$V^{(3)} = 0.125V^{(1)} \tag{2.34}$$

where N_A is Avogadro's constant and x_s is the mole fraction of the solute element in the ordered phase.

Crudden et al. [113] and Saunders et al. [116] have more recently used the same model for the APBE in Ni-based superalloys, using equilibrium precipitation software (Thermo-Calc) to determine the internal enthalpies of γ and γ'. The difference between these values, assuming identical compositions of γ and γ', gives the enthalpy of ordering of the γ'.

$$\Delta H^{\gamma'}_{\mathrm{ord}} = \Delta H^{\gamma'}_{\mathrm{int}} - \Delta H^{\gamma}_{\mathrm{int}} \tag{2.35}$$

Alternatively, density functional theory (DFT) has been used to computationally determine the APBE in Ni-based superalloys [104,117–120]. Crudden et al. [113] also used a DFT method to determine APBEs, but subsequently defined a second, simplified approach using these DFT results to determine coefficients (k_i) linearly linking the solute content (x_i) to the APBE. The effect of each element is then simply summed to give the overall APBE in an alloy of n different elements.

$$\Delta E_{\mathrm{APB}} = \Delta E^0_{\mathrm{APB}} + \sum_{i=1}^{n} k_i x_i \tag{2.36}$$

in which $\Delta E^0_{\mathrm{APB}}$ is the APBE of pure Ni_3Al. This method was deemed to be more reliable than the original theory of Inden [112] through closer fit to experimental data. However, this method was only applicable to low solute concentrations. Experimentally, the APBE of the {111} planes in stoichiometric Ni_3Al has been measured to be 195 ± 13 $\mathrm{mJ\,m^{-2}}$ [103] and 180 ± 30 $\mathrm{mJ\,m^{-2}}$ [121].

Other methods of modelling the APBE computationally do exist, but are not detailed within this thesis. These include embedded atom methods [122, 123], linear muffin-tin orbital methods [124] and further DFT-based approaches [104, 117–120].

It should be noted that APBE is very closely linked to the precipitate composition, and this has been shown to vary with precipitate size [23]. Therefore, the magnitude of the APBE will differ between precipitates, in particular, between precipitates of different size distributions (secondary and tertiary γ'). This could result in large differences in the order strengthening effect of the secondary and tertiary γ', thereby affecting the predicted yield strength. Such compositional variations must be carefully considered in yield strength models, although currently this is not seen in the literature.

Orowan Bowing

At large particle size, Rao et al. [70] observed a transition to Orowan looping, with a corresponding decrease in CRSS as precipitate size increased. This is consistent with classical theories in the literature for strengthening by precipitates [125], but is in contrast to Preuss et al. [71] who stated that Orowan looping is not commonly seen in polycrystalline Ni-base superalloys. A number of reasons were given for this conclusion, including the fact that superalloys generally do not contain large precipitates, the low lattice misfit in these alloys, or the bi- or tri-modal size distribution of precipitates.

Orowan looping (or bowing) around precipitates occurs when the stress reaches a value given by [93]

$$\tau = \frac{Gb}{L} \tag{2.37}$$

although other comprehensive treatments of Orowan looping also exist in the literature [126–128]. This mechanism is well-established in other alloy systems [129–131], but the role in Ni-based superalloys is often omitted.

Coherency Strengthening

Many equations and models exist with the aim of describing the effect of coherency strengthening, but different assumptions are used and the fit to experimental data is poor. However, the one consistent observation is the fact that coherency strengthening is dependent on the *magnitude* of the lattice misfit, irrespective of its sign.

To quantify misfit, values for the lattice parameters of each phase are required. These can be deduced experimentally or by using thermodynamic equilibrium phase modelling (Thermo-Calc). Alternatively, in the alloys-by-design model, Reed et al. [132] defined equations for the lattice parameters (in units of Å) of the γ and γ' phases as

$$a_\gamma = 3.559257 + 0.0000198T + \sum_i \Gamma_i^\gamma x_i \tag{2.38}$$

$$a_{\gamma'} = 3.552743 + 0.0000552T + \sum_i \Gamma_i^{\gamma'} x_i \tag{2.39}$$

respectively, where Γ_i^γ and $\Gamma_i^{\gamma'}$ are Vegard coefficients, x is mole fraction, and T is temperature (kelvin). The misfit is then calculated using Equation 2.4. Equations 2.38 and 2.39 were developed by fitting experimental data for the single-crystal alloy CMSX-4 at 900°C [132]. As such, these equations cannot be assumed to be valid for any other alloy.

Models in the literature rarely define whether the constrained or unconstrained values are required as input for lattice misfit. Grose and Ansell [133] have shown that although the values of the constrained and unconstrained lattice parameters differ, the trend for decreasing misfit as temperature increases is consistent in the alloys studied, although it is less pronounced in the constrained case. However, Grose and Ansell conclude that the temperature dependence can be represented by the unconstrained misfit.

The constrained (ε) and unconstrained (δ) misfits may be related by

$$\varepsilon = \delta\left(\frac{1+\nu}{1+2K+\nu(1-4K)}\right) \tag{2.40}$$

where K is the ratio of the matrix and precipitate shear modulii, and ν is the precipitate phase Poisson's ratio. However, Equation 2.40 applies to coherent, spherical precipitates only [133].

Alternatively Grose and Ansell defined the unconstrained misfit as

$$\delta = \frac{(a'_\gamma - a_\gamma)}{a_\gamma} \tag{2.41}$$

Alternatively, Fährmann et al. [40] simply multiplied the constrained lattice misfit by a factor of 2/3 to find the unconstrained value. Evidently, further studies are required to link the constrained and unconstrained lattice parameters, although a unified equation is unlikely to suffice for all alloys, due to differences in composition and microstructure.

There is a significant lack of consensus in the literature as to the significance of coherency strengthening, and the mathematical descriptions used to define the effect. For example, it has been concluded that the yield strength of several austenitic steels was not affected by misfits between 0 and 0.4% [33]. In contrast, other studies have concluded that coherency strain in γ' strengthened alloys does have a significant effect on yield strength, for misfits between 0.2 and 0.8% [53,55]. In fact, an increase in lattice misfit from 0.2% to 0.8% was seen to double the hardness of ternary Ni-Al-X alloys. At the other extreme, at times the effect of coherency is completely ignored [7].

Alternatively, Decker [14] states that coherency strengthening is only important in certain alloys, due to the effects of certain elements. For example, it is stated that Mo would reduce the coherency strain because it preferentially partitions to the γ phase and (as the atomic radius of Mo is large) therefore increases the lattice parameter of the matrix phase. Hence, Decker concludes that alloys strengthened by the coherency effect would have no Mo content. However, this conclusion cannot be drawn consistently, as in negatively misfitting alloys (where the γ phase has the larger lattice parameter), adding more Mo would actually increase the misfit.

Oblak et al. [24,134] studied the effect of γ'' precipitates in alloy 718. It was found that the effect on CRSS ($\Delta\tau$) due to coherency strains from γ'' precipitates on {100} is approximately given by

$$\Delta\tau = 1.7G|\epsilon|^{3/2}\left(\frac{h^2 f_{\gamma''}(1-\beta)}{2bR}\right)^{1/2} \tag{2.42}$$

where ϵ is the tetragonal misfit (i.e. of type $\{\epsilon, 0, 0\}$), β is the fraction of precipitates with c-axis perpendicular to the Burgers vector and $f_{\gamma''}$ is the volume fraction of the γ'' phase. h and R are the half-thickness and radius of the precipitates [24]. It was concluded that coherency strengthening is the major source of strength in superalloys containing $D0_{22}$ phase γ'' precipitates. Order strengthening was also considered but was found to be less significant. However, it was stated that in traditional γ' strengthened alloys, order, not coherency hardening, is the primary strengthening mechanism. It is not clear why the conclusions drawn for coherency strengthening in the γ'' strengthened alloy 718 cannot also be applied to γ' strengthened alloys. Besides the tetragonal shape of the precipitates in the former, there is no other significant difference. Therefore this study could be more evidence for the importance of coherency strengthening.

Gerold and Haberkorn [53] also attempted to model the effect of coherency strain, which is taken to be the dominant strengthening mechanism in alloys with spherical, coherent precipitates. They derived the equation

$$\Delta\tau = 3G\delta^{3/2}\left(\frac{df_{\gamma'}}{2b}\right)^{1/2} \tag{2.43}$$

where G is the shear modulus of the γ phase, δ is the misfit and d is the mean particle diameter [53]. This equation was used in various subsequent models in the literature [14,60]. In their analysis, the effect of the strain field on edge dislocations was taken as the cause of the coherency strengthening, and so an expression of the form

$$\Delta\tau_0 = \frac{K}{bL} \tag{2.44}$$

could be derived for the increase in CRSS caused by coherency. K is the maximum force on a dislocation of Burgers vector b, caused by the strain field of a single precipitate and L is the distance between precipitates. Equation 2.43 follows from Equation 2.44 by substituting in derived expressions for K and L.

In the later study by Decker [14], which utilised Equation 2.43, Equation 2.41 was used to define the misfit, and it was concluded that the analysis only applies to misfits of the order of 1%.

Conversely, Mott and Nabarro [135] described coherency strain without considering the effect of dislocations at all by simply defining the hydrostatic pressure caused by a misfitting volume.

In contrast, Gleiter and Hornbogen [34] define the increase in critical shear stress caused by the presence of a coherency strain as

$$\Delta\tau = \frac{3G_{\mathrm{av}}(b_p - b_m)^2}{bd} \tag{2.45}$$

where G_{av} is the average shear modulus of the matrix and precipitate phases, b is the Burgers vector, d is the dislocation length within the precipitate, and b_{p} and b_{m} are the particle and matrix slip vectors, respectively [34].

Evidently, a systematic and fundamental study of the role of coherency strengthening in Ni-based superalloys is required to enable the design of new alloys with superior mechanical properties. A detailed understanding of the variation of misfit with temperature is also lacking in the literature. This is consequential since these materials exist at high temperatures during service, so it is the high temperature misfit that influences the mechanical properties in service.

Grain Boundary Strengthening

The pile-up of dislocations at grain boundaries is understood to result in an increased yield strength, and it is commonly established that the extent of this grain boundary strengthening is described well by the Hall-Petch relationship [136, 137];

$$\sigma_{\mathrm{HP}} = \frac{K_{\mathrm{HP}}}{\sqrt{D}} \tag{2.46}$$

where D is the grain size and K_{HP} is a constant.

Previous studies have shown that the Hall-Petch equation applies well to various multiphase Ni-based superalloys, however in these materials, the constant, k_{HP}, has been found to be proportional to the spacing between γ' precipitates [25]. This has been rationalised by a work-hardening model, in which the interaction between dislocations, rather than the pile-up of dislocations at grain boundaries, governs the yield strength [25]. The synergistic effects of strengthening by grain boundaries and by γ' precipitates imply that these two mechanisms are not necessarily entirely independent [155], and may not be simply combined together additively [156]. However, there has been no comprehensive study to quantitatively separate these effects.

Additionally, the precipitation of other phases may affect the resulting strengthening contribution of the grain boundaries in Ni-based superalloys. In the commercial Ni-based superalloy NIMONIC PE16, it has been found that carbide formation at the grain boundaries lowered the yield strength sufficiently so that the yield strength did not follow the classical Hall-Petch relationship [25].

For the case of superalloys, it must also be noted that there are two components to grain boundary strengthening; in addition to strengthening from the grain boundaries in the γ matrix phase, the large, primary γ' precipitates also contribute. Equation 2.46 should be modified to account for the finite volume of material applicable to grain boundary strengthening - that is, regions of γ matrix phase, and regions of neighbouring primary γ' precipitates. This may be simply done by multiplying by a prefactor, $\frac{2}{3}f$, where f is the total fraction of the material that is either γ matrix or primary γ' precipitate phase. The factor $\frac{2}{3}$ has been estimated experimentally as the fraction of primary γ' precipitates that are neighbouring to another primary γ' precipitate [7].

The extent of grain boundary strengthening by primary γ' precipitates has been found to give rise to an increment of around 50 MPa in the yield strength of subsolvus IN100, compared to the supersolvus variant [7]. However, since other strengthening mechanisms also vary between these alloys, this increase is not reproduced in the overall yield strength. The extent of grain boundary strengthening by the γ phase was more significant, reaching approximately 300 MPa in subsolvus IN100.

Total Yield Strength

Evidently there are many underlying mechanisms that add to the appreciable yield strength of Ni-based superalloys. However, there is a lack of consensus in the literature as to how these mechanisms combine to give an overall, measurable yield strength. Some authors conclude that a single mechanism is the major cause of strengthening in Ni-based superalloys [24, 52, 60, 114]. However many authors combine some, or all, of the various mechanisms to determine the overall yield strength [7, 33, 53, 65, 133]. For example, Singhal and Martin [60] take into account precipitation and coherency strengthening, by adding together the equations given by Gleiter and Hornbogen [98] and Gerold and Haberkorn [53] (Equation 2.43) for APBE and coherency strengthening respectively. This was concluded to fit with the experimental data.

In general, it may be agreed that the total yield strength is a sum of the individual strengthening mechanisms;

$$\tau_{\text{total}}^{q} = \sum_{i=1}^{n} \Delta\tau_{i}^{q} \tag{2.47}$$

The exponent q is disputed in the literature, although is often found to be between 1 and 2, by fitting to experimental data [96]. Some authors have concluded that the total yield strength is simply a linear sum of the individual strengthening mechanisms ($q = 1$) [7,65]. In contrast, others have described dependence with exponent of 2 [92,138]. Alternatively, Ardell [52] used a value of 1.8 when all precipitates are uniformly sized (either weak- or strong-pair coupling occurs in all precipitates). When a distribution of precipitate sizes occurs, and therefore a mixture of weak- and strong-pair coupling, an exponent of 1.4 was suggested. This method has been utilised by subsequent authors [96].

The selection of an appropriate value for the exponent q is not trivial and in general it is unlikely that one exponent will be appropriate for all alloys. In the literature, Equation 2.47 is used empirically, with a value for q determined through fitting to experimental data. An advantage of using a linear summation of the strengthening mechanisms is that this minimises the number of fitting factors in the model. It should however be acknowledged that the choice of exponent will affect the overall predicted yield strength, with a larger value of q more heavily weighting the strongest contributions to yield strength.

2.8 Summary and Outlook

It is clear that there are currently many issues with modelling the strength of Ni-based superalloys. There is a significant lack of agreement on which mechanisms are dominant, or even which are operative. The details of how to model precipitation and coherency strengthening are particularly varied in the literature, and there is no unanimously agreed standard for modelling any of the strengthening mechanisms, or how to combine them to give an overall yield strength. The individual shortcomings identified above that limit each model demonstrate that there is no single model that addresses all the issues found in Ni-based superalloys. The effect of temperature adds another complication.

It has been suggested by Kozar et al. [7] that the variation of the particular active strengthening mechanism could account for some of this difficulty. For example, cross-slip induced hardening is said to occur in both primary and secondary γ' precipitates, whereas strong-pair coupling occurs in the secondary and tertiary particles. In contrast, solid-solution strengthening and hardening from grain boundaries are most important in the γ matrix. Many of the models detailed in this review do not ever consider the concurrent operation of multiple modes of dislocation propagation (for example bowing and strong-pair coupling occurring simultaneously), but simply consider one at a time. This is non-physical, since precipitates of different sizes exist in real microstructures (or at least the apparent precipitate size is different depending on the slip plane of the dislocation), and therefore this must clearly affect the resulting yield strength. Parthasarathy et al. [101] go as far as noting that precipitate cutting can actually be *aided* by bowing of the dislocation slightly around the precipitate beforehand. This lowers the critical stress required for cutting, thereby affecting the modelled yield strengths.

A comprehensive understanding of the extent of the many concurrent strengthening mechanisms operative in Ni-based superalloys is essential to enable the design of superior alloys for present and future applications. If these mechanisms are fully understood, alloys can be designed with microstructures optimised to the strengthening mechanisms that are known to be occurring. An attempt has been made to use yield strength modelling to design an optimised new Ni-based superalloy [114], however, it was found that although the 'ideal' alloy showed increased strength, it lacked ductility. In that study, only strengthening via precipitates was taken into account. Clearly multiple mechanical properties must be taken into account to design optimised superalloys. In the end, this will overcome the current limitation

of aircraft engine design - the materials.

Chapter 3

Yield Strength Modelling of Commercial Alloys

3.1 Introduction

As discussed in detail in Chapter 2, due to their exceptional mechanical properties, polycrystalline Ni-based superalloys are used in many extreme engineering applications where the yield strength is of particular importance, such as gas turbine engines. However, as the many different strengthening mechanisms discussed in Chapter 2 contribute to the overall yield strength, establishing a physically based model for yield strength is complex. Furthermore, the extent of each individual strengthening mechanism is difficult to isolate, since they are often affected by the same microstructural features, e.g. composition or phase fraction.

The precipitate size at which peak strength is obtained is often deemed to correspond to the transition from weak- to strong-pair dislocation coupling (Section 2.6), and as such, varies between different commercial alloys due to their differing composition. For example, optimum precipitate size has been concluded to occur for 55-85 nm γ' precipitates in commercial alloy Nimonic 105, but at just 26-30 nm for alloy PE16 [5]. However, a unimodal distribution of such fine precipitates is difficult to achieve in practice, and has been associated with reduced ductility [114] and creep performance [139,140]. Different polycrystalline Ni-based superalloys employ different proportions of each strengthening mechanism to achieve optimum strength, with some favouring high γ' contents, whilst others rely on the properties of the γ matrix itself. Whilst the majority of studies have concluded that order strengthening is the most significant mechanism [7,51], the importance of other strengthening mechanisms is debated (Chapter 2). To the author's knowledge, the combined effects of strengthening from grain boundaries, solid solutions within both the γ and γ' phases, coherency strains and precipitates have not yet been combined together to predict an overall yield strength.

Recently, yield strength modelling has been increasingly exploited in computational alloy design. In such schemes, the composition and microstructures are identified that optimise the properties deemed most important [132, 141]. These schemes seek a balance between the strengthening mechanisms, since some changes augment one strengthening mechanism whilst being detrimental to another. In a similar manner, computational models have been used to predict the mechanical properties arising from a specific microstructure, and to subsequently optimise heat treatments [114]. Alternatively, complex models have been simplified by fitting to equations, which are then used to design superior alloys. For example, data from dislocation simulation models have been used to predict yield strength from microstructural parameters [101]. Similarly, data from the literature have been used to create empirical models, which

have been used to optimise mechanical properties [142]. Such studies highlight the potential value of models of yield strength in superalloys, but the different schemes adopted and different strengthening mechanisms included suggest that further studies may be useful in identifying the key contributions and how these add to give an overall, measurable yield strength.

In this chapter, the individual strengthening mechanisms of various commercial polycrystalline Ni-based superalloys have been determined and combined using models available in the literature. To highlight the roles of composition and microstructure on yield strength, a detailed assessment of the strengthening mechanisms in coarse-grained (CG) RR1000 has been carried out. These data identify the most significant strengthening mechanisms present in Ni-based superalloys and give an indication of how they may be tailored through alloy modification. In the design of future alloys, this will allow the microstructure and composition to be optimised for maximum performance.

3.2 Methods

Alloys Studied

To determine the extent of the multiple concurrent strengthening mechanisms in current Ni-based superalloys, 5 commercial polycrystalline Ni-based alloys were studied. The compositions and microstructural parameters of these alloys, obtained from the literature and used as inputs for the strength models, are detailed in Tables 3.1, 3.2 and 3.3 respectively.

Table 3.3 contains stereological data used as inputs for the strength models discussed in this chapter. Although these are taken from experimental data in the literature, these are not presented with associated experimental uncertainties because these were not given with the original data. In addition (and more importantly), these microstructural parameters may vary relatively significantly even for a particular alloy, due to the wide variety of possible fabrication methods and heat treatments used commercially. The resulting wide range of input parameters would impede the modelling of the effect of these microstructural parameters on yield strength, and the subsequent visualisation of trends. The present work aimed to determine the effect of these microstructural parameters on yield strength and its underlying mechanisms. As such, in the present work, microstructural parameters typical of those commonly achieved experimentally were used as inputs for the yield strength models. These are the values given in Table 3.3.

To gain further insight into the effect of composition on the extent of the individual strengthening mechanisms present in superalloys, further predictions were made for the alloy RR1000. Calculations were performed whilst varying the bulk composition of RR1000 within the range given in the original patent [147] (Table 3.4) to determine the different possible yield strengths within this specification, and within a wider range of compositions, indicative of the array of current commercial alloys (Table 2.3). Compositional variation was achieved by substituting each individual element with Ni. In this way, as a particular element was varied, the concentration of all other elements (except Ni) remained constant at the patented value. The minimum Al content was taken as the minimum content at which Thermo-Calc still predicted γ' phase to be present, with all phases allowed in the thermodynamic calculations. At lower Al contents, the η phase forms preferentially over the γ' phase and, as such, this compositional range was deemed irrelevant, as such alloys would not be commercially useful due to inferior mechanical properties. For each composition within the range, the yield strength and its associated mechanisms were determined using models available in the literature.

Alloy	Cr	Co	Mo	W	Nb	Al	Ti	Ta	Hf	Fe	V	C	B	Zr	Ni	Ref.
IN100	12.3	18.3	3.3			4.9	4.3			0.1	0.7	0.06	0.03	0.05	Bal.	[7]
Rene88DT	16.0	13.0	4.0	4.0	0.7	2.1	3.7					0.03	0.0015	0.03	Bal.	[5]
RR1000	15.0	18.5	5.0			3.0	3.6	2.0	0.5			0.027	0.015	0.06	Bal.	[5]
Udimet720	17.9	14.7	3.0	1.25		2.5	5.0					0.035	0.033	0.03	Bal.	[5]
Waspaloy	19.5	13.5	4.3			1.3	3.0					0.08	0.006		Bal.	[5]

Table 3.1: Compositions of commercial alloys studied, in wt.%.

Alloy	Cr	Co	Mo	W	Nb	Al	Ti	Ta	Hf	Fe	V	C	B	Zr	Ni	Ref.
IN100	12.9	17.0	1.9			9.9	4.9			0.098	0.75	0.27	0.10	0.012	Bal.	[7]
Rene88DT	17.9	12.8	2.4	1.3	0.4	4.5	4.5					0.15	0.081	0.019	Bal.	[5]
RR1000	16.5	17.9	3.0			6.3	4.3	0.63	0.16			0.13	0.08	0.04	Bal.	[5]
Udimet720	19.3	14.0	1.8	0.38		5.2	5.9					0.16	0.17	0.018	Bal.	[5]
Waspaloy	21.3	13.0	2.5			2.7	3.6					0.38	0.032		Bal.	[5]

Table 3.2: Compositions of commercial alloys studied, in at.%.

	Grain Size	Pri. γ' Size	Sec. γ' Size	Ter. γ' Size	Pri. γ' Vol.%	Sec. γ' Vol.%	Ter. γ' Vol.%	Total γ' Vol.%
IN100 [7, 143]	3.1 µm	1430 nm	170 nm	12 nm	21	34	4.2	59.2
Rene88DT [144–146]	60 µm	-	100 nm	20 nm	-	36	6	42
Fine grained (FG) RR1000 [147]	10 µm	3000 nm	225 nm	15 nm	15	25	5	45
Coarse grained (CG) RR1000 [147]	49 µm	-	225 nm	15 nm	-	40	5	45
Udimet720 [148–150]	10 µm	2000 nm	100 nm	20 nm	11.5	30	2	43.5
Waspaloy [151, 152]	52 µm	-	195 nm	23.9 nm	-	17.9	4.9	22.8

Table 3.3: Microstructural parameters of the commercial alloys studied

Element	Cr	Co	Mo	Al	Ti	Ta	Ni
Min. wt.% (at.%)	0	0	0	1.4 (3.1)	0	0	Bal.
Min. patent wt.% (at.%)	14.35 (15.7)	14 (13.5)	4.25 (2.5)	2.85 (6.0)	3.45 (4.1)	1.35 (0.4)	Bal.
Max. patent wt.% (at.%)	15.15 (16.7)	19 (18.5)	5.25 (3.1)	3.15 (6.7)	4.15 (5.0)	2.15 (0.7)	Bal.
Max. wt.% (at.%)	30 (32.4)	24 (23.3)	6 (3.6)	6 (12.3)	6 (7.1)	4 (1.3)	Bal.

Table 3.4: Composition range of RR1000 studied in wt.% (the content of Hf, C, B and Zr were kept constant at the patent values). Values in at.% are shown in brackets.

Thermodynamic Modelling

The Thermo-Calc software package with the TCNi7 database was used to predict the equilibrium phase compositions and volume fractions of each alloy. It must be noted that Thermo-Calc only provides a single value for the γ' phase composition, and as such, this composition was used for both the secondary and tertiary distributions of γ' in the subsequent calculations of yield strength. The equilibrium calculations were carried out with the allowed phases constrained to only γ and γ'. Although this was therefore not representative of the predicted thermodynamic equilibrium, superalloys are typically produced in the metastable condition, which is of commercial relevance. This method was utilised in order to determine the trends with composition in the metastable state and, as such, there were compositional regions included in the present work that may not be typical of current commercial alloys.

The lattice misfit of each alloy was determined using the molar volumes (V_{m}) of the phases predicted by Thermo-Calc. These enabled calculation of the lattice parameters (a) of the γ and γ' phases via

$$a = \left(\frac{4V_m}{N_A}\right)^{1/3} \tag{3.1}$$

where N_A is Avogadro's constant. The lattice misfit (δ) could subsequently be determined using Equation 2.4. These input data enabled the yield strength and its multiple underlying mechanisms to be calculated using the models detailed in the following section. Comparison was also made between the yield strength calculated using the predicted equilibrium phase compositions from Thermo-Calc and phase compositions determined experimentally in previous studies.

Yield Stress Modelling

The overall yield strength (σ_{Y}) is obtained by summing the individual contributions of each underlying mechanism. These include solid solution strengthening of both the γ and γ' phases (σ_{sss}), precipitation strengthening (σ_{p}), coherency strengthening arising from the lattice misfit at the γ/γ' interface (σ_{coh}), grain boundary strengthening (σ_{HP}) and the Orowan effect of dislocation bowing around large precipitates (σ_{Oro}). In previous studies, this summation has been achieved by numerous methods (see Section 2.7) but a linear approach (Equation 3.2) has been used in the present study.

$$\sigma_{\mathrm{Y}} = \sigma_{\mathrm{HP}} + \sigma_{\mathrm{p}} + \sigma_{\mathrm{sss}} + \sigma_{\mathrm{Oro}} + \sigma_{\mathrm{coh}} \tag{3.2}$$

Solid Solution Strengthening, σ_{sss}

Disparities in atomic size and modulus of solute elements occur in both the γ and γ' phases, but the latter is commonly disregarded in the literature (see Section 2.7). In the disordered matrix phase, the degree of solid solution strengthening (S_i^{γ}) was modelled as

$$S_i^{\gamma} = \beta_i^{\gamma} {x_i^{\gamma}}^{1/2} \tag{3.3}$$

where x_i^{γ} is the concentration of element i in the matrix [66, 81]. The constants β_i^{γ} are dependent on both the atomic size and modulus, and the values, determined from experimental data in the literature [66, 67, 82, 86, 87], are reproduced in Table 2.4.

In the ordered γ' phase, the effect of the differing propensities for atomic bonding between neighbouring atoms also influences the resultant solid solution strengthening [67]. This is accommodated by varying the exponent in the resulting strength equation [67, 91] (Equation 2.10), with constants again given in Table 2.4. Data could not be found to determine the solid solution strengthening coefficients

($\beta_i^{\gamma'}$) for Co and V in the γ' phase, however, since the content of both elements in this phase is low, the solid solution strengthening effects of both are considered likely to be negligible and may therefore be disregarded.

To determine the overall effect of solid solution strengthening, the contribution from each element i was summed [85], taking into account the volume fraction of each phase, giving

$$\sigma_{\mathrm{SSS}}^{\gamma} = (1 - f_{\gamma'}) \left(\sum_i \left(S_i^{\gamma} \right)^2 \right)^{1/2} \tag{3.4}$$

for the matrix phase, and

$$\sigma_{\mathrm{SSS}}^{\gamma'} = f_{\gamma'} \left(\sum_i S_{i,\mathrm{sec}}^{\gamma'} w_{\mathrm{sec}} + \sum_i S_{i,\mathrm{ter}}^{\gamma'} w_{\mathrm{ter}} \right) \tag{3.5}$$

for the precipitate phase, where w_{sec} and w_{ter} are the number density of secondary and tertiary γ' respectively, and f_{γ} and $f_{\gamma'}$ are the volume fractions of the γ and γ' phases respectively.

Precipitation Strengthening, σ_{p}

The strengthening effect of precipitates in alloy systems is heavily discussed in the literature [7, 33, 53, 54, 58, 65, 72, 101] (see Section 2.7 for more detail). However, classical models of superlattice-structured precipitates, which define the maximum strength as the transition between strong- and weak-pair coupling (defined for a precipitate size giving maximum strength, r_{m}), are insufficient in the case of superalloys. They have been found to result in non-physical predictions (a negative yield strength) for very small precipitate sizes, are only valid for low precipitate volume fractions, and are limited at the transition from weak- to strong-pair coupling, which often coincides with the precipitate size found in Ni-based superalloys [65]. The effect of multimodal precipitate size distributions is also often omitted from classical models [33, 53, 54, 58, 72].

A model that unites the classical regimes of weak- and strong-pair coupling in order to overcome these limitations [65] is used in the present work to predict the extent of precipitation strengthening. Primary γ' precipitates are not included in this cutting model, as these are bypassed by Orowan looping instead. For a bimodal precipitate size distribution, the precipitation strengthening is given by

$$\sigma_{\mathrm{p}} = \mathrm{M} \left(\tau_{\mathrm{p,sec}} \frac{\mathrm{N_{sec}}}{\mathrm{N_{sec}} + \mathrm{N_{ter}}} + \tau_{\mathrm{p,ter}} \frac{\mathrm{N_{ter}}}{\mathrm{N_{sec}} + \mathrm{N_{ter}}} \right) \tag{3.6}$$

where $\mathrm{N_{sec}}$ and $\mathrm{N_{ter}}$ are the number densities of the secondary and tertiary γ' precipitates respectively, and M is the Taylor factor. $\tau_{\mathrm{p,sec}}$ and $\tau_{\mathrm{p,sec}}$ are the shear stresses required for a dislocation to cut a secondary and tertiary γ' precipitate of size r, respectively. These may be calculated using a unified model [65] arising from the force balance between the two dislocations of the pair. The leading and trailing dislocations feel a force balance given by Equations 3.7 and 3.8 respectively.

$$\tau_p b \Lambda_1 + F_{\mathrm{pair}} \Lambda_1 - \gamma_{\mathrm{APB}} l_1 + 2 \tau_p b r = 0 \tag{3.7}$$

$$\tau_p b \Lambda_2 - F_{\mathrm{pair}} \Lambda_2 = 0 \tag{3.8}$$

in which γ_{APB} is the anti-phase boundary energy (APBE) of the γ' precipitates, b is the Burgers vector, l_1 is the length of the leading dislocation cutting the precipitate, Λ_1 and Λ_2 are defined as the distance between precipitates being cut by the leading and trailing dislocations respectively, and F_{pair} is the

dislocation pair force per unit length. These equations may be rearranged to give

$$\tau_p = \frac{\gamma_{\mathrm{APB}} l_1}{2b(\Lambda_1 + r)} \tag{3.9}$$

which is calculated for the secondary and tertiary γ' individually ($\tau_{\mathrm{p,sec}}$ and $\tau_{\mathrm{p,ter}}$). It should be noted that in the original work [65], this equation is incorrect, containing an additional factor of 2. A Taylor factor of 3 was used to convert the shear stress, τ_{p}, to a normal stress.

The shear stress is dependant on the regime of coupling; with the length of the leading dislocation given as

$$l_1 = 2\sqrt{r^2 - (r - r_m)^2} \tag{3.10}$$

$$l_1 = 2r_m \tag{3.11}$$

for strong- and weak-pair coupling respectively. Within the model utilised for the present work, to link these two regimes,

$$\Lambda = \max\left(\sqrt{\frac{Gb^2}{2\gamma_{\mathrm{APB}} r}}\sqrt{\frac{2\pi}{3f_{\gamma'}}}r, \sqrt{\frac{2\pi}{3f_{\gamma'}}}r - l_1\right) \tag{3.12}$$

where G is the shear modulus.

The original model in [65] is based upon an average precipitate diameter, where the precipitates are all spherical. However, dislocations travel on slip planes that cut through the precipitates on a 2D plane that does not necessarily contain the equatorial section of the precipitate. The dislocations therefore interact with each individual precipitate via a 2D circular intersection that is likely to be smaller than the full diameter ($2r$) (Figure 3.1). As such, an improvement to the original model can be obtained by using a reduced, effective diameter ($2r_{\mathrm{eff}}$), to take into account that the slip plane does not intersect precipitates only at the diameter. This reduced diameter ($2r_{\mathrm{eff}}$) is the average intersection between the slip plane and the precipitate, and is given by the average length of a chord of a spherical precipitate with radius r.

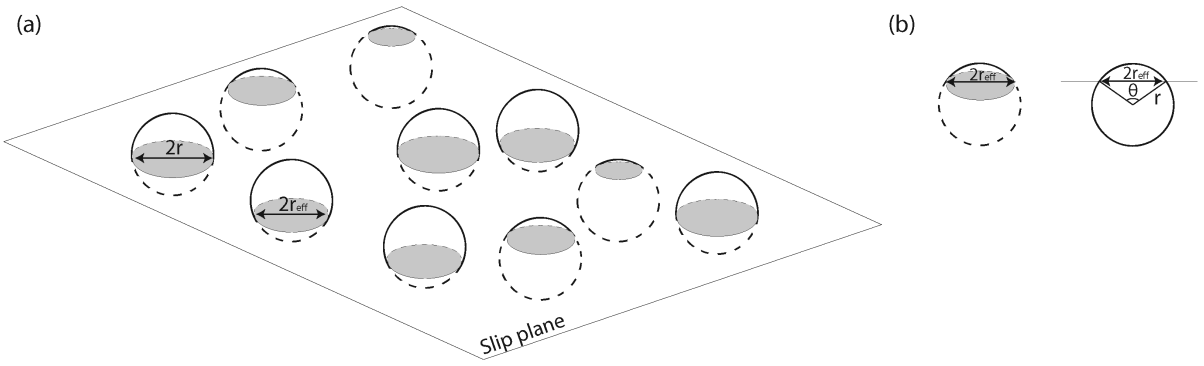

Figure 3.1: (a) Schematic illustration of a {111} slip plane cutting a number of spherical precipitates of radius, r. The random positioning of each precipitate normal to the slip plane results in a different effective radius, r_{eff}, for each precipitate. (b) The average value of $2r_{\mathrm{eff}}$ is the average length of the chord bisecting the circular intersection of the precipitate and the slip plane.

The length of a chord cutting a sphere of radius r (Figure 3.1b) is given by

$$2r_{\mathrm{eff}} = 2r \sin\frac{\theta}{2} \tag{3.13}$$

where θ may be between 0 and π radians. The average length of r_{eff} is given by

$$\left\langle r_{\text{eff}} \right\rangle = r\frac{\int_0^\pi \sin\frac{\theta}{2}d\theta}{\pi} = \frac{2r}{\pi} \tag{3.14}$$

Therefore, the precipitate radius used in Equation 3.9 is modified by a factor of $2/\pi$ in the instances where it defines precipitate cutting. In instances where r is used to define values such as volume fraction, the original precipitate radius, r, is still required.

Anti-Phase Boundary Energy (APBE)

A CalPhaD-based approach was used to determine the APBE required in the yield strength models. A full description of this method is provided in [113]. In the CalPhaD-based approach, an Ising model is employed to determine long-range ordering between nearest-neighbour interactions by relating interchange energies between the ordered (γ') and disordered (γ) phases. Therefore, in addition to the γ' phase composition, this APBE model required values for the enthalpy of the γ' phase and that of a disordered phase of the same composition. These parameters were determined using Thermo-Calc. These were converted to interaction energies for the first, second and third nearest neighbour atoms ($V^{(1)}$, $V^{(2)}$, $V^{(3)}$) by the method detailed by Crudden et al. [113] (Section 2.6), and the APBE could then be calculated using Equation 2.30.

Coherency Strengthening, σ_{coh}

The extent of coherency strengthening arising from a lattice misfit, δ, was modelled using the approach described by Reppich [153], which was itself based on previous studies [7, 93, 154]

$$\tau_{\text{coh}} = \alpha G\delta^{2/3}\left[\frac{f_{\gamma'}r}{b}\right]^{1/2} \tag{3.15}$$

where r is the average precipitate size, and the constant α is ascribed an average value of 3.7 [153]. This shear stress is converted to a normal stress using the Taylor factor, M=3.

The present model for the coherency strength increment may predict a significant coherency strengthening effect. Whilst there is no upper limit set by Equation 3.15, the extent of coherency strengthening must necessarily be limited by the strength of the γ phase itself, as larger coherency strains cannot be supported by this phase, leading to plastic deformation of the γ matrix or a breakdown of coherency. Therefore, in the present work, the coherency strength (σ_{coh}) was limited to a maximum equalling the solid solution strength of the matrix phase ($\sigma_{\text{sss}}^{\gamma}$).

Grain Boundary Strengthening, σ_{HP}

The role of grain boundary strengthening was studied using the range of grain sizes allowable in the RR1000 patent; from 6 to 45 µm, with the nominal value being 30 µm. Grain boundary strengthening is well described in single phase alloys by the Hall-Petch equation (Equation 2.46) [136, 137], and was discussed in more detail in Section 2.7.

The constant k_{HP} has been found experimentally to lie within the range of 710 to 760 MPa ± 100 $\mu\text{m}^{-1/2}$ for polycrystalline Ni-based superalloys [25, 157], and values within this range have subsequently been used in the Hall-Petch equation by other authors [7, 65]. In contrast, in the single-phase matrix, a much lower value for k_{HP} (371 MPa ± 100 $\mu\text{m}^{-1/2}$) was found [25], implying a reduced strengthening effect of the grain boundaries, compared to a multiphase alloy. In the present work, a value of 750 MPa ± 100 $\mu\text{m}^{-1/2}$ was used, in line with these data.

Orowan Strengthening, σ_{Oro}

Large particles may be bypassed by Orowan looping. In the present work, the extent of strengthening imparted by this mechanism is taken as

$$\sigma_{\text{Oro}} = M\frac{3Gb}{2L} \tag{3.16}$$

where L is the mean precipitate spacing [153].

3.3 Results and Discussion

Strengthening Contributions

The calculated contributions from the individual strengthening mechanisms operative in 6 commercial alloys are shown in Figure 3.2, with the alloys presented in order of increasing γ' volume fraction. Evidently, the extent of each strengthening mechanism differs between the commercial alloys. It can be seen that for all of the alloys considered, the most significant mechanism is precipitation strengthening and this tended to decrease as the volume fraction of γ' increased. Although counterintuitive, this was in fact due to the differing composition of the γ' phase in these alloys, which therefore affected the APBE (Table 3.5). Additionally, the γ' size and the ratio of the secondary and tertiary γ' volume fractions affects the resulting yield strength, thereby further complicating the conventional expectation of increasing γ' volume fraction resulting in increasing yield strength. It is worth noting that the precipitation strengthening effect is dominated by the tertiary γ', as this distribution has the highest number density. This explains the similar magnitude of precipitation strengthening in CG and FG RR1000, despite the latter containing a significant amount of primary γ'.

Alloy	APBE (Jm^{-2})
IN100	0.307
Rene88DT	0.339
FG RR1000	0.322
CG RR1000	0.322
Udimet720	0.338
Waspaloy	0.345

Table 3.5: Calculated APBEs for each of the commercial alloys studied.

The extent of solid solution strengthening is approximately constant, ∼200-300 MPa, across all alloys studied. In contrast, hardening through the presence of grain boundaries varies strongly, being largest, ∼400 MPa, in IN100 (nominal grain size of 3.1 µm) and smallest, ∼100 MPa, in Rene88DT (nominal grain size of 60 µm). Many alloys are commonly used in both fine- and coarse-grained varieties and it is interesting to note that for RR1000, the fine-grained variant has approximately 100 MPa more strength arising from the smaller grain size. The variation in solid solution strengthening in the fine- and coarse-grained variants arises from differences in the intragranular γ' volume fraction. Combining these mechanisms results in similar modelled yield strengths for the coarse and fine-grained variants (1330 and 1370 MPa respectively). The role of coherency strengthening also varies significantly, resulting in 300 MPa of strength in Rene88DT but only 9 MPa in IN100.

In all alloys, the model predictions follow the same trends as the experimentally determined yield strengths obtained from the literature [7, 158–161]. However, the models overpredict the yield strength by approximately 300 MPa, or more in the cases of Waspaloy and Udimet720. It is important to note that these models were created for each individual strengthening mechanism and, as such, do not quantitatively

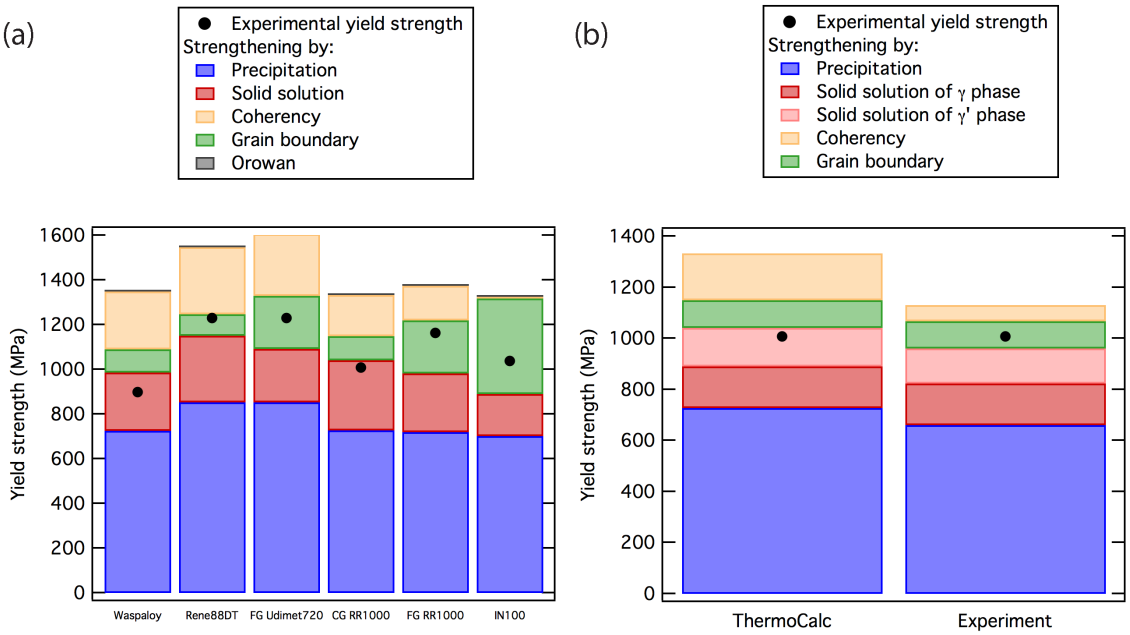

Figure 3.2: (a) The extent of individual strengthening mechanisms in a selection of current commercial superalloys, in order of increasing γ' content. Experimental yield strength values [7, 158–161] are included for comparison to modelled results. (b) Predicted yield strength contributions in CG RR1000 using phase compositions calculated by Thermo-Calc compared to those measured experimentally.

agree with experiment when all of the individual strengthening mechanisms are taken into account. This is significant, since in reality, each individual strengthening mechanism will have an effect on the overall mechanical properties and therefore all should be considered, and the models corrected as necessary.

The phase compositions are required as inputs to the yield strength models studied. These may be obtained experimentally, or predicted using Thermo-Calc software. These two methods, however, give different results, thereby affecting the calculated yield strength. Figure 3.2b shows the yield strength contributions in CG RR1000 obtained using Thermo-Calc-predicted equilibrium phase compositions and those obtained using experimentally determined compositions. Evidently there is no effect on grain size hardening, but the role of coherency and precipitation strengthening vary. In both cases, higher strengths are predicted when Thermo-Calc is used to predict phase compositions. The extent of solid solution strengthening does not appear to be significantly affected by using experimental or Thermo-Calc phase compositions. Clearly, the accurate determination of phase composition is essential for reliable yield strength modelling. Notably, the yield strength predictions for RR1000 are significantly closer to the experimental yield strength when using the experimentally measured phase compositions, rather than those predicted by Thermo-Calc (Figure 3.2b). This is mainly due to differences in the predicted coherency strengthening effect.

Whilst these models evidently cannot predict absolute values of strength when all of the individual strengthening mechanisms are taken into account, they may assist in predicting relative changes. They therefore offer the possibility of assessing how compositional and microstructural modifications to an alloy may affect the individual strengthening mechanisms. This provides insight into the sensitivity of the yield strength to such variations and the extent to which it may be optimised. In this study, the alloy CG RR1000 was used as the base for these analyses.

The Effect of Grain Size

Figure 3.3 shows the variation in the strengthening contribution of grain boundaries in RR1000 as a function of grain size. The range of grain sizes specified in the RR1000 patent is also shown and it was found that, within this range, changing the grain size resulted in a change in yield strength of 200 MPa, with the smallest grain sizes resulting in higher strengths. Extrapolating to grain sizes beyond the patent, further strength can be obtained at the smallest grain sizes. However, such grain sizes will inevitably be limited by processing considerations.

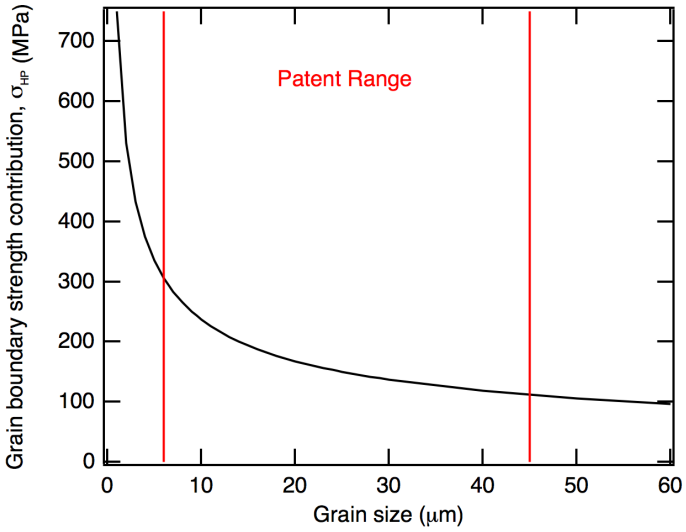

Figure 3.3: Variation in grain boundary strengthening in RR1000. The range of grain sizes quoted in the RR1000 patent is indicated by the red lines.

The Effect of Compositional Modification on Individual Strengthening Mechanisms

Solid Solution Strengthening

In considering the effect of compositional modifications on the yield strength of RR1000, it should be noted that altering the concentration of each individual element affected the partitioning of all other elements between the γ and γ' phases. This complexity has been hinted at in previous literature [162]. These effects are shown in Figures 3.4, which illustrate the predicted γ phase composition as the concentration of one element is varied above and below that of the nominal patent composition, substituting for nickel. Figures 3.4a-c show that increasing the concentration of Cr, Co or Mo (the γ partitioning elements) in the bulk alloy is expected to lead to an approximately linear increase in the content of those elements in the γ phase, as may be expected. In the case of Co or Mo, the concentrations of the remaining elements in the matrix phase remained approximately constant. At zero bulk Cr content, however, the contents of the other γ-partitioning elements decreased concurrently. Altering the bulk content of Cr, Co or Mo did not appreciably affect the concentration of any of the γ'-partitioning elements in the γ matrix phase.

The effects of these variations in the bulk composition on the solid solution strengthening of the γ phase are shown in Figure 3.4g-i. It should be noted that the volume fraction of the γ' phase is not taken into account in Figure 3.4. Therefore, the values of solid solution strength displayed are the change in the yield strength of the γ phase alone and not that weighted by the volume fraction, which would give $\sigma^{\gamma}_{\mathrm{SSS}}$. This approach was adopted to highlight the effect of elemental variations on the solid solution strength, decoupled from other effects associated with these compositional changes. Increasing

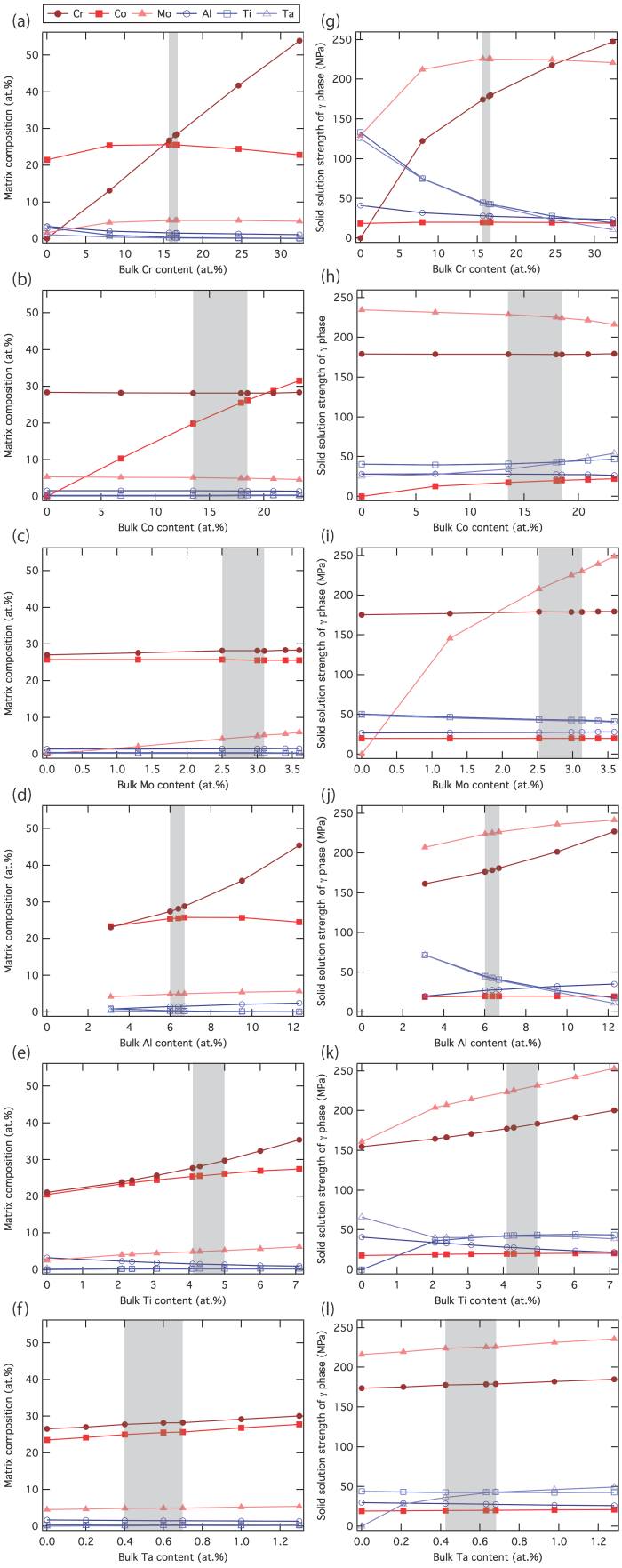

Figure 3.4: Predicted matrix phase composition as the bulk content of (a) Cr, (b) Co, (c) Mo, (d) Al, (e) Ti, and (f) Ta are changed. The associated solid solution strength of the matrix phase is shown in (g)-(l) for changing Cr, Co, Mo, Al, Ti and Ta respectively. For each element, the RR1000 patent range is shaded.

the bulk concentration of each of the γ-partitioning elements (Cr, Co, Mo) resulted in increased solid solution strengthening in the γ phase from that particular element alone. The fact that Mo increases alloy strength was in fact used to tailor the composition of alloy RR1000, although the rationale for this strength increase was not specified [5]. Since the partitioning of other elements was slightly affected, increasing Co resulted in increased solid solution strengthening in the γ phase from Ti and Ta, whereas increasing Cr resulted in decreased solid solution strengthening of these elements, and a small decrease in solid solution strengthening by Al. Of the three γ-partitioning elements, Mo had the largest effect on solid solution strengthening in the matrix; a 3.5 at.% increase in bulk Mo content increased the solid solution strengthening by that element alone by 250 MPa.

In contrast, altering the bulk concentration of the γ'-partitioning elements (Al, Ti, Ta) affected the phase partitioning of all elements in the γ phase (Figure 3.4d-f). Increasing bulk Al, Ti or Ta content increased the concentration of Cr, Co and Mo in the γ phase, with the Cr increase being particularly pronounced. An Al content of 12 at.% resulted in a Cr content of the γ phase of $\sim$45 at.%. This has important implications for microstructural stability, since increased Cr content in the γ matrix is a strong promoter of the σ phase and severe instability towards the formation of this phase would therefore be expected for an alloy with such a high Al content.

Increasing the bulk Al, Ti or Ta content increased the solid solution strengthening of the γ phase derived from that particular element. However, in all three cases, the solid solution strengthening effect of the other two γ'-partitioning elements decreased. The extent of solid solution strengthening of Cr and Mo increased when bulk Al, Ti or Ta content was increased. In contrast, solid solution strengthening from Co remained approximately constant.

Figure 3.5 shows the corresponding effect on the γ' precipitate phase, with Figure 3.5a-f displaying the phase composition as the bulk composition of each element is individually altered, and Figure 3.5g-l showing the associated extent of solid solution strengthening.

Figure 3.5d and e clearly show that increasing the bulk Al content is predicted to give rise to a concurrent decrease in the Ti content of the γ' phase, and vice versa. This implies that there is a limiting overall concentration of these elements in the γ' phase, defining the sublattice occupancy of the ordered $L1_2$ lattice. Both elements also caused a slight decrease in the Ta content. Increasing Al or Ti content also resulted in an increase of the γ-partitioning elements in the γ' phase, particularly Co. Increased bulk Ti content also reduced the Cr and Mo content of the γ' phase. The third γ'-partitioning element, Ta, was seen to reduce the concentration of the γ-partitioning elements in the γ' phase and to cause a slight decrease in Ti content.

Varying the concentration of the γ-partitioning elements also affected the γ' phase composition. Figure 3.5c shows that increasing bulk Mo content had no effect on the γ' composition, apart from a slight increase in the Co content. Figure 3.5b demonstrates that increasing bulk Co content caused the concentration of Co in the γ' phase to increase significantly, even though this element is classically expected to partition to the matrix phase. Bulk Co content has no effect on the concentration of other elements present in the γ' phase. Previous studies have found a non-linear partitioning effect of Co, with Co contents above 8 at.% resulting in partitioning to the γ phase, whilst below 8 at.%, partitioning to the γ' phase [163]. This is in agreement with the present study. Finally, in Figure 3.5a it is clear that increasing the bulk Cr content had an effect on the concentration of the other γ-partitioning elements in the γ' phase. Cr increased the Co content of the γ' phase, but decreased the Mo content. At zero bulk Cr content, the composition of the γ' phase was higher in the other γ-partitioning elements (Co and Mo), and lower in the γ'-partitioning elements.

Figure 3.5g-l show the corresponding predicted solid solution strength of the γ' phase. It is seen that Ti had a significant solid solution strengthening effect on the γ' phase. This may be attributed to its high concentration in the γ' phase. Additionally, as shown in Table 2.4, Mo and Ta had the largest solid

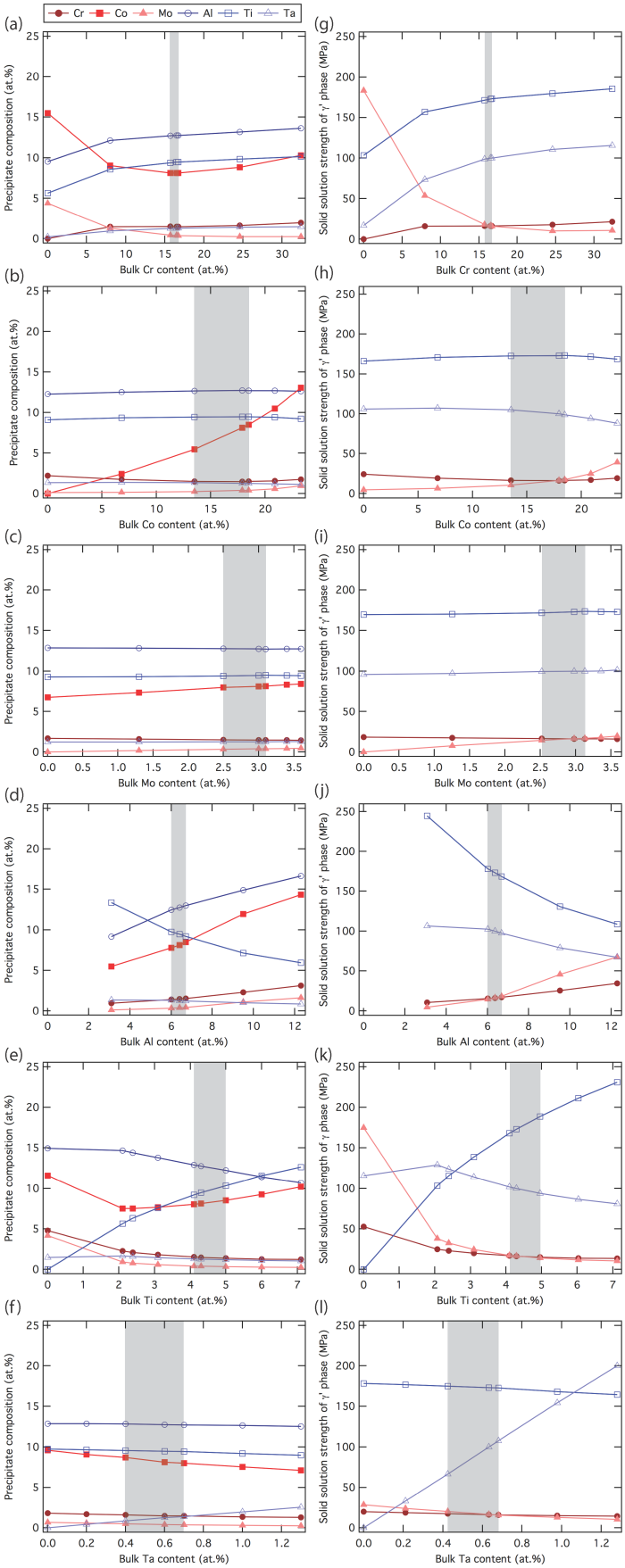

Figure 3.5: Predicted precipitate phase composition as the bulk content of (a) Cr, (b) Co, (c) Mo, (d) Al, (e) Ti, and (f) Ta are changed. The associated solid solution strength of the precipitate phase is shown in (g)-(l) for changing Cr, Co, Mo, Al, Ti and Ta respectively. For each element, the RR1000 patent range is shaded.

solution strengthening coefficients in the γ' phase per volume. Therefore, small changes in Mo or Ta contents lead to significant changes in the solid solution strength of the γ' phase.

Increasing bulk Cr content resulted in increased solid solution strength of the γ' phase by Ti and Ta, and to a lesser extent, by Cr itself (Figure 3.5a). However, this was accompanied by a corresponding decrease in Mo content ($\sim$5 at.%), giving rise to a significant drop in solid solution strength, from $\sim$180 MPa to $\sim$10 MPa. Changing the bulk Co or Mo content did not result in significant changes to the predicted solid solution strength of the γ' phase (Figure 3.5b and c).

As the bulk Al content was increased, there was a corresponding decrease in solid solution strength of the γ' phase. Although Al itself has no role as a solid solution strengthener in this phase, it caused a decrease in Ti content, which does have a strengthening effect (Figure 3.5j). A higher Al content increased the strengthening derived from the γ-partitioning elements (Cr and Mo), but decreased that of the other γ'-partitioning elements (Ti and Ta). As previously mentioned, when increasing the bulk Ti concentration, the high Ti content in the γ' phase gave rise to significant solid solution strength (Figure 3.5k). However, there was a corresponding decrease in the strengthening effect of Ta, Cr and Mo, except at zero bulk Ti content. At this point the pronounced increase in Cr and Mo contents, and decrease in Ta content, gave rise to relatively significant increases and decrease in the solid solution strengthening from these elements respectively. Finally, Figure 3.5l clearly shows that increased bulk Ta content caused the solid solution strength of the γ' phase to increase by up to $\sim$200 MPa over the range of concentrations considered. Notably, the contribution of all other elements remained approximately constant as Ta content was altered.

Evidently, each individual element has a contribution to the overall solid solution strength in both the γ and γ' phases. The overall solid solution strength of the γ and γ' phases are shown in Figure 3.6a and b respectively, as a function of changing bulk alloy composition. Each data point on these graphs is the total combination of the individual strengthening increments detailed in Figure 3.5, but with the associated γ' volume fraction taken into account.

It is seen in Figure 3.6a that increasing bulk Cr or Mo content increased the solid solution strength of the γ phase and this was approximately linear. In contrast, increased bulk Al content resulted in a linearly decreasing solid solution strength of the matrix, due to the increasing volume fraction of γ' (and corresponding decrease in volume fraction of γ), even though the solid solution strength of the γ itself increased with Al content. Bulk Co content had very little effect on the solid solution strength of the matrix, although the strength was slightly decreased at the highest and lowest Co contents. Bulk Ta content gave rise to the same trend of decreased matrix strength at the highest and lowest Ta contents due to the increasing strength but decreasing volume fraction of the γ phase. Finally, increasing bulk Ti content was seen to result in an approximately linearly decreasing solid solution strength of the matrix phase, except for the case of zero bulk Ti, at which point the solid solution strength was around the same magnitude as that of the alloy with patent composition.

As shown in Figure 3.6b, the effect of changing bulk alloy concentration on the solid solution strength of the γ' phase showed almost inverse trends to that of the matrix. As expected, increased bulk content of the γ'-partitioning elements resulted in increased solid solution strength of the γ' phase. However, interestingly, increased bulk Mo content also increased the strength of this phase. The effects of Cr and Co were not linear, resulting in increased solid solution strength of the γ' phase towards the highest and lowest concentrations.

The data in Figure 3.6 is simply a summation of the individual solid solution strengthening effects in Figure 3.4 and 3.5, weighted by the γ' volume fraction predicted by Thermo-Calc. In interpreting these results there therefore exists the added complexity of changing γ' volume fraction. Specifically, increased bulk Al, Ti or Ta content significantly increased the volume fraction of γ', leading to large increases in the overall strength of the alloy derived from the solid solution strengthening of this phase, even if the

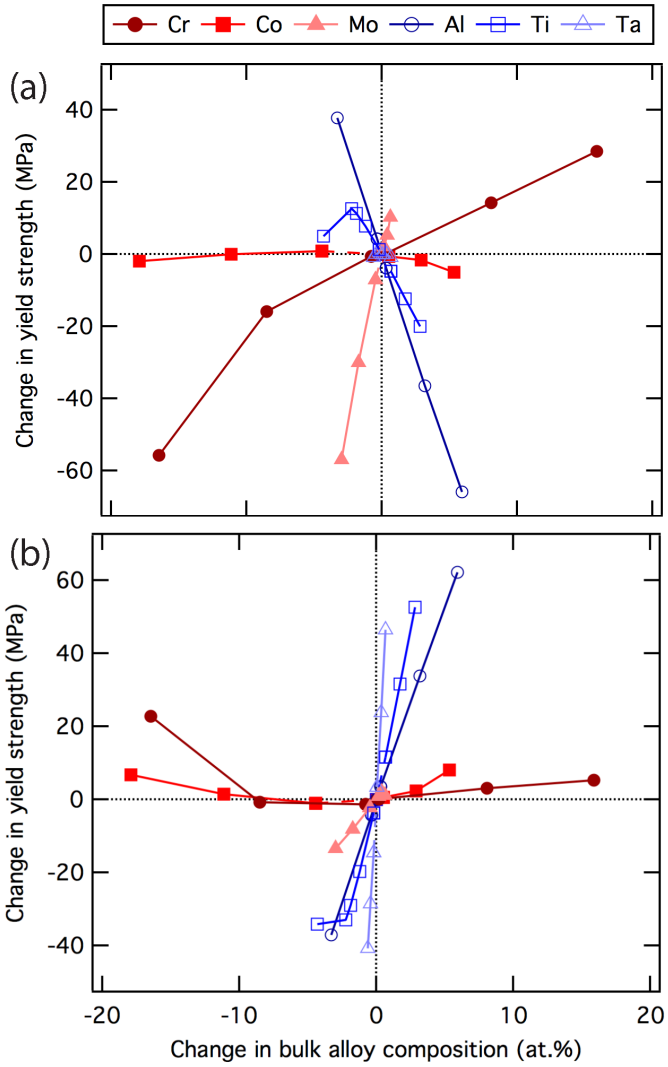

Figure 3.6: The effect of changing the bulk content of individual elements on solid solution strengthening in the (a) matrix and (b) precipitate phases.

atomic mismatch is relatively small (or meaningless in the case of Al, which is an essential part of the γ' structure). In contrast, increasing bulk Cr content decreased the predicted γ' volume fraction by ∼10 %, whilst Co and Mo had a negligible effect. As the solid solution strengthening trends from these additions do not follow their associated effects on the γ' volume fraction, it is clear that the strengthening effects derived from these elements are much more significantly related to the atomic size mismatch.

Precipitation Strengthening

The effect of changing alloy composition on precipitation strengthening, taking into account γ' volume fraction, is shown in Figure 3.7a. Precipitation strengthening is strongly dependant on the APBE and the volume fraction of γ', being linearly proportional to the APBE and to the number density of the γ' precipitates (Equation 3.9). For clarity, the effect of changing composition on the APBE and γ' volume fraction are shown in Figs. 3.7b and c respectively.

The most significant precipitation strengthening effect is found by changing Ti content, with a 2.8 at.% increase of the patent Ti content resulting in a ∼90 MPa increase in precipitation strength. Reducing the Ti content had a more pronounced effect, with a decrease of 4.3 at.% resulting in a decrease of ∼280 MPa in precipitation strength. Ta also had a proportional increase in precipitation strength, whilst Cr had a relatively large negative effect over its larger compositional range, and Mo also decreased precipitation strength. In agreement with the present data (Figure 3.7b), it has been previously shown that Ti increases the APBE and resulting precipitation strengthening, whilst increasing contents of Mo and Cr cause a decrease [113]. However, in the same study Ta is seen to reduce the APBE, in contradiction to the present results. Evidently, such high Cr and Mo contents are likely to have undesirable consequences for phase stability. Whilst TCP phases such as σ may not be initially present in the microstructure, upon high temperature exposure as is seen in service, σ phase may be likely to form, thereby further modifying the phase compositions by removing certain elements from the matrix and γ' phases.

In contrast, Co and Al contents did not proportionally affect the precipitation strength, with both elements resulting in a maximum strength near the RR1000 patent content; if the bulk content of Co or Al were increased or decreased, there was a resulting decrease in the contribution to the yield strength from precipitation strengthening.

The non-proportional effect of Al on precipitation strength arises from the competition between volume fraction and APBE (Figs. 3.7b and c). Increased Al content decreases APBE since it is an integral part of the $L1_2$ γ' structure, and therefore although it has no direct effect on APBE, it reduces the available space for other elements that occupy the same sublattice in the γ' structure, thereby reducing the APBE. However, increased Al content also increases the volume fraction of γ', thereby increasing precipitation strength. These two effects are in direct opposition, leading to maximum precipitation strength at an intermediate Al content.

A similar rationale describes the non-linearity of the role of Co, with the effect on precipitation strengthening again being defined by the competition between volume fraction and APBE. However, both of these effects are also non-linear in the case of Co. This arises from the complex phase partitioning behaviour, as discussed earlier. The role of Co on APBE is a contentious point. Crudden et al. [113] did not include Co in the total solute concentration, using the rationale that Co has a very similar size and behaves very similarly to Ni, and therefore will not affect the APBE. A separate study [164] has found that increased Co content does increase the hardness of quinary Ni-Co-Al-Ti-Cr alloys, although the specific strengthening mechanism behind this trend was not discussed. A third study on the role of composition on APBE found that Co reduces the APBE, although this effect is not very pronounced [165].

In general, the determination of APBEs experimentally is very difficult. There exist multiple different methods of modelling APBEs, yet due to the experimental issues, it is extremely difficult to determine

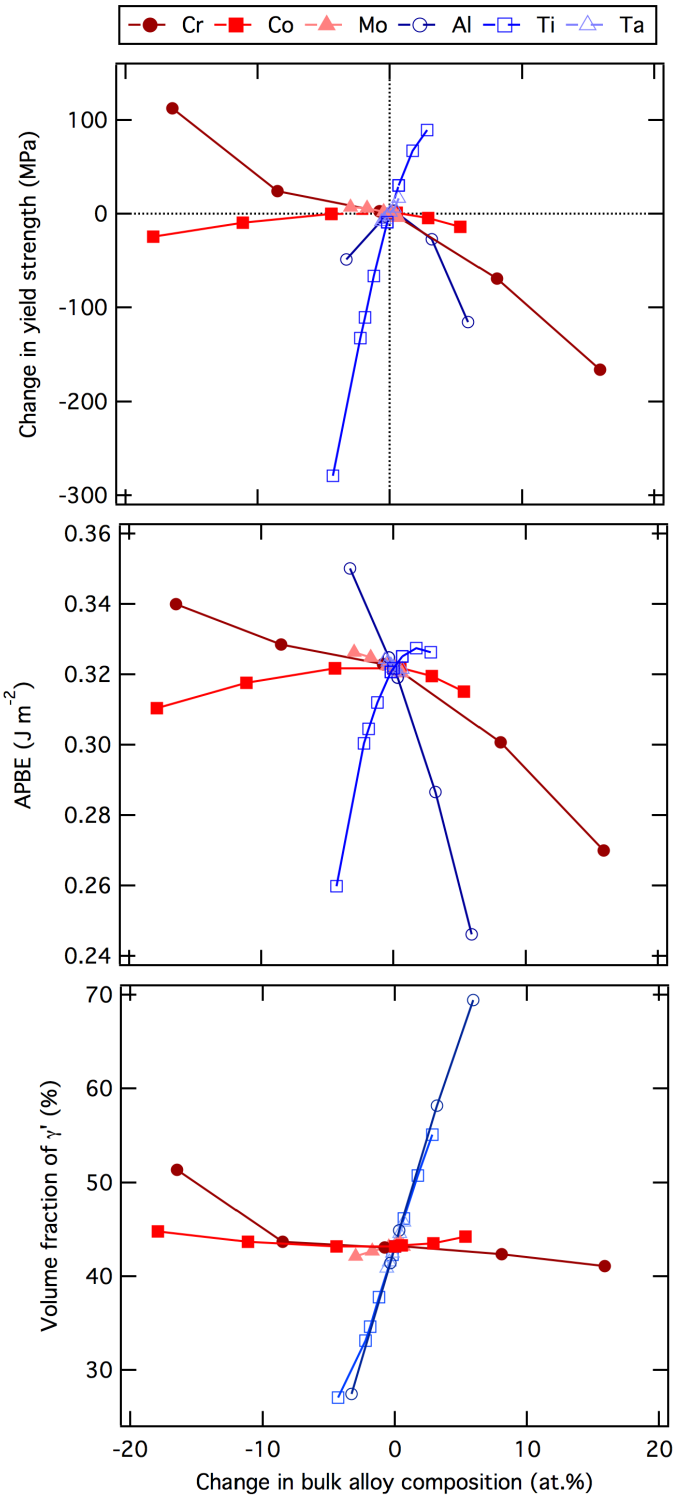

Figure 3.7: The effect of changing the bulk content of individual elements on (a) precipitation strengthening, (b) APBE and (c) volume fraction of γ'.

which models are more accurate. In the present work, the CalPhaD-based approach of Crudden et al. [113] was used. In line with their study and those it is based upon [112], Co was not included as a solute atom in the calculation. In [113], a short-range ordering parameter is also inserted into the model. However, this was not taken into account in the present work as no data were available to guide the selection of an appropriate value for this parameter. Separately in the study by Crudden et al. [113], the solute concentration was fixed to 0.25, and a DFT-based approach was also tested. All of these methods result in different calculated APBEs. The variation in APBE predicted with these differing approaches is shown in Table 3.6.

Method	{111} APBE (mJm^{-2})
Co not included in solute concentration†	322
All elements included in solute concentration	179
Solute concentration = 0.25	336
Short-range order factor included	165
DFT method	323

Table 3.6: Different values for APBE calculated by the different methods detailed in [113]. †Method used in the present work.

With such significant differences in the APBEs predicted using the currently accepted methods, obtaining accurate values of APBEs remains challenging. In spite of this apparent disparity, experimentally determining accurate APBEs is equally problematic and subject to significant uncertainty. As such, APBEs for calculations of alloy strength are still most commonly obtained by modelling-based methods. Given the increasing desire to predict alloy properties for optimal alloy design, further research on the accurate quantitative prediction of APBEs would be valuable.

The Role of Precipitate Size and Volume Fraction

In addition to phase composition, the size and volume fraction of the γ' precipitates play a significant role on the resulting yield strength. The effects of these parameters on the precipitation strength are shown in Figure 3.8a and b for the secondary and tertiary γ' respectively. In Figure 3.8a, the radii of the tertiary γ' were fixed at 7.5 nm and in Figure 3.8b, the radii of the secondary γ' were fixed at 112.5 nm. This enabled the effect of the individual size distributions to be isolated. For both figures, the total γ' volume fraction was fixed at 0.45.

Figure 3.8a shows that varying the size of the secondary γ' precipitates had very little effect on the precipitation strength. As the volume fraction of the secondary γ' was increased, the precipitation strength decreased, primarily as a result of the associated reduction in tertiary γ' volume fraction. However, this loss of strength was not significant, with an increase in volume fraction of 0.3 decreasing precipitation strengthening by ∼30 MPa.

In contrast, the role of tertiary γ' had a much greater effect on precipitation strength. This has previously been deduced in alloys of varying Nb/Ti ratio, but was not confirmed [166]. Figure 3.8b shows that the optimal size for tertiary γ' precipitates was ∼19 nm, which corresponds to the strong-weak transition. Interestingly, the optimum γ' size increases from ∼12 nm at a tertiary γ' volume fraction of 1% to the strong-weak transition size (∼19 nm) at 10%. Notably, this implies that at lower tertiary γ' volume fractions, the optimum γ' size is below the transition, in the weak-pair coupling regime.

Tertiary precipitates larger or smaller than the optimum resulted in decreased precipitation strength. In general, increased volume fraction of tertiary γ' resulted in increased precipitation strength. However, for sizes below the optimum, there was very little effect of volume fraction. For example, for the smallest tertiary γ' considered (5 nm), the precipitation strength remained ∼700 MPa for all volume fractions

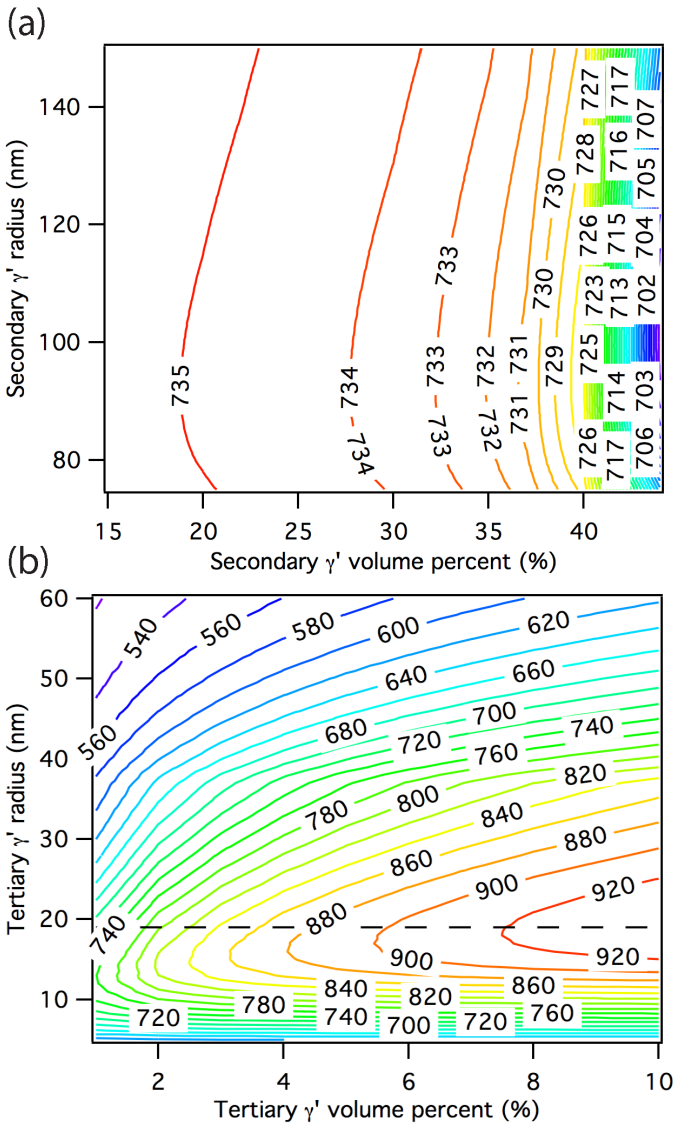

Figure 3.8: The contribution to the yield strength of RR1000 derived from precipitate strengthening as a function of precipitate size and volume percent for the (a) secondary and (b) tertiary γ'.

between 1 and 10%.

It should be noted that in Figure 3.8a, the tertiary γ' were chosen to be of size *below* the peak of tertiary γ' strength of Figure 3.8b. In other words, they are of a size where the yield strength does not vary significantly with tertiary γ' volume fraction. In contrast, if the tertiary γ' were of a size corresponding to the peak ($\sim$19 nm), a much stronger effect of secondary γ' size and volume fraction on yield strength would be observed.

Previous studies have found that increased yield strength coincides with increased size of the tertiary γ', while the secondary γ' size remains constant [167]. Similarly, differences of 20% in tertiary γ' size have been shown to alter the yield strength by over 100 MPa [7]. However, many studies simply do not determine the size of the tertiary γ' [168], often assuming that it is constant. Jones et al. [169] found that changing Co and Ti content resulted in an increased yield stress of alloy RR1000 and justified this in terms of a 5% increase in volume fraction of the secondary γ'. However, the size and volume fraction of the tertiary γ' were not determined. In fact, the approximate size of the tertiary γ' corresponds to the peak in Figure 3.8b of the present work, suggesting that the large increase in yield strength could in fact be due to the changing volume fraction of tertiary γ'. These observations may explain the reported disparity in the relative importance of secondary or tertiary γ' on overall alloy strength, and highlight the importance of fully characterising both distributions if alloy strength is be understood. Alternatively, it has been shown by a previous modelling study that although the tertiary γ' act as barriers to dislocation motion, thereby increasing yield strength, the width of the γ channel between precipitates and the stacking fault energy have more effect on the dissociation behaviour of dislocations [170].

In the model for precipitation strengthening used in the present study [65], the number density of γ' precipitates controls the yield strength (Equation 3.6), and therefore for a fixed total volume fraction, a greater number of smaller precipitates provides a greater strengthening effect. However, extrapolating to the extreme of a unimodal distribution of $\sim$15 nm tertiary γ' does not necessarily infer the optimal mechanical properties and has been shown to be detrimental to other alloy properties such as ductility [114].

The Effect of Compositional Modification on Overall Yield Strength

Multiple mechanisms contribute to the strength of superalloys. The compositional dependencies of each of these mechanisms are shown together in Figure 3.9, along with the overall yield strength. Importantly, all of the strengthening contributions have been calculated taking into account the effect of composition on γ' volume fraction. The maximum yield strengths obtained whilst varying the content of each individual element, were achieved at minimum Cr or Co contents (0 at.%), maximum Ta content ($\sim$1.3 at.%) and intermediate values of Mo or Ti content ($\sim$2.5 and $\sim$4.1 at.% respectively). When varying Al, the maximum yield stress was achieved at both the highest and lowest Al contents, with a minimum yield strength at $\sim$6 at.% Al.

For the γ'-partitioning elements, the increased γ' volume fraction acted to either accentuate or diminish the trends for each strengthening mechanism, depending on whether the strength was directly or inversely proportional to the content of that element. For example, increased Al content caused a decrease in precipitation strengthening due to the significantly decreased APBE (from 0.35 $\mathrm{Jm^{-2}}$ to 0.25 $\mathrm{Jm^{-2}}$), but since the volume fraction of γ' was increased, the overall trend was not as significantly decreased. In contrast, increased Ti content increased the precipitation strengthening, and the fact that there was also an associated increase in γ' volume fraction acted to accentuate this increase. The γ' volume fraction was less dependent on the content of the γ-partitioning elements.

It was found that increasing bulk Co content from 0 to 24 at.% decreased yield strength. This was almost entirely due to the coherency strength, which decreased by $\sim$100 MPa due to a corresponding

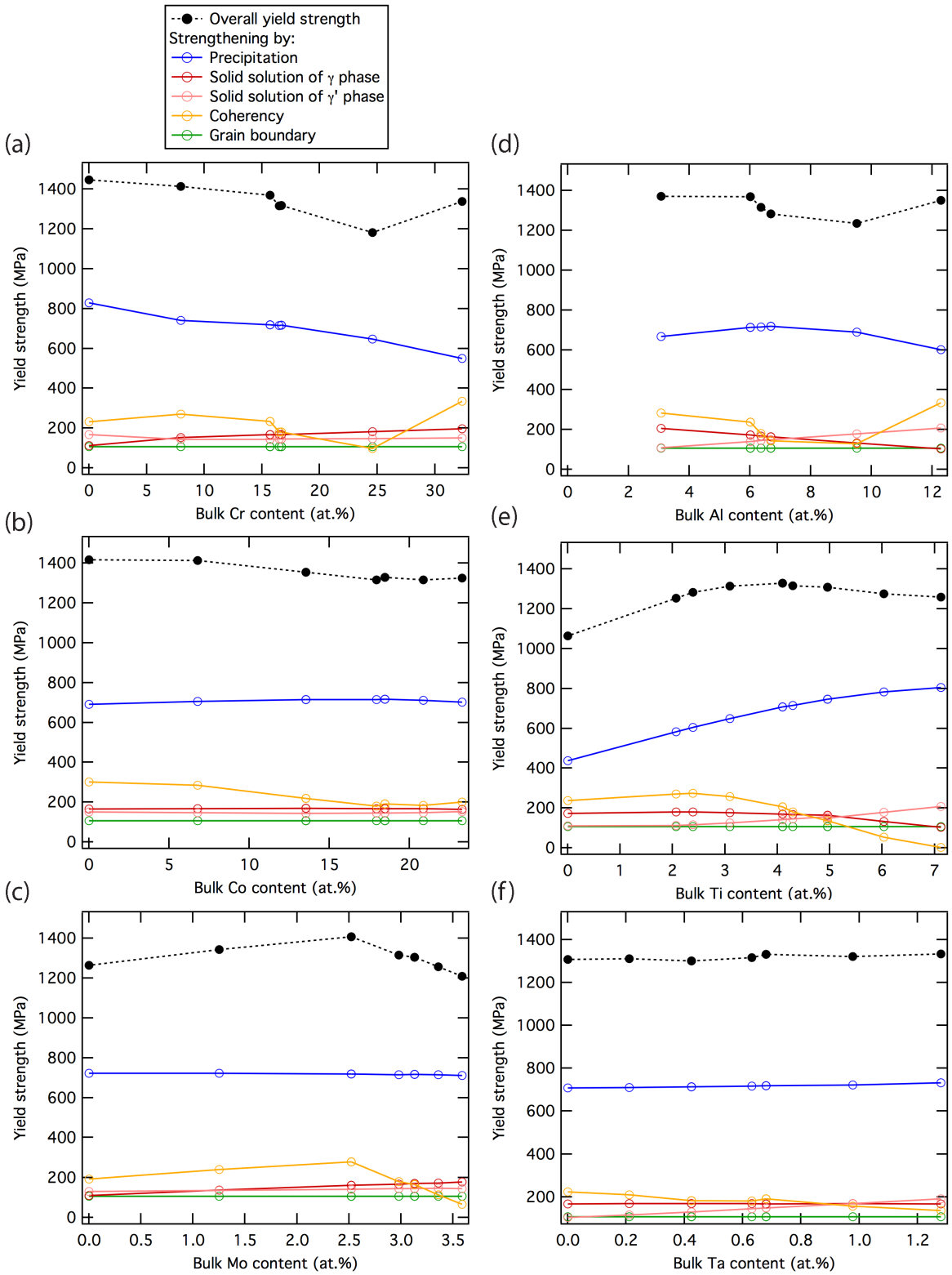

Figure 3.9: The predicted yield strength of RR1000 and the extent of each individual strengthening mechanism as the content of (a) Cr, (b) Co, (c) Mo, (d) Al, (e) Ti and (f) Ta is changed.

decrease in the lattice misfit (from 0.36 to 0.27%). Increasing bulk Ta content by 1.3 at.% resulted in a yield strength increase of just ∼30 MPa, due to increasing precipitation and solid solution strengthening. Some counterintuitive trends are noticeable in Figure 3.9, for example the fact that increasing Ta content resulted in decreased coherency strengthening. This is unexpected, since Ta is a large atom which partitions preferentially to the γ' phase, and therefore should increase the lattice parameter of the γ' phase faster than that of the γ, leading to increasing (positive) lattice misfit. However, the Ta content increases to a similar extent in both γ and γ' phases (∼1.7 and ∼2.6 at.% respectively) whilst it also causes Mo to partition more into the γ phase. The combination of these effects results in the lattice parameter of the γ phase increasing more than that of the γ', leading to a decreasing lattice misfit. The other elements studied did not give linear trends due to the non-linear precipitation and coherency strengthening effects. The non-linear precipitation strengthening cases are discussed above in relation to Figure 3.7.

A second counterintuitive trend is that Cr was seen to decrease the lattice misfit. Since Cr is a small atom which partitions to the γ phase, it should be expected to decrease the lattice parameter of the γ phase more than that of the γ', leading to an increasing (positive) lattice misfit. In fact, Cr modifies the elemental partitioning of Mo (Figure 3.4a and 3.5a), further raising the Mo content in the γ and reducing it in the γ' at high Cr contents. Mo, as a large atom, has a significant effect on lattice parameter, resulting in a decreasing lattice misfit as Cr content is increased.

As mentioned above, the extent of coherency strengthening was capped at the maximum solid solution strength of the γ phase, as greater coherency strength would be associated with local stress that could not be supported elastically, causing yield of the matrix. This gave rise to nonlinear yield strength variations in the case of changing Cr, Al, Ti or Mo content. For example, Mo is a large atom which tends to partition to the matrix phase (Figures 3.4c and 3.5c), thereby resulting in a decreasing (if positive) lattice misfit. However, Mo additions concurrently increased the solid solution strength of the gamma phase (Figure 3.4i). For low Mo additions, the large predicted coherency strength was limited by the solid solution strength of the matrix phase, and as this increased with Mo addition, the benefit that could be derived from coherency strengthening also increased. However, after ∼2.5 at.% Mo, the coherency strengthening effect was less than the solid solution strength of the matrix, and was no longer limited in this way. Therefore, the natural tendency of Mo to decrease lattice misfit and the resulting coherency strengthening is visible in Figure 3.9c from this point.

The extent of coherency strengthening is dependent on the magnitude of the lattice misfit, irrespective of the sign. The non-linear change in coherency strengthening with bulk Cr content is explained by the fact that the lattice misfit continually decreases on Cr addition. Above the patented composition range, the lattice misfit was found to be negative, whilst at the nominal composition and below, it was positive. The magnitude of the lattice misfit, therefore, does not linearly decrease, but decreases to a minimum at ∼8 at.% Cr above the nominal composition, and then increases. The same effect occurs on changing the Al content, with the minimum at ∼3 at.% Al above the nominal composition. The highest Ti content alloy also had a negative misfit, explaining the slight gradient change at ∼1.7 at.% Ti above the nominal composition. All of the other RR1000 variant alloys had a positive lattice misfit.

The present chapter of work has sought to explore the extent to which theoretical predictions for alloy strength may be used to gain insight into the effect of alloying. This has highlighted the importance of elemental partitioning and how this modifies the fraction of equilibrium phases and their compositions. As seen in Figure 3.4, however, this may not exactly describe the situation in reality. The significant role of Mo on coherency strengthening (Figure 3.6c) arises from the large atomic size misfit between Mo and Ni atoms, and the fact that Mo is expected to partition almost entirely to the γ matrix phase. However, this may not be the case experimentally (Chapter 4) and therefore this effect is likely to be less than predicted. A similar effect is seen with Co, but to a much lesser extent, since the atomic size

of Co is much closer to that of Ni and it consequently causes less lattice expansion. Therefore, accurate determination of the experimental phase compositions and microstructural features remains essential for reliable modelling of mechanical properties.

3.4 Conclusions

The contributions of the individual strengthening mechanisms to the overall yield strength of six commercial polycrystalline Ni-based superalloys have been modelled and, when combined together, found to agree well with the trends in experimental data. However, when all of the individual strengthening mechanisms are considered, the magnitude of the yield strength is overpredicted by $\sim$300 MPa. Precipitation strengthening was found to be the most significant mechanism and decreased with total volume fraction of γ' due to the combination of multiple factors. The effect of varying alloying element concentration on the various strengthening mechanisms of RR1000 was elucidated, and the content of individual elements was found to have a complex role on yield strength. This is due to the multifaceted effect on elemental phase partitioning, which was often found to be more significant than the variations in the γ' volume fraction. The phase partitioning of individual elements in superalloys is relatively well understood. However, this belies the complex effects that varying the concentration of an individual element has on the remaining elements, which can lead to counterintuitive consequences for the various strengthening mechanisms. Differences in chemistry of the secondary and tertiary γ' have a significant effect on individual strengthening mechanisms. In addition to phase composition, microstructural parameters were shown to affect the yield strength, with minor deviations of the tertiary γ' size or volume fraction leading to significant changes in yield strength. These parameters may be carefully controlled through sagacious selection of heat treatment, enabling the yield strength of Ni-based superalloys to be optimised to meet the needs of industrial applications. However, for such activities to be effective, further work is required on the sub-models describing the individual strengthening mechanisms so that reliable quantitative predictions can be made.

Chapter 4

Characterisation of Model Quinary Alloys

4.1 Introduction

In Chapter 3, the link between microstructure and the individual strengthening mechanisms occurring in a selection of commercial polycrystalline Ni-based superalloys was investigated. It was found that phase composition, precipitate size and precipitate volume fraction were important parameters that may significantly affect the overall yield strength. As such, microstructural features such as γ' size and volume fraction are carefully controlled through sagacious selection of heat treatments during alloy fabrication. However, since Ni-based superalloys are often utilised in high temperature applications such as gas turbine engines, their microstructural stability at high temperatures is therefore critical for maintaining performance during service.

The evolution of the γ' particle size distribution during high-temperature service will affect the mechanical properties and must therefore be understood. Computational tools based upon thermodynamic and kinetic models exist to predict such precipitate evolution [171–174]. However, further experimental studies are needed to validate the assumptions made in these models, particularly the compositions of the γ' precipitates, as these are known to differ between primary, secondary and tertiary distributions and will change with time at temperature. As was shown in Chapter 3, experimentally determined phase compositions enable more accurate predictions of yield strength than when the compositions are predicted using Thermo-Calc. It is therefore evident that accurate determination of phase composition, particularly that of the different γ' distributions is required for quantitative yield strength prediction.

In this chapter, the γ and γ' phase compositions and the distribution of the γ' precipitates have been investigated in one alloy of a series of model superalloys, as a function of time at temperature, using a combination of transmission electron microscopy and atom probe tomography. The resulting effect on lattice misfit has also been studied using neutron diffraction. These data identify the key discrepancies between thermodynamically predicted and experimentally measured precipitate compositions, in particular a notably high Mo content within the tertiary γ' phase, which may have significant implications for the modelling of precipitate evolution and alloy strength.

4.2 Methods

Alloy Fabrication

Alloy Design To further investigate the extent of the multiple strengthening mechanisms present in Ni-based superalloys, a model series of six alloys was designed. In order to extract the role of coherency strengthening, the Mo content was varied between 0 and 5 at.%. Since Mo is typically expected to partition to the γ phase only, it was expected to increase the lattice parameter of the matrix due to its large atomic size, whilst leaving the lattice parameter of the γ' phase unchanged. Therefore, the model alloy series was designed to have a decreasing lattice misfit, and a corresponding decrease in the extent of coherency strengthening. Whilst the extent of solid solution strengthening of the γ phase would also be expected to change, the extent of the other strengthening mechanisms would be unchanged, as the γ' phase composition was not expected to be affected by Mo content, and microstructural parameters such as precipitate size, grain size or γ' volume fraction were not expected to change with Mo content. The designed compositions of the model alloys are given in Table 4.1.

Alloy	Cr	Al	Ti	Mo	Ni
0	15	6	5	0	bal.
1	15	6	5	1	bal.
2	15	6	5	2	bal.
3	15	6	5	3	bal.
4	15	6	5	4	bal.
5	15	6	5	5	bal.

Table 4.1: Model alloy compositions (at. %)

Alloy Production Each of the constituent elements (as either pure element or binary alloy) (of ≥99.9% purity) were weighed out and vacuum arc melted together using an Edmund Buhler arc melter to form the model alloys. High currents were required in order to melt the constituent elements, which may result in volatilisation of lighter elements such as Cr and Al. In order to obtain the desired alloy composition, 1.08 times the desired mass of Cr and 1.09 times the desired mass of Al were weighed out and included in the melt. Each bar was inverted and remelted a minimum of 5 times to ensure complete compositional homogeneity. The resulting bars weighed ∼300 g.

The arc melted bars subsequently underwent Vacuum Induction Melting (VIM) to further homogenise the alloy composition, and were cast into 10 mm diameter steel moulds, of length ∼10 cm.

DSC Differential Scanning Calorimetry (DSC) was used to determine the temperatures of the phase transformations in the model alloys studied. The DSC technique works by independently measuring the temperatures of both a sample and a reference material, as the furnace temperature is increased. Temperature differences between the sample and the reference materials are caused by energy flow from the endothermic or exothermic phase transformations of the sample material.

DSC was carried out on the as-cast material using a NETZSCH 404 instrument. 1-2 mm sections of each sample were sliced from the VIM bars, and ∼1 mm discs were spark eroded from these sections. The edges and surfaces of each disc were ground to 1200 and 2500 grit to ensure the flat surface provided good contact with the alumina crucible of the DSC machine. Samples were heated at 10 K min^{-1} to 1450°C before cooling at the same rate to room temperature. An example thermogram acquired using this technique on the 3 at.% Mo sample is shown in Figure 4.1. From the thermograms acquired, the γ' solvus and solidus temperatures were determined (Figure 4.2) using the guidelines published by Boettinger et al. [175]. Deviation from the linear baseline at points 2 and 3 in Figure 4.1 represent the solidus

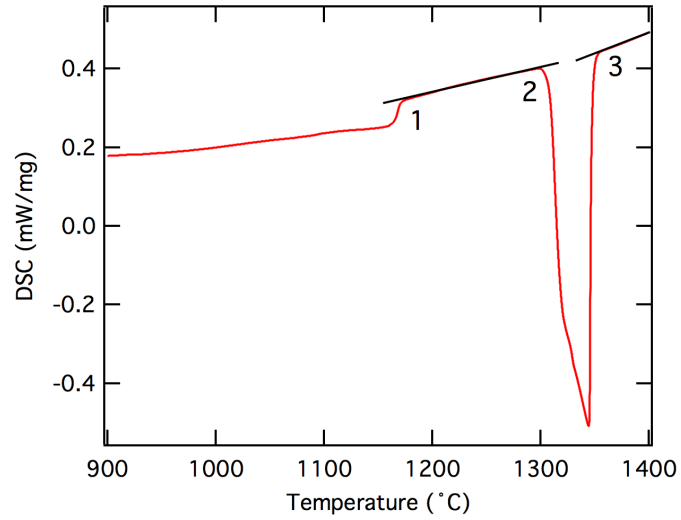

Figure 4.1: Example DSC data from the 3 at.% Mo alloy, with point of phase transformation indicated.

and liquidus respectively. Deviation from the baseline at point 1 represents the solvus, above which temperature no γ' phase is present.

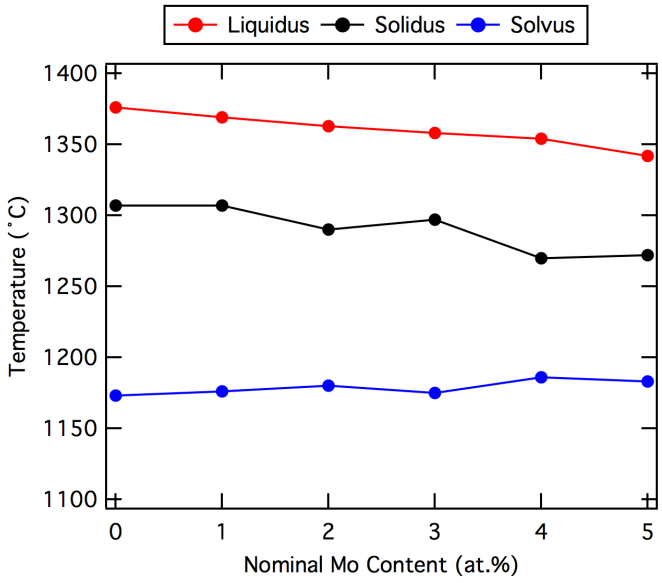

Figure 4.2: Liquidus, solidus and solvus temperatures of the model alloy series as a function of Mo content.

This enabled a suitable homogenisation heat treatment to be identified within the single phase γ phase field. It was seen that bulk Mo additions very slightly increased the γ' solvus temperature, whilst decreasing the liquid and solidus temperatures. Mo additions therefore act to reduce the temperature range of the single phase region, in which homogenisation treatments are commonly carried out. From these data, a temperature of 1250°C was chosen to carry out homogenisation of the alloy series.

Heat Treatment Ni-based superalloys require complex heat treatments in order to obtain an optimised microstructure for the mechanical properties required. Homogenisation is required to remove compositional macrosegregation or unwanted phases, and is most often carried out within the single phase γ phase, in which diffusion is faster. Subsequent to homogenisation, ageing heat treatments may be utilised to create the desired γ' distribution.

Homogenisation of each of the model alloys was conducted for 22 hours at 1250°C (as determined from the DSC results) in an Ar-backfilled quartz ampoule, to avoid oxidation. Subsequent air cooling occurred at an average rate of $\sim 7.8°C\,s^{-1}$ for the initial 200°C, slowing to an average of $\sim 1.6°C\,s^{-1}$ between 1000°C and 400°C.

All alloys were subsequently aged at 760°C for 16 hours. This temperature was based on the typical ageing treatment of commercial alloy RR1000. Air cooling from the ageing temperature occurred at an average rate of $\sim 4.4°C\,s^{-1}$.

Sections of the homogenised 3 at.%Mo alloy were subjected to additional ageing heat treatments at 760°C for durations of 1, 2, 100, 200 and 1000 hours. This alloy is investigated in detail in the present chapter, while the full alloy series is discussed in Chapter 5.

Thermodynamic Modelling

Computational modelling is increasingly common in materials science, particularly in the design of new Ni-based superalloys, where the large number of constituent elements results in an impossible number of compositional degrees of freedom. Specifically, CalPhaD (Calculation of Phase Diagrams) techniques based on thermodynamics and kinetics enable the prediction of equilibrium microstructures and the associated mechanical properties.

In the present work, the Thermo-Calc software package was used with the TCNi7 database to predict equilibrium compositions and chemical driving forces, as a supplement to the experimental data acquired. The Thermo-Calc software computes equilibrium through the minimisation of Gibbs free energy, with thermodynamic data supplied from the TCNi7 database created by Thermo-Calc.

Equilibrium Phase Compositions For comparison to experimental data, the equilibrium phase compositions of each alloy were predicted by thermodynamic modelling using the Thermo-Calc software package along with the TCNi7 database. It should be noted that, since Thermo-Calc is only able to predict the equilibrium composition, this composition was taken for both the secondary and tertiary γ' phases. The equilibrium phase compositions at 760°C were calculated, excluding all other phases from the calculation.

Lattice Parameters and Lattice Misfit Using the equilibrium phase compositions from Thermo-Calc at 760°C, Thermo-Calc was used to determine the molar volumes of those γ and γ' phases at room temperature. In order to do this, all other phases were suppressed, and global minimisation was turned off to ensure that the phase composition did not change with temperature.

The equilibrium compositions at 760°C were taken as the room temperature phase compositions because in reality, diffusion is limited at low temperatures. It is generally assumed that equilibrium may be achieved after the ageing heat treatment, but on subsequent cooling there is limited diffusion, so the room temperature phase composition may be assumed to be the same as that at 760°C.

The lattice parameters of the γ and γ' phases were obtained using the predicted molar volumes (V_m) using Equation 3.1, and the lattice misfit was then calculated with Equation 2.4.

Scanning Electron Microscopy (SEM)

All scanning electron microscopy described in the present thesis was carried out using an FEI Nova NanoSEM FEG SEM. This was operated at ∼5 keV for imaging, with an aperture of 30 µm (aperture 7) and a spot size position of 4, giving a current of 170 pA. A backscatter (CBS) detector and working distance of ∼3.5 mm was found to produce optimal image quality when using the immersion lens.

Sample Preparation Samples were prepared for SEM by conventional grinding and polishing techniques. Representative sections of the arc-melted bars were cut using a diamond-edged cutting disc (Secutom, Struers, Denmark) and mounted in conductive Bakelite. These sections were then ground with progressively fine SiC paper, from 1200 to 4000 grit, to remove surface flaws from the cutting process. Subsequent polishing was carried out with 3 µm, 1 µm and 1/4 µm diamond suspension, followed by a 0.06 µm colloidal silica solution. It was found that polishing with colloidal silica solution resulted in sufficient etching of precipitates and grain boundaries, such that no specific etching stage was required.

Bulk Alloy Composition To confirm that the bulk alloy compositions were as desired, Energy-Dispersive X-Ray (EDX) analysis was carried out on large areas (∼30 µm x 20 µm) of each sample surface at low magnification (x 5,000). For each sample, 5 area scans were taken at distinct areas of the sample surface, and the compositions averaged to determine the bulk composition and its heterogeneity. The results are shown in Table 4.2.

Alloy	Cr	Al	Ti	Mo	Ni
0	15.2 ± 0.1	5.9 ± 0.5	5.09 ± 0.06	0	73.8 ± 0.2
1	15.4 ± 0.3	6.1 ± 0.4	5.0 ± 0.1	0.69 ± 0.05	72.9 ± 0.4
2	15.4 ± 0.1	6.0 ± 0.2	5.22 ± 0.09	1.72 ± 0.08	71.7 ± 0.2
3	15.2 ± 0.2	5.7 ± 0.1	5.0 ± 0.1	2.66 ± 0.06	71.4 ± 0.2
4	15.4 ± 0.1	5.5 ± 0.3	5.12 ± 0.02	3.55 ± 0.06	70.4 ± 0.2
5	15.5 ± 0.4	5.7 ± 0.2	5.1 ± 0.1	4.5 ± 0.2	69.3 ± 0.3

Table 4.2: Bulk alloy compositions (in at. %), as measured experimentally by SEM EDX

Volume Fraction The volume fraction of secondary γ' precipitates was determined from 4 disparate areas of each sample surface. Images were taken at 5 keV and x20,000 magnification using the backscatter electron (BSE) detector at a working distance of ∼3.5 mm, a spot size of 4 and an aperture of 7.

The area fraction of γ' was quantified in each image by automatically colour-thresholding using ImageJ software (Figure 4.3). Since the precipitates were equiaxed, the calculated area fraction was assumed representative of the volume fraction. Comparison of the multiple images of each sample showed that the γ' volume fraction was homogeneous across the sample surface.

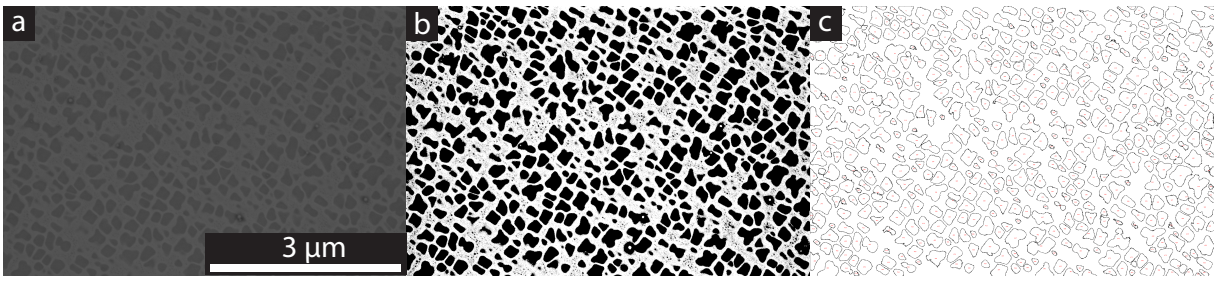

Figure 4.3: (a) Example micrograph of the 3 at.% Mo alloy aged for 16 hours, (b) thresholded using ImageJ, and (c) with precipitates delineated.

Transmission Electron Microscopy (TEM)

All microstructural imaging was carried out by Scanning Transmission Electron Microscopy (STEM) using an FEI Tecnai Osiris TEM, operated at an accelerating voltage of 200 keV. Compositional analyses were performed by Energy-Dispersive X-ray Spectroscopy (EDX) in the same instrument, using an FEI Super-X EDX detector.

Sample Preparation Electron transparent samples of the heat-treated alloy for microstructural analysis by TEM were prepared by two distinct techniques; electropolishing and as carbon replicas.

Electropolishing Electropolishing of TEM specimens was carried out using a Struers Tenupol-5 Twin-Jet electropolisher, on thin slices of each alloy cut using a diamond-edged cutting disc (Accutom, Struers, Denmark). A solution of 5 % perchloric acid in methanol was used at a temperature of $\sim -5°C$, a voltage of 20 V and a current of ~ 180 mA.

Carbon Replicas The carbon replica extraction process was carried out on material that was previously ground and polished to a 0.5 µm finish. Samples were obtained by electrolytically etching at room temperature in 10% phosphoric acid in water solution at ∼3 V until a blue halo appeared. After cleaning with ethanol, formvar in chloroform solution was deposited on the sample surface and used to attach a piece of acetate sheet. Once dry, the acetate sheet was removed to eliminate any over-etched γ' particles from the sample surface. The samples were then sputter coated with carbon, and this carbon coating was scored into ∼2mm squares. Finally, electrolytic etching at room temperature in a 20% perchloric acid in ethanol solution at 10 V was carried out until the carbon coat began to blister. These fragments were then floated onto copper TEM grids for analysis.

Imaging STEM images were taken of all samples, in both the electropolished and carbon replica conditions. Images of the electropolished specimens were obtained at the thinnest region near the central hole. Images of carbon replicas were taken at multiple positions across the sample surface.

Particle Size Distributions (PSDs) Particle size distributions (PSDs) for each ageing time were determined by manually tracing around a minimum of 300 secondary γ' particles on TEM images of the carbon replica samples. This approach was required due to the presence of overlapping particles, which could not be distinguished automatically using ImageJ software. Subsequent measurement of the precipitate outlines was performed using ImageJ on the manual tracings (Figure 4.4), from which the equivalent circular diameters of each precipitate were obtained. Analysis of the tertiary γ' precipitates was carried out via the same method, but using higher resolution STEM micrographs.

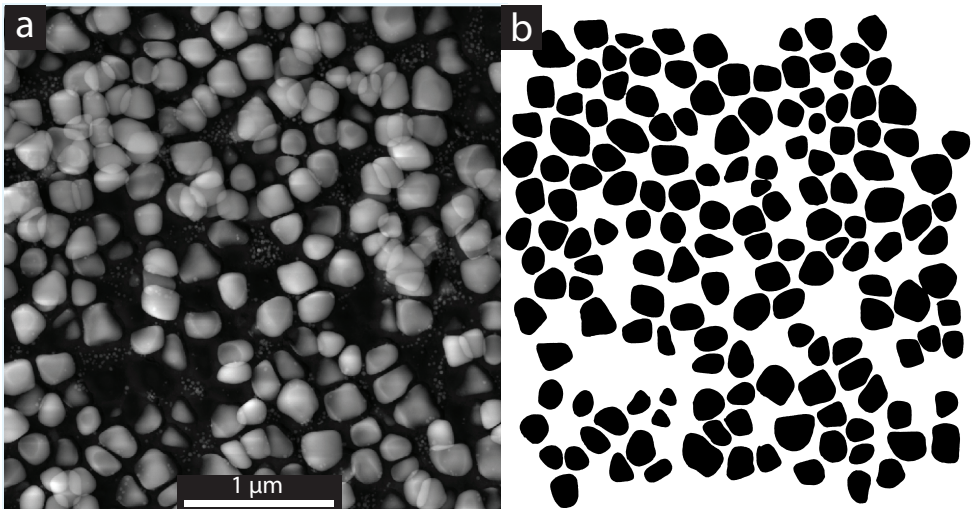

Figure 4.4: (a) Example STEM micrograph of the 3 at.% Mo alloy aged for 16 hours and (b) the tracing of this micrograph after thresholding using ImageJ.

The equivalent circular diameters were binned to a histogram using the Freedman-Diaconis method [176] and fitted with lognormal distribution functions, given in Equation 4.1, using Igor Pro (WaveMetrics,

Lake Oswego, OR). The average precipitate size after each heat treatment was taken as the median of the lognormal function (e^{μ}) and the associated uncertainties were taken to be the width of the function away from the median value ($e^{(\mu+\sigma)}$ and $e^{(\mu-\sigma)}$), where σ is the error (standard deviation) associated with the coefficient given by the Igor Pro software.

$$f(x) = \frac{1}{xw\sqrt{2\pi}} \exp\left(- \left[\frac{(\ln(x) - \mu)^2}{2w^2} \right] \right) \tag{4.1}$$

Phase Composition The electropolished samples were used for compositional analysis of the γ phase using STEM-EDX. Data were acquired from the regions of these samples between the γ' precipitates. The same method could not reliably be used for the γ' precipitates, however, as it was not possible to ensure that the electron beam did not pass through γ phase above or below the γ' precipitates. To address this, compositional analysis of the γ' precipitates was performed on the samples prepared as carbon extraction replicas, which were devoid of the γ phase.

EDX point scans were obtained to quantify the composition of the γ phase. A minimum of 15 spectra were analysed and averaged for each sample, with the resulting standard deviation giving a representation of compositional homogeneity across the sample. Point scans were also used to quantify the composition of the secondary γ' phase. Analysis of the tertiary γ' particles, however, could not be accurately determined using point scans, as the position of the electron beam (and therefore the point scan) cannot be determined sufficiently accurately. Instead, area scans containing a number of separate γ' precipitates were obtained. A minimum of 3 area scans were averaged to provide a quantitative value for the composition of the γ' precipitates.

Atom Probe Tomography (APT)

Sample Preparation APT was carried out on the 3 at.%Mo alloy in all ageing conditions. Additionally, APT was carried out on the 0 at.%Mo alloy aged for 16 hours. Due to time constraints, the other alloys could not be analysed by APT.

APT samples were prepared from needles (of dimensions 2 cm x 0.5 mm x 0.5 mm) that were cut by electro-discharge machining from the alloy in each ageing condition (0-1000 hours). Each needle was subsequently electropolished down to a size appropriate for APT. Electropolishing was performed in two stages: firstly using a solution of 10 % perchloric acid in acetic acid at a voltage of 22 V, and secondly using a solution of 2 % perchloric acid in 2-butoxythanol at 23 V.

During the first electropolishing stage, each needle was repeatedly dipped into the acid solution, causing progressive necking until the needle split into two smaller pieces, each with a very fine necked point. Both sections were then cleaned with methanol. The second electropolishing stage was effectively a repeat of the first but on a smaller scale. A very small droplet of acid solution was held by surface tension in a small ring, and the necked sample was repeatedly dipped into this solution, forming a neck which eventually broke off to leave a very sharp point that was suitable for APT.

Experimental Technique All microstructural characterisation using atom probe tomography (APT) was carried out at the University of Oxford, using a LEAP 5000 XR instrument in laser mode with a wavelength of 355 nm. APT data were acquired at -223°C using a pulse rate of 200 kHZ and a pulse energy of 50 pJ.

Analysis Methods The compositions of the γ, secondary γ' and tertiary γ' phases were obtained by summing the atoms inside a selected area. For the γ phase, an area far from any precipitate phase was manually defined. For the secondary γ' phase, an area within each precipitate present was manually

defined, since the secondary γ' were often too large to be complete within the sample. For the tertiary γ' phase, the composition of up to 10 (or simply all) of the tertiary precipitates were measured separately and averaged to give an idea of the compositional variation between tertiary γ' precipitates.

To determine the compositional variations across the γ/γ' interfaces, isosurfaces of 15 at.% Cr were set up in order to define the interfaces, and proximity histograms (proxigrams) of phase composition were plotted across these boundaries. Both secondary and tertiary γ/γ' interfaces were analysed.

All proxigrams were subsequently fitted by sigmoid functions using Igor Pro. Quantitative values for the interface width of each element were defined as the distance between 1 % above and 1 % below the minimum and maximum compositions, respectively.

Neutron Diffraction (ND)

Sample Preparation Cylindrical samples of diameter 5 mm and length 55 mm were electro-discharge machined from the 3 at.%Mo alloy in each ageing condition, for neutron diffraction. Additionally, the 0-5 at.%Mo alloys aged for 16 hours were studied.

Experimental Technique Neutron diffraction was carried out on the C2 powder diffractometer at the Canadian Neutron Beam Centre (CNBC), Chalk River, Canada. The wavelength of the incident beam was determined to be ~ 1.33 Å using an Al_2O_3 standard. Data were acquired from each sample for 3 hours at room temperature, using a position-sensitive detector over a 2θ range of 36° to 116°. All alloys and ageing conditions were analysed at room temperature and the samples were rotated during data collection to improve the counting statistics. In addition to this, the 0-5 at.%Mo alloys aged for 16 hours were studied at 700°C. However, since this required each sample to be held within a furnace, the samples could not be rotated during data collection. Due to the very large grain size of each alloy caused by the arc melting fabrication process, the resulting diffraction patterns were strongly textured, making accurate analysis of the data difficult. Fortuitously, these high temperature data were able to be repeated at another neutron facility at a later date. As such, these data are not discussed in the present chapter, but are detailed in Chapter 5.

Analysis Methods The very similar crystal structures and lattice parameters of the γ and γ' phases in Ni-based superalloys result in overlapping peaks from each phase in the diffraction patterns, and these are often indistinguishable. The disordered nature of the FCC γ phase results in systematic absences where h, k and l are mixed odd and even. Fortunately, the ordered nature of the γ' phase results in no systematic absences, and superlattice reflections exist, arising purely from the γ' phase. These may be used to determine the lattice parameter of the γ', and in this way, the single peaks arising from the γ' phase in the mixed fundamental reflections may be fixed, and the peak position (and therefore lattice parameter) of the γ phase found. An example diffraction pattern obtained during this experiment is shown in Figure 4.5. For each sample, the γ' superlattice reflections were fitted individually in Igor Pro using Gaussian functions (Equation 4.2).

$$f(x) = y_0 + A \exp\left(- \left[\frac{(x - x_0)}{w} \right]^2 \right) \tag{4.2}$$

The associated lattice parameter was determined from the fitted superlattice positions using the Nelson-Riley method [177], in which the equivalent lattice parameters from each peak were plotted against the associated absorption error ($\frac{\delta a}{a}$) (Equation 4.3) and the lattice parameter taken as the linear intercept.

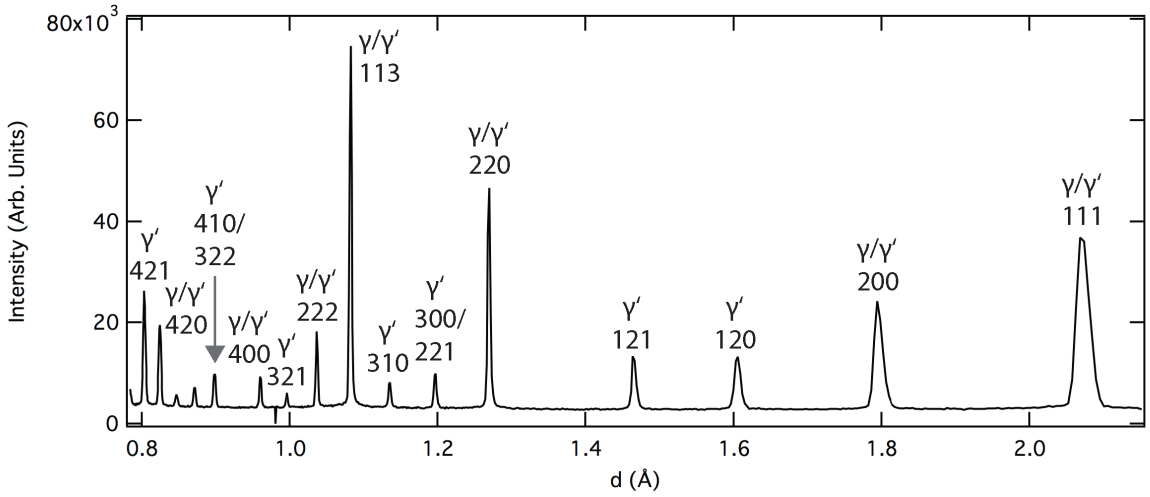

Figure 4.5: Example diffraction pattern of the 3 at.% Mo alloy aged for 16 hours, with peaks indexed and showing the phase(s) contributing to each peak.

$$\left(\frac{\delta a}{a}\right)_{\text{abs}} = \frac{1}{2}\left(\frac{\cos^2\theta}{\sin\theta} + \frac{\cos^2\theta}{\theta}\right) \tag{4.3}$$

The positions of the γ peaks were obtained by fitting the fundamental reflections with two Gaussian functions, one of which was constrained to the position associated with the previously determined γ' lattice parameter. As for the γ' phase, the γ lattice parameter was obtained from the fitted peak positions using the Nelson-Riley function (Equation 4.3). Conversion of the measured lattice parameters to the constrained lattice misfit was performed using Equation 2.4.

Microhardness Testing

Microhardness testing was carried out on the 3 at% Mo alloy after the different ageing times to investigate the change in hardness with ageing time. For this technique, each sample was mounted in bakelite, ground and polished to a flat finish. A Qness Q30 fully automatic microhardness tester with a Vickers indenter was used to indent each sample surface with a load of 5 kgf. 20 repeat measurements at disparate locations on the sample surface were taken on each sample, to give an average and an uncertainty given by the standard deviation.

4.3 Results

Microstructural Characterisation

Morphology

STEM images of the γ' phase from the carbon replicas of the 3 at.% Mo alloy in each heat treatment condition are shown in Figure 4.6. With the exception of the sample aged for 1000 hours, all conditions exhibited bimodal PSDs of secondary and tertiary γ'. On ageing for 1000 hours, only secondary γ' were visible in the microstructure. As a consequence of the different precipitate sizes, images of the secondary (Figure 4.6, left hand side images) and tertiary γ' (Figure 4.6, right hand side images) have been displayed at different magnifications.

The morphology of the secondary γ' showed no appreciable change with ageing time up to 16 hours, with all secondary precipitates remaining approximately cuboidal. On further ageing up to 100 hours,

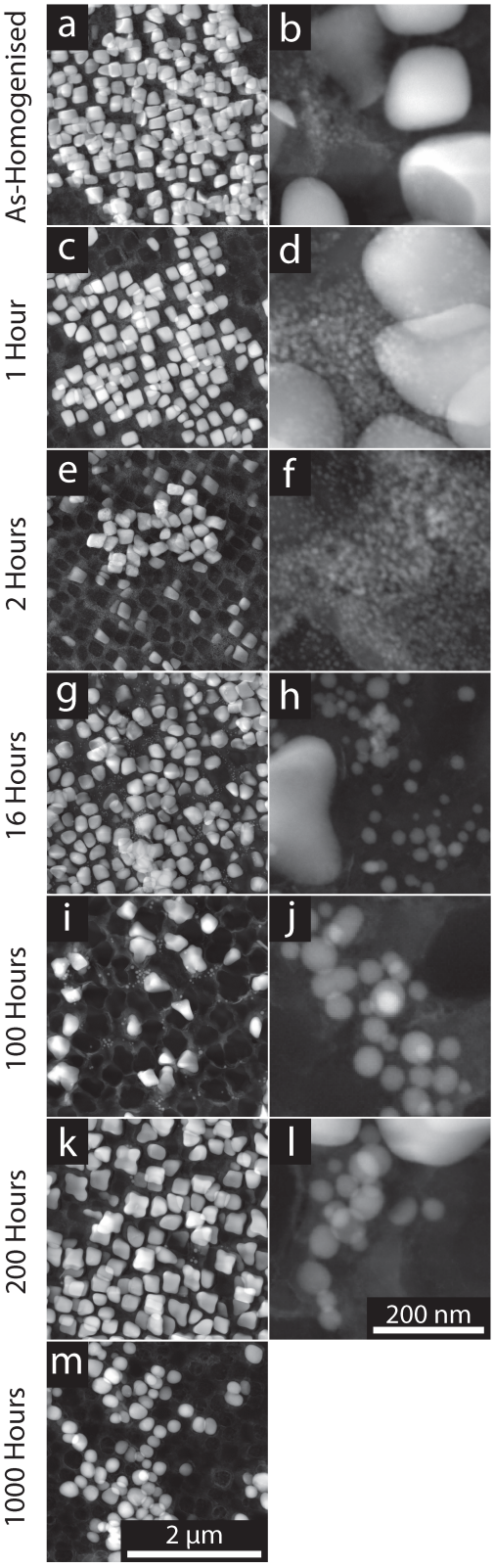

Figure 4.6: STEM images of extraction replicas of the 3 at.%Mo alloy in the as-homogenised state (a, b) and after 1 (c, d), 2 (e, f), 16 (g, h), 100 (i, j), 200 (k, l) and 1000 (m) hours of ageing at 760°C. Secondary γ' precipitates are shown on the left hand side (a, c, e, g, i, j, m) and tertiary γ' precipitates on the right hand side (b, d, f, h, j, l). No tertiary γ' were visible after 1000 hours of ageing.

octodendritic precipitates alongside smaller, cuboidal precipitates were observed, characteristic of the morphological instabilities associated with precipitate splitting [20, 178].

Following ageing for 200 hours, only octodendritic precipitates were observed throughout the sample. After 1000 hours, the secondary γ' appeared finer and more spherical than those observed during shorter duration exposures. In contrast to the secondary γ', the tertiary γ' remained approximately spherical throughout ageing and increased continually in size up to 200 hours, after which they were no longer present within the microstructure.

Particle Size Distributions (PSDs)

PSDs of both the secondary and tertiary γ' obtained from analysis of the STEM images of the 3 at.% Mo alloy in the as-homogenised condition and following ageing for 1, 16, 100 and 1000 hours are shown in Figure 4.7. All PSDs were well described by a lognormal function. The single additional peak visible between the distributions of secondary and tertiary γ' precipitates in the alloy after ageing for 16 hours is due to the presence of one large tertiary precipitate and one small secondary precipitate, of similar intermediate size, being identified in the microstructural regions examined. Example PSDs of the secondary and tertiary precipitates, alongside the fitted lognormal distributions, for the 3 at.% Mo alloy aged for 16 hours are shown in Figure 4.8 to demonstrate the quality of the fit to the data.

The median diameters of the secondary and tertiary γ' precipitates are presented in Figure 4.9. The median diameters of the secondary γ' remained approximately constant at $\sim$200 nm throughout ageing, although the sample aged for 100 hours displayed a noticeably lower median value. This was also associated with a broader PSD, as indicated by the larger error bars quoted with this data point. This arose as a result of the presence of regions containing smaller, cuboidal precipitates alongside regions of larger, octodendritic precipitates in this sample. With increasing ageing time, the size of the tertiary γ' increased monotonically, accompanied by a progressive increase in the width of the PSDs. Unlike the secondary γ', no changes associated with splitting instabilities were observed. These data are in agreement with [166], in which the secondary γ' size was independent of ageing time, whilst exhibiting morphological splitting, and the tertiary γ' coarsened on ageing.

Volume Fraction

The volume fractions of secondary precipitates obtained from analysis of the BSE images from the 3 at.% Mo alloy are presented in Figure 4.10. These results indicate that the volume fraction increases with ageing time from $37 \pm 1\%$ after 1 hour to $46 \pm 3\%$ after 1000 hours. Given the constant precipitate size of the 3 at.% Mo alloy shown in Figure 4.9, this suggests that the number density of secondary γ' precipitates increases during ageing. The larger uncertainty associated with the volume fraction measurements after 100 hours may be attributed to variations in the observed volume fractions in regions of the sample at different stages of precipitate splitting, with octodendritic regions exhibiting a higher volume fraction of γ', whilst a lower volume fraction was associated with the regions of spherical precipitates. The volume fraction of the tertiary γ' was observed to decrease throughout ageing, although this could not be described quantitatively due to the small precipitate size preventing SEM analysis, and unknown specimen thickness preventing volume fraction measurements by TEM. The dissolution of tertiary γ' is driven by Oswald ripening, enabling the growth of the larger secondary γ' precipitates.

TCP precipitation

After exposure to high temperatures for long time, Ni-based superalloys may precipitate TCP phases. The precipitation of such phases is encouraged by the presence of elements such as Mo, Cr, W and Re. Analysis of the SEM micrographs of the present alloy series showed no sign of TCP phases in any

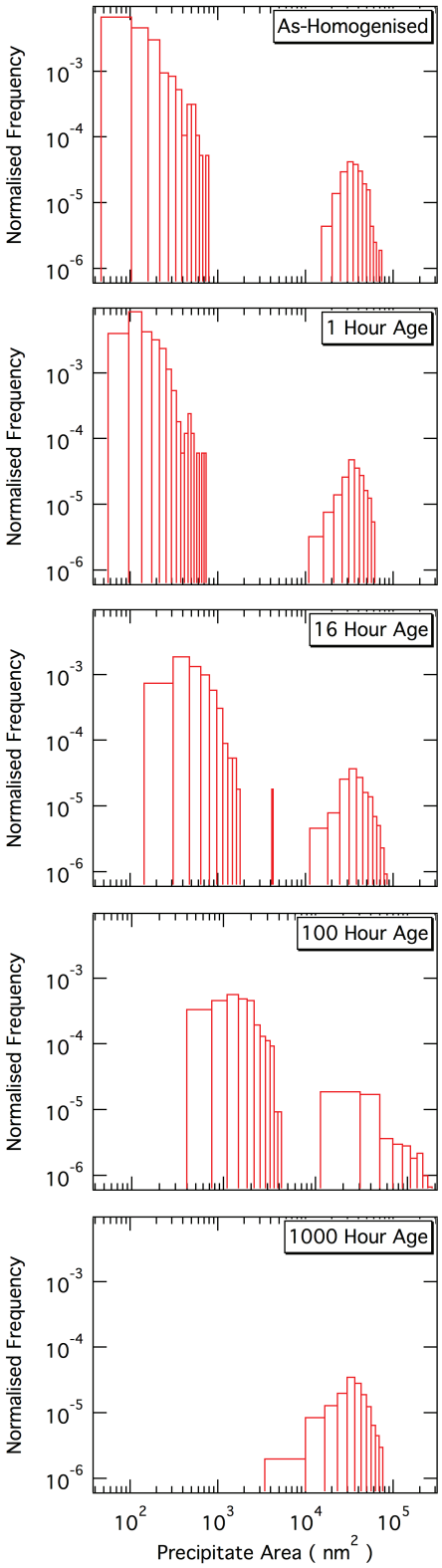

Figure 4.7: Particle size distributions (PSDs) of γ' in the 3 at.% Mo alloy as a function of ageing time.

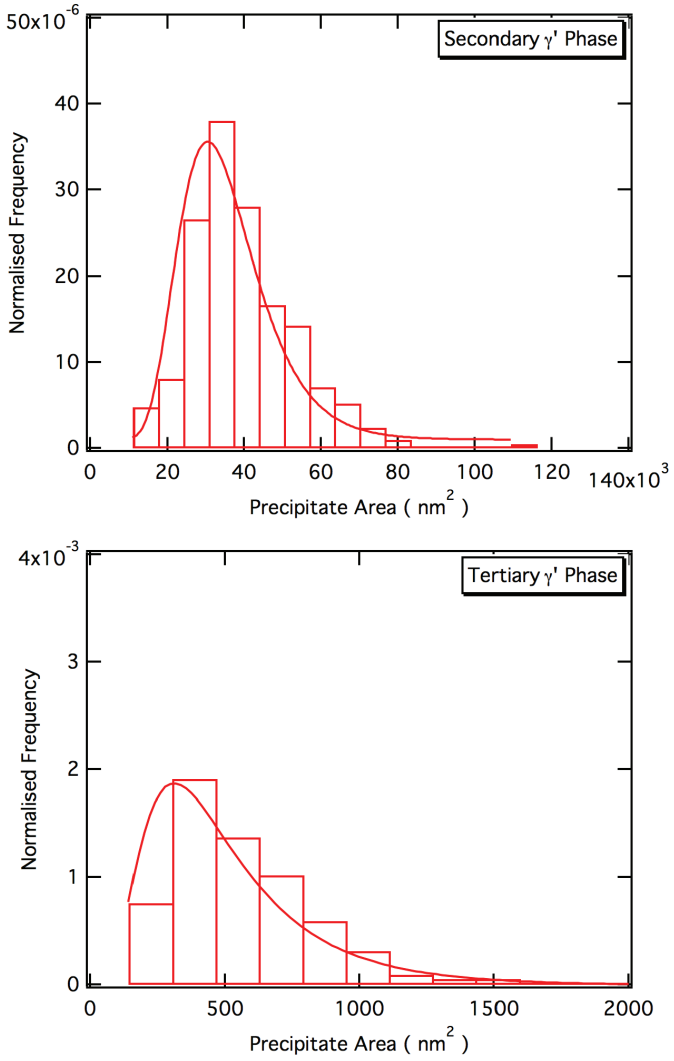

Figure 4.8: Particle size distributions (PSDs) of the (a) secondary and (b) tertiary γ' in the 3 at.% Mo alloy, with fitted lognormal functions shown to demonstrate the satisfactory fit to the experimental data.

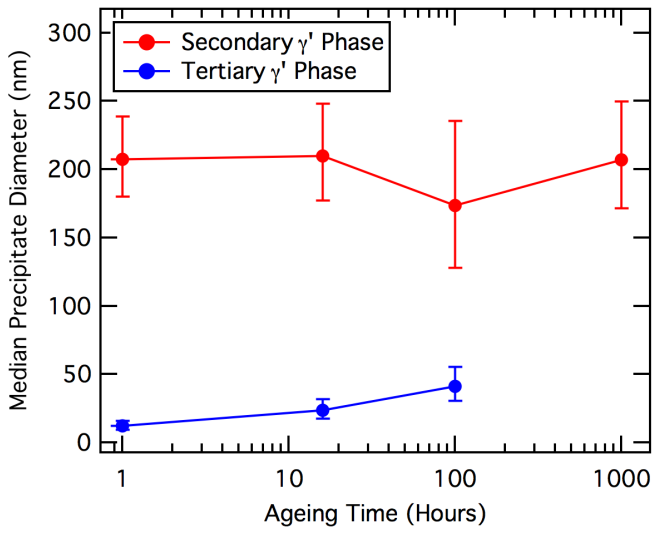

Figure 4.9: Precipitate size as a function of ageing time for the 3 at.% Mo alloy.

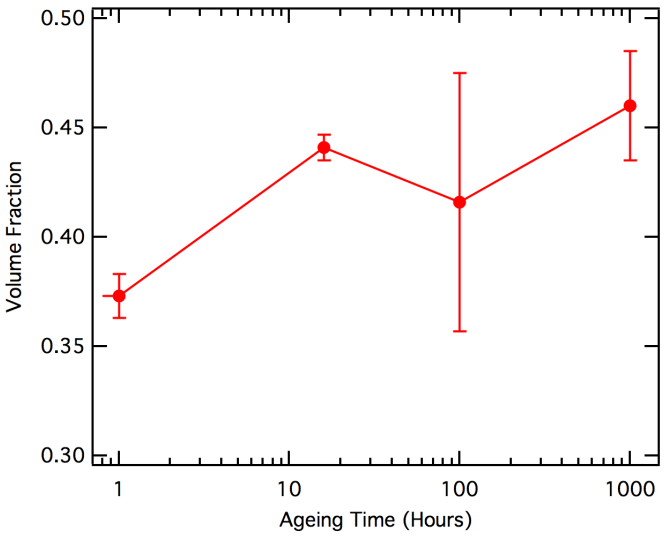

Figure 4.10: Volume fraction of γ' as a function of ageing time for the 3 at.% Mo alloy.

alloy except that containing 5 at.% Mo after ageing for 1000 hours (Figure 4.11). STEM EDX of these phases confirmed that they were σ phase, with high Cr and Mo content. In the 5 at.% Mo alloy, the σ phase was visible as a blocky morphology on the grain boundaries and as thin plates (Figure 4.11a and b respectively).

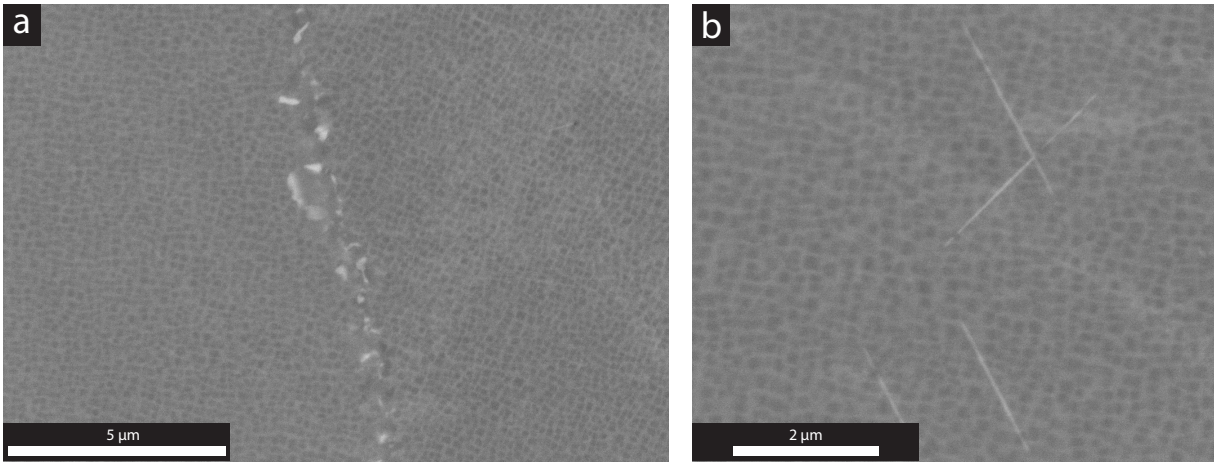

Figure 4.11: SEM micrographs showing precipitation of TCP phases in the 5 at.% Mo alloy.

Phase Composition

The APT reconstructions of the 3 at.% Mo alloy following the different heat treatment durations showed tertiary γ' distributions consistent with those obtained by STEM imaging of the carbon replicas, although statistical analysis of the PSDs was limited by the low number of precipitates in each APT needle. An example of one of the APT reconstructions, from the 3 at.% Mo alloy aged for 16 hours, is shown in Figure 4.12. In this figure, each green spot represents a Cr ion and each blue spot represents an Al ion. Isosurfaces corresponding to Cr concentrations of 15 at.% have been included to delineate the matrix/precipitate boundaries. A large range of tertiary γ' sizes can be seen, along with a region bounding a secondary γ' precipitate in which no tertiary γ' precipitates are present.

The compositional variation of each phase as a function of ageing time for the alloy containing

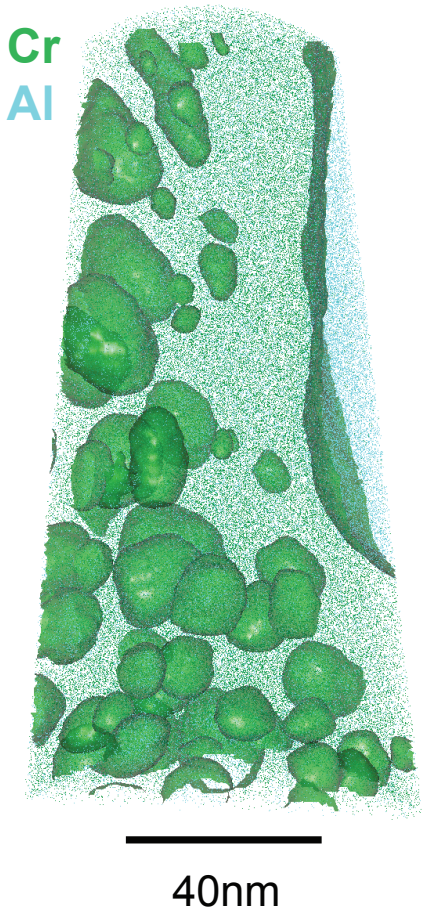

Figure 4.12: APT reconstruction of the 3 at.%Mo alloy after 16 hours of ageing at 760°C. Green spots represent the detection of one Cr ion, while blue spots represent one Al ion. γ' precipitates have been highlighted by the addition of an isosurface at 15 at.%Cr. One secondary and many tertiary precipitates are visible.

3 at.% Mo is shown in Figure 4.13. The STEM-EDX data are presented as open markers, with error bars corresponding to the standard deviation of the values obtained. APT data are presented as solid lines between solid markers and the Thermo-Calc predictions of the equilibrium compositions are given as dashed lines.

Measurements of the matrix composition of the 3 at.% Mo alloy following the various heat treatments (Figure 4.13a) indicated that it contained high levels of Cr and Mo, as well as low levels of Al and Ti, relative to the nominal alloy composition. These results were consistent with the established elemental partitioning behaviour between the phases of commercial Ni-based superalloys [18]. There is good agreement between the experimentally determined STEM-EDX and APT data for all elements, with differences typically lying within the range of experimental uncertainty. With increasing ageing time, the concentration of each element was observed to be approximately constant and generally corresponded well with the equilibrium concentrations predicted by Thermo-Calc. Of the elements present, only the Cr concentration was consistently different to the Thermo-Calc predictions, being underpredicted by ∼2 at.%.

The variation in elemental concentration with ageing time in the secondary γ' in the 3 at.% Mo alloy following the various heat treatments is shown in Figure 4.13b. As expected, the Al and Ti concentrations are comparatively high compared to the nominal alloy composition, while the Cr and Mo levels are comparatively low. As with the γ matrix composition, there is generally good agreement between the elemental concentrations measured by STEM-EDX and those obtained with APT. However, a notable disparity exists between the Al concentrations measured with the two techniques. This is due to the fact that the Kα emissions from Al have very low energy and are therefore easily absorbed by the sample without being detected during STEM-EDX, resulting in an underestimation of the Al concentration by this method [179]. As a consequence, where the experimental data for Al differed in this way, the APT data were deemed to be more reliable.

Progressive variations in elemental concentrations with ageing time in the secondary γ' phase for the 3 at.% Mo alloy can be discerned from the data presented in Figure 4.13b. The APT data for Al suggest that the concentration of this element increases from 11.3 at.% after 1 hour of ageing to 12.5 at.% after 1000 hours. These values bound the equilibrium concentration of ∼12 at.% predicted for the γ' phase by Thermo-Calc. The Cr and Ti show evidence of a decrease in concentration with increasing ageing time, although these changes are small and were not significantly beyond the experimental uncertainty. While the measured Cr concentration trended towards that predicted by Thermo-Calc, the Ti concentration differed markedly, being approximately 1 to 2 at.% below the predicted values. Notably, the concentration of Mo in the secondary γ' increased from 0.7 at.% after ageing for 1 hour to 1.5 at.% after 1000 hours. This change in Mo concentration was unexpected as it tended away from the predicted concentration of ∼0.1 at.%.

Analyses of the elemental concentrations in the tertiary γ' for the 3 at.% Mo alloy after the various heat treatments (Figure 4.13c) also identified unexpectedly high levels of Mo, which were in excess of 2 at.% and varied from 2.9 at.% after 1 hour of ageing to 2.1 at.% after 100 hours of ageing from the APT data. Both the Al and Ti contents increased slightly on ageing to 100 hours, although the Ti content was markedly lower than that of the secondary γ'. Significant differences were observed between the Cr concentrations measured by APT and STEM-EDX. The APT data were consistent in the range of 4 to 6 at.%, while the STEM-EDX data varied from 5 to 14 at.%. While it may be possible that these discrepancies arose as a result of statistical variations in between the precipitates sampled, the effect of retained γ within the carbon replica samples cannot be entirely dismissed and would account for the anomalously high Cr levels in the STEM-EDX measurements at 1, 2 and 200 hours. With the exception of Al, the equilibrium elemental concentrations predicted by Thermo-Calc do not agree well with the experimentally measured values, nor do they appear to be trending toward the predicted values with

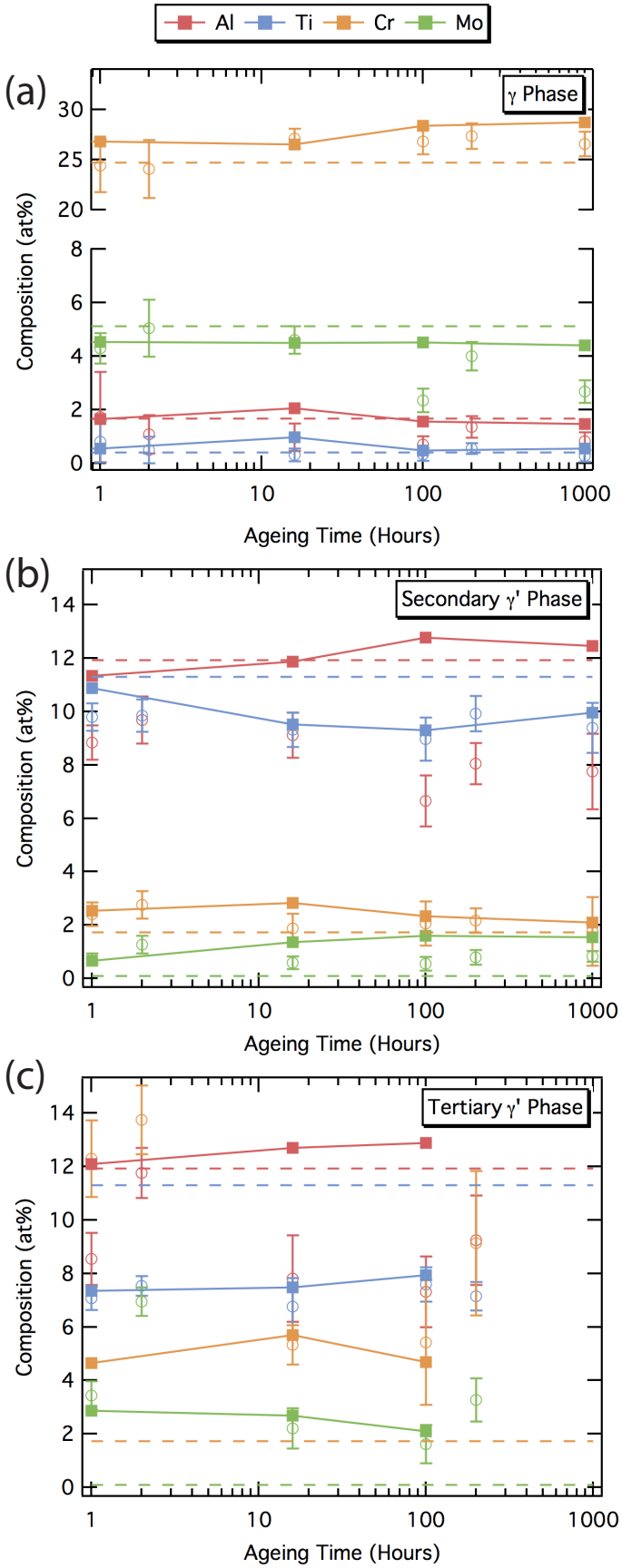

Figure 4.13: Composition of the matrix (a), secondary (b) and tertiary (c) γ' precipitates in the 3 at.% Mo alloy as a function of ageing time at 760°C. Experimental APT data are shown as square markers joined by solid lines, while STEM-EDX data are displayed as open markers. Predicted equilibrium phase compositions from Thermo-Calc are displayed as dotted lines.

prolonged time at temperature.

Interface Widths

Figure 4.14 shows the proxigrams of the elemental concentrations across the secondary and tertiary γ/γ' interfaces measured by APT of the 3 at.%Mo sample aged from 0 to 1000 hours. In this figure, all distances are quoted with respect to the 15 at.%Cr isosurface. The elemental concentration profiles all showed sigmoidal variations. As with previous studies in the literature [180], an accumulation of nickel was observed ∼2 nm into the γ matrix.

The quantitative analysis of the secondary γ' interface width for each element is presented in Figure 4.15. These data show a progressive decrease in the width of the interface for all elements with increasing ageing time, from which it can be seen that Mo has the largest interface width and Ni has the smallest.

Lattice Parameters and Lattice Misfit

The lattice parameters of the γ and γ' phases and the associated lattice misfit obtained by neutron diffraction for the 3 at.% Mo alloy are presented in Figure 4.16. These results indicate that the lattice parameters and lattice misfit are approximately constant throughout ageing for this alloy, within the experimental uncertainty. This is consistent with the nearly constant compositions of the γ and γ' phases as measured by APT (Figure 4.13). The average measured lattice misfit was determined to be $-0.050 \pm 0.008\%$. In comparison, the lattice misfit predicted using Thermo-Calc was 0.45%. The inconsistency of this prediction with the experimental results cannot be attributed to the effect of lattice constraint between the two phases, since the signs of the predicted and measured lattice misfits differ. Similarly, the discrepancy cannot be ascribed to differences between the measured and predicted compositions, as a larger, positive lattice misfit is predicted when using the experimentally determined compositions within Thermo-Calc.

Microhardness

The hardness of the 3 at.% Mo alloy is shown as a function of ageing time at 760°C in Figure 4.17. It may be seen that the hardness of the alloy increases with ageing time, although the change is very small; after 1 hour of ageing the alloy had a hardness of ∼397 VH, increasing to ∼403 VH after 1000 hours. Notably, in the as-homogenised condition, the alloy had an appreciably lower hardness, of ∼367 VH.

4.4 Discussion

Precipitate Morphology

During the early stages of ageing of the 3 at.% Mo alloy at 760°C, the secondary γ' size remained approximately constant while the volume fraction increased by ∼7% (Figures 4.9 and 4.10). This suggests that this distribution is in a growth phase, leading to an increased number density of precipitates. The apparent absence of coarsening during this period differs from previous studies of precipitate evolution in other superalloys [181–183] and could be a consequence of the low lattice misfit, and associated strain energy, between the γ and γ' phases providing a minimal driving force for this process. A constant lattice misfit has previously been observed in a similar alloy on ageing up to 12 hours and linked to a constant secondary γ' precipitate size [182].

After 100 hours of ageing, the secondary γ' showed evidence of morphological changes, with cuboidal and octodendritic precipitates being observed in the microstructure. In alloys with moderate to high

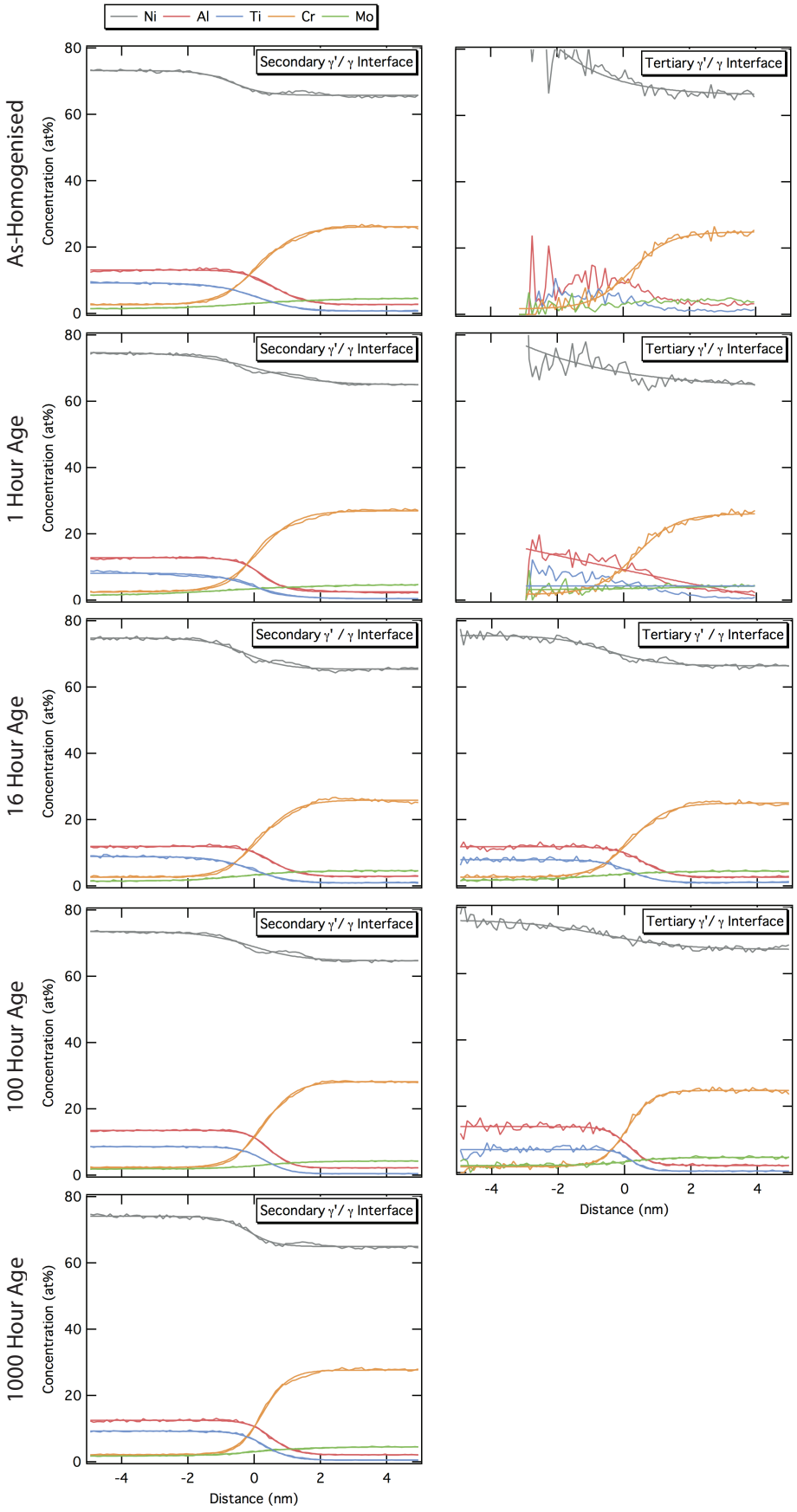

Figure 4.14: Proximity histograms of elemental concentrations across the secondary and tertiary γ'/γ interfaces in the 3 at.%Mo alloy, for ageing times up to 1000 hours.

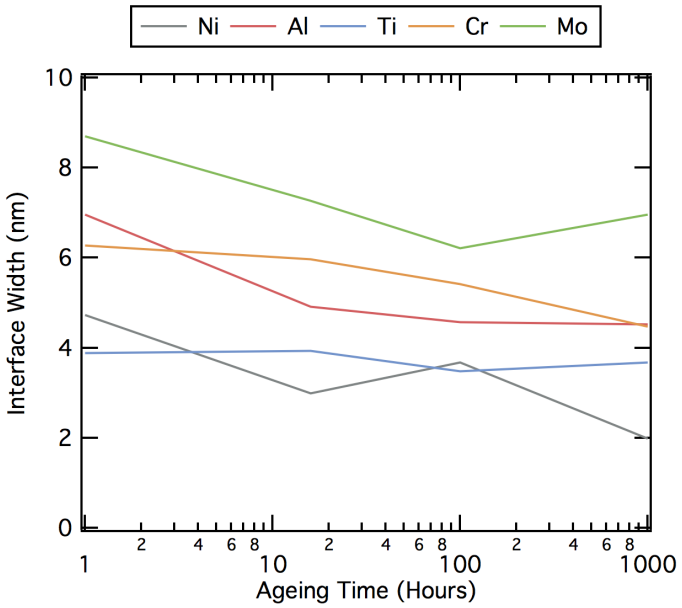

Figure 4.15: The variation of the secondary γ'/γ interface width as a function of ageing time for the 3 at.% Mo alloy.

lattice misfits, morphological changes of this type are commonly associated with the magnitude of the lattice misfit, with a progression from spheres to cuboids and finally to octodendrites, in order to minimise the elastic strain energy of the matrix as the precipitates coarsen [20, 178]. However, in this alloy, the lattice misfit is low and therefore the precipitates would be expected to remain spheroidal throughout ageing.

The splitting of octodendritic precipitates into smaller spherical or cuboidal precipitates is also driven by a reduction in the overall energy of the system and occurs when the overall elastic strain energy overcomes the increased interfacial energy of the split precipitates [23,35,36,39,41–43]. Although splitting is commonly associated with high misfit alloys [42], it has been observed previously in low misfit alloys such as RR1000 and UCO1 [39, 43]. The morphological instabilities that can lead to precipitate splitting [184, 185] are known to occur in alloys of varying misfit. It must be noted, however, that the mechanism leading to these instabilities differs depending on the magnitude of the lattice misfit. Alloys with low lattice misfits may form precipitates with such morphologies as a result of diffusion-induced interface instabilities [186, 187]. In contrast, in alloys with larger misfits, the process is governed almost entirely by the strain energy [184].

Evidence of this process was observed in the microstructure after ageing for 100 hours (Figure 4.6i). Some regions of this sample contained large, octodendritic precipitates indicative of the precursor to splitting, while other regions contained only smaller, spherical/cuboidal secondary γ' precipitates, characteristic of splitting having occurred. Splitting does not occur instantaneously across the sample, hence the sample aged for 100 hours contained both larger and smaller secondary γ' precipitates, resulting in a wider particle size distribution. Additionally the regions with smaller, spherical/cuboidal precipitates exhibited locally lower volume fraction than those containing larger octodendritic precipitates. This accounts for the large uncertainty associated with the volume fraction data from this condition (Figure 4.10).

In addition, after the onset of splitting, there appeared to be a decrease in the amount of tertiary γ' visible in the STEM images of the samples. This is consistent with previous reports [39]. However, quantification of the tertiary γ' volume fraction could not be reliably performed from the analysis of the STEM images acquired due to difficulties in accurately determining the local foil thickness. The splitting

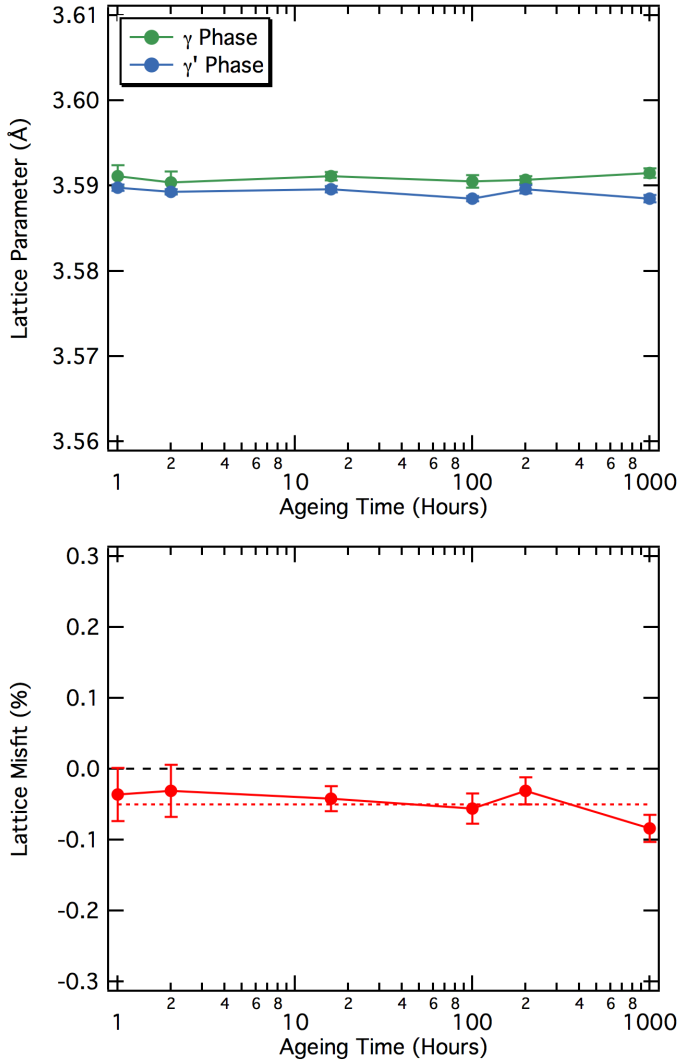

Figure 4.16: The variation of the lattice parameter of each phase, and the lattice misfit of the alloy as a function of ageing time at 760°C for the alloy with 3 at.% Mo. The average lattice misfit during ageing is shown as a dotted line.

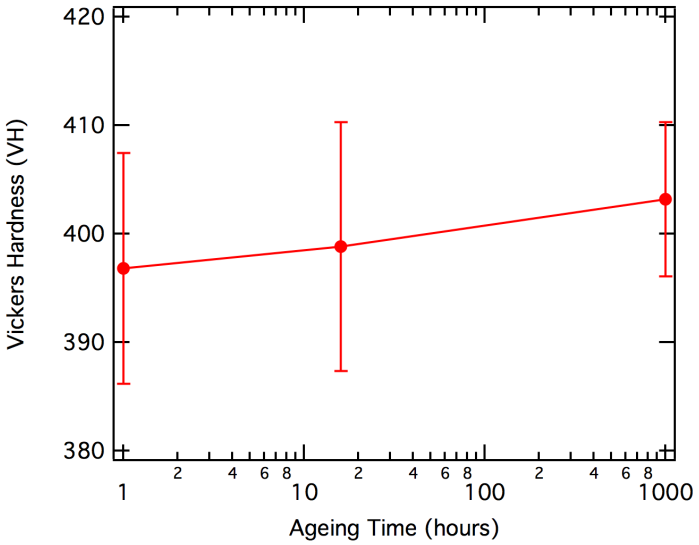

Figure 4.17: The Vickers hardness of the 3 at.% Mo alloy as a function of ageing time at 760°C.

phenomenon also serves to explain the reduced size of the secondary γ' after 1000 hours, with these precipitates having completed the splitting process. Importantly, the morphological changes observed are not consistent with those that would be expected from instabilities governed by fast growth in selected directions due to supersaturation of the matrix phase [42].

The tertiary γ' precipitates were observed to increase in size during ageing (Figure 4.9), approximately following a $t^{1/3}$ relationship (as shown in Figure 4.18), as would be expected from classical Lifshitz-Slyozov-Wagner (LSW) theory [37, 38, 188]. However, using this relationship and extrapolating the coarsening of the tertiary γ' to 1000 hours, the predicted size would remain below that of the secondary γ' precipitates. This confirms that the absence of tertiary γ' after 1000 hours of ageing is due to resolution of the precipitates, as opposed to coarsening to a size sufficient to merge with that of the secondary γ'.

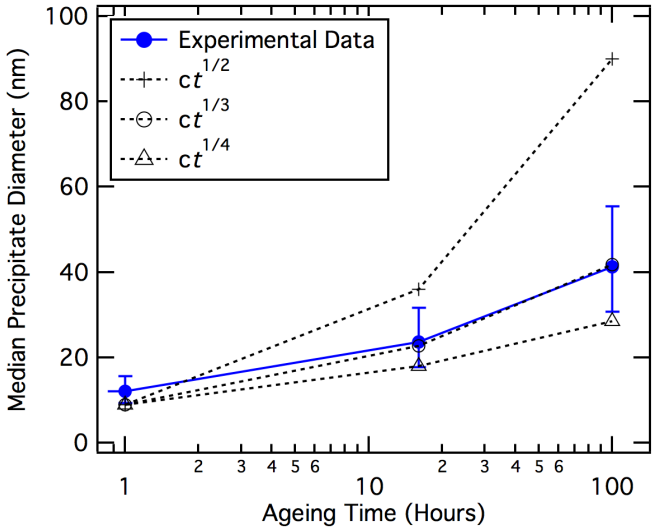

Figure 4.18: Tertiary γ' precipitate size as a function of ageing time for the 3 at.% Mo alloy, showing a superior fit to the LSW theory, when the time exponent is 1/3, compared to alternative exponents of 1/2 or 1/4. c is a constant.

Precipitate Composition

In the as-homogenised condition and in the majority of the aged samples, the 3 at.% Mo alloy exhibited a bimodal size distribution of secondary and tertiary precipitates. Both the secondary and tertiary γ' form on cooling from the homogenisation temperature, with the secondary γ' forming before the tertiary γ', at higher temperature [189, 190]. The higher elemental mobility during the formation of the secondary γ' produces larger precipitates and facilitates the movement of Mo and Cr out of the γ' and into the matrix phase, in which they preferentially reside. In contrast, as a result of the lower temperature and therefore reduced diffusion during the formation of the tertiary γ', this distribution is generally enriched in those elements that partition to the γ phase during secondary formation, resulting in a composition further from the equilibrium predicted value [191]. The Mo content of the γ' precipitate phase has been shown to decrease with increasing ageing temperature, in agreement with this principle [192].

During ageing of the alloy, relatively modest changes in the composition of the phases present in the 3 at.% Mo alloy were observed (Figure 4.13). Most notably, the tertiary γ' phase contained markedly higher concentrations of Mo and Cr and a lower concentration of Ti than the secondary γ' precipitates. While the Mo and Al concentrations in the two precipitate size distributions appear to be converging with increasing ageing time (as seen in [193]), it is not clear that this is true of the Cr and Ti concentrations.

The elevated Mo concentrations observed in the γ' precipitates are consistent with data reported by Jou et al. [194] on IN100. Similarly, a significant Mo concentration in the secondary γ' phase has also been reported by Loomis et al. [195] in an investigation of similar model alloys to those studied here. However, a previous study comparing experimental compositions from APT to equilibrium predictions by Thermo-Calc did not find the Mo content in the γ' to be as high as the present study [196].

It has been shown previously that the composition of the γ' precipitates is dependent on size within the range of 5 nm to 3 µm [23]. In contrast, in the present work no link was found between the size of the γ' precipitates within each size distribution and the composition, as has been found previously by Collins *et al.* [197]. However, the range of precipitate sizes within each distribution in the current study is small and, therefore, a wider range of precipitate sizes may have revealed compositional variations.

The concentration profile widths in Figure 4.15 decreased continuously during ageing for all elements. This is consistent with the studies of Ni-Al [198], Ni-Al-Cr [199] and Ni-Al-Cr-Ta [180] alloys, which showed rapid decreases in the interface widths in the early stages of ageing and lower rates of decrease with prolonged time at temperature, as the precipitates entered the coarsening regime. However, it is noted that the opposite behaviour of increasing interfacial width has been reported during the ageing of secondary γ' precipitates in the commercial superalloy Rene 88DT [77,193]. This suggests that a number of factors may influence interfacial width. For example, it has been shown that a sharper interface results from slower cooling rates in AM1 [196]. The relative magnitudes of the interfacial width differ for each element, with the faster diffusing species, Al and Ti, exhibiting narrower interfaces than those that diffuse more slowly. This is particularly notable for Mo, which displays the widest interface despite having the smallest difference in concentration between the γ and γ' phases. Theoretical descriptions exist that account for the finite width of the γ/γ' interface, as observed in this work. These include the original work by Cahn and Hilliard [200] that utilised gradient energy coefficients to account for the free energy of regions of non-constant composition, and the more recent trans-interface chemical diffusion model by Ardell [201,202], where the kinetics are controlled by diffusion through, rather than to, the γ/γ' interface.

Composition has previously been linked to precipitate morphology in a study on the low misfit alloy RR1000, where it was shown that restricted elemental diffusion resulted in cyclic coarsening and splitting of the secondary γ' [43]. It was shown that the Al concentration of the γ' phase generally increased on ageing at 800°C, reaching a maximum immediately following splitting. In contrast, the concentration of Ti remained approximately constant during ageing but exhibited a local minimum after splitting. The overall trends in the composition of Al and Ti in the alloy studied in the present work are not inconsistent with these results, although sampling at more regular intervals would be required to determine the local changes associated with splitting.

Lattice Misfit

The difference between the secondary and tertiary γ' compositions would be expected to result in differing lattice parameters for these distributions and, consequently differing lattice misfits. However, the broad intrinsic peak width and comparatively low volume fraction of the tertiary γ' phase prohibited separation of the contributions of this distribution to the superlattice reflections in the neutron diffraction data, which were therefore dominated by the secondary γ' [203]. Since the composition of both the γ matrix and the secondary γ' precipitates remained approximately constant across the alloy series, the resulting lattice misfit also remained approximately constant. However, these data are in contrast to a previous study which found that both the γ and γ' lattice parameters decrease on ageing due to diffusion of solute atoms between the phases, rather than stress relaxation on ageing [197].

Consequences for Mechanical Properties

The differences between the measured compositions of the γ' precipitates and those predicted by Thermo-Calc have implications for the estimation of alloy strength using empirical relations (as discussed in Chapter 3) [7,65,114]. Specifically, the high Mo and low Ti concentrations will affect multiple mechanisms of alloy strengthening concurrently, including solid solution, coherency and order strengthening. Previous literature exists on the role of Mo as a solid solution strengthener in the matrix phase [204], but the full extent of the multiple effects in the current alloy series require further investigation. The contribution from each strengthening mechanism will also vary between the secondary and tertiary γ' populations as a result of their different compositions. Therefore, relationships describing the properties of superalloys may require modification to accommodate the compositional differences between the γ' populations, to further improve their fidelity.

4.5 Conclusions

The microstructure and phase composition of a model polycrystalline Ni-based superalloy have been characterised using STEM-EDX and APT, following ageing at 760°C for durations of up to 1000 hours. Microstructural analysis revealed that the size of the secondary γ' precipitates remained approximately constant during the early stages of ageing, but exhibited the morphological instabilities associated with precipitate splitting following longer duration exposures. In contrast, when the tertiary γ' precipitates were present in the microstructure, they were observed to coarsen in line with LSW theory. The experimentally determined phase compositions were compared to equilibrium predictions made using Thermo-Calc. The composition of the γ phase was seen to remain approximately constant during ageing, with elemental concentrations similar to the equilibrium phase compositions predicted by Thermo-Calc. Compositional analysis of the secondary and tertiary γ' precipitates revealed small changes in elemental concentration with increasing ageing time, and notably, higher Mo and lower Ti concentrations were observed than those predicted using Thermo-Calc. These results are believed to have implications for models describing alloy mechanical properties, which currently employ thermodynamic equilibrium predictions of phase composition.

Chapter 5

Yield Strength Modelling of Model Alloys

5.1 Introduction

Chapter 4 identified that different γ' size distributions display variations in chemical composition, corroborating previous literature [77, 78]. Such variations may be expected to significantly affect the mechanical properties, but these effects have not been quantified within existing physical models of superalloy strength. A unified model of the main strengthening mechanisms that takes into account variations in the size and composition of the phases is necessary if such predictions are to be effectively used to optimise the properties of superalloys, and to define processing routes that can deliver specific microstructures.

In this chapter, the series of model quinary, polycrystalline Ni-based superalloys with varying Mo content defined in Section 4.2 was investigated to assess the extent of individual strengthening mechanisms on the overall yield strength, in a more focussed and systematic way than in Chapter 3. The variation in Mo content was chosen to explore its role on the various strengthening mechanisms, as it is a strong matrix solid solution hardener and affects the coherency strength via the lattice misfit, due to its large atomic radius. The alloys were studied using SEM, TEM and APT to fully characterise the particle size distributions and phase chemistries. This enabled the yield strength to be predicted using the physically based models described in Chapter 3, using experimentally determined input values.

Experimental measurements of the mechanical properties were obtained by compression testing and these results were compared to the model predictions. In addition to the overall yield strength, the individual effects of solid solution, precipitation, coherency and grain boundary strengthening were determined. Mo additions were found to affect multiple underlying strengthening mechanisms concurrently, and the role of solid solution strengthening in the γ' phase was found to be significant.

5.2 Methods

The fabrication of the model alloy series and the methods of microstructural characterisation are discussed in Section 4.2. The microstructure, phase compositions and lattice parameters of each alloy were fully characterised in order to obtain the input parameters required for the models. This allowed the quantification of each strengthening mechanism and the prediction of the factors controlling the yield stress.

The modelling methods discussed in this section are discussed in Section 3.2. The only material constants required for the models are the shear modulus and the Burgers vector; these values were

assumed equal to those for typical superalloys, $\mu = 80\,\text{GPa}$ and $b = 0.248\,\text{nm}$ respectively [65].

Additional methods only are described here in the present chapter.

In the present chapter, the APBE was modelled by two methods to show that the effect of variations in chemical composition on particle shear are not method-specific; the CalPhaD-based (Calculation of Phase Diagrams) approach detailed in [113] and by a simple linear mixtures approach based on density functional theory (DFT) calculations derived in the same work [113]. The phase compositions determined experimentally for both the secondary and tertiary γ' phases were used to obtain a distinct value of the APBE in both distributions of γ'. It has been shown previously that the APT technique is much better suited to determination of the Al content in Ni-based superalloys than TEM (Chapter 4). Therefore, throughout this Chapter, an average of the APT data was used to describe the Al content of these alloys, and this was assumed to be the same in each alloy studied. STEM EDX was used to determine the content of the remaining elements since this technique provides a convenient method for taking multiple repeat measurements, which was not possible with APT. Additionally, a very good correlation between APT and STEM EDX data has been shown previously for elements other than Al (Chapter 4).

The CalPhaD-based method is described in Chapter 3. The DFT approach is summarised here. The DFT approach approximates the interchange energy by comparing the internal energy of supercells of ternary Ni_3(Al,X) and A1 random solid solution, where X is the alloying element in the γ'. Crudden et al. [113] proposed a model for the APBE in multicomponent Ni-based superalloys based on these results by extrapolating the values predicted between Ni-25Al (at.%) and Ni-12.5Al-12.5X (at.%) with a linear fit according to the equation

$$E_{\text{APB}} = E^0_{\text{APB}} + \sum_i k_i x_i^{\gamma'} \tag{5.1}$$

where E^0_{APB} is the APBE of Ni_3Al and $x_i^{\gamma'}$ is the concentration of element i in the γ'. The coefficients k_i are constants specific to each element (Table 5.1). The value for the APBE of pure Ni_3Al is taken as $150\,\text{Jm}^{-2}$, in agreement with TEM observations and *ab initio* calculations [113].

	Ti	Cr	Mo
k_i (mJ m^{-2}/at.)	15	-1.7	-1.7

Table 5.1: APBE coefficients (k_i) for the DFT-based method for APBE prediction.

Compression Testing

To experimentally determine the mechanical properties of the alloys, compression testing was carried out at room temperature, 700°C and 800°C using a low cycle fatigue machine comprising a 100kN Mayes servohydraulic frame with an Instron 8800 controller. Cylindrical specimens of diameter 5 mm and length 7 mm were compressed at a rate of $0.5\,\text{mm min}^{-1}$ up to a maximum load well past the yield stress, up to approximately 30 kN. Extension was measured by the machine itself, rather than an attached strain gauge, which was not possible due to the small sample size. Both toe and compliance corrections were manually applied to the data. The associated uncertainty in the data was taken as the standard deviation of 3 repeat measurements of each data point.

5.3 Results

Grain Size

Each alloy consisted of very large grains, that were of similar size in each alloy (approximately 1 grain boundary per mm) due to the VIM and homogenisation heat treatments.

Particle Size Distributions (PSDs)

A characteristic STEM micrograph of each alloy is shown in Figure 5.1. Each alloy contained a bimodal precipitate size distribution, comprising secondary and tertiary γ'. Secondary γ' are shown at the same magnification in the left hand column, whilst the tertiary γ' are shown at a higher magnification in the right hand column. Increasing Mo content is shown vertically. The average precipitate volume fractions and sizes are shown in Table 5.2.

Alloy (at.% Mo)	Secondary γ' Volume %	Secondary γ' Size (nm)	Tertiary γ' Size (nm)
0	40.3 ± 0.4	299 + 45 − 39	35 + 14 − 10
1	46.9 ± 1.0	463 + 86 − 72	36 + 20 − 13
2	39.2 ± 0.8	374 + 73 − 61	20 + 6 − 5
3	44.1 ± 0.6	210 + 38 − 32	24 + 8 − 6
4	40.0 ± 0.7	342 + 67 − 56	15 + 4 − 3
5	40.0 ± 1.0	291 + 52 − 44	13 + 5 − 4

Table 5.2: Experimentally determined volume fractions of the secondary γ' precipitates, and average sizes of both the secondary and tertiary γ' precipitates across the model alloy series.

It is clearly seen that the morphology of the secondary γ' changed progressively from spherical to cuboidal as the nominal Mo content of the alloy was increased. The smallest secondary γ' occurred in the 3 at.% Mo alloy (210 nm), whilst the largest occurred for the 1 at.% Mo case (463 nm). Large secondary γ' precipitates were also associated with "flowery" morphologies characteristic of splitting, as seen in a number of the alloys (Figure 5.1 c, e, i and k).

In all alloys, the tertiary γ' were spherical and showed no sign of precipitate splitting. The size of the tertiary γ' decreased as the nominal Mo content increased. The smallest average tertiary γ' were found in the 5 at.% Mo alloy (13 nm) whilst the largest were found in the 1 at.% Mo alloy (36 nm). The volume fraction of the tertiary γ' was difficult to estimate with the given magnification, and was taken to be 5% for the model calculations, since the total equilibrium fraction of γ' predicted by Thermo-Calc was ∼45% in all alloys, and the average measured volume fraction of secondary γ' was ∼40% in most cases (Table 5.2). This value has also previously been determined for the tertiary γ' volume fraction in RR1000 [205].

Phase Compositions

As mentioned in Section 4.2, large-area EDX scans were carried out and confirmed that the composition of each of the samples was homogeneous. Average values of the experimentally measured bulk compositions are given in Table 4.2.

Figure 5.2a, b and c show the compositions of the γ, secondary γ' and tertiary γ' phases respectively and how they vary across the alloy series. Solid lines represent the experimental STEM EDX data, whilst the dashed lines represent Thermo-Calc predictions for the equilibrium composition of each phase. In addition to STEM EDX, APT was carried out on the 0 at.% Mo and 3 at.% Mo samples, and these data are depicted as points in Figures 5.2a-c.

The experimental compositions of the γ phase (Figure 5.2a) showed classic elemental partitioning [18], with high Cr and Mo but low Al and Ti contents compared to the nominal bulk alloy composition. With

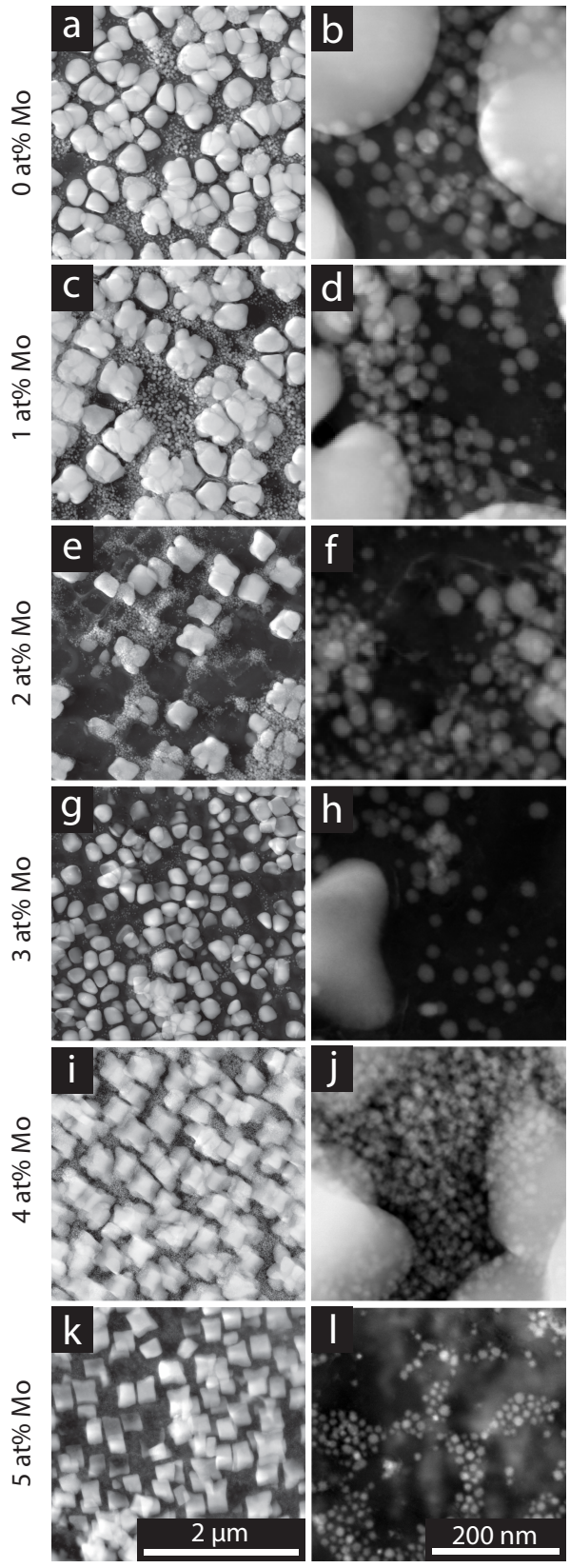

Figure 5.1: Particle size distributions (PSDs) of γ' as a function of Mo content.

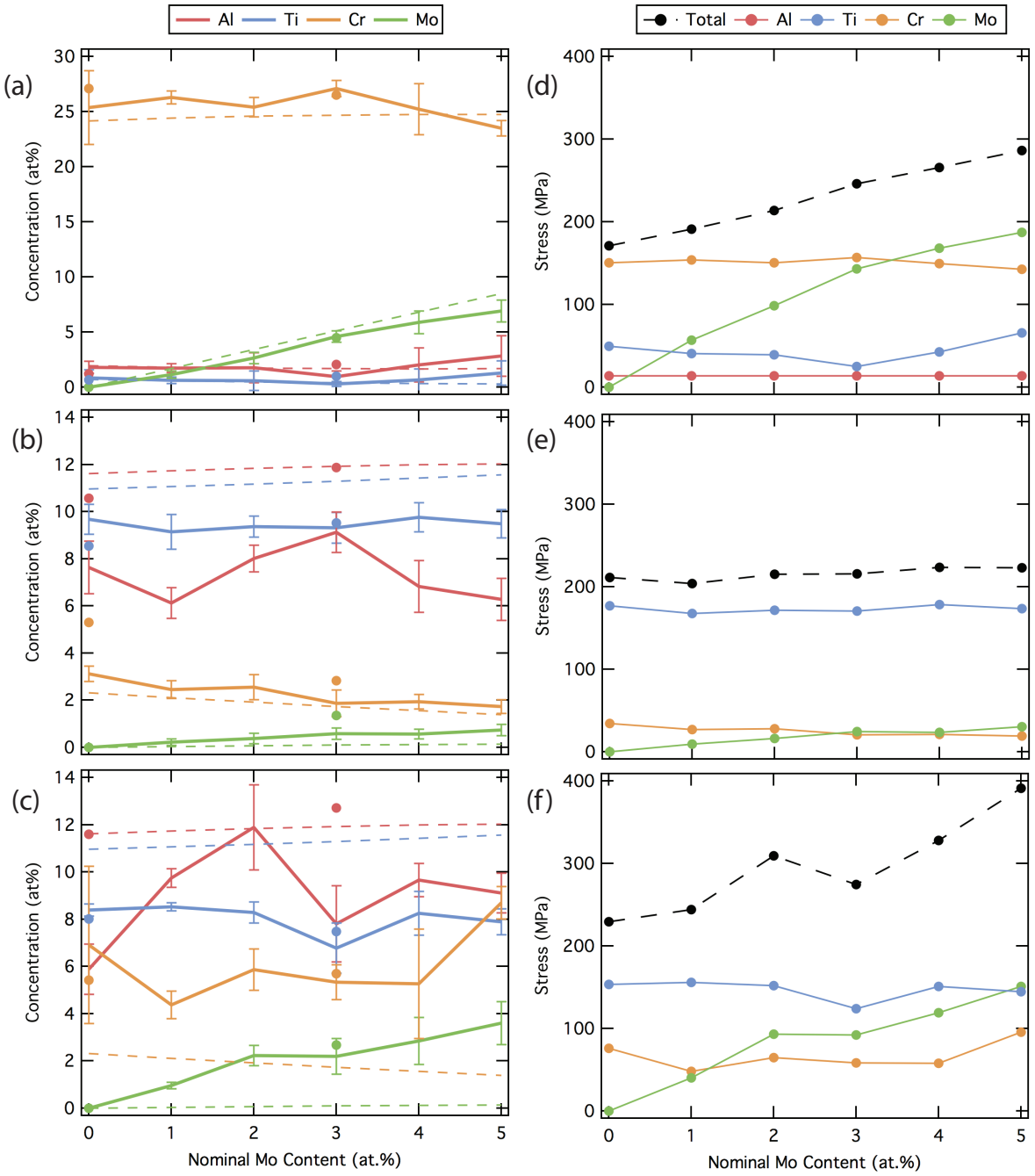

Figure 5.2: Composition of the γ phase (a), the secondary γ' phase (b) and the tertiary γ' phase (c), as a function of the nominal Mo content. Solid lines represent experimental STEM EDX data, points represent experimental APT data, and Thermo-Calc equilibrium composition predictions are shown as dashed lines. The ensuing effect on the extent of solid solution strengthening in the γ (d), secondary γ' (e) and tertiary γ' (f) is given on the right.

the exception of Mo, the composition of each element in the γ phase remained constant as the nominal Mo content of the alloy was increased from 0 to 5 at.%.

The equilibrium predictions for the composition of the γ'-partitioning elements (Al and Ti) in the γ matrix phase were very close to the experimental STEM EDX results. However, the γ-partitioning elements were less well predicted; Thermo-Calc underpredicted the Cr content but overpredicted the Mo content, although the differences are small.

The secondary γ' phase compositions also exhibited the expected elemental partitioning behaviour (Figure 5.2b). The Cr and Mo contents were low, whilst the Al and Ti contents were high relative to the bulk alloy composition. As the nominal Mo content of the alloy was increased, there was a concurrent decrease in the Cr content of the secondary γ', accompanied by a clear increase in the Mo content. The Ti content was constant throughout the alloy series and a similar argument could be made for the Al content. However, as discussed in Chapter 4, the determination of Al content by STEM EDX is prone to much more uncertainty than the other elements, due to the very low energy of the Kα emissions being easily absorbed by the sample. This results in potentially significant underestimates of the Al content, therefore the APT data was deemed to provide a more accurate value of the Al composition for the subsequent discussions.

It is seen in Figure 5.2b that Thermo-Calc provides reasonable predictions of the Cr and Mo content of the secondary γ' phase, although they are slightly underpredicted and overpredicted respectively. The over-prediction of Cr is equivalent to that in the γ phase, whereas the Mo content was underpredicted in the γ. The equilibrium predictions of the Ti content in the secondary γ' were very far above those measured experimentally. However, the Al content, as measured by APT, was relatively consistent with the Thermo-Calc predictions.

Figure 5.2c shows the experimentally determined composition of the tertiary γ' across the alloy series, along with the predicted equilibrium composition. High concentrations of Al and Ti exist in the tertiary γ' phase, as expected from classical partitioning theory. In comparison with the secondary γ', the tertiary γ' have higher Al content and lower Ti content. Notably, unexpectedly high contents of the γ-partitioning elements (Cr and Mo) were measured in the tertiary γ' phase, compared to the nominal bulk alloy composition. This was not predicted by Thermo-Calc.

Overall, there was more variation within the experimental compositions of the tertiary γ' phase, and there was a weaker correlation with the equilibrium Thermo-Calc predictions than seen with the γ phase and the secondary γ'. The equilibrium Cr content was predicted by Thermo-Calc to decrease as the nominal Mo content of the alloy increased, contraposing the experimental data. The equilibrium prediction of the Mo content of the tertiary γ' was negligible, in stark contrast to the experimental data. For example, Thermo-Calc predicted the Mo content of the tertiary γ' to be 0.13 at.% in the nominally 5 at.% Mo alloy alloy, which differed markedly from the experimentally determined concentration of 3.6 $\pm$ 0.9 at.%.

Solid Solution Strengthening

Figures 5.2d-f illustrate the predicted effect that the phase compositions have on solid solution strengthening in each phase across the alloy series. It must be noted that phase fraction is not taken into account in this figure, so the strengthening contributions apply to each single phase alone. The increasing bulk Mo content of the alloy series causes an increase in the strength of the γ phase by almost 200 MPa (Figure 5.2d), principally associated with the increase of $\sim$7 at.% Mo in the γ matrix phase. The high Mo content in the tertiary γ' also has a significant effect on the solid solution strengthening of this phase (Figure 5.2f), with the $\sim$4 at.% Mo giving rise to $\sim$150 MPa of strengthening in the tertiary γ'. Within the γ matrix phase, Cr is also seen to have a significant effect on the solid solution strengthening, due to its

high concentration within that phase. In contrast, in the γ' precipitate phases, the main contribution to solid solution strengthening comes from the Ti.

Notably, the tertiary γ' phase benefitted from greater solid solution strengthening than either the γ or secondary γ' phases. Mo has the strongest effect on the tertiary γ' phase (Figure 5.2f), increasing the solid solution strength from 220 MPa (in the 0 at.% Mo alloy) to 400 MPa (in the 5 at.% Mo alloy). This significant increase in strength would not have been obtained if it were assumed that the tertiary γ' had the equilibrium compositions predicted by Thermo-Calc.

Lattice Misfit and Coherency Strengthening

The lattice parameters of the γ and γ' phases, and the associated lattice misfits are shown as a function of nominal Mo content in Figure 5.3. For comparison to experimental data, a value for the *predicted* lattice parameter (a) of each phase at 760°C was attained using Equation 3.1. Predictions of the molar volumes (V_m) of each phase were made with Thermo-Calc, using both the experimentally determined phase compositions, and the predicted equilibrium compositions. Subsequent calculation of the lattice misfit (δ) was via Equation 2.4.

Figures 5.3a and d show the lattice parameters and lattice misfit, respectively, predicted by Thermo-Calc using the equilibrium predicted phase compositions. It should be noted once again that Thermo-Calc only predicts one composition for the γ' phase - the equilibrium value. Figures 5.3b and e display the lattice parameters and lattice misfit of the alloys predicted by Thermo-Calc using the experimental phase compositions found via STEM EDX and APT. The differing phase compositions of the secondary and tertiary γ' result in differing lattice parameters and misfit. Finally, Figures 5.3c and f show the experimental lattice parameters and misfit determined by neutron diffraction. Due to the low volume fraction of the tertiary γ', the diffraction data associated with this population could not be separated from that of the secondary γ', which dominated the diffraction data. As such, the lattice parameters quoted are those of the γ and secondary γ' phases only.

The Thermo-Calc predictions of the γ and γ' phase compositions at equilibrium resulted in linear increases in the matrix and precipitate phase lattice parameters with nominal Mo content (Figure 5.3a). This, in turn, resulted in a linear decrease in the predicted lattice misfit with increasing Mo content (Figure 5.3d), since the lattice parameter of the matrix phase increased faster than that of the precipitate phase. All alloys were predicted to have a positive lattice misfit.

When Thermo-Calc was used to predict the lattice parameters and misfit resulting from the experimental phase compositions, the general trends with Mo content were the same as those using the equilibrium compositions. However, the magnitudes differed and the trends were significantly less linear. Experimentally, the secondary and tertiary γ' precipitates have different compositions, resulting in a greater lattice parameter in the tertiary γ' phase. In turn, this produces a larger lattice misfit between the γ matrix and the tertiary γ' phase. The lattice parameter of the secondary γ' phase was approximately constant, at ~3.585 Å, across the alloy series investigated. The 5 at.% Mo alloy alone was predicted to have a negative lattice misfit between the γ matrix and the secondary γ' phase.

The experimental lattice parameters of the matrix and precipitate phases measured were found to increase with the nominal alloy Mo content (Figures 5.3c and f), as predicted by Thermo-Calc. The experimentally measured lattice misfit was seen to decrease as nominal Mo content was increased, becoming negative between 1 and 2 at.% Mo. Importantly for later discussion, the magnitude of the lattice misfit of the 0 and 5 at.% Mo alloys were approximately the same, at ~0.15%. The experimental diffraction data indicated that the two phases had much more similar lattice parameters than those predicted using the Thermo-Calc-based method. At this point it must be noted that neutron diffraction measured the constrained lattice parameters, whereas Thermo-Calc predicted the unconstrained values. However, this

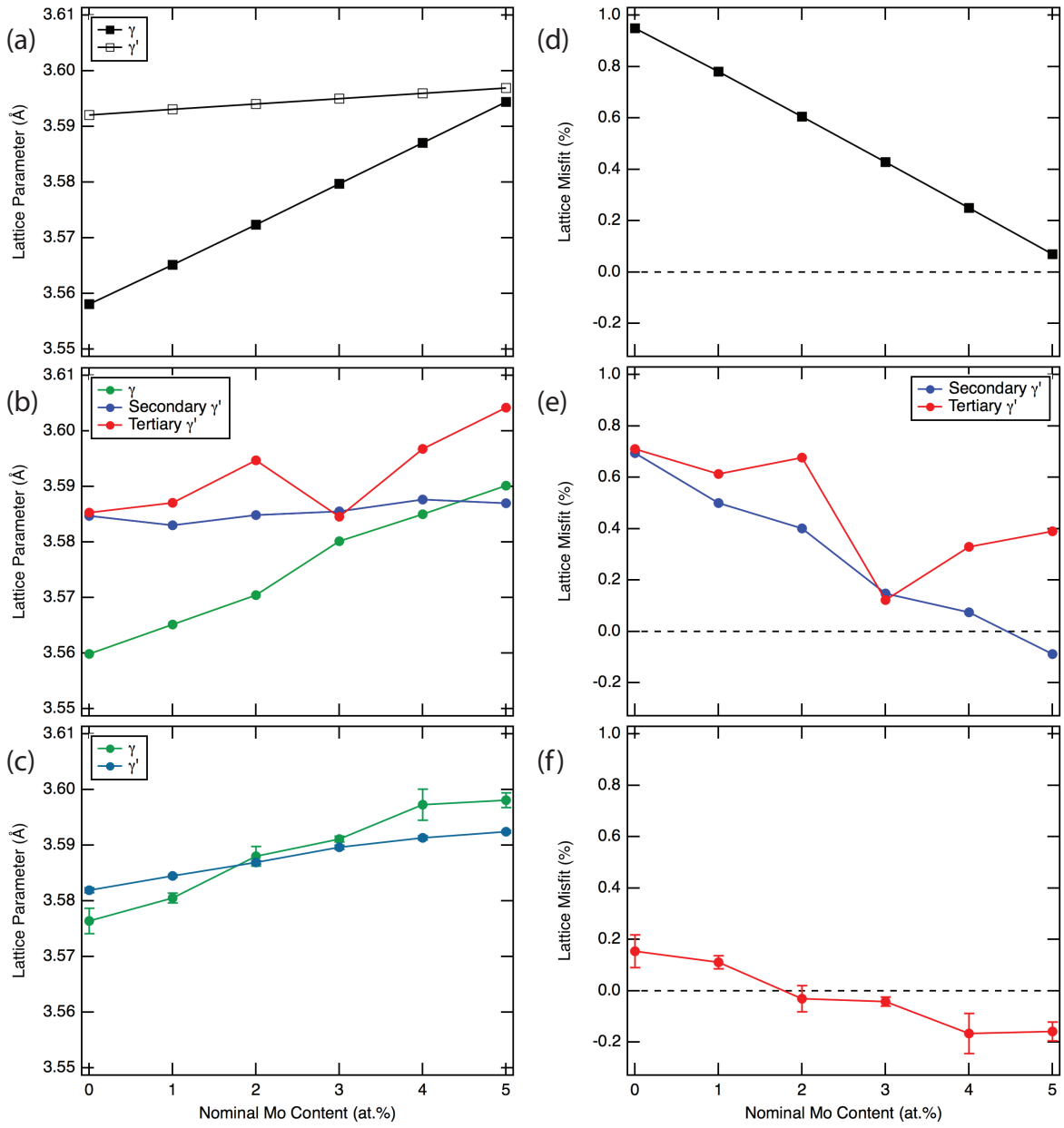

Figure 5.3: Lattice parameters (a) and lattice misfit (d) predicted by Thermo-Calc using the equilibrium phase compositions with the TCNi7 database. Lattice parameters (b) and lattice misfit (e) predicted by Thermo-Calc using the experimental phase compositions with the TCNi7 database. Experimental lattice parameters (c) and lattice misfit (f) determined by neutron diffraction. All given as a function of nominal Mo content.

cannot fully explain the results, since the lattice misfit of the 5 at% Mo alloy is relatively well predicted by Thermo-Calc (when comparing Thermo-Calc predictions using the secondary γ' composition).

The changing Mo content across the alloy series resulted in a decreasing lattice misfit, which influences the yield strength through coherency strengthening. The effect of the experimentally determined lattice misfit on the overall yield strength is shown in Figure 5.4. As seen in Equations 2.43 and 3.15, the coherency strengthening increment is anticipated to be proportional to the magnitude of the lattice misfit to the power of 3/2. Hence, the predicted coherency strength increment (Figure 5.4) is largest for the low and high Mo content alloys, where the lattice misfit has the largest magnitude (Figure 5.3). Similarly, the very low lattice misfits of the alloys with 2 and 3 at.% Mo result in negligible coherency strengthening. The maximum coherency strengthening contribution was predicted to be ~300 MPa in the alloys studied. As discussed in Chapter 3, the maximum coherency strengthening is capped at the value of the solid solution strength of the γ phase. In the present model alloy series, this cap reduced the coherency strengthening of the 0, 1, 4 and 5 at.% Mo alloys. The negligible strengthening effect from the very low lattice misfit alloys of the series (2 and 3 at.% Mo) did not reach the limiting strength of the γ phase.

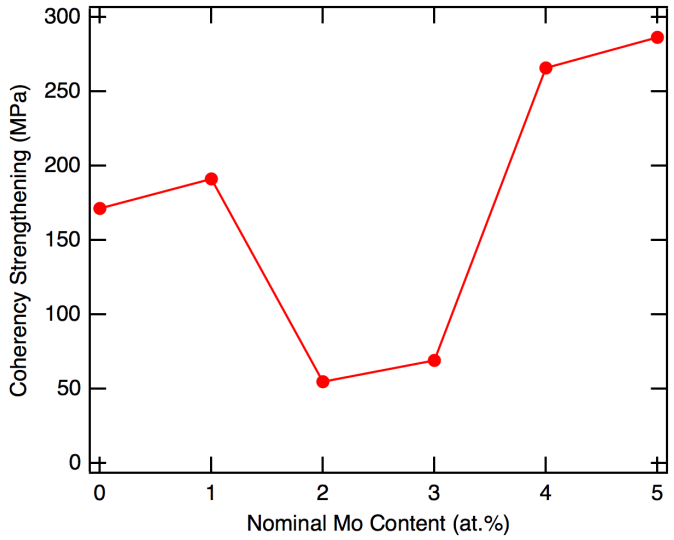

Figure 5.4: The extent of coherency strengthening determined from the experimentally measured lattice parameters, as a function of Mo content.

Precipitation Strengthening

The Anti-Phase Boundary Energies (APBEs) that were obtained using the experimental phase compositions of the alloys are shown in Figure 5.5, as a function of the nominal bulk Mo content of the alloy series. Using both the CalPhaD and DFT approaches for relating the experimental γ' compositions to the APBE, the APBE of the secondary γ' was determined to remain approximately constant as the nominal Mo content of the alloy was increased, although the two approaches yielded slightly different values. With CalPhaD, an APBE of ~310 mJ m^{-2} was obtained for the secondary γ', compared to ~290 mJ m^{-2} using DFT.

The APBE of the tertiary γ' was calculated to be lower than that of the secondary γ'. Using the CalPhaD approach, the APBE decreased from 240 ± 5 mJ m^{-2} to 172 ± 5 mJ m^{-2} on the {111} planes as the nominal bulk Mo content was increased from 0 to 5 at.%, whereas with the DFT approach it was calculated to decrease from ~260 mJ m^{-2} to ~250 mJ m^{-2}. These variations correspond to an experimental Mo increase in the secondary γ' of 0 to 3.6 ± 0.9 at.%Mo. Although the trends in APBE with nominal

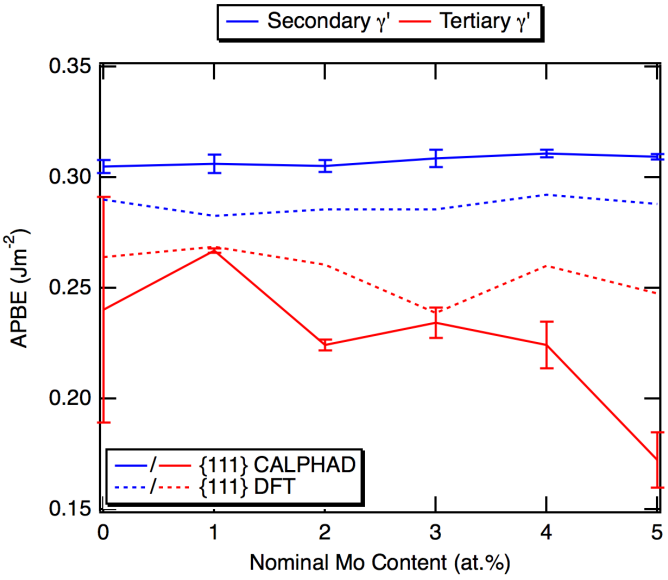

Figure 5.5: The predicted APBEs on the {111} planes of the secondary and tertiary γ' as a function of the nominal bulk Mo content of the alloys. Predictions using a CalPhaD approach are given as solid lines, whilst dashed lines represent the DFT approach.

bulk Mo content using both approximations were in agreement, the CalPhaD approach suggested greater effects from variations in Mo and Cr.

The error associated with the calculated APBEs were determined from the errors associated with the experimentally-measured γ' compositions. The maximum content of those elements seen to increase the APBE (Al, Ti and Mo), and the minimum content of those which decrease the APBE (Cr) was selected, and the corresponding maximum value of the APBE possible from the compositional range was determined. The difference between this maximum APBE and the calculated APBE was taken as the uncertainty in the APBE, caused by the uncertainty in the experimental measurement of γ' composition.

The effect of the APBE on the overall alloy yield strength arising from precipitate hardening is shown in Figure 5.6, in which calculations for APBE by both CalPhaD and DFT methods are shown. The extent of precipitation strengthening from the secondary γ' phase was predicted to be almost exactly the same by both methods (and therefore indistinguishable in Figure 5.6), since the predicted APBEs were very similar. However, CalPhaD and DFT approximations of the APBE gave different results for the extent of precipitation strengthening by the tertiary γ' phase. Increasing bulk Mo content was seen to decrease the extent of precipitation strengthening, although there is an anomalously high value for the 2 at.%Mo alloy. The trend with nominal alloy Mo content was less pronounced using the DFT method. It is worth noting that the extent of precipitation strengthening by the tertiary γ' in these alloys is an order of magnitude greater than that of the secondary γ', even though the volume fraction is only 5%, compared to ∼40% for the secondary γ'.

Yield Strength

The effect of nominal Mo content on the experimental compressive strength of the alloys with varying Mo content is shown in Figure 5.7. Increasing the nominal Mo content from 0 to 5 at.% raised the 0.2% compressive proof stress from 710 ± 30 MPa to 840 ± 20 MPa. Increasing temperature from room temperature to 800°C reduced the yield strength by an approximately constant amount, independent of Mo content. An approximately similar (∼100 MPa) decrease in yield strength was found when the

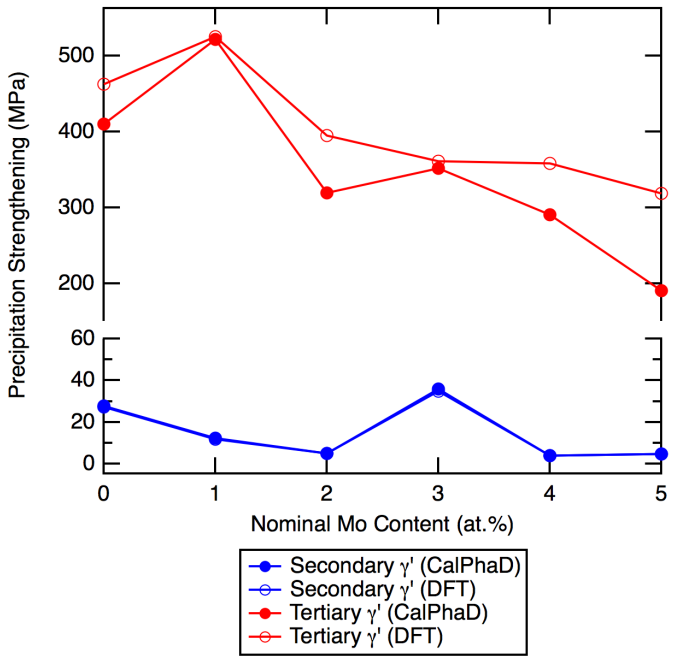

Figure 5.6: The extent of precipitation strengthening arising from the secondary and tertiary γ' precipitates as a function of nominal bulk Mo content. Predictions using the CalPhaD approach are given as closed circles, whilst DFT predictions are given as open circles.

temperature was increased from room temperature to 700°C and from 700°C to 800°C.

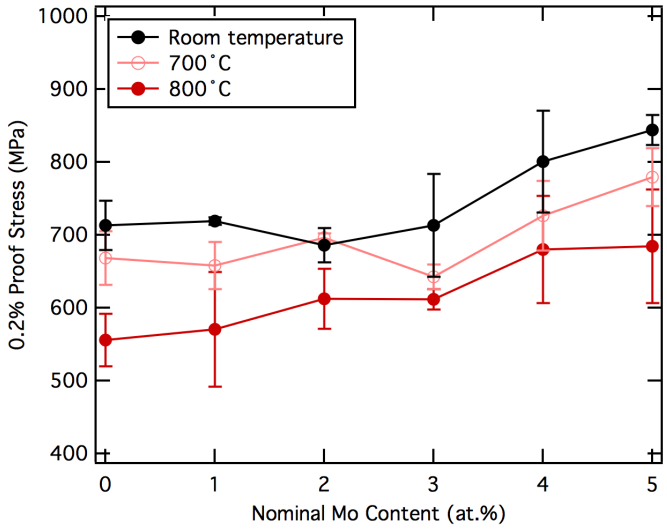

Figure 5.7: Experimental 0.2% proof stress at room temperature, 700°C and 800°C as a function of the nominal Mo content of the alloy.

The overall modelled yield strength as a function of nominal Mo content is shown in Figure 5.8, in addition to a breakdown of the contributions from the individual strengthening mechanisms. The experimental room temperature compressive strength is also shown for comparison. Figure 5.8a gives the model predictions obtained using the CalPhaD approach for the APBE calculations, whereas Figure 5.8b uses the DFT approach. It is seen that by using a CalPhaD-based approach, the experimental yield strength is well predicted, except for the anomalously high strength predicted for the 2 at.%Mo alloy. Using a DFT-based approach, the yield strength is overpredicted by ~200 MPa for the high lattice misfit alloys, although the fit to experiment is much improved for the low lattice misfit alloys (2 and 3 at.%Mo).

Using both methods to calculate the APBE, the overall yield strength followed the experimental fluctuations relatively well, with a drop in the yield strength of the alloys at intermediate Mo contents, and higher yield strengths found for the very low and high Mo contents, although experimentally this drop was much less pronounced. However, the 2 at.%Mo alloy was predicted to have an anomalously high yield strength due to a peak in precipitation strengthening. The more extreme trend in decreasing precipitation strength seen using the CalPhaD-based approach suggests that the influence of Mo and Cr on the APBE is more pronounced than when the APBE is predicted using the DFT-based approach.

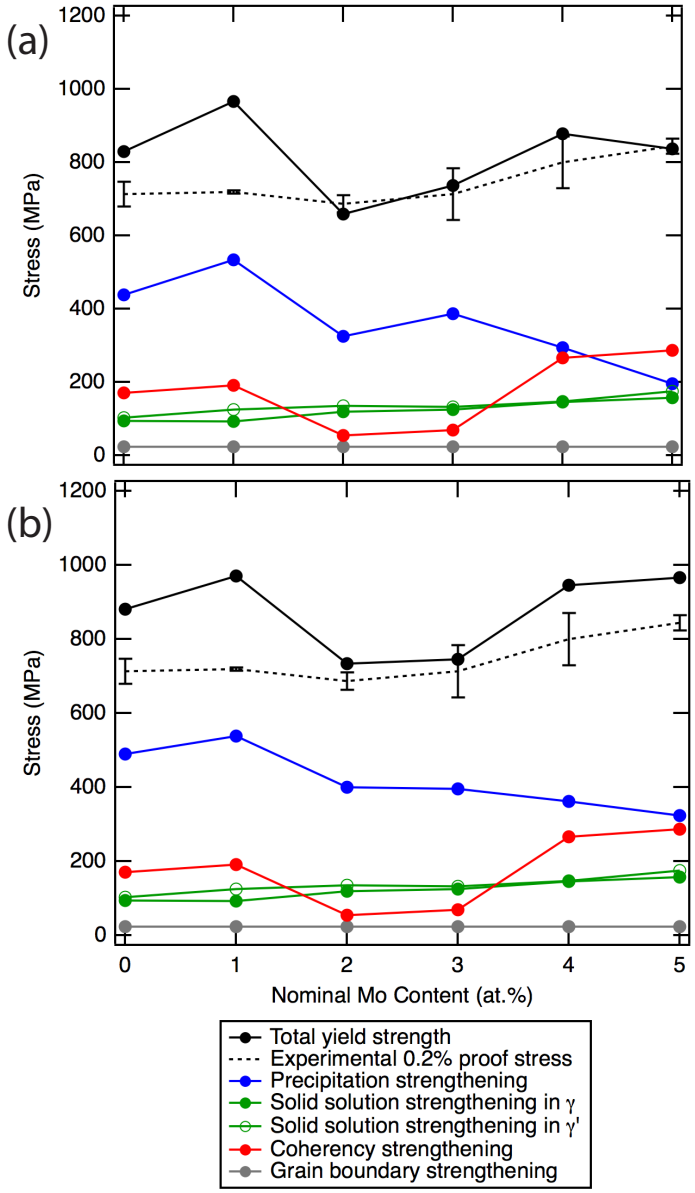

Figure 5.8: Predicted yield strength contributions as a function of bulk Mo content, with the experimental 0.2% compressive proof stress shown, with the inputted APBE calculated using a CalPhaD-based approach (a) and a DFT-based approach (b).

The extent of solid solution strengthening in the γ matrix phase increases with nominal Mo content. Notably, so does that of the γ' precipitate phase. The contribution of coherency strengthening does not vary linearly (Figure 5.4). The role of grain boundary strengthening in the alloy series studied is negligible, due to the very large grain size present in the microstructures.

5.4 Discussion

Comparison of the experimental and modelled phase compositions indicate that Thermo-Calc was capable of accurately predicting the composition of the γ matrix phase and suitably predicted the content of the γ-partitioning elements of the secondary γ' phase. However, it could not be used as a tool for reliable prediction of the Ti content of the precipitate phases, and most clearly, was unable to predict the composition of the tertiary γ'. This limitation is to be expected, since tertiary γ' precipitates form during cooling and as such, there is limited opportunity for solute exchange to occur via diffusion between the phases present [21]. This results in a composition of the secondary γ' that is closer to the expected values for equilibrium. However, it should be noted that the non-equilibrium compositions of the tertiary γ' may be retained during high temperature exposure for many hundreds of hours (Chapter 4).

Increasing the bulk Mo content was seen to have little to no effect on the partitioning of the Al, Ti or Cr within the matrix phase (Figure 5.2a). The same can be said for the Ti content of the secondary and tertiary γ' precipitates (Figures 5.2b and c). However, it is clear that the increasing bulk Mo content across the alloy series did have an effect on the partitioning of Cr in the secondary γ', with a higher Mo content reducing the Cr content. However, it is difficult to ascribe a trend to the Cr content in the tertiary γ' due to larger scatter in the experimental data.

The composition of each phase directly affects the extent of solid solution strengthening. Table 2.4 shows that Mo is the most potent solid solution strengthener in the γ' precipitate phase [67] and that Ti and Mo additions have the largest effect on solid solution strengthening in the γ matrix phase [65]. These effects are evident in Figures 5.2d-f. It can be seen that the Ti content actually had the largest contribution to solid solution strengthening in the secondary γ' phase, since the contents of the other potent strengtheners in this phase were very low. In contrast, although it is the most potent solid solution strengthener in the γ phase, Ti had very little effect due to its low concentration in the matrix. Instead, Cr provided the most significant strengthening contribution. As expected, in the γ matrix, the solid solution strengthening of Mo increased with its nominal content in the alloy, becoming the most potent strengthener in the 4 and 5 at.% Mo alloys. A very similar trend was visible in the tertiary γ' phase. The magnitude of the total solid solution strengthening in the γ and tertiary γ' phases increased with nominal Mo content across the alloy series, although the contribution of the secondary γ' was approximately constant.

The largest strengthening effect is shown to arise through precipitation strengthening, for which the presence of Mo in these alloys is significant. Mo is classically expected to partition to the matrix phase and therefore have a minimal effect on the APBE of the γ'. In this work, however, it was shown that the tertiary γ' had a substantial Mo content, with a resulting decrease in the APBE. Consequently, there was a decrease in the predicted precipitation strengthening of these alloys (Figures 5.6 and 5.8). This was more significant when using the CalPhaD method for APBE determination, than when using the DFT approach.

Importantly, the extent of precipitation strengthening from the tertiary γ' was an order of magnitude larger than that from the secondary γ' (Figure 5.6). The transition between weak- and strong-pair coupling in the alloy series was found to occur at precipitate sizes between 16 and 29 nm, depending on the APBE of the alloy (and via which method the APBE was calculated). Therefore the more significant strengthening arising from the tertiary γ' is due to their size being closer than that of the secondary γ' to the optimum for precipitate shearing resistance. It is seen in Equation 3.6, that the number density, rather than the volume fraction of γ', is the important parameter affecting the extent of precipitation strengthening in the present model. This is rationalised by the fact that strengthening arises from the additional stress required for a dislocation to enter a precipitate, and so a larger number of precipitate interfaces would result in a higher strength, rather than fewer large precipitates. Therefore, the secondary

γ' precipitates offer less resistance to dislocation motion and provide a smaller contribution to the overall alloy strength.

The APBEs shown in Figure 5.5 were calculated using the experimental phase compositions of each alloy, in which the content of each element varies (except Al, which was kept at a constant average value of the APT data). To determine the effect of the Mo content alone, the APBE was again estimated with the experimental Mo content, but with an average constant value for the content of Al, Ti and Cr (Figure 5.9). This also resulted in a decreasing APBE as the nominal (and experimental) Mo content was increased. It is therefore clear that Mo additions have the effect of reducing the APBE in these alloys. This has been shown previously [113] using both the CalPhaD and DFT methods.

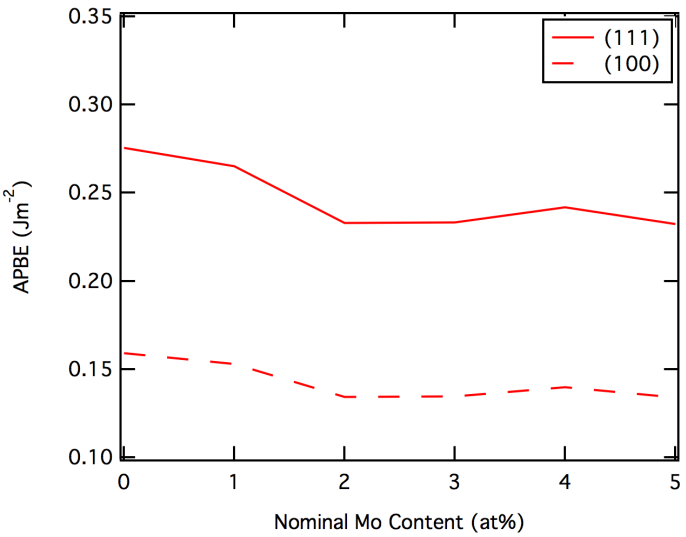

Figure 5.9: The APBE as a function of Mo content, with Al, Ti and Cr content kept constant.

Using both the CalPhaD- and DFT-based methods to calculate the APBE from the experimental phase compositions resulted in a non-linear overall predicted yield strength variation with Mo content. These were more pronounced than seen experimentally (Figure 5.7), which showed a clear rise as the nominal Mo content was increased. In both cases, the extent of precipitation strengthening was clearly shown to decrease as nominal alloy Mo content increased. The anomalously high extent of precipitation strengthening in the 2 at.%Mo alloy is rationalised by noting that the corresponding APBE is also anomalously high. This in turn is caused by phase composition - notably the lower Cr and Mo content in the alloy.

In terms of coherency strengthening, the smallest strengthening contribution was seen for the 2 and 3 at.% Mo alloys (Figure 5.4), in which the magnitude of the experimentally measured lattice misfit was a minimum (Figure 5.3). The magnitude of the experimentally measured lattice misfit, and therefore the coherency strengthening, was similar for the 0 and 5 at% Mo alloys, although the low Mo alloys displayed a positive misfit and the high Mo alloys showed a negative misfit. This gives rise to a non-linear coherency strengthening effect across the alloy series. The larger extent of coherency strengthening in the 5 at.%Mo alloy compared to the 0 at.%Mo alloy, even though both have similar magnitude of lattice misfit, arises due to the higher solid solution strength of the γ matrix phase in the high Mo case.

The trends in the lattice misfit between the γ matrix and the secondary γ' predicted with Thermo-Calc using the experimentally measured phase compositions (Figure 5.3e) were in better agreement with the experimentally determined misfits (Figure 5.3f) than those predicted using the tertiary γ' composition (Figure 5.3e). Evidently, misfit decreased with increasing Mo content of the alloy. The predicted misfit in the tertiary γ' also decreased up to 3 and 4 at.% Mo alloys. This could be attributed to the higher

Mo content within the tertiary γ' phase in these alloys. These results indicate that the assumption of modelling the coherency strengthening as arising from only the secondary γ' precipitates (Equations 2.43 and 3.15) gives consistent results to the experimental variations of the total lattice misfit. The non-linear predicted contribution to the yield stress from coherency strengthening is also evident experimentally. No other mechanism was non-linearly dependant on bulk Mo content, thereby providing evidence that this coherency strengthening trend must be authentic.

The increasing yield stress cannot be attributed to differences in the volume fraction of the γ' precipitates as there was no significant trend in the volume fraction of secondary γ' with nominal alloy Mo content, which was approximately constant around 40%. The only contribution to strength that increased across the alloy series was that of solid solution strengthening. In this regard, it should be noted that the solid solution strengthening of the ordered γ' precipitate phase is as significant as that of the matrix phase. This result is not prevalent in the literature. Without the solid solution strengthening effect of the γ' precipitate phase, the yield strength predictions would be significantly divergent from the experimental results. The increased strength ($\sim$150 MPa in the nominally 5 at.% Mo alloy) can therefore be attributed to the significantly increased solid solution strengthening caused by the presence of Mo in the tertiary γ' precipitate phase. To the author's knowledge, this is the first time that such effects have been reported and predicted in superalloys with varying Mo additions.

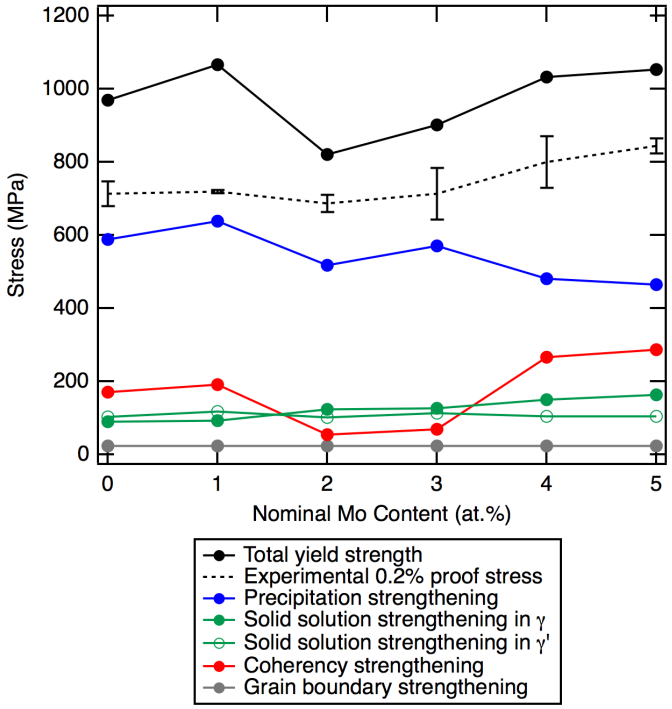

Figure 5.10: Contributions to the total yield strength using a DFT approach to APBE calculation, using the equilibrium phase compositions predicted by Thermo-Calc with the TCNi7 database.

To demonstrate the significance of this effect, Figure 5.10 was plotted showing the model predictions for each strengthening component, using the equilibrium phase compositions determined by Thermo-Calc. The DFT model was used to calculate the APBE from the equilibrium phase composition, and therefore the extent of precipitation strengthening. All other factors, such as precipitate size and volume fraction, were consistent with the previous data (Figure 5.8). It is clearly evident that by approximating phase compositions to those at equilibrium (Thermo-Calc), the experimental yield strength is less accurately reproduced than when using experimentally-measured phase compositions. Notably, the contribution from precipitation strengthening is much greater using the predicted equilibrium compositions than those

determined experimentally. This disparity is most marked for the alloys containing the highest Mo concentrations, where the extent of precipitation strengthening differs by ∼200 MPa between these two techniques. In addition, the contribution from solid solution strengthening of the γ' precipitate phase is lower with calculations based on the predicted equilibrium phase composition, which remained constant across the alloy series. Since the equilibrium predictions for the composition of the γ phase were similar to those found experimentally, the extent of solid solution strengthening in the matrix phase is consistent using both experimental and modelled compositions.

Overall, approximating the phase compositions to those predicted at equilibrium resulted in much higher yield strengths for all alloys studied and these are not representative of the actual alloy behaviour. The yield strength is well predicted using the experimental phase composition data, due to the solid solution strengthening of the ordered γ' precipitate phase, and the decreasing degree of precipitation strengthening as the Mo content of the γ' phase is increased.

5.5 Conclusions

The yield strengths of a series of model polycrystalline Ni-based superalloys with varying Mo content have been predicted using current models available in the literature. Using a CalPhaD approach for calculating the APBE from the experimentally measured phase compositions, the alloy strength was predicted to be reduced in the lowest lattice misfit alloys. This is more pronounced than that measured experimentally, which generally increased with bulk Mo content. The magnitude of experimental yield strength is well predicted by the models used in the present work. Of all the hardening mechanisms present, that of precipitation strengthening resulted in the largest contribution to alloy strength, and this decreased in the tertiary γ' phase with bulk addition of Mo. This is caused by a decreasing APBE with increasing Mo content. The effect of solid solution strengthening in the γ matrix phase was significant, giving up to ∼300 MPa additional strength. However, notably the solid solution strengthening effect of the ordered γ' phase was also substantial and equivalent to that of the matrix phase. Evidently, the effect of solid solution strengthening in the ordered phase must be taken into account when modelling the mechanical properties of Ni-based superalloys. Without this strengthening mechanism, the yield strength of Ni-based superalloys cannot be accurately predicted.

Chapter 6

In-Situ Neutron Diffraction of Model Alloys

6.1 Introduction

As discussed in Chapters 3 to 5, a full understanding of the links between bulk alloy composition, phase composition and lattice misfit, and how this may vary between room temperature and service temperature, is paramount for the effective optimisation of alloy properties such as yield strength. Chapter 3 introduced current strengthening models and the role of composition and microstructural parameters on yield strength. Chapters 4 and 5 looked at these models in more detail using a model series of quinary Ni-based superalloys that were extensively characterised to ensure accurate input data for the models.

The alloy series contained varying Mo content in order to try to elucidate the effect of the individual strengthening mechanisms, as introduced in Chapter 3. Mo is a key alloying element in Ni-based superalloys, and is mainly added to improve the solid solution strength of the γ matrix phase [204, 206] and to increase the tendency for carbide and boride formation [18, 19], which is beneficial in grain refinement and to improvements in mechanical properties. However, an excess of Mo promotes the formation of deleterious topologically close packed (TCP) phases [207, 208], which may lead to embrittlement. Similarly, the segregation of various elements at the grain boundaries has been shown to be influenced by Mo content; additions less than 6.7 wt.% have been shown to reduce elemental segregation to grain boundaries, whilst an excess of this amount promotes segregation [209]. It has also been shown that Mo additions slow γ' coarsening and increase alloy hardness [210] by reducing lattice misfit and diffusion [18].

In addition to the accepted improvement in solid solution strengthening, alloying additions such as Mo, with large atomic radius and strong phase partitioning, will affect the lattice misfit and consequently the mechanical properties [133]. Mo has been shown to partition strongly to the γ phase in a number of Ni-based superalloys [211], and as a result, causes a reduction in the lattice misfit of positively misfitting alloys [18]. Addition of Mo to reduce the lattice misfit has previously been shown to benefit creep rupture life [212] by supporting larger γ/γ' interfacial dislocation networks and by lowering stacking fault energy [213]. The lattice misfit of Ni-superalloys is of significant importance, both for the minimisation of precipitate coarsening during service, and for alloy strength.

In order to further investigate the link between microstructure and yield strength, this chapter elucidates the role of lattice misfit on the deformation behaviour of the series of polycrystalline model Ni-based superalloys previously introduced (Chapter 4). The variation of the lattice misfits of the alloys with temperature was determined and the load partitioning between grain orientations and between the γ and γ' phases was investigated through in-situ compression testing. The results demonstrate that there is a

change in deformation behaviour during loading, with load initially partitioned between grain orientations, and then between the γ and γ' phases after higher loading. The magnitude of the lattice misfit was shown to affect deformation behaviour in a complex manner due to the concurrent effects of individual phase strength.

6.2 Methods

In this chapter, neutron diffraction has been used to determine the lattice parameters of the γ and γ' phases, and the resulting lattice misfit of the series of model superalloys introduced in Chapter 4 with varying Mo content. Data were acquired between room temperature and 700°C to deduce the temperature dependence.

Larger ingots of the model alloys suitable for mechanical testing were fabricated using the methods detailed in Chapter 4. In summary, the alloys were produced by vacuum induction melting at Imperial College London from elements of ≥99.9% purity, after which they were homogenised at 1250°C for 22 hours in Ar-backfilled glass ampoules. Following the same method as detailed in Chapter 4, the experimentally-determined average bulk alloy compositions are given in Table 6.1. In contrast to the alloys described in Chapter 4, each alloy was subsequently hot rolled at Imperial College London at 1250°C (above the γ' solvus temperature, Figure 4.2) to reduce the grain size. An example SEM image of the resulting grain structure is shown in Figure 6.1 for the 3 at.% Mo alloy. The roll speed was 22 Hz (11 rpm) and a strain of 15% was inputted on each pass, increasing on the final passes in order to reach the required final strain (∼17%). On average, the alloys underwent 7 passes to reach the final thickness, and between passes each alloy was put back into the furnace for approximately 2 minutes to re-heat back to the required rolling temperature.

Alloy (at.% Mo)	Al	Ti	Cr	Mo	Ni
0	5.42 ± 0.1	5.12 ± 0.06	14.18 ± 0.07	0	75.29 ± 0.1
1	5.19 ± 0.1	4.97 ± 0.08	13.66 ± 0.06	0.73 ± 0.02	75.45 ± 0.07
2	5.54 ± 0.09	5.27 ± 0.04	14.52 ± 0.1	1.72 ± 0.02	72.94 ± 0.1
3	4.99 ± 0.2	5.06 ± 0.05	14.05 ± 0.1	2.58 ± 0.04	73.33 ± 0.1
4	4.85 ± 0.1	4.52 ± 0.1	12.82 ± 0.09	3.13 ± 0.07	74.68 ± 0.2
5	5.24 ± 0.06	5.02 ± 0.05	14.26 ± 0.1	4.48 ± 0.04	71.00 ± 0.1

Table 6.1: Average bulk composition of each of the model alloys, as determined experimentally by SEM EDX.

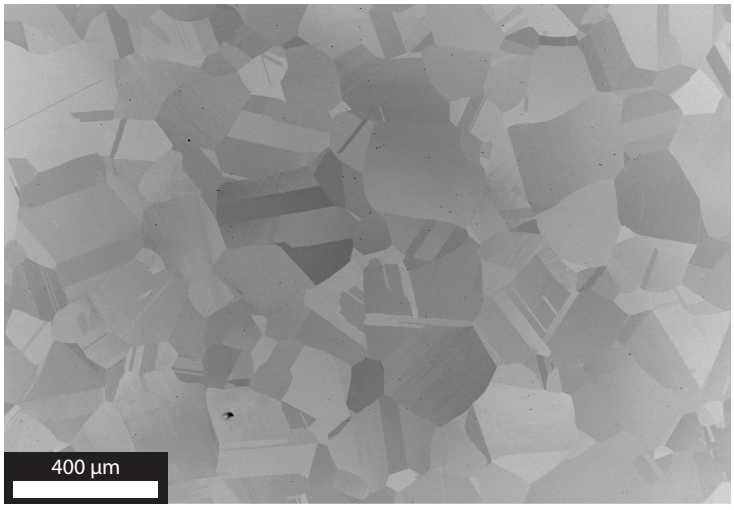

Figure 6.1: SEM image of the 3 at.% Mo alloy after hot rolling.

Cylindrical specimens of length 8 mm and diameter 5 mm were electro-discharge machined from the hot rolled bars for in situ neutron diffraction during compression testing. After machining, each sample was aged at 760°C for 16 hours and the alloys were air cooled to room temperature.

Carbon replica samples were produced for microstructural analysis, full details of these methods may be found in Chapter 4. Analysis of precipitate size and composition was carried out using Scanning Transmission Electron Microscopy (STEM) on an FEI Tecnai Osiris TEM operated using at 200 keV. An FEI Super-X EDX detector on the same instrument was used to obtain compositional information via Energy-Dispersive X-ray Spectroscopy (EDX).

Neutron diffraction was carried out at the ISIS neutron and muon source, Rutherford Appleton Laboratory, UK, on the ENGIN-X instrument [214]. Each sample was initially held at a load of 50 MPa before the stress was increased in 100 MPa increments to 600 MPa in load control. At each step, the load was held for ∼20 minutes to allow for neutron diffraction data collection. The scattering vector was orientated along the length of the sample. After 600 MPa load, the loading rig was changed to position control and the strain increased in increments up to ∼10% before switching back to load control and unloading to 50 MPa. All loading data were acquired at room temperature to avoid stress relaxation during testing. In addition to room temperature measurement, an optical furnace was used to heat the samples in air to 400°C, 600°C and 700°C, with each sample held at 50 MPa load for neutron collection. Sample temperature was measured and controlled using a K-type thermocouple in contact with the samples. The experimental set-up is shown in Figure 6.2, and full details of this setup are found in [215]. Due to time constraints, loading data could not be acquired for the 2 at.% Mo alloy.

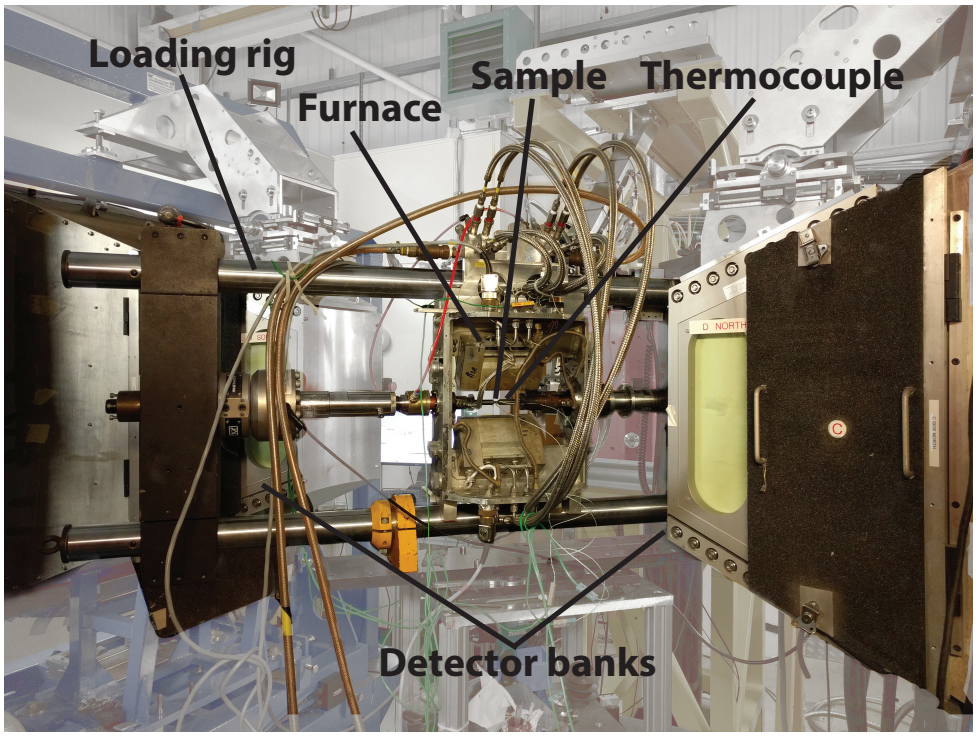

Figure 6.2: Experimental setup of ENGIN-X used in the present work.

To determine the lattice parameters of the γ and γ' phases, GSAS software [216] was used to fit each full spectrum using a Le-Bail method [217], with each peak fitted using a convolution of two back-to-back exponentials and a pseudo-Voigt (an example of a diffraction pattern with full pattern fit and residual is shown in Figure 6.3), to take into account the source effect of neutrons slowed down by the moderator in spallation sources such as at ENGIN-X. Although both the γ and γ' phase are cubic, the disordered γ matrix phase is FCC and only those planes with h, k and l all odd or all even are present. In contrast,

the ordered nature of the γ' precipitate phase leads to additional superlattice reflections. Due to the very similar lattice parameters and crystal structures of the γ and γ' phases, individual peaks are often overlapping and indistinguishable. This has led to previous authors fitting the superlattice peaks from the γ' structure first, then fixing the associated γ' peaks in the fundamental peaks and subsequently fitting the γ peaks [218–220]. In the present study, however, fitting the γ and γ' peaks separately or fitting the full pattern together resulted in negligible difference in the calculated lattice parameters. Therefore the full pattern was fitted when determining the unloaded (50 MPa) lattice parameters, with fundamental peaks consisting of one peak from the γ phase and one from the γ' phase.

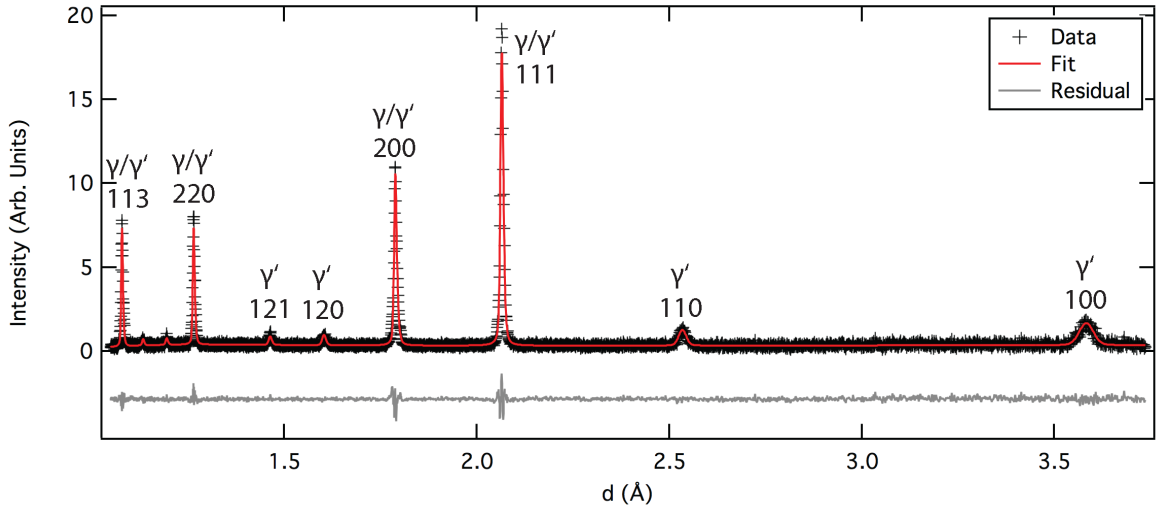

Figure 6.3: Diffraction pattern of the 3 at% Mo alloy, obtained at room temperature using time of flight neutron diffraction, with indexed peaks, the full pattern fit obtained using GSAS, and the associated residual.

Analysis of the diffraction data during loading was carried out by fitting individual peaks using Igor Pro software (WaveMetrics, Lake Oswego, OR, USA). The method described above was used for peak fitting in the present study, with the superlattice peak positions determined by fitting with a single Gaussian convoluted with an exponential function, as detailed in [221], as rationalised above. The γ' peak position in the corresponding fundamental peak was then fixed whilst the γ peak position was found, by fitting with two peak functions. Additionally, to determine the phase average deformation behaviour, each fundamental peak was fitted as a single function, even though each peak is composed of two components (from the γ and γ' phases). These methods are displayed in Figure 6.4 for the 200 peak of the 0 at.% Mo alloy. This alloy has the largest lattice misfit (as expected from Figure 4.16) and therefore the greatest peak separation. However, it is clearly seen that the two peaks cannot be resolved. At zero applied load, the peak may be fitted as a single peak (Figure 6.4a) or as two separate peaks from the γ and γ' phases (Figure 6.4b). At maximum applied load the same method is applied (Figure 6.4c and d respectively). It is evident on comparison of these fitting methods that double peak fitting results in a closer fit to the data.

Previous studies have concluded that full pattern fitting with a Rietveld refinement enabled determination of the bulk behaviour and was comparable to single peak fitting [222, 223]. However, single peak fitting was preferred in the present study to enable investigation of the orientation-specific grain behaviour.

The load partitioning behaviour of the alloy series was determined via the following method. First, the interplanar spacings (d) for each plane of interest were plotted against bulk applied stress (σ), and the y-intercept taken as the unstrained interplanar spacing (d_0). This value was then used to calculate the elastic lattice strain ($(d - d_0)/d_0$) for each hkl plane of interest, and these data were plotted against

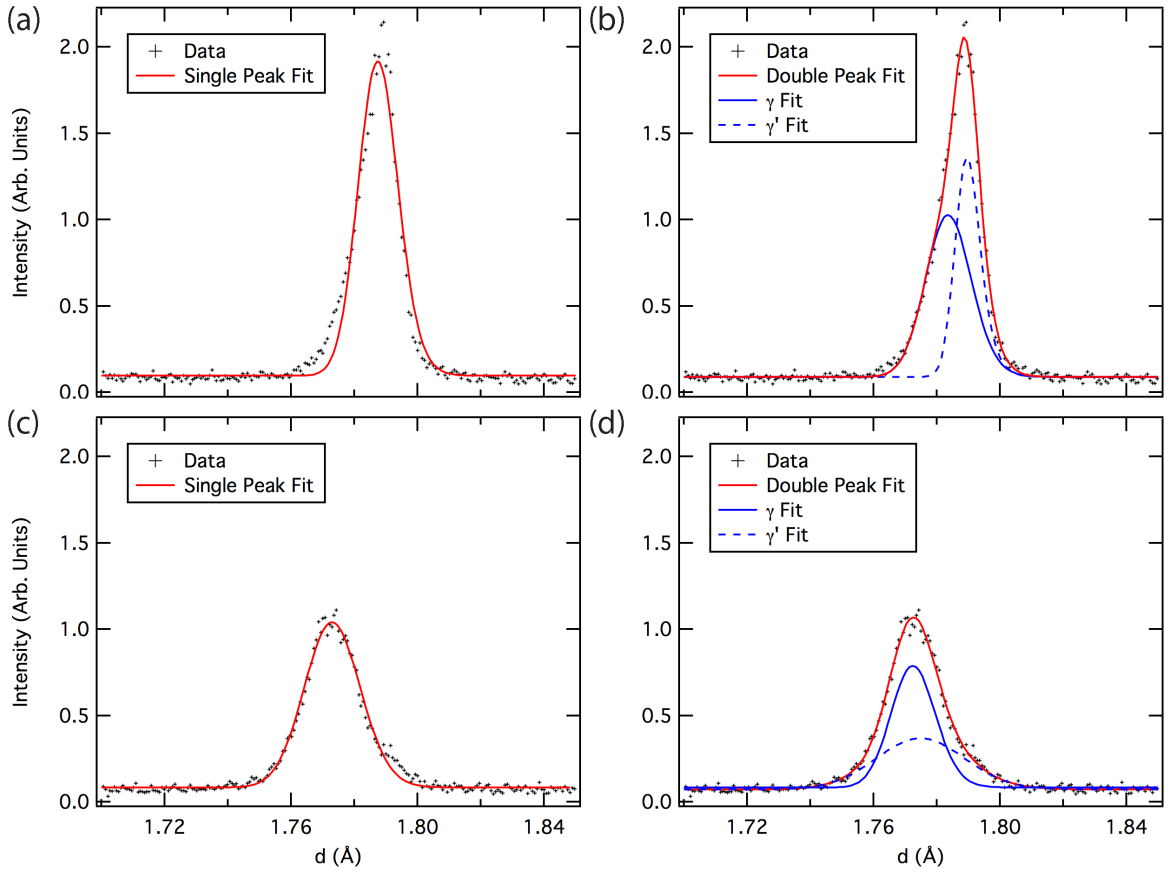

Figure 6.4: The 200 peak of the 0 at% Mo alloy, at zero (a, b) and maximum (c, d) applied load, fitted using a single (a, c) or double (b, d) Gaussian function convoluted with an exponential function.

bulk applied stress. The elastic strain components of these data were subsequently calculated by fitting a straight line with gradient E and y-intercept, c, to these data for each hkl orientation. This enabled calculation of the hkl-specific residual lattice strain ($\varepsilon_{\mathrm{res}}$) using Equation 6.1. The diffraction elastic constants (DECs) of each hkl plane of interest were also noted as the gradient (E) of this linear function fitted to the elastic region on loading.

$$\varepsilon_{\mathrm{res}} = \frac{d - d_0}{d_0} - \frac{\sigma - c}{E} \tag{6.1}$$

Thermodynamic modelling using Thermo-Calc software was carried out to predict the lattice parameters of the model alloys, and to predict the lattice misfit, as described in Chapter 4. The effect of temperature is added in the present chapter. Equilibrium compositions of the matrix and precipitate phases at the ageing temperature of 760°C were determined using the TCNi7 database, with all other phases excluded. Maintaining this composition by turning off global minimisation, the predicted molar volumes (V_{m}) of the γ and γ' phases were calculated as a function of temperature, thereby enabling determination of the lattice parameters using Equation 3.1 and the lattice misfit using Equation 2.4. Global minimisation was turned off to enable calculation of thermal expansion alone, without additional complication arising from compositional changes with temperature, since these equilibrium predictions are unlikely to be achieved in the short ageing times experimentally. It should be noted that the lattice parameters predicted by Thermo-Calc are unconstrained, and little thermodynamic data exists below 600°C and therefore these data are less likely to closely fit experiment.

6.3 Results and Discussion

Lattice Parameters and Lattice Misfits

It should be noted that Ni-based superalloys often contain complex multi-modal precipitate size distributions (large intergranular primary γ' and intragranular secondary and smaller tertiary γ'), which differ in average composition [31]. Although this compositional variation would be expected to result in differing diffraction peak positions, due to the very similar lattice parameters of these distributions and that of the matrix itself, diffraction peaks from individual precipitate size distributions cannot be distinguished and each peak is an averaged combination of these individual reflections. Additionally, the volume fraction of secondary γ' is much larger than that of the tertiary γ' and therefore the tertiary peak intensity is unlikely to be distinguished. As the material investigated in this study was heat-treated in the single phase field, no primary γ' was present on the grain boundaries. Figure 2 shows characteristic intragranular STEM images of each alloy in the series studied. It is evident that most of the alloys showed a unimodal precipitate size distribution and will therefore contain only a single γ' peak, with the exception of the 0 and 2 at.% Mo alloys, which are bimodal with larger secondary and smaller tertiary γ' (Figure 6.5a and c respectively). Since the volume fraction of the tertiary γ' is significantly smaller than that of the secondary γ', the calculated peak positions and lattice parameters will predominantly originate from the secondary γ'.

As seen in Figure 6.5, the γ' precipitates in the alloys with low Mo contents were spherical, becoming progressively more cuboidal as the bulk Mo content was increased. In most alloys, the secondary γ' were of similar size (Table 6.2). However, the 1 at.% Mo alloy contained smaller precipitates than the other alloys and these were closer in size to the tertiary γ' of the 0 at.% Mo alloy. γ' size directly affects alloy hardness and yield strength, with maximum strength obtained at an intermediate particle size reflecting the transition from weak- to strong-pair dislocation coupling [14, 114, 167].

The size of the γ' precipitates is strongly linked to deformation mechanism, with smaller γ' yielding

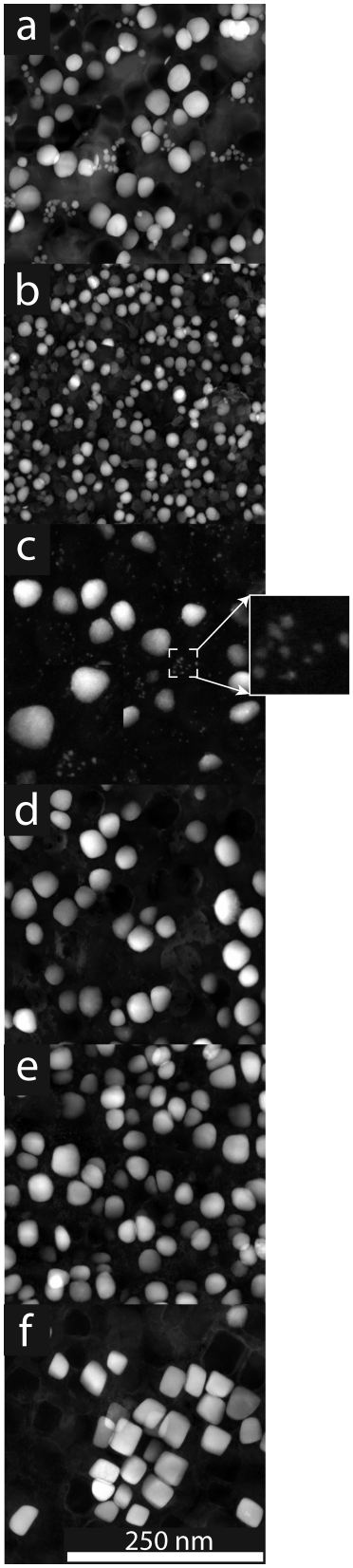

Figure 6.5: STEM micrographs of carbon replica samples of each alloy in the series, with varying Mo content ((a) 0 at% Mo, (b) 1 at% Mo, (c) 2 at% Mo (with inset showing higher magnification of tertiary γ'), (d) 3 at% Mo, (e) 4 at% Mo, and (f) 5 at% Mo,). The 0 at% Mo (a) and 2 at% Mo (c) alloys show bimodal particle size distributions, whereas all other alloys are unimodal.

	Precipitate size (nm)	
Alloy (at.% Mo)	Secondary γ'	Tertiary γ'
0	76 ± 14	20 ± 5
1	41 ± 8	-
2	92 ± 18	12 ± 3
3	89 ± 16	-
4	85 ± 11	-
5	105 ± 18	-

Table 6.2: Average precipitate diameters of the secondary and tertiary γ' in each alloy of the series.

with the γ phase by dislocation cutting, and larger γ' being bypassed by Orowan looping [224, 225]. It has also been found previously that the morphology of γ' is linked to the size and lattice misfit [20], with the sphere-cuboid transition occurring at lower ageing times in alloys with higher lattice misfits. The link between morphology and lattice misfit is understood to be caused by coherency strain, with larger misfits resulting in greater coherency strain and therefore a more facetted precipitate morphology to minimise the internal stored energy. In Chapter 4, the model alloy series was studied in the form of vacuum induction melted bars containing larger γ' precipitates. In agreement with the work of Ricks et al. [20], these larger precipitates are more cuboidal than the small precipitates within the hot rolled bars discussed in the present chapter.

The predicted lattice parameters of the model alloys at thermodynamic equilibrium are shown in Figure 6.6a, as a function of bulk Mo content, at varying temperature between 20°C and 700°C (the room temperature data is as shown in Figure 5.3a and d). These calculations were in agreement with literature [18, 211], with increasing bulk Mo content causing an increase in the lattice parameter of both phases, since Mo has a larger atomic radius than Ni. This increase was much more pronounced in the γ phase than in the γ', since Mo preferentially partitions to the matrix phase. However, Thermo-Calc predicts the equilibrium phase compositions, which are not necessarily obtained in commercial superalloys at short ageing times. As found in Chapters 4 and 5 and in agreement with [206], high Mo contents have been also found in the precipitates, particularly the tertiary γ'. The non-equilibrium composition of the γ' precipitates in this model quinary alloy series is fully described in Chapters 4 and 5 in which it was shown to have implications for the lattice parameters and lattice misfit, and therefore the resulting yield strength.

Increasing temperature was predicted to increase the lattice parameters of both phases, but to a larger extent in the matrix phase. This arises due to the different thermal expansion coefficients of the γ and γ' phases, with the lattice parameter of the disordered γ matrix phase increasing faster with temperature than the ordered γ' phase [226]. Therefore, for the highest Mo contents, although at low temperatures the γ' phase was predicted to have the largest lattice parameter, the γ phase had the largest lattice parameter at high temperatures.

For comparison, experimental results obtained from neutron diffraction are shown in Figure 6.6b. Qualitatively, the trends predicted by Thermo-Calc are seen experimentally, with increasing lattice parameters observed for both phases as both the Mo content and temperature were increased. However, the quantitative values are not well predicted, particularly for the γ' phase, and the lattice parameters of the two phases were found to be much more similar than predicted by Thermo-Calc. These data contradict previous studies, which found that increasing the Mo content had no effect on the γ' lattice parameter, and only resulted in an increase of that of the γ phase [207]. It must be noted that Thermo-Calc predicts the unconstrained lattice parameters, whereas experimentally the two phases are naturally constrained to be closer in lattice parameter. Therefore, Thermo-Calc predictions were not expected to quantitatively match experiment, instead providing a useful comparison to the qualitative trends [133].

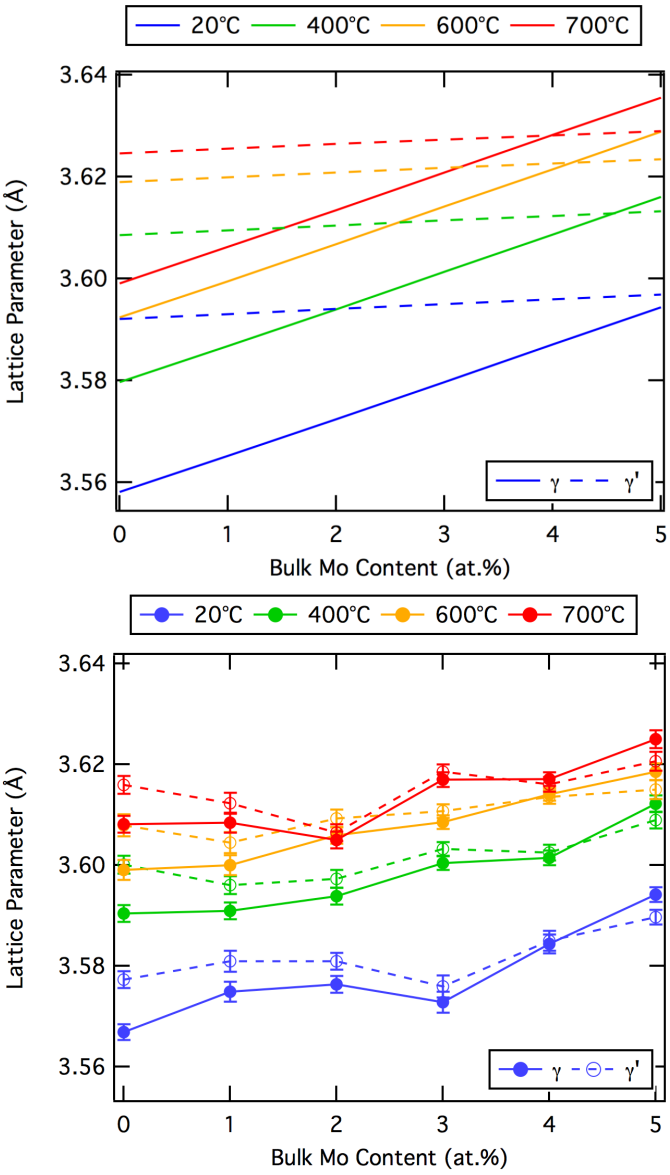

Figure 6.6: Lattice parameter of the γ and γ' phases as a function of bulk Mo content, determined (a) via prediction with Thermo-Calc and (b) experimentally via neutron diffraction.

The link between lattice parameter and temperature is dependent on many factors, such as thermal expansion, elemental partitioning and coherency. These factors all vary with time at temperature. It has previously been found that slower cooling rates result in reduced sphericity of secondary γ' precipitates and an increase in the unconstrained lattice misfit caused by a γ' composition closer to equilibrium [32, 35]. Interestingly, the constrained lattice misfit was only seen to vary slightly with cooling rate due to the formation of complex γ' morphologies with associated compressive strains. A separate study has found that increased ageing time resulted in increased γ' size and increased lattice misfit, whilst a more complex two-stage heat treatment resulted in more complex γ' morphologies and associated lattice misfit dependence [39]. It was concluded that these effects arise due to compositional variations, with faster cooling rates or shorter ageing times resulting in γ' precipitates with compositions further from the predicted equilibrium. The effect of this on the present alloy series is that large atoms such as Mo do not have time to diffuse to the γ phase, in which they preferentially partition. The γ' precipitate phase therefore has a higher Mo content, and larger lattice parameter, as Mo has a large atomic radius.

The experimental results for lattice parameter (Figure 6.6b) included some slight outliers (e.g. the 3 at.% Mo alloy at room temperature, and the 2 and 3 at.% Mo alloys at 700°C). These arose from the inevitable uncertainty in the peak fitting procedure.

Interestingly, the lattice parameter of the γ phase in the 5 at.% Mo alloy is very well predicted by Thermo-Calc. However, that of the γ' is not, and is predicted to be larger than the γ, when in fact experimentally it was found to be smaller. This resulted in a positive predicted lattice misfit (Figure 6.7a) but a negative experimental lattice misfit (Figure 6.7b).

The predicted and experimentally determined lattice misfit of each alloy at varying temperature are shown in Figures 6.7a and b respectively. Predicted trends were reproduced experimentally, whilst the magnitudes differed. The more significant increase in the lattice parameter of the γ phase with Mo content resulted in a decreasing lattice misfit. At room temperature, the lattice misfit was predicted to be positive at all Mo contents, however at higher temperatures the lattice misfit was predicted to become negative for the alloys containing 4 and 5 at.%Mo. The non-equilibrium phase composition of the alloys (Chapters 4 and 5) will affect the experimentally determined lattice parameters. For example, a higher Mo content in the γ' phase will increase the lattice parameter relative to that obtained with equilibrium phase compositions, leading to a larger lattice misfit in positively misfitting alloys and a smaller lattice misfit in negatively misfitting alloys. This is not seen in the present results (Figures 6.7a and b). However, it is believed that the difference in constrained and unconstrained lattice parameters outweigh the compositional effect.

The experimentally derived lattice misfits indicated that alloys containing less than 4 at.% Mo were positively misfitting at all temperatures, whilst the 5 at.% Mo alloy was negatively misfitting at all temperatures. In contrast, the 4 at.% Mo alloy, with the smallest misfit both experimentally and predicted, became negatively misfitting between 400°C and 600°C. For all alloys, the lattice misfit decreased with increasing temperature. In the positively misfitting alloys, this resulted in a lower, positive value of misfit whilst misfit of the negatively misfitting 5 at.% Mo alloy increased.

A noticeable discrepancy between the predicted and experimental lattice misfit is the magnitude of the change with temperature. Thermo-Calc predicted a relatively large and linear change with temperature. In contrast, there was little change between the experimentally measured lattice parameters between room temperature and 400°C, and a much larger decrease between 600°C and 700°C.

The morphological results of the present work is in agreement with previous studies [20], with smaller precipitates tending to be more spherical, and the negatively misfitting 5 at.% Mo alloy being more facetted. Lattice misfit also has important implications on alloy properties, and has been shown to affect yield behaviour in a similar alloy series to the present study [20]. Large negative lattice misfits have been shown to improve creep life [207], whereas smaller misfits have been found to benefit stress

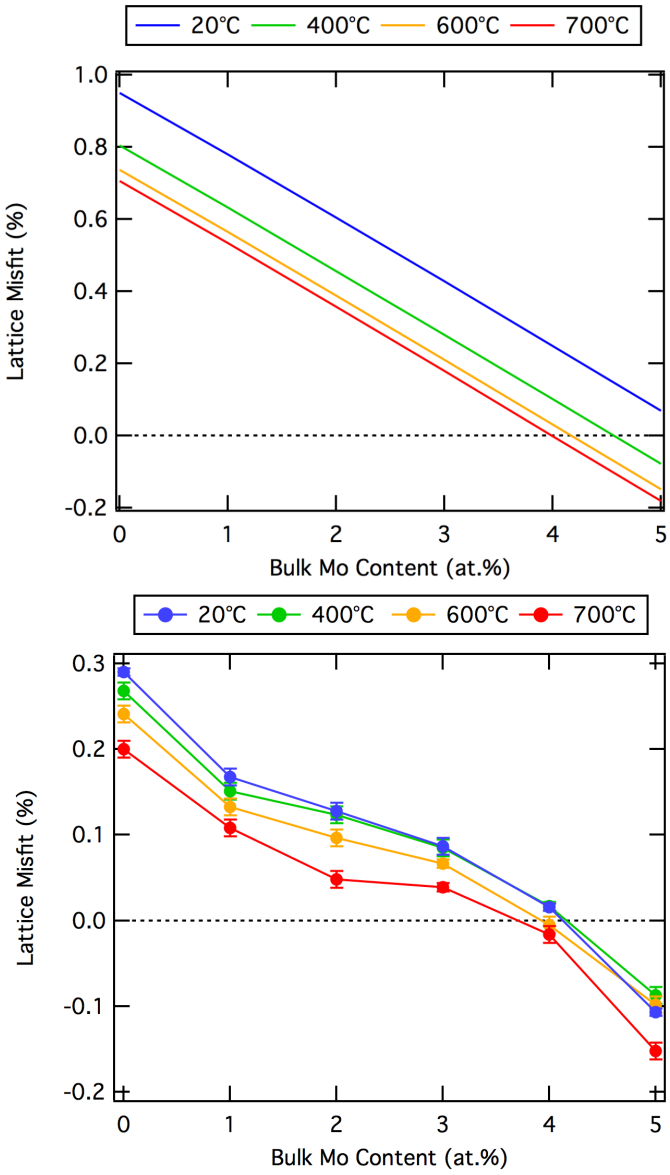

Figure 6.7: Lattice misfit as a function of bulk Mo content, determined (a) via prediction with Thermo-Calc and (b) experimentally via neutron diffraction.

rupture life [212]. It is generally considered desirable for commercial alloys to have a lattice misfit as close to zero as possible, to minimise coarsening at the high temperatures experienced during operation [74]. Misfits near zero have also previously been shown to result in properties unaffected by γ' size [207]. Therefore in this context, in the present model quinary alloy series, the 4 at.% Mo alloy is the most desirable. This Mo content is slightly higher than the 3 at.% Mo found in the commercial alloy RR1000 [147], that is of similar composition to the model alloys in the present study. Other typical commercial alloys, such as Waspaloy, Rene88DT and Udimet720 typically contain Mo contents below 2.5 at.%. However, in contrast, a larger lattice misfit has been previously found to be beneficial to mechanical properties by favouring the creation of a higher dislocation density at the γ/γ' interfaces which impedes the passage of dislocations into the precipitates [79]. However, the effect of Mo content on lattice misfit alone cannot be used in isolation for alloy design, since other factors, for example the propensity for TCP formation must be taken into account.

Load Partitioning

As mentioned previously, the alloy series was selected to elucidate the role of lattice misfit on load partitioning behaviour. The 0 at.% Mo alloy had the largest positive lattice misfit, and this decreased with Mo addition, reaching zero in the 4 at.%Mo alloy and being relatively large and negative in the 5 at.%Mo alloy (Figure 6.7b).

A representative STEM micrograph of each alloy is shown in Figure 6.5 and discussed above. The size distributions of the γ' precipitates in Ni-based superalloys have important implications for the mechanical properties such as yield strength. Classically it has often been concluded that optimum strengthening is achieved with a γ' size corresponding to the transition between strong- and weak- pair dislocation coupling [14,114,167]. However, recent studies have argued that this is an oversimplification [65]. Previous in-situ loading studies have found that the precipitate size affects the loading behaviour in polycrystalline Ni-based superalloys [224, 227], with smaller γ' deforming concurrently with the γ phase, while larger γ' take up more strain as the γ phase deforms plastically. With increasing γ' size, the γ matrix was reported to yield at lower applied stress [227]. These observations were rationalised in terms of initiation of Orowan looping at high stresses in alloys with large particle size, whereas small precipitates deform by dislocation cutting [224]. In the present study, the similar sizes of the secondary γ' in each alloy allowed the effect of precipitate size to be removed from the analysis, and the specific role of composition to be investigated.

Fitting each fundamental peak in the diffraction pattern gives an average measure of the grain behaviour and therefore enables characterisation of the intergranular strain accumulation across the alloy series. The effect of applied stress on the lattice strain on the 111, 200, 220 and 311 planes, fitted as single peak functions for each alloy in the series is shown in Figure 6.8. As expected, the 111 planes were elastically stiffest and the 200 planes were most compliant. This is in agreement with previous studies [228]. However, in contrast, in the present study, the 220 orientations in each alloy had comparable stiffness to the 111 planes. The 311 planes had intermediate elastic stiffness. All alloys in the series followed this same trend, implying that Mo does not have an effect on the elastic anisotropy.

The bulk applied stress at which each individual family of grains yields is dependent on the elastic and plastic anisotropy. Typically, since the stiffness increases from 100 to 110 to the 111 planes, the latter would be expected to yield first if based on an elastic argument alone, since for a particular applied strain, the 111 planes will experience the highest stress. However, plastic anisotropy also plays a role. Based on a plastic argument, the 111 orientations would be expected to yield last, since the Schmid factor of both the 100 and 110 grains are the same for $a/2\langle 110\rangle$ slip, and are much larger than that for the 111 orientations. Previous modelling work has found that the amount of elastic anisotropy affects the yield

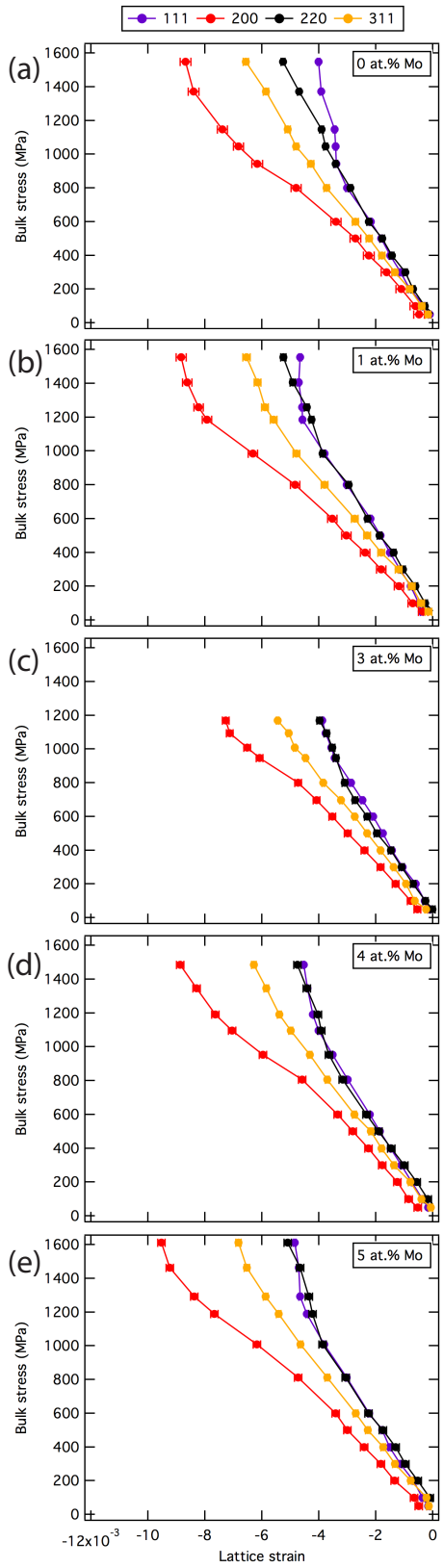

Figure 6.8: Variation with bulk applied stress of the phase-averaged lattice strain on the 111-, 200-, 220- and 311-orientated grain families for the (a) 0, (b) 1, (c) 3, (d) 4 and (e) 5 at.% Mo alloys.

behaviour, with increased anisotropy leading to stress repartitioning during elastic loading, with load transferred to 111 orientations from the 100 and 110 [228]. These modelled results are in agreement with the present work. Additionally, the added effect of constraint caused by the orientation of neighbouring grains complicates the situation in reality, although this is less significant than the interplay of elastic and plastic anisotropy. Therefore in the present alloys, the bulk stress increased on all grains in all orientations according to their specific elastic modulus, and the 111-orientated grains yielded first even though these orientations had a lower Schmid factor than alternative orientations.

Independent of the bulk Mo content, in all alloys the 111 and 220 grains yielded first and at the same time. This is evident in Figure 6.8 from the sharp change in gradient of these grains. At this point during loading, the 111 and 220 grains take up no further load elastically, but instead yield plastically though the passage of dislocations. To accommodate this, the 200 planes take up more load, with an associated large increase in the lattice strain. In Figure 6.8, this is visible as a change to a lower gradient. The behaviour of the 200 and 220 grain families is consistent with previous literature, however the evident yielding of the 111 orientations is inconsistent [219, 220]. On further loading, the 200-orientated grains deviate and tend to vertical, implying progressive yielding. In the case of perfect plasticity, one would expect the elastic strains on all planes to reach a saturation value at a given bulk stress, beyond which no further increases would be seen. However, the 200 curves in Figure 6.8 do not reach vertical, nor do they stop at a certain bulk stress. This may be attributed to work hardening. As with previous studies [222, 228], the 311-orientated families of grains show limited intergranular strain accumulation, with deviations indicative of tensile intergranular strains developing as plastic deformation proceeds.

There were no significant differences in the stresses at which intergranular load partitioning occurred as bulk Mo content was varied. This may be attributed to the similar yield strengths of each alloy (Table 6.3). It was shown in Chapter 5 that Mo increased the solid solution strength of the γ phase, but concurrently decreased the precipitation strength by a similar magnitude, leading to very little effect on the overall yield strength. Since deformation behaviour is dependant on the yield strength and critical resolved shear stress, bulk Mo additions did not strongly affect the deformation behaviour.

Alloy (at.% Mo)	0	1	2	3	4	5
0.2% Yield Stress (MPa)	851	918	-	918	863	1020

Table 6.3: 0.2% yield stresses of each alloy in the series, determined during in-situ compression testing.

Some subtle differences in deformation behaviour with bulk Mo content were visible, with more spreading of the curves for the high and low Mo contents. These data imply that a larger degree of load partitioning occurs in alloys with larger magnitudes of lattice misfit, independent of the sign of the misfit. Additionally in the 3 and 4 at.% Mo alloys, the 111 and 220 grains deform together, whereas these grains show a divergent behaviour in the highest misfit alloys. This implies that the magnitude of the lattice misfit has an effect on the work hardening behaviour of these alloys, with a higher misfit leading to increased work hardening on the 220 planes.

To further elucidate this effect, the intergranular strain was determined as a function of the bulk plastic strain, again as an average measure of grain behaviour. Figure 6.9 shows that there was rapid development of intergranular strains during the early stages of deformation. This has previously been seen in similar alloy systems [228, 229]. Compressive residual lattice strains were observed on the 200-orientated grains whilst positive residual strains accumulated on the 220-orientated grains. Meanwhile both the 111- and 311-orientated grains displayed relatively modest residual lattice strain accumulation. It should be noted that the current work was carried out in compressive loading, and these data are in agreement with previous literature on tensile loading, albeit of the opposite sense [218–220, 222].

In general, the 200-orientated grains initially accumulated strain faster than other grain orientations,

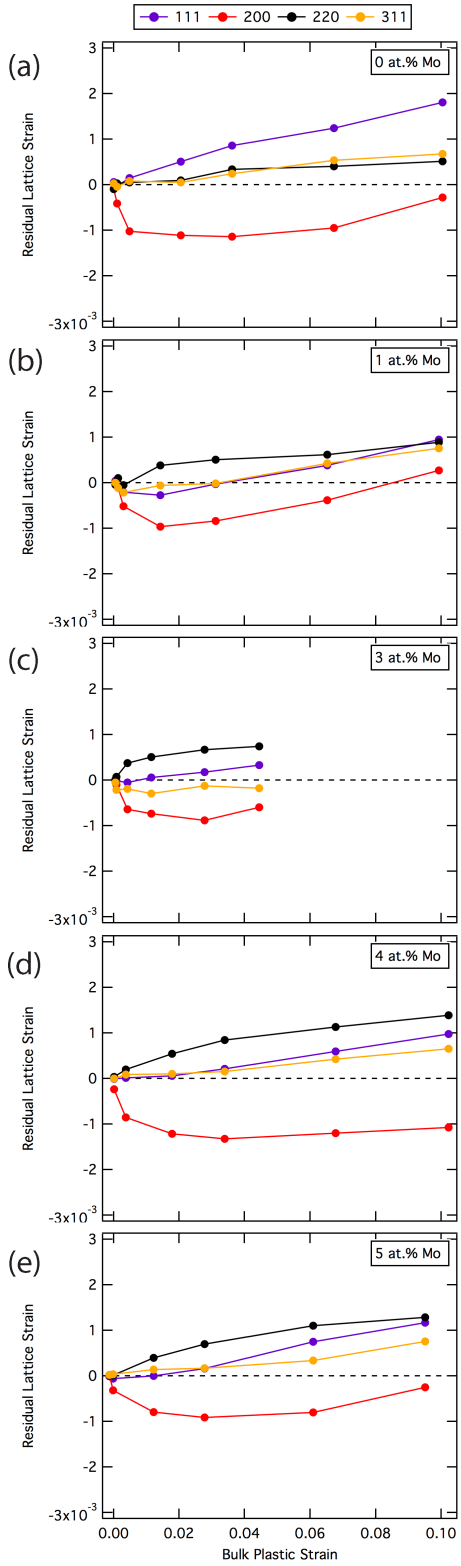

Figure 6.9: Variation with bulk applied plastic strain of the phase-averaged lattice strain on the 111-, 200-, 220- and 311-orientated grain families for the (a) 0, (b) 1, (c) 3, (d) 4 and (e) 5 at.% Mo alloys.

followed by the 220 orientations. The 111- and 311-orientated grains showed less rapid strain accumulation in general. The fact that there was visible strain accumulation on the 111-orientated grains in the present work is not consistent with the idealised behaviour determined using elastoplastic self-consistent modelling in previous studies [228, 230], although the deformation behaviour of the 200- and 220-orientated grains is in agreement. However, both the present data and modelled data in [228] show that 111-orientated grains accumulate positive residual lattice strain, even though the former loading was tensile and the latter was compressive. The inverse sign of the residual lattice strains of the 200- and 220-orientated grains are in agreement with the previous study (200-orientated grains accumulated compressive strain when loaded in compression, and vice versa for the 220 orientations).

The 311-orientated grains accumulate the least strain of the grain orientations studied in the present alloy system. As identified in previous studies [228], these orientations therefore offer the best choice for the determination of macroscopic residual strains or stresses, as they are least affected by microscopic strains.

Mo additions are not expected to affect the elastic or plastic anisotropy of the current alloy series, but the weak effect of Mo on the yield strength (Table 6.3) may be expected to affect the magnitude of the residual strain accumulation. Figure 6.9 shows a similar behaviour for all Mo contents, except that containing 0 at.% Mo, with the greatest tensile strain accumulation in the 220-orientated grains. In all of the alloys containing Mo, the 111-orientated grains accumulated strain later than the other orientations. Once again, the exception is the 0 at.% Mo alloy, in which strain accumulation on 111 orientations was visible from the onset.

This picture is complicated by the fact that Ni-based superalloys contain two phases in each grain, to which load may be further partitioned non-equally. Whilst the preceding description refers to grain average behaviour, the interphase partitioning effect should be separated from that of the interphase behaviour. Evidence of interphase load partitioning is visible in Figure 6.9, particularly at larger applied strains. Initially, there is compressive strain accumulation on the 200-orientated grains, but on further loading this becomes more positive. In the situation of perfect plasticity, a maximum residual lattice strain would be expected, with the curves in Figure 6.9 reaching a plateau at which point deformation proceeds purely through the passage of dislocations. In the case of work hardening, a progressive and monotonic divergence would be expected (like [228]). In contrast, the present results show a sign change (e.g. Figure 6.9b), which may be attributed to interphase load partitioning between the γ and γ' phases. This behaviour is more pronounced in the alloys with the largest lattice misfits. The unique behaviour of the 0 at.% Mo alloy in the series, in which the 111-orientated grains, rather than the 220 orientations, accumulate the most residual lattice strain, may also be attributed to interphase load partitioning.

The interphase load partitioning behaviour may be determined using pairs of related peaks in the diffraction pattern. For example, the interplanar spacing of the 100 planes in the γ' phase may be easily determined by fitting a single function to the 100 superlattice peak of the diffraction pattern. This then allows determination of the interplanar spacing of the 200 planes in the γ' phase. By fixing this value during two peak fitting of the 200 fundamental peak, the interplanar spacing of the 200 planes in the γ phase may be determined. Within the angular range of the detectors, it was only possible to fit two pairs of peaks using this method, the 100 and 200, and the 110 and 220.

The variation in lattice strain in the γ and γ' phases extracted from the 200 and 220 peaks with bulk applied stress are shown in Figure 6.10. It is clear that 200-orientated grain families are less elastically stiff than the 220 orientations. In the elastic regime, the γ and γ' phases show similar stiffnesses. As deformation initiates, load partitioning between grain families is seen to occur before any interphase load partitioning. In all alloys of the series, the 220-orientated grain families deform plastically first, with the passage of dislocations in these grains leading to no additional lattice strain on loading. As this happens, a higher load is experienced by the 200 orientations to accommodate further loading.

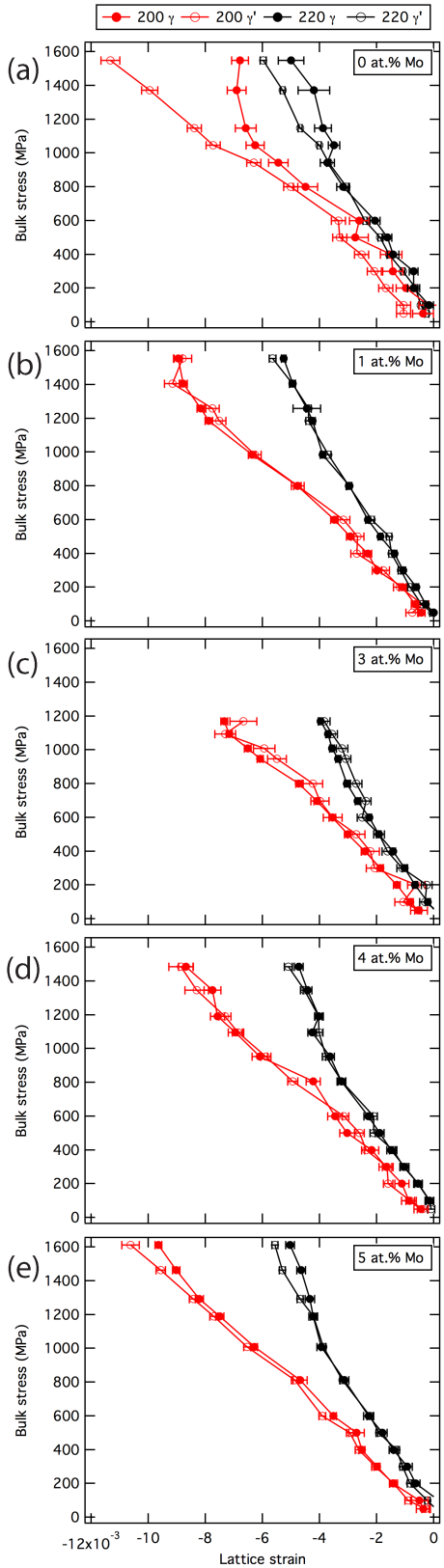

Figure 6.10: Variation with bulk applied stress of the lattice strain in the γ and γ' phases on the 200- and 220-orientated grain families for the (a) 0, (b) 1, (c) 3, (d) 4 and (e) 5 at.% Mo alloys.

Although the intergranular deformation behaviour was similar across the alloy series, the extent of interphase load partitioning differs. Alloys containing intermediate Mo content (1, 3 and 4 at.% Mo) showed no interphase load partitioning, with both phases showing the same deformation behaviour up to the maximum load. In contrast, the 0 and 5 at.% Mo alloys showed pronounced interphase load partitioning. In both alloys, the γ phase deformed plastically first, leading to increased load being supported by the γ' phase. This interphase partitioning behaviour is most pronounced in the 0 at.% Mo alloy, occurring earlier on loading than the 5 at.% Mo alloy.

A previous study has found that load partitions to the γ' phase at room temperature, whilst little interphase load partitioning occurs at high temperature [231]. Although this may be consistent with the present study, these data are in contrast to a previous study [229], which found that at room temperature, the γ' phase yielded first with an associated increase in strain taken up by the γ phase. At high temperatures (650°C and 750°C), the γ phase was found to yield first. This inconsistency between the present work and previous studies is unlikely to be attributed to differences in the lattice misfit of the alloys in these studies, as at room temperature, the alloy 720Li in [229] had a similar misfit to the 1 at.% Mo alloy of the present study. However, the differing compositions of alloy 720Li and the present alloy series may be expected to affect the strength of the γ and γ' phases, and therefore the load partitioning behaviour. In the present 4 at.% Mo alloy, with zero lattice misfit, the instantaneous yielding seen around -4×10^{-3} strain (Figure 6.10d) is consistent with that seen in [229].

In the 0 at.% Mo alloy, the γ phase in the 220-orientated grains yielded at relatively low stresses, with subsequent load being taken up by the γ' phase. After yielding of the γ' phase at higher applied stresses, both phases appear to deform with similar rates of work hardening, shown by the similar gradients of these phases in Figure 6.10a. In contrast, although the γ phase also yields first in the 200-orientated grains, with subsequent load supported more by the γ' phase, very little work hardening is visible in either phase. These data imply an orientation dependence of work hardening in these alloys, with more extensive work hardening on the 220-orientated grains compared to the 200 orientations. These data may be rationalised by previous model results [228], which found a higher number of operative slip systems on $\langle 110 \rangle$ orientated grains, compared to $\langle 100 \rangle$ orientated grains. This may lead to increased dislocation interaction, and therefore increased work hardening on $\langle 110 \rangle$ directions. The very pronounced interphase partitioning behaviour visible in the 0 at.% Mo alloy will affect the grain average behaviour, (Figures 6.8a and 6.9a). It is therefore unsurprising that the grain average behaviour of the 0 at.% Mo alloy differs to the other alloys of the series. For example, this behaviour explains the modest grain average behaviour of the 220-orientated grains (Figures 6.8a and 6.9a), which must be intermediate between the behaviours of both phases, whereas the other alloys show the largest positive residual lattice strain on the 220-orientated grains. Such interphase partitioning behaviour may also explain the high degree of residual lattice strain apparent on the 111-orientated grains, but this cannot be confirmed as it is not possible to separate the phase contributions without access to an associated superlattice reflection.

The effect of interphase partitioning behaviour may be most effectively visualised through the residual lattice strains (Figure 6.11). Data from additional superlattice reflections (210 and 211) are included in Figure 6.11, but it was not possible to determine the associated γ data for grains in these orientations due to insufficient detector range to capture the 420 and 422 reflections. Figure 6.11 shows that in all alloys there is pronounced splitting of the γ and γ' loading responses, resulting in more negative residual lattice strains in the γ' phase compared to the γ phase. In the 200 orientations, which, as a phase average gain negative residual lattice strain, once interphase load partitioning starts, the residual lattice strain of the γ phase becomes less negative, and in the case of the 0 at.% Mo alloy, becomes tensile. The 220 orientations show inverse behaviour to the 200, but in both these orientations, the γ phase accumulates more positive residual lattice strain compared to the γ'. The present work is in agreement with previous studies [218], but it should be noted that inverse results are seen since the present work was carried

out in compressive testing rather than tensile. Initially on loading, both phases develop comparable microstrains (compressive in 200 orientations, and tensile in 220 orientations). This occurs in all alloys, but is most visible in the 0 and 5 at.% Mo cases, which have the largest lattice misfit. At this point during loading, intergranular microstrains develop with little interphase load partitioning. At larger strains, the γ and γ' phase behaviour diverges, with more tensile strain development in the γ phase, and more compressive strain development in the γ'. After this point, interphase microstrains accumulate without any further intergranular load partitioning. In all alloys there is very little microstrain development on 211 orientations (Figure 6.11), and only slight tensile microstrain development in 210 orientations, except in the 0 at.% Mo alloy, in which it is compressive. Although this anomalous behaviour of the 210 orientation in the 0 at.% Mo alloy may be rationalised by interphase load partitioning behaviour, to confirm this, analysis of the 420 reflection is required. This was not available in the field of view of the experimental setup.

The above arguments do not factor in the effect of the pre-existing interphase strains arising as a result of the intrinsic lattice misfit between the γ and γ' phases, which will be most significant in the 0 and 5 at.% Mo alloys. In the case of the 0 at.% Mo alloy (positively misfitting), the γ phase is in a state of tension before any loading, whilst the γ' phase is in compression. The inverse is true in the case of the 5 at.% Mo alloy, which is negatively misfitting. In principle, Figures 6.8 to 6.11 in the present work could be modified to include this intrinsic stress. In the positively misfitting alloys, this would mean that all the γ data should become more positive, whilst the γ' data is shifted to more negative values. The inverse is true of the negatively misfitting alloy.

The variations in deformation behaviour with bulk Mo content may be rationalised in terms of the underlying strengthening mechanisms present in these alloys. As mentioned previously (Figure 6.7b), the 0 and 5 at.% Mo alloys have the largest lattice misfit (being positive in the former and negative in the latter), whilst the intermediate alloys have lower lattice misfit, which is approximately zero for the 4 at.% Mo alloy. It is evident in Figure 6.10 that the γ and γ' phases deform together in the low misfit alloys, but in the alloys with high lattice misfit, the γ phase deforms first. The higher the magnitude of the lattice misfit, irrespective of sign, the earlier the load partitioning between the γ and γ' phases. However, complicating these matters, the sign of the lattice misfit is not manifest as a change in the load partitioning behaviour between phases, because other underlying mechanisms are occurring concurrently, as discussed throughout this thesis. These other strengthening mechanisms are operative in the alloy series and are affected by bulk Mo content. Although the overall yield strength of these alloys is not strongly linked to Mo content (Chapter 5), increasing bulk Mo content results in increased solid solution strengthening of the γ phase, but simultaneously reduces the precipitation strengthening effect of the γ' phase, by reducing the Anti-Phase Boundary Energy. Therefore, there is a competing effect between lattice misfit, increasing strength of the γ phase, and decreasing strength of the γ' phase.

To rationalise the effect of each of these parameters in the present alloy series, three limiting cases may be compared. The 0 at.% Mo alloy represents a case of high positive lattice misfit, weak γ strength and high γ' strength caused by a large APBE (Figure 5.5) giving rise to more extensive precipitation strengthening. In contrast, the 4 at.% Mo alloy has zero misfit and moderate γ and γ' strengths. Finally, the 5 at.% Mo alloy has a high negative lattice misfit, high γ strength and weaker γ' strength. In comparing these three cases, the effect of each parameter may be determined.

In the case of the 0 at.% Mo alloy, which is positively misfitting and therefore originally contained γ phase in tension and γ' in compression, compressive loading such as in the present study would decrease the strains in both phases. This would lead to the stresses in the γ phase reducing through zero and becoming compressive. In the case of the 0 at.% Mo alloy, the γ phase is weak, and therefore yields early, at low applied compressive stress. This gives rise to a significant interphase load partitioning response, as seen in Figures 6.10a and 6.11a. In the case of the 4 at.% Mo alloy, compressive loading also reduces

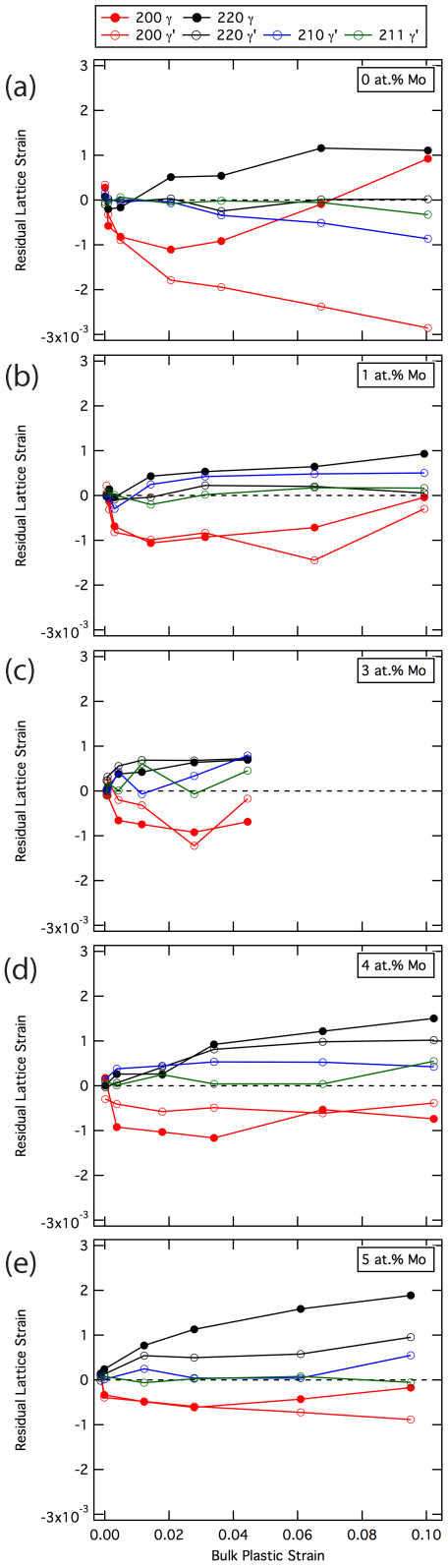

Figure 6.11: Variation with bulk applied plastic strain of the lattice strain in the γ and γ' phases on the 200- and 220-orientated grain families for the (a) 0, (b) 1, (c) 3, (d) 4 and (e) 5 at.% Mo alloys.

the lattice parameter of both phases, but in contrast to the 0 at.% Mo case, both phases yield together because the γ phase is sufficiently strong to avoid yield at low stresses. Therefore, no significant interphase load partitioning is seen. In the third case of the 5 at.% Mo alloy, with high negative misfit, the γ' phase is initially in tension whilst the γ phase is in compression. As in all other cases, during compressive loading the stresses in both phases becomes more negative. Despite the strong γ phase in this high Mo alloy, the γ phase yields first. This result is similar to the case of the 0 at.% Mo alloy, but the mechanism is different. In the negatively misfitting alloy, the γ phase is initially in a state of compression, so any compressive loading acts to accentuate this effect, thereby reaching the yield stress earlier in loading. This leads to significant visible interphase load partitioning, as seen in Figures 6.10e and 6.11e. Overall, a larger disparity in the strength of the γ and γ' phases is required for visible interphase load partitioning to occur.

It is perhaps valuable to consider the equivalent deformation behaviour of these alloys under tensile loading. Although these data could not be obtained, the outcome may be predicted following the rationale described above. The positively misfitting 0 at.% Mo alloy contains γ phase that is originally in tension. Due to the absence of Mo, the γ phase is weak, and therefore on loading, strain accumulation in the γ phase is increasingly tensile. This leads to the γ phase yielding early, with extensive load partitioning. The case of the zero misfit alloy (4 at.% Mo) would be equivalent to that under compressive loading, since there is an absence of misfit strains complicating matters. In contrast, the behaviour of the 5 at.% Mo alloy would differ in tensile loading. No interphase load partitioning may occur because the γ phase is initially in compression in this negatively misfitting alloy, and therefore, on tensile loading, the stresses in the γ phase reduce, becoming more positive. The γ phase is stronger due to the high Mo content, and therefore the γ phase may not yield at all and no interphase load partitioning would be visible. In the extreme case, the γ' phase may yield instead. It is important to note that arguments describing how tension or compression aid or hinder plastic flow are only really applicable to the γ' phase, since, modelled as an ellipsoidal inclusion the γ' phase has a perfectly uniform stress field [232], but the γ phase does not.

As discussed, Mo has a complicated effect on the deformation behaviour of the current Ni-based superalloys through multiple concurrent mechanisms. To elucidate this further, Figure 6.12a and b show the diffraction elastic constants as a function of Mo content. It may be seen that in the γ phase, Mo did not have much effect on the stiffness of either the 200 or 220 orientations. In contrast, addition of Mo lead to a decrease in stiffness of the γ' phase in the 200, 220 and 210 orientations, with negligible effect on the 211 orientation. In a particular orientation, the γ phase was seen to be less elastically stiff than the γ' phase of the same orientation.

The fact that Mo has a larger effect on the diffraction elastic constants of the γ' phase, compared to the γ phase, may be attributed to the phase composition in addition to crystallographic structure. Although Mo is classically expected to partition to the γ matrix phase, previous work on the same alloy series has shown that bulk Mo additions also affect the content of other elements, particularly Cr, in the γ' phase (Chapter 4). Mo was seen to have a particularly large effect on the composition of the tertiary γ' phase. Since the γ and γ' phases have different crystal structures, with the latter being ordered, Mo additions are likely to have a different effect on the stiffnesses in each phase.

The diffraction elastic constants may also be plotted against orientation parameter (Figure 6.13) to elucidate the orientation dependence of stiffness, in addition to the compositional dependence that is clearly visible in Figure 6.12. The orientation parameter is given as

$$\Gamma = \frac{h^2k^2 + k^2l^2 + h^2l^2}{(h^2 + k^2 + l^2)^2} \tag{6.2}$$

In agreement with previous studies [223], the 111 orientations are stiffest, followed by 220, 311 and

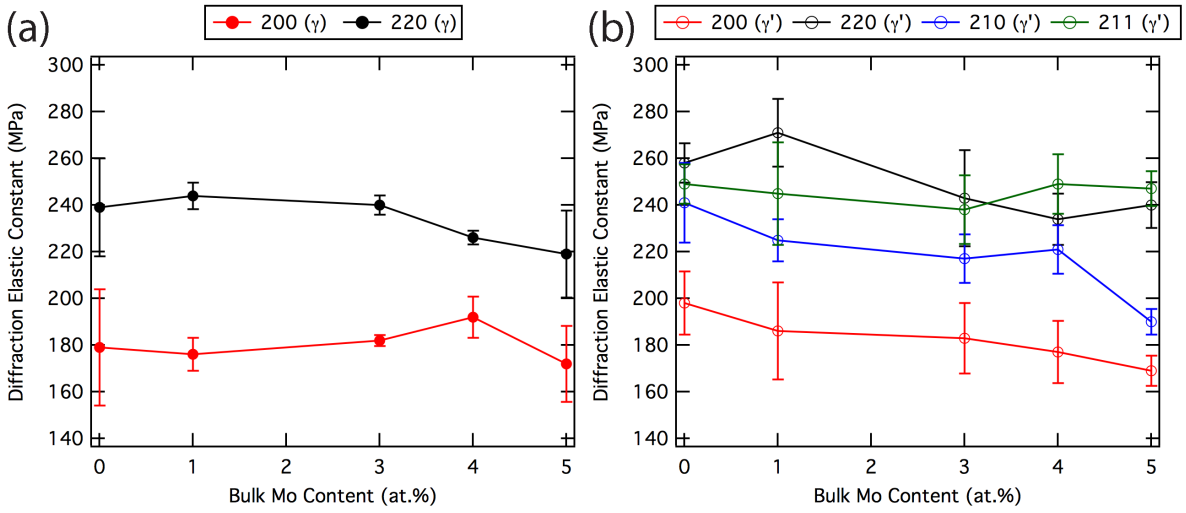

Figure 6.12: Diffraction elastic constants of the γ and γ' phases as a function of Mo content.

200. The inverse diffraction elastic constant increases for the γ' phase with bulk Mo additions (Figure 6.13a-e). In other words, the stiffness of all orientations decreases with Mo content. However, there does not appear to be an orientation dependence of the stiffness with Mo content, with all gradients of the γ' phase in Figure 6.13 being within the uncertainty of each other. Similarly, Mo does not appear to affect the stiffness anisotropy of the γ phase. Although the 4 at.% Mo alloy shows an anomalously low gradient, this is the same as the other alloys within experimental uncertainty. As Mo is added to the alloy series, however, it is clear that the γ' diffraction elastic constants become closer to those of the γ phase. In alloys with 3 at.% Mo or less, the γ phase is always less stiff than the γ', irrespective of the specific *hkl* orientation considered. In the high Mo alloys, although this remains true for high orientation parameters, the 200 orientations are stiffest in the γ phase.

6.4 Conclusions

In conclusion, the variation of the lattice parameters and lattice misfit with temperature of a model series of quinary Ni-based superalloys have been determined experimentally and compared to equilibrium predictions. It was found that increasing bulk Mo content and increasing temperature led to larger lattice parameters of both the γ and γ' phase, even though Mo is expected to partition only to the matrix phase. The lattice misfit was found to decrease with Mo content, being positive for low Mo contents, negative for the highest Mo contents, and passing through zero in the 4 at.% Mo alloy. Increased temperature decreased the lattice misfit, thereby reducing the lattice misfit of the positively misfitting alloys whilst increasing the magnitude of the lattice misfit of the negatively misfitting alloy. These data have important consequences for alloy design, in which a minimised lattice misfit is desired at operating temperatures.

The room temperature deformation mechanisms of a series of model polycrystalline Ni-based superalloys have been studied by compressive loading during neutron diffraction. It was found that intergranular load partitioning was operative on initial loading, evolving to interphase load partitioning at higher applied stresses. Grain averaged behaviour demonstrated that the 111-orientated grains yielded first, with the 200 orientations taking up more of the applied load. High positive residual strains were accumulated on the 220- and 111-orientated grains, whilst large negative residual strains accumulated on the 200 orientations. In the interphase load partitioning regime, the γ phase yielded first, with subsequent load taken up by the γ' phase. This interphase load partitioning occurred at lower applied stress in alloys with larger lattice misfit, irrespective of the sign of the misfit. Significantly, the complicated interplay of lattice

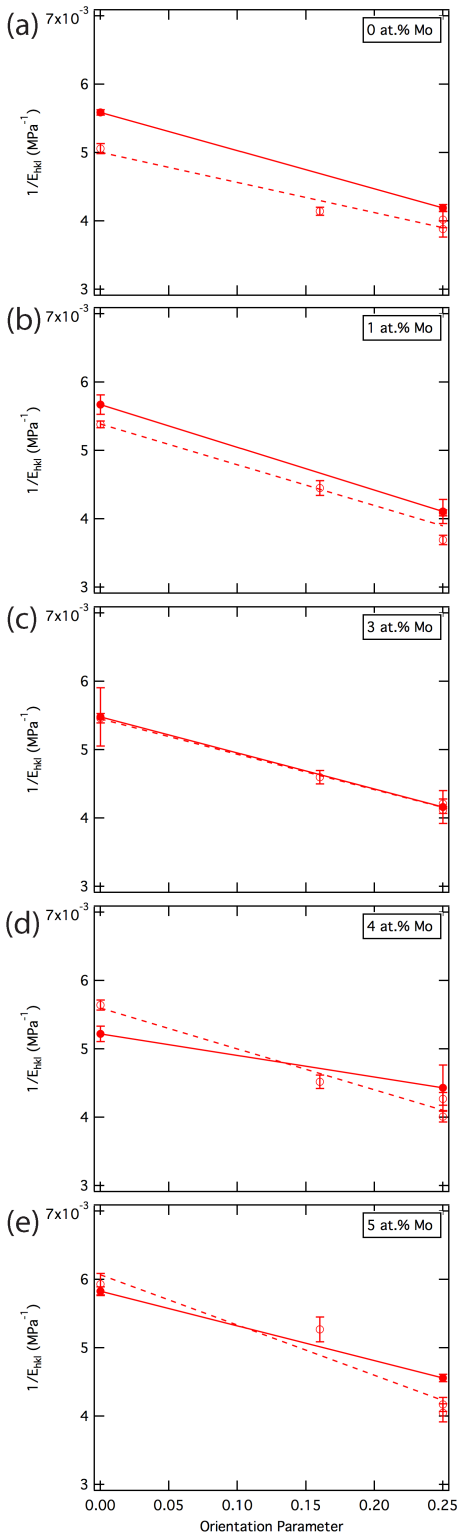

Figure 6.13: Diffraction elastic constants of the γ and γ' phases as a function of orientation parameter in the (a) 0, (b) 1, (c) 3, (d) 4 and (e) 5 at.% Mo alloys.

misfit and phase strength was elucidated, with deformation behaviour found to be strongly dependent on both parameters. These results have important implications for the design of superior superalloys, by enabling microstructural features such as lattice misfit and phase composition to be optimised for maximum yield strength.

Chapter 7

Conclusions and Further Work

Ni-based superalloys are ubiquitous in high temperature, high stress environments such as gas turbine engines due to their remarkable mechanical properties. The excellent yield strengths of these materials stem from many concurrent underlying strengthening mechanisms, which are dependent on the microstructural properties such as phase composition and volume fraction. Only by fully understanding the extent of each of these individual mechanisms, and the features that affect them, can new superalloys be designed with microstructures tailored specifically to optimise the yield strength. Throughout this study, currently accepted models in the literature have been used to predict the yield strength contributions of a number of commercial alloys. A more detailed investigation has been carried out on a series of model quinary Ni-based superalloys, the microstructures of which have been fully characterised for use as inputs to the models. Finally, a thorough investigation on the deformation behaviour of these model alloys has been carried out to elucidate the role of these microstructural parameters. This chapter summarises the findings of this investigation, and suggests possibilities for further work to continue this study.

7.1 Conclusions

The literature contains many models to describe the individual strengthening mechanisms of Ni-based superalloys, however there is no consistent, all-encompassing description that involves all of the underlying strengthening mechanisms. In this thesis, models for each of the individual strengthening mechanisms that operate in Ni-based superalloys at room temperature are combined to create an overall yield strength model for deformation at room temperature. The trends predicted by this model closely fit with experimental yield strength data for six commercial polycrystalline Ni-based superalloys, however the magnitude of the yield strength is overpredicted by $\sim$300 MPa.

Of all the multiple concurrent strengthening mechanisms, precipitation strengthening was found to be the most significant, accounting for approximately half of the overall yield strength in the commercial alloys studied. Perhaps counterintuitively, the extent of precipitation strengthening was found to decrease as the total γ' volume fraction was increased. This was in fact due to compositional variation in the particular alloys studied, which affected the APBE and the resulting extent of precipitation strengthening.

The role of composition was found to be complex due to the multifaceted elemental partitioning behaviour, even though the partitioning behaviour of each individual element is relatively well understood. This gave rise to counterintuitive effects of bulk composition on yield strength, such as the non-linear effect of bulk Al content on precipitation strengthening.

Microstructural parameters such as grain size, γ' size and volume fraction were shown to play an important role on yield strength. Notably, in the model utilised in this work, the number density of γ' precipitates is more important than the volume fraction. Phase composition is a significant input

parameter in yield strength modelling, and as such, the differing compositions of the secondary and tertiary γ' distributions should be determined and inputted into model descriptions. As a result, this work highlighted the importance of accurate input parameters for the accurate prediction of yield strength.

To this end, in the present work a model series of quinary, polycrystalline Ni-based superalloys was carefully characterised to investigate the effect of ageing on these microstructural parameters. It was found that in these bimodal alloys, the secondary γ' precipitates did not coarsen to any significant extent on ageing up to 1000 hours, however morphological instabilities and splitting were seen. In contrast, the tertiary γ' precipitates did coarsen, but were not present after 1000 hours of ageing, having redissolved into the γ matrix.

The experimental data obtained by characterisation of this alloy series was compared to that predicted by thermodynamic modelling using Thermo-Calc software. Although the γ phase composition was well predicted by Thermo-Calc, and remained approximately constant on ageing, the compositions of the secondary and particularly the tertiary γ' phases were not well predicted. The precipitate phase composition changed on ageing, but did not necessarily tend to the predicted equilibrium precipitate composition. For example, the Mo content of the secondary γ' phase increased on ageing to $\sim$2 at.%, and also tended to this content in the tertiary γ' phase. These data have important implications for the modelling of mechanical properties such as yield strength, as described above.

As such, these data were used to model the yield strengths of the alloy series, and this was compared to experimental data for the yield strengths of each alloy. It was found that the yield strength increased slightly with Mo content, however a local minimum occurred for the lowest lattice misfit alloys. Model predictions confirmed this reduced strength at reduced lattice misfit, however model predictions were more pronounced than that found experimentally. In contrast to the commercial alloys studied, the magnitudes of the yield strengths of the model alloy series were well predicted by the model utilised in the present work. As in the commercial alloys, precipitation strengthening was found to be the most significant strengthening mechanism, again accounting for approximately half of the total yield strength. Across the alloy series, as bulk Mo content was increased, the increase in total yield strength was not particularly significant. This was found to be due to a decreasing extent of precipitation strengthening (caused by a reduced APBE) with Mo additions, and a simultaneous increase in the extent of solid solution strengthening in both the γ and γ' phases. Notably, the extent of solid solution strengthening in the γ' phase was found to be as significant as that in the γ phase. As such, this strengthening mechanism should not be ignored in yield strength models, as is currently common in the literature.

To elucidate the deformation behaviour further, and the role of the individual strengthening mechanisms, in-situ compression testing was carried out on the model alloy series. Pronounced intergranular load partitioning was visible on initial loading, with the 111-orientated grains yielding first whilst the 200 orientations withstood an associated higher strain. On further loading, interphase load partitioning was visible. In all alloys, the γ phase yielded first, with the γ' phase withstanding further strain. Although intergranular load partitioning was seen in all alloys of the series, interphase load partitioning was only found to occur in the alloys with the largest lattice misfit, irrespective of whether this was positive or negative. However, this observed behaviour is a sum of multiple concurrent mechanisms, as discussed above in relation to yield strength. It was found that the complex interplay between lattice misfit and phase composition gave rise to the observed deformation behaviour. As discussed above, across the alloy series, as bulk Mo content was increased the solid solution strength of the γ phase also increased, whilst the precipitation strengthening effect decreased. In addition to this, there was a non-linearly dependent effect of lattice misfit and the associated coherency strengthening. The sum of these three effects gave rise to the observed interphase load partitioning behaviour. Although both the alloys with the highest lattice misfit (0 and 5 at.%Mo) showed significant interphase load partitioning, this arose for differing reasons since the phase strength differs markedly in these alloys. Therefore, in addition to the role on

yield strength, the underlying strengthening mechanisms investigated in this work have been shown to affect the deformation behaviour after yield.

7.2 Further Work

This work attempts to elucidate the effect of each individual strengthening mechanism on the yield strength of polycrystalline Ni-based superalloys, and as such, several aspects warrant further work in order to complete the understanding of this topic.

In Chapter 3, models for individual strengthening mechanisms in the literature were used to determine the overall yield strength, and its various components, of several commercial polycrystalline Ni-based superalloys. As discussed in this chapter, the models overpredict the total yield strength of these alloys, and as such, further work is necessary to improve these models in order to enable accurate quantitative prediction of yield strength. Suggestions to improve the precipitation strength model, for example, include use of an interparticle spacing that differs for the secondary and the tertiary γ', and the use of two particle size distributions with these separate interparticle spacings for each distribution. The interparticle spacing is also important for the Orowan strengthening mechanism. The current model utilised in the present study uses an interparticle spacing L, however an improvement may be to use $L - 2r$ instead, since a spacing of L is meaningless as the particle radius, r, approaches L. Clearly the models used in the present work require further work to improve the accuracy of their quantitative yield strength prediction and this would be of huge importance to the superalloy community.

A fuller investigation of the strengthening mechanisms of the γ' phase would significantly aid understanding of yield strength in these alloys. A suggested method for further investigation would be fabrication of alloys of 100% γ' phase, with compositions equal to those of the secondary and tertiary γ' precipitates of the model alloy series. These alloys could be mechanically tested by hardness testing or, ideally, compression testing in order to irrefutably determine the strength of this phase. These data would enable more accurate clarification on the extent of solid solution strengthening in the γ' phase, and as such would allow validation of the modelled data.

Currently, the models described in this study are only applicable at room temperature. However, since Ni-based superalloys have application at very high temperatures, further work of the utmost importance would be the extension of the current models to these high temperatures. As a starting point, Chapter 4 described the high temperature compressive yield strength of the model alloy series and Chapter 6 details the lattice parameter and lattice misfit at temperatures up to 700°C. However, no further information on phase composition or precipitate morphology or volume fraction was obtained at these high temperatures. As such, heat treatments could be carried out to create microstructures equivalent to those found at high temperature, and the samples quenched to allow for characterisation of the high temperature microstructures. These data would give a starting point for extension of the current models to high temperature. Ideally, *in situ* TEM characterisation of phase composition could be carried out by using a high temperature stage within the TEM, however this is fraught with difficulty due to oxidation and deterioration of the sample. Although in theory most of the models in the present thesis are semi-empirical and could be extended for use at high temperature, the extent of each strengthening mechanism is likely to change with temperature and critically, the deformation mechanisms themselves are dependent on temperature and become dominant in different regimes of temperature and applied stress (Figure 7.1). All of these factors must be taken into account in order to extent the present models for use at high temperature.

Chapter 4 described the detailed characterisation of a series of model quinary Ni-based superalloys. Although these alloys were fully characterised, some aspects would benefit from further work. Of signifi-

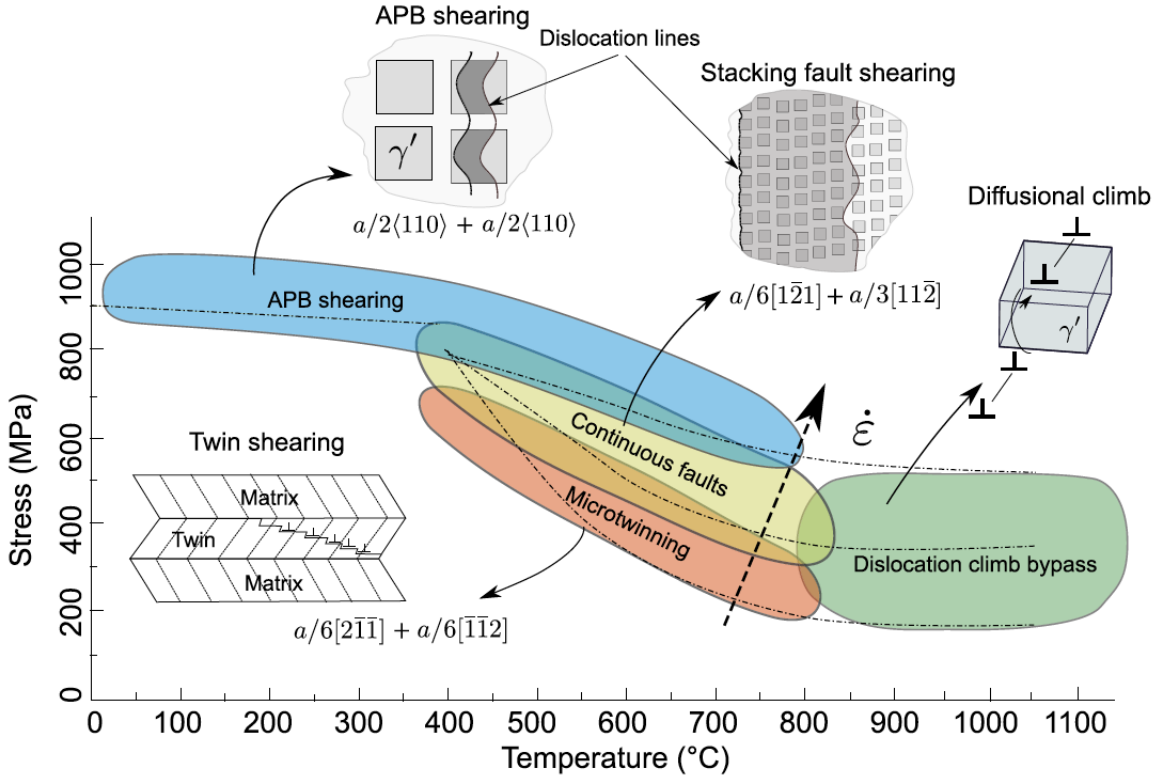

Figure 7.1: Deformation mechanisms in Ni-based superalloys as a function of applied stress, temperature and strain rate [233].

cant interest would be the full quantification of the tertiary γ' volume fraction, which was not able to be determined in the current work. Additionally, convergent beam TEM could be used to quantify the lattice parameters and associated lattice misfit of the secondary and tertiary γ' distributions [234], to enable more accurate input into the yield strength models. As discussed in Chapters 3 and 5, the tertiary γ' are the most significant strengthening phase and have composition further from the predicted equilibrium. As such, accurate determination of the volume fraction would likely enable much more accurate yield strength predictions as discussed in Chapter 5.

Chapter 3 emphasises the importance and complexity of elemental partitioning in the commercial Ni-based superalloys studied in the present work. However, no experimental data were obtained on these alloys to compare to the thermodynamic predictions of Thermo-Calc. A study of the elemental partitioning during ageing of these more complex commercial alloys (to augment the study of ageing of the model alloy series) would be of importance in improving the accuracy of yield strength prediction and the extent of the individual strengthening mechanisms. A detailed study of the phase composition of these commercial alloys on ageing for $\geq$1000 hours is suggested, and the phase compositions after 1000 hours should be compared to the equilibrium compositions predicted by Thermo-Calc. As utilised in Chapter 4, compositional analysis could be carried out by STEM EDX or APT.

This work very briefly noted the formation of TCP phases on ageing of the highest Mo alloys of the model series (Chapter 4). However, no accurate determination was made of the structure or composition of these phases. STEM and STEM EDX of these regions would allow for characterisation of these phases, which would aid in understanding the formation and evolution of these phases. To specifically locate these phases in the TEM sample, it is believed that focussed ion beam (FIB) milling would be required, rather than the electropolishing or carbon replica processes utilised in the present work.

As mentioned in Chapter 4, the secondary γ' precipitates in the model alloy series in this work were

not seen to coarsen extensively on ageing, but did evidence the morphological instabilities associated with splitting. An in-depth investigation of this phenomenon would be of interest. In the present work it was found that single specimens of each alloy evidencing splitting did not show split precipitates across the whole sample, but instead the splitting phenomenon was limited in extent, and the γ' precipitates across the full sample did not all split at the same time on ageing. This is of interest and, to the author's knowledge, has not been previously found in the literature. A large-scale SEM map across a full sample surface would enable investigation of the extent of the splitting phenomenon, and allow a fuller understanding of this process. Additionally, a study of the role of cooling rate on the extent of precipitate splitting would be a valuable addition to the literature.

The alloy series studied in this investigation would also allow for an interesting study on the effect of cooling rate and ageing time on the γ' particle size distributions, along with comparison to computational predictions using TC-PRISMA software. The full analysis of the factors affecting yield strength outlined in Chapters 3 and 5 would allow for an interesting study of microstructural optimisation for yield strength. The models could be used to determine the optimum microstructure for a particular alloy, and TC-PRISMA software could be used to determine the heat treatment and cooling rates required to fabricate this microstructure.

7.3 Concluding Remarks

Evidently these data provide useful insight into the factors that affect the yield strength of Ni-based superalloys. However, further work is required on each of the underlying models for the individual strengthening mechanisms in order to make reliable quantitative predictions of yield strength. If this were achieved, the microstructures and compositions of new alloys could be designed specifically to optimise the yield strength, thereby further progressing the capability of the jet engine.

Bibliography

[1] P. Argüelles, J. Lumsden, M. Bischoff, D. Ranque, P. Busquin, S. Rasmussen, B. Droste, P. Reutlinger, R. Evans, R. Robins, W. Kröll, H. Terho, Lagardére, A. Wittlöv, and A. Lina. European aeronautics: A vision for 2020: Report of the group of personalities, January 2001.

[2] Flightpath 2050: Europe's vision for aviation: Report on the high level group on aviation research. European Commission, 2011.

[3] Rolls-Royce. *The Jet Engine*. St Ives Westerham Ltd., 2005.

[4] D M Collins. *Modelling and characterisation of the microstructure in a polycrystalline nickel-base superalloy*. PhD thesis, University of Cambridge, 2012.

[5] R C Reed. *The Superalloys: Fundamentals and Applications*. Cambridge University Press, September 2006.

[6] C Rae. Alloys by Design: modelling next generation superalloys. *Materials Science and Technology*, 25(4):479–487, April 2009.

[7] R W Kozar, A Suzuki, W W Milligan, J J Schirra, M F Savage, and T M Pollock. Strengthening mechanisms in polycrystalline multimodal nickel-base superalloys. *Metallurgical and Materials Transactions A*, 40(7):1588–1603, 2009.

[8] J Miao, T M Pollock, and J Wayne Jones. Crystallographic fatigue crack initiation in nickel-based superalloy René 88DT at elevated temperature. *Acta Materialia*, 57:5964–5974, 2009.

[9] Y Gao, M Kumar, R K Nalla, and R O Ritchie. High-cycle fatigue of nickel-based superalloy ME3 at ambient and elevated temperatures: Role of grain-boundary engineering. *Metallurgical and Materials Transactions A*, 36:3325–3333, 2005.

[10] A Pineau and S D Antolovich. High temperature fatigue of nickel-base superalloys - a review with special emphasis on deformation modes and oxidation. *Engineering Failure Analysis*, 16:2668–2697, 2009.

[11] K R Bain, M L Gambone, J M Hyzak, and M. C. Thomas. Development of damage tolerant microstructures in udimet 720. In S Reichman, D N Duhl, G Maurer, S Antolovich, and C Lund, editors, *Superalloys*, pages 13–22. TMS, 1988.

[12] D P Mourer and J L Williams. Dual heat treat process development for advanced disk applications. In K A Green, T M Pollock, H Harada, T E Howson, R C Reed, J J Schirra, and S Walston, editors, *Superalloys*. TMS, 2004.

[13] J Gayda, T P Gabb, and P T Kantzos. The effect of dual microstructure heat treatment on an advanced nickel-base disc alloy. In K A Green, T M Pollock, H Harada, T E Howson, R C Reed, J J Schirra, and S Walston, editors, *Superalloys*. TMS, 2004.

[14] R F Decker. Strengthening mechanisms in nickel-base superalloys. In *Steel strengthening mechanisms symposium*, 1969.

[15] H Okamoto. Al-Ni (Aluminium-Nickel). *Journal of Phase Equilibria*, 14(2):257–259, 1993.

[16] J P Minshull. *A1-L12 alloys based on the Al-Co-Ni-Ti quaternary system*. PhD thesis, University of Cambridge, 2012.

[17] C T Sims, N S Stoloff, and W C Hagel, editors. *Superalloys II*. John Wiley and Sons, 1987.

[18] A. K Jena and M. C. Chaturvedi. The role of alloying elements in the design of nickel-base superalloys. *Journal of Materials Science*, pages 3121–3139, 1984.

[19] B Geddes, H Leon, and X Huang. *Superalloys: alloying and performance*. ASM International, 2010.

[20] R A Ricks, A J Porter, and R C Ecob. The growth of γ' precipitates in nickel-base superalloys. *Acta Metallurgica*, 31(1):43–53, 1983.

[21] R Radis, M. Schaffer, M. Albu, G. Kothleitner, P. Pölt, and E Kozeschnik. Multimodal size distributions of γ' precipitates during continuous cooling of UDIMET 720 Li. *Acta Materialia*, 57:5739–5747, 2009.

[22] J W Cahn. On spinodal decomposition. *Acta Metallurgica*, 9(9):795–801, 1961.

[23] Y Q Chen, E Francis, J Robson, M Preuss, and S J Haigh. Compositional variations for small-scale gamma prime (γ') precipitates formed at different cooling rates in an advanced Ni-based superalloy. *Acta Materialia*, 85:199–206, 2015.

[24] J M Oblak, D F Paulonis, and D S Duvall. *Coherency Strengthening in Ni Base Alloys Hardened by $D0_{22}$ Precipitates*. Metallurgical Transactions, 1974.

[25] W Mangen and E Nembach. The effect of grain size on the yield strength of the γ'-hardened superalloy NIMONIC PE16. *Acta Metallurgica*, 37(5):1451–1463, 1989.

[26] S Tin, T M Pollock, and W T King. Carbon additions and grain defect formation in high refractory nickel-base single crystal superalloys. In T M Pollock, R D Kissinger, R R Bowman, K A Green, M McLean, S Olson, and J J Schirra, editors, *Superalloys*, volume 1001, pages 201–210. TMS, 2000.

[27] Q Z Chen, N Jones, and D M Knowles. The microstructure of base/modified RR2072 SX superalloys and their effects on creep properties at elevated temperatures. *Acta Materialia*, 50:1095–1112, 2002.

[28] C Rae, M. S. A. Karunaratne, C J Small, R. W. Broomfield, N G Jones, and R C Reed. Topologically close packed phases in an experimental rhenium-containing single crystal superalloy. In T M Pollock, R D Kissinger, R R Bowman, K A Green, M McLean, S Olson, and J J Schirra, editors, *Superalloys*, pages 767–776. TMS, 2000.

[29] A K Sinha. Topologically close-packed structures of transition metal alloys. *Progress in Materials Science*, 15(2):81–185, 1972.

[30] J Jones and D J C MacKay. Neural network modelling of the mechanical properties of nickel base superalloys. In R D Kissinger, D J Deye, A D Anton, D L abd Cetel, M V Nathal, T M Pollock, and D A Woodford, editors, *Superalloys*, pages 417–424. TMS, 1996.

[31] Y Q Chen, T J A Slater, E A Lewis, E M Francis, M G Burke, M Preuss, and S J Haigh. Measurement of size-dependent composition variations for gamma prime (γ') precipitates in an advanced nickel-based superalloy. *Ultramicroscopy*, 144:1–8, 2014.

[32] R J Mitchell, M Preuss, S Tin, and M C Hardy. The influence of cooling rate from temperatures above the γ' solvus on morphology, mismatch and hardness in advanced polycrystalline nickel-base superalloys. *Materials Science and Engineering A*, 473:158–165, 2008.

[33] D Raynor and J M Silcock. Strengthening mechanisms in γ' precipitating alloys. *Metal Science Journal*, 4(1):121–130, 1970.

[34] H Gleiter and E Hornbogen. Precipitation hardening by coherent particles. *Materials Science and Engineering*, 2(6):285–302, 1967.

[35] R J Mitchell, M Preuss, M C Hardy, and S Tin. Influence of composition and cooling rate on constrained and unconstrained lattice parameters in advanced polycrystalline nickel-base superalloys. *Materials Science and Engineering A*, 423:282–291, 2006.

[36] A C Lund and P W Voorhees. The effects of elastic stress on coarsening in the Ni-Al system. *Acta Materialia*, 50:2085–2098, 2002.

[37] I M Lifshitz and V V Slyozov. The kinetics of precipitation from supersaturated solid solutions. *Journal of Physics and Chemistry of Solids*, 19:35–50, 1961.

[38] C Wagner. Theory of precipitate change by redissolution. *Zeitschrift für Elektrochemie*, 65(7/8):581–591, 1961.

[39] R J Mitchell and M Preuss. Inter-relationships between composition, γ' morphology, hardness, and γ - γ' mismatch in advanced polycrystalline nickel-base superalloys during aging at 800°C. *Metallurgical and Materials Transactions A*, 38A:615–627, 2007.

[40] M Fährmann, P Fratzl, O Paris, E Fährmann, and W Johnson. Influence of coherency stress on microstructural evolution in model Ni-Al-Mo alloys. *Acta metallurgica et materialia*, 43(3):1007–1022, 1995.

[41] M Doi and T Miyazaki. Microstructural development under the influence of elastic energy in Ni-base alloys containing γ' precipitates. In S Reichman, D N Duhl, G Maurer, S Antolovich, and C Lund, editors, *Superalloys*, pages 663–672. TMS, 1988.

[42] Y S Yoo. Morphological instability of spherical γ' precipitates in a nickel base superalloy. *Scripta Materialia*, 53:81–85, 2005.

[43] Y Chen, R Prasath Babu, T J A Slater, M Bai, R Mitchell, O Ciuca, M Preuss, and S J Haigh. An investigation of diffusion-mediated cyclic coarsening and reversal coarsening in an advanced Ni-based superalloy. *Acta Materialia*, 110:295–305, 2016.

[44] C L Qui and P Andrews. On the formation of irregular-shaped gamma prime and serrated grain boundaries in a nickel-based superalloy during continuous cooling. *Materials Characterization*, 76:28–34, 2013.

[45] P A Flinn. Theory of deformation in superlattices. *Transactions of the Metallurgical Society of AIME*, 218(1):145–154, 1960.

[46] J H Westbrook and R L Fleischer, editors. *Intermetallic Compounds Principles and Practice*, volume 2, chapter 2. Wiley & Sons, 1995.

[47] D M Wee, O Noguchi, Y Oya, and T Suzuki. New $L1_2$ ordered alloys having the positive temperature dependance of strength. *Transactions of the Japan Institute of Metals*, 21(4):237–247, 1980.

[48] B H Kear and H G F Wilsdorf. Dislocation configurations in plastically deformed polycrystalline Cu_3Au alloys. *Transactions of the Metallurgical Society of AIME*, 224:382–386, 1962.

[49] A E Staton-Bevan and R D Rawlings. The deformation behaviour of single crystal Ni_3(Al, Ti). *Physica Status Solidi (a)*, 29(2):613–622, 1975.

[50] P Beardmore, R G Davies, and T L Johnston. On temperature dependence of flow stress of nickel-base alloys. *Transactions of the Metallurgical Society of AIME*, 245:1537–1545, 1969.

[51] J H Westbrook and R L Fleischer, editors. *Intermetallic Compounds Principles and Practice*, volume 2, chapter 12. Wiley & Sons, 1995.

[52] A J Ardell. Precipitation hardening. *Metallurgical Transactions A*, 16A:2131–2165, 1985.

[53] V Gerold and H Haberkorn. On the critical resolved shear stress of solid solutions containing coherent precipitates. *Physica Status Solidi (b)*, 16(2):675–684, January 1966.

[54] M R Ahmadi, E Povoden-Karadeniz, and L Whitmore. Yield strength prediction in Ni-base alloy 718Plus based on thermo-kinetic precipitation simulation. *Materials Science and Engineering A*, 608:114–122, 2014.

[55] R F Decker and J R Mihalisin. Coherency strains in γ' hardened nickel alloys. *Transactions of American Society for Metals*, 62:481–489, 1969.

[56] R F Miller and G S Ansell. Low temperature mechanical behavior of Ni-15Cr-Al-Ti-Mo alloys. *Metallurgical Transactions A*, 8(12):1979–1991, 1977.

[57] E J Lee and A J Ardell. Superposition of precipitation-hardening mechanisms. In P Haasen, V Gerold, and G Kostorz, editors, *Strength of metals and alloys*, volume 1, pages 633–638. Pergamom press, 1979.

[58] A Melander and P A Persson. Strength of γ' hardened nickel-base alloy. *Metal Science*, 12(9):391–398, 1978.

[59] V A Phillips. Hardening mechanisms in a precipitation hardenable nickel-12.71 at.% aluminium alloy. *Philosophical Magazine*, 16(139):103–117, 1967.

[60] L K Singhal and J W Martin. The mechanism of tensile yield in an age-hardened steel containing γ' (ordered Ni_3Ti) precipitates. *Acta Metallurgica*, 16(7):947–953, 1968.

[61] V Munjal and A J Ardell. Precipitation hardening of Ni-12.19 at.% Al alloy single crystals. *Acta Metallurgica*, 23:513–520, April 1975.

[62] M. C. Chaturvedi and Y Han. Strengthening mechanisms in Inconel 718 superalloy. *Metal Science*, 17:145–149, March 1983.

[63] R L Fleischer. Substitutional solution hardening. *Acta Metallurgica*, 11:203–209, March 1963.

[64] R L Fleischer. Solution hardening. *Acta Metallurgica*, 9(11):996–1000, November 1961.

[65] E I Galindo-Nava, L D Connor, and C M F Rae. On the prediction of the yield stress of unimodal and multimodal γ' nickel-base superalloys. *Acta Materialia*, 98:377–390, 2015.

[66] Y Mishima, S Ochiai, N Hamao, M Yodogawa, and T Suzuki. Solid solution hardening of nickel - role of transition metal and b-subgroup solutes -. *Transactions of the Japan Institute of Metals*, 27(9):656 – 664, 1986.

[67] Y Mishima, S Ochiai, M Yodogawa, and T Suzuki. Mechanical properties of Ni_3Al with ternary addition of transition metal elements. *Transactions of the Japan Institute of Metals*, 27(1):41–50, 1986.

[68] E Nembach. In situ deformation of the γ' hardened superalloy Nimonic PE16 in high-voltage electron microscopes. *Philosophical Magazine A*, 51(4):607–618, 1985.

[69] L Thébaud, P Villechaise, C Crozet, A Devaux, D Béchet, J M Franchet, A L Rouffié, M Mills, and J Cormier. Is there an optimal grain size for creep resistance in Ni-based disk superalloys? *Materials Science and Engineering A*, 2018.

[70] S I Rao, T A Parthasarathy, D M Dimiduk, and P M Hazzledine. Discrete dislocation simulations of precipitation hardening in superalloys. *Philosophical Magazine*, 84(30):3195–3215, October 2004.

[71] M Preuss, J Quinta da Fonseca, B Grant, E Knoche, R Moat, and M Daymond. The effect of γ' particle size on the deformation mechanism in an advanced polycrystalline nickel-base superalloy. In R D Kissinger, D J Deye, A D Anton, D L abd Cetel, M V Nathal, T M Pollock, and D A Woodford, editors, *Superalloys*, pages 405–414. TMS, 2008.

[72] W Hüther and B Reppich. Interaction of dislocations with coherent, stress-free, ordered particles. *Zeitschrift für Metallkunde*, 69(10):628–634, 1978.

[73] S Gao, M Fivel, A Ma, and A Hartmaier. Influence of misfit stresses on dislocation glide in single crystal superalloys: A three-dimensional discrete dislocation dynamics study. *Journal of the Mechanics and Physics of solids*, 76:276–290, 2014.

[74] H Mughrabi. The importance of sign and magnitude of γ/γ' lattice misfit in superalloys—with special reference to the new γ'-hardened cobalt-base superalloys. *Acta Materialia*, 81:21–29, 2014.

[75] A Müller and W Reimers. Small lattice mismatches in highly imperfect single crystals (i). *Physica Status Solidi (a)*, 156(47):47–58, 1996.

[76] C H Zenk, S Neumeier, H J Stone, and M Göken. Mechanical properties and lattice misfit of γ/γ' strengthened Co-base superalloys in the Co-W-Al-Ti quaternary system. *Intermetallics*, 55:28–39, 2014.

[77] J Y Hwang, S Nag, A R P Singh, R Srinivasan, J Tiley, H L Fraser, and R Banerjee. Evolution of the γ/γ' interface width in a commercial nickel base superalloy studied by three-dimensional atom probe tomography. *Scripta Materialia*, 61:92–95, 2009.

[78] P A J Bagot, O B W Silk, J O Douglas, S Pedrazzini, D J Crudden, T L Martin, M C Hardy, M P Moody, and R C Reed. An atom probe tomography study of site preference and partitioning in a nickel-based superalloy. *Acta Materialia*, 125:156–165, 2017.

[79] J X Zhang, J C Wang, H Harada, and Y Koizumi. The effect of lattice misfit on the dislocation motion in superalloys during high-temperature low-stress creep. *Acta Materialia*, 53:4623–4633, 2005.

[80] J Svoboda and P Lukáš. Model of creep in 001-oriented superalloy single crystals. *Acta Materialia*, 46(10):3421–3431, 1998.

[81] R Labusch. A statistical theory of solid solution hardening. *Physica Status Solidi*, 41:659–669, 1970.

[82] H A Roth, C L Davis, and R C Thomson. Modeling solid solution strengthening in nickel alloys. *Metallurgical and Materials Transactions A*, 1997.

[83] H Suzuki. Chemical interaction of solute atoms with dislocations. *Science reports of the Research Institutes, Tohoku University. Ser. A, Physics, chemistry and metallurgy*, 4:455–463, 1952.

[84] P Feltham. Solid solution hardening of metal crystals. *Journal of Physics D: Applied Physics*, 1:303–308, 1968.

[85] L A Gypen and A Deruyttere. Multi-component solid solution hardening. *Journal of Materials Science*, 12:1028–1033, 1977.

[86] Y Gu, T L Lin, and J Guo. Ductilization of Ni_3Al by alloying with zirconium. *Scripta Materialia*, 35(5):609–613, 1996.

[87] J A Horton, C T Liu, and M L Santella. Microstructures and mechanical properties of Ni_3Al alloyed with iron additions. *Metallurgical Transactions A*, 18:1265–1277, 1987.

[88] B Reppich, P Schepp, and G Wehner. Some new aspects concerning particle hardening mechanisms in γ' precipitating nickel-base alloys—II. Experiments. *Acta Metallurgica*, 30(1):95–104, 1982.

[89] J A Lopez and G F Hancock. The effects of non-stoichiometry and titanium additions on the mechanical behaviour of Ni_3Al (γ'). *Physica Status Solidi (a)*, 2:469–474, 1970.

[90] F Heredia and D P Pope. Strengthening of Ni_3Al by ternary additions. *MRS Online Proceedings Library Archive*, 81, 1986.

[91] K Aoki and O Izumi. The relation between defect hardening and substitutional solid solution hardening in an intermetallic compound Ni_3Al. *Physica Status Solidi (a)*, 38:587–594, 1976.

[92] A J E Foreman and M J Makin. Dislocation movement through random arrays of obstacles. *Philosophical Magazine*, 14(131):911–924, 1966.

[93] L M Brown, R K Ham, A Kelly, and R B Nicholson. *Strengthening methods in crystals*, chapter 2, pages 9–135. Elsevier publishing company ltd, 1971.

[94] A Melander. The influence of the finite size of inpenetrable obstacles on the critical resolved shear stress. *Physica Status Solidi (a)*, 43:223–230, 1977.

[95] B Reppich. Some new aspects concerning particle hardening mechanisms in γ' precipitating Ni-base alloys. Theoretical concept. *Acta Metallurgica*, 30(1):87–94, 1982.

[96] M R Ahmadi, E Povoden-Karadeniz, K I Öksüz, A Falahati, and E Kozeschnik. A model for precipitation strengthening in multi-particle systems. *Computational Materials Science*, 91:173–186, August 2014.

[97] B Sonderegger, I Holzer, E Kozeschnik, and C Sommitsch. Particle distance distributions and their effect on precipitation strengthening. *Computer Methods in Materials Science*, Vol. 11, No. 1:148–153, 2011.

[98] H Gleiter and E Hornbogen. Theorie der wechselwirkung von versetzungen mit kohärenten geordneten zonen (i). *Physica Status Solidi*, 12:235–250, 1965.

[99] E Nembach. The dependence of the Hall-Petch slope on the γ' precipitate dispersion of polycrystals of a nickel-base superalloy. *Scripta Metallurgica et Materialia*, 24(4):787–792, 1990.

[100] N Saunders, Z Guo, X Li, A P Miodownik, and J P Schille. Modelling the material properties and behaviour of Ni-based superalloys. In K A Green, T M Pollock, H Harada, T E Howson, R C Reed, J J Schirra, and S Walston, editors, *Superalloys*, pages 849–858. TMS, 2004.

[101] T A Parthasarathy, S I Rao, and D M Dimiduk. A fast spreadsheet model for the yield strength of superalloys. *Superalloys 2004*, pages 887–896, 2004.

[102] L M Brown. The self-stress of dislocations and the shape of extended nodes. *Philosophical Magazine*, 10(105):441–466, 1964.

[103] T Kruml, E. Conforto, B Lo Piccolo, D. Caillard, and J L Martin. From dislocation cores to strength and work-hardening: a study of binary Ni_3Al. *Acta Materialia*, 50(20):5091–5101, 2002.

[104] K V Vamsi and S Karthikeyan. Effect of off-stoichiometry and ternary additions on planar fault energies in Ni_3Al. *Superalloys 2012*, 1:521–530, 2012.

[105] M J Marcinkowski, N Brown, and R M Fisher. Dislocation configurations in $AuCu_3$ and AuCu type superlattices. *Acta Metallurgica*, 9(2):129–137, 1961.

[106] P A Flinn. Solute hardening of close-packed solid solutions. *Acta Metallurgica*, 6(10):631–635, 1958.

[107] J B Cohen and M E Fine. Some aspects of short-range order. *Journal of Physics Radium*, 23(10):749–762, 1962.

[108] R O Williams. Origin of strengthening on precipitation: ordered particles. *Acta Metallurgica*, 5(5):241–244, 1957.

[109] G Inden. Determination of interchange energies from thermodynamic and structural data. *Journal de physique*, 38:373–377, 1977.

[110] A Bieber and F Gautier. Are multiatom interactions relevant for the determination of stability of ordered structures and short range order in binary transition metal alloys? *Journal of the Physical Society of Japan*, 53:2061–2074, 1984.

[111] A Bieber and F Gautier. Multiatom interactions, order and stability in binary transition metal alloys. *Zeitschrift für Physik B Condensed Matter*, 57(4):335–343, 1984.

[112] G Inden, S Bruns, and H Ackermann. Antiphase boundary energies in F.C.C. alloys. *Philosophical Magazine A*, 53(1):87–100, 1986.

[113] D J Crudden, A Mottura, N Warnken, B Raeisinia, and R C Reed. Modelling of the influence of alloy composition on flow stress in high strength nickel-based superalloys. *Acta Materialia*, 75:356–370, 2014.

[114] D M Collins and H J Stone. A modelling approach to yield strength optimisation in a nickel-base superalloy. *International Journal of Plasticity*, 54:96–112, 2014.

[115] A G Khachaturyan and J W Morris Jr. The interfacial tension of a sharp antiphase domain boundary. *Philosophical Magazine A*, 56(4):517–532, 1987.

[116] N Saunders, M Fährmann, and C J Small. The Application of CALPHAD Calculations to Ni-based Superalloys. In T M Pollock, R D Kissinger, R R Bowman, K A Green, M McLean, S Olson, and J J Schirra, editors, *Superalloys*, pages 803–811. TMS, 2000.

[117] M Chandran and S K Sondhi. First-principle calculation of APB energy in Ni-based binary and ternary alloys. *Modelling and Simulation in Materials Science and Engineering*, 19:1–7, 2011.

[118] G Schoeck, S Kohlhammer, and M Fahnle. Planar dissociations and recombination energy of [110] superdislocations in Ni_3Al: Generalized peierls model in combination with ab initio electron theory. *Philosophical Magazine Letters*, 79(11):849–857, 1999.

[119] O N Mryasov, Yu N Gornostyrev, M van Schilfgaarde, and A J Freeman. Superdislocation core structure in $L1_2$, Ni_3Al, Ni_3Ge and Fe_3Ge: Peierls-Nabarro analysis starting from ab-initio GSF energetics calculations. *Acta Materialia*, 50(18):4545–4554, 2002.

[120] A T Paxton and Y Q Sun. The role of planar fault energy in the yield anomaly in L12 intermetallics. *Philosophical Magazine A*, 78(1):85–103, 1998.

[121] P Veyssiere, J Douin, and P Beauchamp. On the presence of super lattice intrinsic stacking faults in plastically deformed Ni_3Al. *Philosophical Magazine A*, 51(3):469–483, 1985.

[122] S Foiles and M Daw. Application of the embedded atom method to Ni_3Al. *Journal of Materials Research*, 2(1):5–15, 1987.

[123] Y Mishin. Atomistic modeling of the γ and γ'-phases of the Ni-Al system. *Acta Materialia*, 52:1451–1467, 2004.

[124] N M Rosengard and H L Skriver. Ab initio study of antiphase boundaries and stacking faults in $L1_2$ and $D0_{22}$ compounds. *Physical Review B*, 50:4848–4861, 1994.

[125] E Nembach. Order strengthening: recent developments, with special reference to aluminium-lithium-alloys. *Progress in Materials Science*, 45:275–338, 2000.

[126] M F Ashby. On the Orowan stress. In A. S. Argon, editor, *Physics of strength and plasticity*, chapter 10, pages 113–131. MIT Press, Cambridge, Massachusetts, 1969.

[127] R O Scattergood and D J Bacon. The Orowan mechanism in anisotropic crystals. *Philosophical Magazine*, 31(1):179–198, 1975.

[128] D J Bacon, U F Kocks, and R O Scattergood. The effect of dislocation self-interaction on the orowan stress. *Philosophical Magazine*, 28(6):1241–1263, 1973.

[129] Z Zhang and D L Chen. Consideration of the orowan strengthening effect in particulate-reinforced metal matrix nanocomposites: A model for predicting their yield strength. *Scripta Materialia*, 54(7):1321–1326, 2006.

[130] Y-C Kang and S Lap-Ip Chan. Tensile properties of nanometric Al_2O_3 particulate-reinforced aluminium matrix composites. *Materials Chemistry and Physics*, 85(2-3):438–443, 2004.

[131] H R Shercliff and M F Ashby. A process model for age hardening of aluminium alloys - I. The model. *Acta metallurgica et materialia*, 38(10):1789–1802, 1990.

[132] R C Reed, T Tao, and N Warnken. Alloys-By-Design: Application to nickel-based single crystal superalloys. *Acta Materialia*, 57(19):5898–5913, 2009.

[133] D A Grose and G S Ansell. The influence of coherency strain on the elevated temperature tensile behavior of Ni-15Cr-A1-Ti-Mo alloys. *Metallurgical Transactions A*, 12(9):1631–1645, 1980.

[134] J M Oblak, D S Duvall, and D F Paulonis. An estimate of the strengthening arising from coherent, tetragonally-distorted particles. *Materials Science and Engineering*, 13:51–56, 1974.

[135] N F Mott and F R N Nabarro. An attempt to estimate the degree of precipitation hardening, with a simple model. *Proceedings of the Physical Society*, 52(1):86–89, January 1940.

[136] E O Hall. The deformation and ageing of mild steel: III discussion of results. *Proceedings of the Physical Society B*, 64:747 – 753, 1951.

[137] N J Petch. The cleavage strength of polycrystals. *Journal of the Iron and Steel Institute*, 174:25–28, 1953.

[138] T J Koppenaal and D Kuhlmann-Wilsdorf. The effect of prestressing on the strength of neutron-irradiated copper single crystals. *Applied Physics Letters*, 4(3):59–61, 1964.

[139] D Locq, P Caron, S Raujol, F Pettinari-Sturmel, A Coujou, and N Clement. On the role of tertiary γ' precipitates in the creep behaviour at 700°C of a PM disk superalloy. In K A Green, T M Pollock, H Harada, T E Howson, R C Reed, J J Schirra, and S Walston, editors, *Superalloys*. TMS, 2004.

[140] R A Stevens and P E J Flewitt. The effects of γ' precipitate coarsening during isothermal aging and creep of the nickel-base superalloy IN-738. *Materials Science and Engineering*, 37:237–247, 1979.

[141] C M Stander. Superalloy design: a Monte Carlo constrained optimization method. *Materials and Design*, 17(1):23–26, 1996.

[142] F Tancret, H K D H Bhadeshia, and D J C MacKay. Design of a creep resistant nickel base superalloy for power plant applications. Part 1 - Mechanical properties modelling. *Materials Science and Technology*, 19(3):283–290, 2003.

[143] W W Milligan, E L Orth, J J Schirra, and M F Savage. Effects of microstructure on the high temperature constitutive behavior of IN100. In K A Green, T M Pollock, H Harada, T E Howson, R C Reed, J J Schirra, and S Walston, editors, *Superalloys*, pages 331–339. TMS, 2004.

[144] S T Wlodek, M Kelly, and D A Alden. The structure of Rene 88 DT. In R D Kissinger, D J Deye, and D L Anton, editors, *Superalloys*, pages 129–136. TMS, 1996.

[145] J MacSleyne, M D Uchic, J P Simmons, and M De Graef. Three-dimensional analysis of secondary γ' precipitates in Rene-88 DT and UMF-20 superalloys. *Acta Materialia*, 57:6251–6267, 2009.

[146] G B Viswanathan, P M Sarosi, M F Henry, D D Whitis, W W Milligan, and M J Mills. Investigation of creep deformation mechanisms at intermediate temperatures in Rene 88 DT. *Acta Materialia*, 53:3041–3057, 2005.

[147] S J Hessell, W Voice, A W James, S A Blackham, C J Small, and M R Winstone. Nickel alloy for turbine engine components. Patent Number 5897718, April 1999.

[148] R R Brooks. *Fatigue damage mechanisms in the nickel-based superalloy Udimet 720*. PhD thesis, University of Sheffield, 1996.

[149] H Monajati, M Jahazi, R Bahrami, and S Yue. The influence of heat treatment conditions on γ' characteristics in Udimet 720. *Materials Science and Engineering A*, 373:286–293, 2004.

[150] M Loo-Morrey and P A S Reed. Anomalous crack shape development (tear drop cracking) in turbine disc material Udimet 720. *Materials Science and Technology*, 16(2):133–146, 2000.

[151] V S K G Kelekanjeri, L K Moss, R A Gerhardt, and J Ilavsky. Quantification of the coarsening kinetics of γ' precipitates in Waspaloy microstructures with different prior homogenizing treatments. *Acta Materialia*, 57:4658–4670, 2009.

[152] H J Penkalla, J Wosik, and A Czyrska-Filemonowicz. Quantitative microstructural characterisation of Ni-base superalloys. *Materials Chemistry and Physics*, 81:417–423, 2003.

[153] H Mughrabi, R W Cahn, P Haasen, and E J Kramer, editors. *Materials Science and Technology*, volume 6. VCH Verlagsgesellschaft mbH and VCH Publishers Inc., 1993.

[154] B Jansson and A Melander. On the critical resolved shear stress from misfitting particles. *Scripta Metallurgica*, 12:497–498, 1978.

[155] F Wallow and E Nembach. Synergisms of grain boundary and γ' particle strengthening in nickel-base superalloys. *Scripta Materialia*, 34(3):499–505, 1996.

[156] E Nembach. Synergetic effects in the superposition of strengthening mechanisms. *Acta metallurgica et materialia*, 40(12):3325–3330, 1992.

[157] L D Connor. *The development of a dual microstructure heat treated Ni-base superalloy for turbine disc applications*. PhD thesis, University of Cambridge, 2009.

[158] E S Huron. Serrated yielding in a nickel-base superalloy. In S D Antolovich, R W Stusrud, R A Mackay, D L Anton, T Khan, R D Kissinger, and D L Klarstrom, editors, *Superalloys*, pages 675–684. TMS, 1992.

[159] C Qiu, X Wu, J Mei, P Andrews, and W Voice. Influence of heat treatment on microstructure and tensile behavior of a hot isostatically pressed nickel-based superalloy. *Journal of Alloys and Compounds*, 578:454–464, 2013.

[160] R R Brooks and W M Rainforth. The effect of microstructure on the morphology of fatigue cracks in UDIMET 720. *Fatigue and Fracture of Engineering Materials and Structures*, 23:725–736, 2000.

[161] R R Stephens, L Grabowski, and D W Hoeppner. The effect of temperature on the behaviour of short fatigue cracks in Waspaloy using an in situ SEM fatigue apparatus. *International Journal of Fatigue*, 15(4):273–282, 1993.

[162] S H Liu, C P Liu, W Q Liu, X N Zhang, P Yan, and C Y Wang. Investigation of the elemental partitioning behaviour and site preference in ternary model nickel-based superalloys by atom probe tomography and first-principles calculations. *Philosophical Magazine*, 96(21):2204–2218, 2016.

[163] M Chandran. Multiscale ab initio simulation of Ni-based alloys: Real-space distribution of atoms in $\gamma + \gamma'$ phase. *Computational Materials Science*, 108:192–204, 2015.

[164] K A Christofidou, N G Jones, E J Pickering, R Flacau, M C Hardy, and H J Stone. The microstructure and hardness of Ni-Co-Al-Ti-Cr quinary alloys. *Journal of Alloys and Compounds*, 688:542–552, 2016.

[165] O I Gorbatov, I L Lomaev, Yu N Gornostyrev, A V Ruban, D Furrer, V Venkatesh, D L Novikov, and S F Burlatsky. Effect of composition on antiphase boundary energy in Ni_3Al based alloys: Ab initio calculations. *Physical Review B*, 93(224106):1–8, 2016.

[166] H Hisazawa, Y Terada, F Adziman, D J Crudden, D M Collins, D E J Armstrong, and R C Reed. The effect of Nb/Ti ratio on hardness in high-strength Ni-based superalloys. *Metals*, 7(71):1–11, 2017.

[167] M P Jackson and R C Reed. Heat treatment of UDIMET 720Li: the effect of microstructure on properties. *Materials Science and Engineering A*, 259:85–97, 1999.

[168] M. V. Nathal, R D Maier, and L J Ebert. The influence of cobalt on the tensile and stress-rupture properties of the nickel-base superalloy MAR-M247. *Metallurgical Transactions A*, 13:1767–1774, 1982.

[169] N G Jones, K A Christofidou, P M Mignanelli, J P Minshull, M C Hardy, and H J Stone. Influence of elevated Co and Ti levels on polycrystalline powder processed Ni-base superalloy. *Materials Science and Technology*, 30(15):1853–1861, 2014.

[170] R R Unocic, L Kovarik, C Shen, P M Sarosi, Y Wang, and J Li. Deformation mechanisms in Ni-base disk superalloys at higher temperatures. In R C Reed, K A Green, P Caron, T P Gabb, M G Fahrmann, E S Huron, and S A Woodard, editors, *Superalloys*, pages 377–385. TMS, 2008.

[171] J Coakley, H Basoalto, and D Dye. Coarsening of a multimodal nickel-base superalloy. *Acta Materialia*, 58:4019–4028, 2010.

[172] H Basoalto and M Anderson. An extension of mean-field coarsening theory to include particle coalescence using nearest-neighbour functions. *Acta Materialia*, 117:122–134, 2016.

[173] J Kundin, L Mushongera, T Goehler, and H Emmerich. Phase-field modeling of the γ'-coarsening behavior in Ni-based superalloys. *Acta Materialia*, 60:3758–3772, 2012.

[174] S Olive, U Grafe, and I Steinbach. The modelling of Ostwald-ripening during non-isothermal heat treatments resulting in temperature dependent matrix solubility of the precipitate forming elements: A further development of the LSW-theory. *Computational Materials Science*, 7:94–97, 1996.

[175] W J Boettinger, U R Kattner, K W Moon, and J H Perepezko. DTA and heat-flux DSC measurements of alloy melting and freezing. Technical report, National Institute of Standards and Technology, 2006.

[176] D Freedman and P Diaconis. On the histogram as a density estimator: l_2 theory. *Zeitschrift für Wahrscheinlichkeitstheorie und verwandte Gebiete*, 57(4):453–476, 1981.

[177] J B Nelson and D P Riley. An experimental investigation of extrapolation methods in the derivation of accurate unit-cell dimensions of crystals. *Proceedings of the Physical Society London*, 57:160–177, 1945.

[178] A Royer and P Bastie. Misfit and lattice parameters of single crystal AM1 superalloy - effects of temperature, precipitate morphology and γ-γ' stresses. In R D Kissinger, D J Deye, A D Anton, D L abd Cetel, M V Nathal, T M Pollock, and D A Woodford, editors, *Superalloys*, pages 221–228. TMS, 1996.

[179] A D Westwood, J R Michael, and M R Notis. Experimental determination of light-element k-factors using the extrapolation technique: oxygen segregation in aluminium nitride. *Journal of Microscopy*, 167(3):287–302, 1992.

[180] C Booth-Morrison, R D Noebe, and D N Seidman. Effects of tantalum on the temporal evolution of a model Ni-Al-Cr superalloy during phase decomposition. *Acta Materialia*, 57:909–920, 2009.

[181] T P Gabb, J Gayda, D F Johnson, R. A. Mackay, R B Rogers, and C K Sudbrack. Comparison of γ-γ' phase coarsening responses of three powder metal disk superalloys. Technical report, NASA, 2016.

[182] S Zhao, J Dong, X Xie, G D Smith, and S J Patel. Thermal stability study on a new Ni-Cr-Co-Mo-Nb-Ti-Al superalloy. In *Superalloys*, 2004.

[183] A Ges, O Fornaro, and H Palacio. Long term coarsening of γ' precipitates in a Ni-base superalloy. *Journal of Materials Science*, 32:3687–3691, 1997.

[184] Y S Yoo, D Y Yoon, and M F Henry. The effect of elastic misfit strain on the morphological evolution of γ'-precipitates in a model Ni-base superalloy. *Metals and Materials*, 1(1):47–61, 1995.

[185] M J Kaufman, P W Vorhees, W C Johnson, and F S Biancaniello. An elastically induced morphological instability of a misfitting precipitate. *Metallurgical Transactions A*, 20:2171–2175, 1989.

[186] M F Henry, Y S Yoo, D Y Yoon, and J Choi. The dendritic growth of γ' precipitates and grain boundary serration in a model nickel-base superalloy. *Metallurgical Transactions A*, 24(1733-1743), 1993.

[187] W W Mullins and R F Sekerka. Morphological stability of a particle growing by diffusion or heat flow. *Journal of Applied Physics*, 34(2):323–329, 1963.

[188] M Hillert, O Hunderi, N Ryum, and T O Sætre. A comment on the Lifshitz-Slyozov-Wagner (L-S-W) theory of particle coarsening. *Scripta Metallurgica*, 23(11):1979–1982, 1989.

[189] P M Sarosi, B Wang, J P Simmons, Y Wang, and M J Mills. Formation of multimodal size distributions of γ' in a nickel-base superalloy during interrupted continuous cooling. *Scripta Materialia*, 57:767–770, 2007.

[190] Y H Wen, J P Simmons, C Shen, C Woodward, and Y Wang. Phase-field modeling of bimodal particle size distributions during continuous cooling. *Acta Materialia*, 51:1123–1132, 2003.

[191] S S Babu, M K Miller, J M Vitek, and S A David. Characterization of the microstructure evolution in a nickel base superalloy during continuous cooling conditions. *Acta Materialia*, 49:4149–4160, 2001.

[192] E H Van der Molen, J M Oblak, and O H Kriege. Control of γ' particle size and volume fraction in the high temperature superalloy Udimet 700. *Metallurgical Transactions*, 2:1627–1633, 1971.

[193] J Y Hwang, R Banerjee, J Tiley, R Srinivasan, G B Viswanathan, and H L Fraser. Nanoscale characterization of elemental partitioning between gamma and gamma prime phases in René 88 DT nickel-base superalloy. *Metallurgical and Materials Transactions A*, 40:24–35, 2009.

[194] H J Jou, P Voorhees, and G B Olson. Computer simulations for the prediction of microstructure/property variation in aeroturbine disks. In K A Green, T M Pollock, H Harada, T E Howson, R C Reed, J J Schirra, and S Walston, editors, *Superalloys*, pages 877–886. TMS, 2004.

[195] W T Loomis, J W Freeman, and D L Sponseller. The influence of molybdenum on the γ' phase in experimental nickel-base superalloys. *Metallurgical Transactions*, 3(4):989–1000, 1972.

[196] X P Tan, D Mangelinck, C Perrin-Pellegrino, L Rougier, Ch-A Gandin, A Jacot, D Ponsen, and V Jaquet. Atom probe tomography of secondary γ' precipitation in a single crystal Ni-based superalloy after ageing at 1100°C. *Journal of Alloys and Compounds*, 611:389–394, 2014.

[197] D M Collins, L Yan, E A Marquis, L D Connor, J J Ciardiello, A D Evans, and H J Stone. Lattice misfit during ageing of a polycrystalline nickel-base superalloy. *Acta Materialia*, 61:7791–7804, 2013.

[198] E Y Plotnikov, Z Mao, R D Noebe, and D N Seidman. Temporal evolution of the γ (fcc)/ γ' ($L1_2$) interfacial width in binary Ni-Al alloys. *Scripta Materialia*, 70:51–54, 2014.

[199] S Meher and R. Banerjee. Partitioning and site occupancy of Ta and Mo in Co-base γ/γ' alloys studied by atom probe tomography. *Intermetallics*, 49:138–142, 2014.

[200] J W Cahn and J E Hilliard. Free energy of a nonuniform system. I. Interfacial free energy. *The journal of chemical physics*, 28(2):258–267, 1958.

[201] A J Ardell and V Ozolins. Trans-interface diffusion-controlled coarsening. *Nature Materials*, 4:309–316, 2005.

[202] A J Ardell. Gradient energy, interfacial energy and interface width. *Scripta Materialia*, 66:423–426, 2012.

[203] L D Connor, H J Stone, D M Collins, M Preuss, M C Hardy, and C M F Rae. The effect of cooling rate from solution on the lattice misfit during isothermal aging of a Ni-base superalloy. *Metallurgical and Materials Transactions A*, 45:2436–2444, 2014.

[204] E Fleischmann, M K Miller, E Affeldt, and U Glatzel. Quantitative experimental determination of the solid solution hardening potential of rhenium, tungsten and molybdenum in single-crystal nickel-based superalloys. *Acta Materialia*, 87:350–356, 2015.

[205] M Preuss, J W L Pang, P J Withers, and G J Baxter. Inertia welding nickel-based superalloy: Part I. Metallurgical characterisation. *Metallurgical and Materials Transactions A*, 33:3215–3225, 2002.

[206] Y F Han, Y M Wang, and M C Chaturvedi. Strengthening in a DS casting Ni_3Al base alloy IC6. *Advanced Performance Materials*, 2:259–268, 1995.

[207] R. A. Mackay, M. V. Nathal, and D D Pearson. Influence of molybdenum on the creep properties of nickel-base superalloy single crystals. *Metallurgical Transactions A*, 21:381–388, 1990.

[208] M Pessah, P Caron, and T Khan. Effect of μ phase on the mechanical properties of a nickel-base single crystal superalloy. In S D Antolovich, R W Stusrud, R A Mackay, D L Anton, T Khan, R D Kissinger, and D L Klarstrom, editors, *Superalloys*, pages 567–576. TMS, 1992.

[209] M M Tavakkoli and S M Abbasi. Effect of molybdenum on grain boundary segregation in Involoy 901 superalloy. *Materials and Design*, 46:573–578, 2013.

[210] V Biss and D L Sponseller. The effect of molybdenum on γ' coarsening and on elevated-temperature hardness in some experimental nickel-base superalloys. *Metallurgical Transactions*, 4:1953–1960, 1973.

[211] P Nash, S Fielding, and D R F West. Phase equilibria in nickel rich Ni-Al-Mo and Ni-Al-W alloys. *Metal Science*, 17:192–194, 1983.

[212] G N Maniar and J E Bridge. Effect of gamma-gamma prime mismatch, volume fraction gamma prime, and gamma prime morphology on elevated temperature properties of Ni, 20 Cr, 5.5 Mo, Ti, Al alloys. *Metallurgical Transactions*, 2:95–102, 1970.

[213] J Zhang, J Li, T Jin, X Sun, and Z Hu. Effect of Mo concentration on creep properties of a single crystal nickel-base superalloy. *Materials Science and Engineering A*, 527:3051–3056, 2010.

[214] J R Santisteban, M R Daymond, J A James, and Edwards L. ENGIN-X: a third-generation neutron strain scanner. *Journal of Applied Crystallography*, 39:812–825, 2006.

[215] M R Daymond and H G Priesmeyer. Elastoplastic deformation of ferritic steel and cementite studied by neutron diffraction and self-consistent modelling. *Acta Materialia*, 50:1613–1626, 2002.

[216] A C Larson and R B Von Dreele. *GSAS - general structure analysis system*. Los Alamos National Laboratory.

[217] A Le Bail. Whole powder pattern decomposition methods and applications: a retrospection. *Powder Diffraction*, 20(4):316–326, 2005.

[218] H J Stone, T M Holden, and R C Reed. On the generation of microstrains during the plastic deformation of waspaloy. *Acta Metallurgica*, 47(17):4435–4448, 1999.

[219] S Ma, P Rangaswamy, and B S Majumdar. Microstress evolution during in situ loading of a superalloy containing high volume fraction of γ' phase. *Scripta Materialia*, 48:525–530, 2003.

[220] S Ma, D Brown, M A M Bourke, M R Daymond, and B S Majumdar. Microstrain evolution during creep of a high volume fraction superalloy. *Materials Science and Engineering A*, 399(1-2):141–153, 2005.

[221] S Ikeda and J M Carpenter. Wide-energy-range, high-resolution measurements of neutron pulse shapes of polyethylene moderators. *Nuclear Instruments and Methods in Physics Research A*, 239:536–544, 1985.

[222] M R Daymond, M A M Bourke, R B Von Dreele, B Clausen, and T Lorentzen. Use of Rietveld refinement for elastic macrostrain determination and for evaluation of plastic strain history from diffraction spectra. *Journal of Applied Physics*, 82(4):1554–1562, 1997.

[223] P E Aba-Perea, T Pirling, P J Withers, J Kelleher, S Kabra, and M Preuss. Determination of the high temperature elastic properties and diffraction elastic constants of Ni-base superalloys. *Materials and Design*, 89:856–863, 2016.

[224] B M B Grant, E M Francis, J Quinta da Fonseca, M R Daymond, and M Preuss. Deformation behaviour of an advanced nickel-based superalloy studied by neutron diffraction and electron microscopy. *Acta Materialia*, 60:6829–6841, 2012.

[225] B M B Grant, E M Francis, J Quinta da Fonseca, M Preuss, and M R Daymond. The effect of γ' size and alloy chemistry on dynamic strain ageing in advanced polycrystalline nickel base superalloys. *Materials Science and Engineering A*, 573:54–61, 2013.

[226] F Pyczak, S Neumeier, and M Göken. Influence of lattice misfit on the internal stress and strain states before and after creep investigated in nickel-base superalloys containing rhenium and ruthenium. *Materials Science and Engineering A*, pages 295–300, 2009.

[227] E M Francis, B M B Grant, J Quinta da Fonseca, P J Phillips, M J Mills, M R Daymond, and M Preuss. High-temperature deformation mechanisms in a polycrystalline nickel-base superalloy studied by neutron diffraction and electron microscopy. *Acta Materialia*, 74:18–29, 2014.

[228] B Clausen, T Lorentzen, and T Leffers. Self-consistent modelling of the plastic deformation mechanisms of F.C.C. polycrystals and its implications for diffraction measurements of internal stresses. *Acta Materialia*, 46(9):3087–3098, 1998.

[229] M R Daymond, M Preuss, and B Clausen. Evidence of variation in slip mode in a polycrystalline nickel-base superalloy with change in temperature from neutron diffraction strain measurements. *Acta Materialia*, 55:3089–3102, 2007.

[230] D Dye, H J Stone, and R C Reed. Intergranular and interphase microstresses. *Current Opinion in Solid State and Materials Science*, 5:31–37, 2001.

[231] D Dye, J Coakley, V A Vorontsov, H J Stone, and R B Rogge. Elastic moduli and load partitioning in a single-crystal nickel superalloy. *Scripta Materialia*, 61:109–112, 2009.

[232] J D Eshelby. The determination of the elastic field of an ellipsoidal inclusion, and related problems. *Proceedings of the Royal Society of London A*, 241(1226):376–396, 1957.

[233] D Barba, E Alabort, S Pedrazzini, D M Collins, A J Wilkinson, P A J Bagot, M P Moody, C Atkinson, A Jérusalem, and R C Reed. On the microtwinning mechanism in a single crystal superalloy. *Acta Materialia*, 135:314–329, 2017.

[234] R C Ecob, R A Ricks, and A J Porter. The measurement of precipitate/matrix lattice mismatch in nickel-base superalloys. *Scripta Metallurgica*, 16:1085–1090, 1982.